Reactive Transport Simulations of the Alteration of Interfaces Between Bentonite/LHHPC/Host Rock and the Impact on Radionuclide Migration

NWMO-TR-2021-14 **July 2021**

Mingliang Xie[1], K. Ulrich Mayer[1] and Kerry T. B. MacQuarrie[2]

[1]Department of Earth, Ocean and Atmospheric Sciences, University of British Columbia

[2]Department of Civil Engineering, University of New Brunswick

nwmo
NUCLEAR WASTE MANAGEMENT ORGANIZATION
SOCIÉTÉ DE GESTION DES DÉCHETS NUCLÉAIRES

Nuclear Waste Management Organization
22 St. Clair Avenue East, 6th Floor
Toronto, Ontario
M4T 2S3
Canada

Tel: 416-934-9814
Web: www.nwmo.ca

Reactive Transport Simulations of the Alteration of Interfaces between Bentonite/LHHPC/Host Rock and the Impact on Radionuclide Migration

NWMO-TR-2021-14

July 2021

Mingliang Xie[1], K. Ulrich Mayer[1] and Kerry T. B. MacQuarrie[2]

[1]Department of Earth, Ocean and Atmospheric Sciences, University of British Columbia
[2]Department of Civil Engineering, University of New Brunswick

Document History

Title:	Reactive Transport Simulations of the Alteration of Interfaces between Bentonite/LHHPC/Host Rock and the Impact on Radionuclide Migration		
Report Number:	NWMO-TR-2021-14		
Revision:	R00	Date:	July 2021
[1]Department of Earth, Ocean and Atmospheric Sciences, University of British Columbia [2]Department of Civil Engineering, University of New Brunswick			
Authored by:	Mingliang Xie[1]		
Verified by:	Kerry T. B. MacQuarrie[2]		
Approved by:	K. Ulrich Mayer[1]		
Nuclear Waste Management Organization			
Reviewed by:	Tammy Yang, Monique Hobbs		
Accepted by:	Paul Gierszewski		

Revision Summary		
Revision Number	**Date**	**Description of Changes/Improvements**
R00	2021-07	Initial issue

ABSTRACT

Title: **Reactive Transport Simulations of the Alteration of Interfaces Between Bentonite/LHHPC/Host Rock and the Impact on Radionuclide Migration**
Report No.: **NWMO-TR-2020-14**
Author(s): Mingliang Xie[1], K. Ulrich Mayer[1] and Kerry T. B. MacQuarrie[2]
Company: [1]Department of Earth, Ocean and Atmospheric Sciences, University of British Columbia
[2]Department of Civil Engineering, University of New Brunswick
Date: July 2021

Abstract

In the Canadian concept for a deep geological repository for used nuclear fuel waste, Highly-compacted Bentonite (HB) and Low-Heat High-Performance Concrete (LHHPC) are potential engineered barrier materials. The initial mineralogy and pore water compositions are different for bentonite, LHHPC and potential host rocks, such as limestone and granite. Consequently, chemical alterations are expected at the interfaces between these materials, which could lead to modifications of the transport properties of the barrier system. One-dimensional isothermal reactive transport simulations have been performed with MIN3P-THCm to investigate long-term chemical interactions driven by diffusive transport across the interfaces. Two scenarios were simulated to investigate the potential alterations in pore water composition, mineralogy, porosity, and diffusive transport in the barrier system: 1) HB/LHHPC/host rock; and 2) HB/host rock. For both scenarios, comparison simulations were undertaken to investigate the impact of excavation damaged zones (EDZs) on reactive transport and radionuclide migration. In the first scenario, simulation results show that due to the relatively high pH of pore water in LHHPC (pH = 9.7), substantial mineral dissolution and precipitation occur at the interfaces of bentonite/LHHPC. After 100,000 years, the alteration reactions remain restricted to a distance of 2 cm from the interfaces. The alteration mechanisms depend mainly on the mineralogy and pore water chemical composition of the host rock. In the case of granitic host rock, Calcium Silicate Hydrate (CSH) phases present in LHHPC are predicted to transform into tobermorite, phillipsite and saponite within 1,000 years. The simulations indicate that a substantial reduction in porosity occurs after about 1,500 years in the concrete adjacent to bentonite due to the precipitation of tobermorite, sepiolite, saponite, phillipsite, gypsum and calcite. In the case of limestone host rock, saponite and sepiolite are the dominant minerals formed in the LHHPC within a time frame of 1,000 years. In this case, complete pore clogging is predicted after about 3,800 years in the limestone adjacent to the LHHPC, mainly due to the precipitation of saponite, sepiolite, calcite and phillipsite. Simulations of diffusive I^- transport across the material interfaces suggest that radionuclide migration can be significantly retarded if interface alteration, due to the presence of LHHPC, leads to clogging before radionuclide release. Due to the higher initial porosities assumed within the EDZs, simulations including EDZs required more time to reach complete pore clogging at the interface between LHHPC and the host rocks. Because of the low reactivity of bentonite compared to LHHPC, only relatively minor mineral volume fraction and porosity changes were predicted for the HB/granite and HB/limestone host rock cases. Radionuclide transport in the HB/host rock cases was not significantly affected by porosity changes or the presence of excavation damage zones.

TABLE OF CONTENTS

LIST OF TABLES

Page

LIST OF FIGURES

Page

1. INTRODUCTION

Bentonite and concrete are potential engineered barrier materials (EBM) to be integrated into the natural barrier system for a deep geological repository (DGR) for used nuclear fuel waste. Due to the distinct differences in mineralogy and pore water composition between the EBM and the surrounding host rocks, chemical reactions between the EBM and host rocks are expected. These reactions may alter the material properties, which may in turn have implications for the evaluation of the long-term performance of the multilayer barrier system.

Low-heat high-performance concrete (LHHPC; Breton 1996) is a potential EBM for deep geological repositories in Canada. LHHPC is concrete with low OPC (Ordinary Portland Cement) content, very low heat of hydration (15 °C), low alkalinity (pH 9.7) and high strength. The key benefit of LHHPC is the low pH of the cement pore water after hydration, which helps minimize clay mineral alteration in adjacent host rocks (Dolder et al. 2016; Savage et al. 2010).

Different countries have developed various types of low pH concrete (Calvo et al. 2010, 2013; Savage and Benbow 2007; Dauzeres et al. 2016). The principle is to modify the cementitious substance through partially replacing the OPC by supplementary substances such as fly ash and/or silica fume (Lothenbach et al. 2011; Deschner et al. 2012). Gaucher and Blanc (2006) provided a comprehensive review of the research on cement/clay interactions. Some of the key findings from experimental studies on cement/clay interactions are:

1. Read et al. (2001) reported results from in situ experiments on different concretes placed in the Boom Clay at the Mol laboratory (Belgium) at 85 °C for 12 to 18 months. The results showed a zoning in element distribution – the 100 to 250 µm wide clay alteration zone was impoverished in Al, Si, and Mg and enriched in Ca with respect to the unaltered clay, and the concrete alteration zone showed the reversed trend with a loss of Ca and enrichment of Al, Si and Mg. A thin layer at the interface (10 µm) was Mg-Al-Si rich, and contained weakly crystalline gel with a composition corresponding to hydrotalcite and sepiolite.
2. Lerouge et al. (2017) reported on in situ experiments conducted over five years on low alkali concrete (LAC) in contact with Opalinus Clay at the Mont Terri Underground Rock Laboratory in Switzerland. The results showed an alteration zone (about 1 mm thick) with highly porous (75% porosity) white crust in the concrete. At the interface, evidence of sulfate and saponite precipitation was detected.
3. Experiments on a FEBEX-bentonite/concrete interface (13 year in situ experiment and laboratory experiments) showed the formation of Al-tobermorite and saponite at the interface, which was the key mechanism leading to the pH buffering (Fernández et al. 2016; Alonso et al. 2017; Fernández et al. 2017).
4. Laboratory experiments on MX-80 bentonite immersed in a highly saline solution, rich in NaCl and $MgCl_2$, for up to 700 days showed mineral structural change and partial loss of water sorption capacity of smectite (Herbert et al. 2004).

All of the above experiments are considered short term given the slow hydration and alteration processes of clay minerals and cement phases.

Natural analogue studies also permit the evaluation of the long-term alteration of clay and cement materials. Roman marine concrete, as an example, was produced over 2000 years ago using volcanic pozzolanic ash and hydrated lime, and has been shown to remain strong and

highly resistant to corrosion in sea water (Hodgkinson and Hughes 1999; Jackson et al. 2017). The key cementitious substances are Al-tobermorite and Phillipsite (Jackson et al. 2017). The high concentration of Al_2O_3 and SiO_2 in the volcanic ash results in the formation of Al-tobermorite, which forms normally only at higher temperatures (>170 °C) (Jackson et al. 2017). The Cyprus Natural Analogue Project (CNAP) has investigated interactions between low alkaline groundwater, similar to the pore waters of low alkali cements, and extensive bentonite deposits (Alexander et al. 2012, 2013). The results showed that chemical reactions lead to the decomposition of montmorillonite and formation of a palygorskite-like mineral, dissolution of amorphous or poorly-crystalline biogenic silica, resulting in high Si pore water. The results also indicate minimal volumetric reaction of bentonite near the surface of the bentonite layer that has been exposed to alkali pore water (Alexander et al. 2013). In the study of the Maqarin natural analogue site, sealing of veins and fractures due to precipitation of CSH phases was observed, attributed to the degradation of naturally occurring cement-like material (Martin et al. 2016). Other natural analogue projects have investigated interactions of highly alkaline (pH > 12.1) solutions with clay rocks (Smellie 1998; Milodowski et al. 2016; Cassagnabère et al. 2001; Tinseau et al. 2006). The findings of these studies are less relevant to the current study and thus not discussed in detail here. Unfortunately for natural analogue studies, the initial conditions and the temporal evolution of the thermodynamic and geochemical conditions remain mostly unknown, which complicates the interpretation of the findings.

Over the past few decades, geochemical or reactive transport simulations have increasingly been applied to analyse laboratory and in situ experiments, and for natural analogue studies. Simulation studies have been used to understand the complex processes governing the interplay between cement and clay, to validate numerical models and thermodynamic databases, and ultimately to develop partially validated predictive tools for the DGR industry (Lothenbach et al. 2012, 2014; Kulik et al. 2013; Savage and Cloet 2018). Savage and Cloet (2018) have presented a detailed review of numerical simulation studies dealing with cement/clay interactions. However, only a few have dealt with the long-term stability of potential barrier materials (i.e. bentonite, LHHPC) specifically for the host rock environments that may be encountered in a Canadian DGR (Wilson et al. 2012). Wilson et al. (2012) used reactive transport modelling to investigate the evolution of two shaft sealing materials and their interfaces with the host geosphere, namely: (a) a bentonite/sand mixture contacting Georgian Bay Shale, and (b) LHHPC in contact with Cobourg Limestone. For the second scenario, which is more relevant to the current work, simulations predicted the alteration of cementitious substances to sepiolite, saponite and thaumasite, which ultimately resulted in pore clogging (Wilson et al. 2012).

This study employs reactive transport simulations to further investigate the processes and alterations occurring near bentonite/LHHPC/host rock interfaces and their potential impact on radionuclide migration. No Canadian site has yet been identified for a DGR for high-level nuclear waste; however, various case studies for sedimentary and crystalline host rocks have been conducted by the NWMO (e.g. NWMO 2017, 2018), as illustrative post closure safety assessments. The simulations included in this report are based on two illustrative case studies of post closure safety for a DGR sited in a hypothetical crystalline Canadian Shield setting (NWMO 2017), and in a hypothetical sedimentary rock setting in Southern Ontario (NWMO 2018).

The reactive transport code used for all simulations is MIN3P-THCm (v1.0.690) which has been developed on the basis of the original MIN3P code (Mayer 1999; Mayer et al. 2002) and further enhancements included in MIN3P-D (Henderson et al. 2009) and MIN3P-NWMO (Bea et al. 2011). MIN3P-THCm is a general purpose multicomponent reactive transport code for variably

saturated porous media. It is characterized by a high degree of flexibility and is applicable to a wide range of hydrogeological and geochemical problems. Chemical processes included are homogeneous reactions in the aqueous phase, as well as a variety of heterogeneous reactions. The code can simulate groundwater flow, advective-diffusive solute transport, multicomponent diffusion and electrochemical migration following the approach of Giambalvo et al. (2002), multisite ion exchange and geochemical reactions under variable density, non-isothermal, and highly saline conditions (Bea et al. 2011; 2012; Xie et al. 2014a, 2014b). For additional details on the general code capabilities, the reader is referred to Mayer et al. (2002), Henderson et al. (2009), Mayer and MacQuarrie (2010) and Bea et al. (2011).

2. SPECIFIC ION INTERACTION THEORY (SIT)

Ion interactions are neglected in dilute solution activity coefficient models, such as Debye-Hückel (DH) and its variants appropriate for solutions with ionic strengths up to 0.7 mol L^{-1} (Debye and Hückel 1923), which is the maximum threshold to ensure the accuracy of applying the extended Debye-Hückel type equations such as the Davies equation (Davies 1962; Grenthe et al. 2013). This is because these approaches are not able to take electrolyte-specific effects into account. However, such effects are stronger when the concentrations of a solution with multiple species are higher. Therefore, various empirical models were developed to estimate the activity coefficients of both components and species at the ionic strength of the solution. For saline solutions, the most popular models can be grouped in two approaches, which are based on: (a) the specific ion interaction theory (SIT) (e.g. the SIT model by Sipos 2008), and (b) the Pitzer equations (Pitzer 1991). Both approaches have their advantages. The SIT approach considers both long-range electrostatic and short-range specific ion-ion interactions. However, the SIT model is relatively simple, only requiring the addition of one term to the Debye-Hückel equation (Spisol 2008). It is thus computationally more efficient and believed to be more practical. The ion interaction coefficients (empirical) have to be determined experimentally. The Pitzer approach uses a more elaborate virial expansion and is able to describe activity coefficients of a large number of electrolytes with high precision over a large concentration range (Grenthe et al. 2013). The key problem when applying the Pitzer model to describe the activity factors is to accurately determine the concentration dependence of the second virial coefficient for complexes, which is often difficult or even impossible, especially for highly charged ions (e.g. Al^{3+}) in salt-brine systems (Grenthe et al. 2013). Extensive comparison of the SIT and Pitzer approaches were undertaken to compare the measured mean activity coefficients to the calculated values using both approaches (Grenthe and Plyasunov 1997). Grenthe and Plyasunov (1997) concluded that SIT showed good agreement to the experiemntal data with an ionic strength up to 3.0 mol L^{-1}. Preis and Gamsjäger (2001) demonstrated that SIT can be successfully employed for ionic products of aqueous solutions at ionic strengths significantly higher than 3.5 mol L^{-1} and up to 6.2 mol L^{-1}, although the Pitzer model produced more accurate results. For the simulations conducted in this study, pore water ionic strengths range up to approximately 5.6 mol L^{-1} and thus an alternative activity coefficient model (i.e. the SIT approach) was implemented.

2.1 SPECIFIC ION INTERACTION THEORY AND IMPLEMENTATION

In concentrated electrolyte solutions, short-range, non-electrostatic interactions must be considered. One possible way is based on the Brönsted–Guggenheim–Scatchard Specific Ion

Interaction Theory (SIT theory), which was first suggested by Brönsted (1922), and further developed by Guggenheim (1955), Scatchard (1936) and Ciavatta (1980). Based on this theory, the activity coefficient (γ_i) is modified by the addition of a linear term to the DH expression (Sipos 2008):

$$log\gamma_i = \frac{-AZ_i^2\sqrt{I}}{1 + B\sqrt{I}} + \sum_k \varepsilon(i,k)\, m_k \qquad \text{Equation 2-1}$$

in which, A is a constant of the DH limiting law (0.509 kg$^{1/2}$ mol$^{-1/2}$ at 25 °C), B is an empirical constant (kg$^{1/2}$ mol$^{-1/2}$), m_k is the molality of the ion k, and $\varepsilon(i,k)$ is an empirical aqueous species interaction coefficient representing the specific short-range interactions between the aqueous species i and k. For uncharged species, or ions of the same charge, $\varepsilon(i,k)$ is assumed to be 0.0. The accuracy of the SIT theory is well accepted when the ionic strength is between 0.5 to 3.5 mol kg^{-1} (Grenthe et al. 2013). Furthermore, it has also been demonstrated that SIT can be successfully employed at ionic strengths (I) significantly higher than 3.5 mol kg^{-1} for aqueous solutions of NaCl (I ≤ 6.00 mol kg^{-1}), KCl (I ≤ 4.57 mol kg^{-1}), CsCl (I ≤ 10.02 mol kg^{-1}), KBr (I ≤ 4.71 mol kg^{-1}), KI (I ≤ 6.96 mol kg^{-1}), and $NaClO_4$ (I ≤ 13.66 mol kg^{-1}) (Preis and Gamsjäger 2001; Sipos 2008). However, relatively little is known about the nature of $\varepsilon(i,k)$ at these high ionic strengths in other electrolytes (Sipos 2008). The most likely reason is the low reliability of a significant fraction of the experimental data due to the difficulties of working with solutions of extremely high ionic strength (Sipos et al. 1994, 1998).

This model (Equation 2-1) has been newly implemented in MIN3P-THCm (v1.0.690) and applied for the simulations in this report. A verification problem for the SIT model implementation is presented in Appendix A.1; the results produced by PHREEQC (Parkhurst and Appelo 2013) and MIN3P-THCm were found to be identical. The SIT thermodynamic database THERMOCHIMIE-TDB Version 9b0 (www.thermochimie-tdb.com) in PHREEQC database format was used for the PHREEQC simulations. The same database was converted into MIN3P-THCm format for the corresponding MIN3P-THCm simulations. The main reason for selecting this database is that it includes consistent thermodynamic data for cementitious and clay systems (Giffaut et al. 2014).

3. MATERIAL PROPERTIES AND INITIAL CONDITIONS

In the following subsections, the material properties, initial mineral compositions and pore water chemical compositions for the host rocks and engineered barrier materials are described. Properties are defined for granite, as a representative crystalline rock, limestone as the sedimentary rock example, and LHHPC and bentonite.

3.1 GRANITE HOST ROCK

As shown in Table 1, the porosity of the intact granite host rock is assumed to be 0.3%. Granite within the inner excavation damage zone (EDZ) in the placement rooms is assumed to extend from the tunnel wall for one metre and the porosity in this zone is 0.6%. The outer EDZ is assumed to extend for two metres beyond the inner EDZ, and its porosity is assigned a value of 0.3% (NWMO 2017). Due to the disturbance of the rock in the inner and outer EDZs, the pore connectivity of the rock in both EDZs is considered to be enhanced. Therefore, the tortuosity of the rock in the EDZs is assumed to be 0.10, compared to the intact rock value of 0.06 (NWMO

2017). Correspondingly, the effective diffusion coefficient within the inner EDZ is higher than that of the outer EDZ, both of which are higher than the intact granite (Table 1, NWMO 2017).

Table 1: Transport Parameters for Granite within EDZ Zones and Intact Rock (NWMO 2017)

Zone	Extent from Placement Room Surface [m]	Porosity [%]	Tortuosity [-]	Effective Diffusion Coefficient [$m^2\ s^{-1}$]
Inner EDZ	1.0	0.6	0.10	1.11×10^{-12}
Outer EDZ	1.0 to 3.0	0.3	0.10	5.55×10^{-13}
Intact	>3.0	0.3	0.06	3.33×10^{-13}

The assumed initial mineralogical composition of granite is given in Table 2; the main minerals for intact granite are quartz, albite and microcline (based on MacQuarrie et al. 2010). Because the porosity of the outer EDZ is assumed to be the same as that for intact granite, the mineral composition is also the same. The volume fractions of minerals within the inner EDZ are scaled down in direct proportions to reflect the porosity increase.

Table 2: Volume Fractions of the Main Minerals in Granite (Based on MacQuarrie et al. 2010)

Mineral	Formula	Density [$g\ cm^{-3}$]	Volume Fraction [%]	
			Intact & Outer EDZ	Inner EDZ
Quartz	SiO_2	2.648	26.50	26.42
Albite(low) (Plagioclase)	$NaAlSi_3O_8$	2.611	32.60	32.50
Microcline-K (K-feldspar)	$K(AlSi_3)O_8$	2.560	32.20	32.10
chloriteca-1 (Clinochlore)	$Mg_5Al_2Si_3O_{10}(OH)_8$	2.628	1.22	1.22
Phlogopite_k (Biotite)	$KMg_3Si_3AlO_{10}(OH)_2$	2.788	4.10	4.09

The chemical composition of the granite pore water, which is a reference crystalline rock groundwater (CR-10) defined for an Illustrative Case Study based on groundwater found at a depth of around 500 m (NWMO 2017), is given in Table 3. These data were re-equilibrated with the minerals composing the granitic host rock (Table 2) using PHREEQC (Parkhurst and Appelo 2013). The PHREEQC-derived component concentrations are listed in Table 3 (Calculated), and were used for the initial chemical composition of the pore water for the intact granite as well as granite in the EDZs (Table 3). Only minor differences exist between the experimental and re-equilibrated component concentrations. The concentration unit of components is mol L^{-1} water for all calculated concentrations using PHREEQC and MIN3P-THCm in this report.

Table 3: Initial Component Concentrations (in mol L^{-1} H_2O) of the Granite Pore Water

Component	CR-10[$]	Calculated[#]
Al^{3+}	n.d.	3.10×10^{-8}
CO_3^{2-}	1.18×10^{-3}	1.18×10^{-3}
Ca^{2+}	5.38×10^{-2}	5.38×10^{-2}
Cl^-	1.74×10^{-1}	1.74×10^{-1}
Fe^{2+}	1.81×10^{-5}	1.81×10^{-5}
K^+	3.88×10^{-4}	1.73×10^{-4}
Mg^{2+}	2.50×10^{-3}	2.55×10^{-3}
Na^+	8.36×10^{-2}	8.38×10^{-2}
SO_4^{2-}	1.05×10^{-2}	1.05×10^{-2}
H_4SiO_4	1.80×10^{-4}	1.81×10^{-4}
Ionic strength	0.25	0.25
pH [-]	7.0	7.33
pe [-]	-3.38	-3.06

n.d. – not determined, [$] - according to NWMO (2017), [#] - the component concentrations of CR-10 re-equilibrated to the minerals in granite calculated using PHREEQC

3.2 LIMESTONE

Limestone (as a potential host rock for a DGR in a sedimentary basin) typically has a low porosity, low permeability, and low effective diffusion coefficient (Table 4, NWMO 2018). The porosity values assigned to the inner and outer limestone EDZs are based on NWMO (2018) (Cobourg limestone Section 7.7). The tortuosity of the inner and outer EDZs is assumed to be 0.0594, which is two-fold higher than that in intact limestone (NWMO 2018). The effective diffusion coefficients within the outer and inner EDZs are thus increased by four- and two-fold from that of the intact limestone (Table 4).

Table 4: Transport Parameters for Limestone within EDZ Zones and Intact Rock (NWMO 2018)

Zone	Extent from Placement Room Surface [m]	Porosity [%]	Tortuosity [-]	Effective Diffusion Coefficient [m^2 s^{-1}]
Inner EDZ	1.0	3.0	5.94×10^{-2}	3.30×10^{-12}
Outer EDZ	1.0 to 3.0	1.5	5.94×10^{-2}	1.65×10^{-12}
Intact	>3.0	1.5	2.97×10^{-2}	8.24×10^{-13}

The assumed initial mineral composition of the limestone is presented in Table 5 (Wilson et al. 2012; Table 2.2.1 and 2.2.2). The volume fractions of minerals in the intact limestone and those

in the outer EDZ are assumed to be the same. The volume fractions of minerals in the inner EDZ are scaled down in proportion to the porosity increase (Table 5).

Table 5: Volume Fractions of the Main Limestone Minerals (Based on Wilson et al. 2012)

Mineral	Formula	Density [g cm^{-3}]	Volume Fraction [%]	
			Intact & Outer EDZ	Inner EDZ
Calcite	$CaCO_3$	2.710	79.84	78.72
Dolomite	$CaMg(CO_3)_2$	2.865	7.48	7.38
Quartz	SiO_2	2.648	3.42	3.37
Chlorite (clinoclore)	$Mg_5Al_2Si_3O_{10}(OH)_8$	2.628	1.98	1.95
Illite	$K_{0.6}Mg_{0.25}Al_{1.8}Al_{0.5}Si_{3.5}O_{10}(OH)_2$	2.825	5.88	5.80

The assumed chemical composition of a reference limestone pore water (SR-270-PW) is based on King et al. (2017) (Table 6). These data were re-equilibrated with the initial mineral volume fractions of limestone (Table 5) using PHREEQC v3.1.1.8288 (Parkhurst and Appelo 2013) and SIT database. The resulting pore water component compositions are listed in Table 6 (Calculated), and these were applied in subsequent simulations as initial conditions in intact limestone as well as in the EDZs (Table 6). The equilibrated (calculated) pore water has somewhat lower ionic strength and Ca^{2+}, and higher pH, Mg^{2+} and H_4SiO_4, than SR-270-PW pore water. The difference is due to the different approaches used when calculating the ion interaction coefficients used for the equilibration. SR-270-PW was equilibrated with minerals using the Pitzer database (NWMO internal document, email communication). It is important to point out that SR-270-PW is highly saline and thus the Pitzer model and the corresponding database are deemed more accurate to calculate the geochemical speciation than the SIT approach. However, for geochemical systems including solid phases in LHHPC (cement + granite aggregate) and bentonite, Al and Si are required and these elements are not included in the PHREEQC v3.1.1.8288 Pitzer database. Therefore, the database THERMOCHIMIE-TDB Version 9b0, including SIT parameters (Giffaut et al. 2014), was applied for the current equilibration calculations and for subsequent reactive transport simulations.

Table 6: Initial Component Concentrations (in mol L^{-1} H_2O) of Pore Water in Limestone

Component	SR-270-PW[$]	Calculated[#]
Al^{3+}	n.d.	7.59×10^{-11}
CO_3^{2-}	2.52×10^{-3}	1.90×10^{-3}
Ca^{2+}	1.10	2.33×10^{-1}
Cl^-	6.53	6.53
Fe^{2+}	7.38×10^{-4}	7.38×10^{-4}
K^+	4.39×10^{-1}	4.39×10^{-1}
Mg^{2+}	4.63×10^{-1}	1.33
Na^+	2.99	2.99
SO_4^{2-}	6.29×10^{-3}	6.29×10^{-3}
H_4SiO_4	1.96×10^{-4}	1.31×10^{-3}
Ionic strength	7.19	5.62
pH [-]	5.80	6.45
pe [-]	-1.29	-2.33

n.d. – not determined, [$]according to King et al. (2017), [#] - SR-270-PW re-equilibrated with minerals using PHREEQC and SIT database

3.3 LHHPC

Low-Heat High-Performance Concrete (LHHPC) has a very low cement content (4.0 wt%) and high strength, low heat of hydration, excellent volumetric stability, low chloride permeability and low pH (Breton 1996). The initial mineral composition of fully-hydrated LHHPC was established using thermodynamic modelling as discussed in detail in Appendix A.2.

The mineral volume fractions for LHHPC are given in Table 7, while the reactions considered for subsequent simulations are presented in Table 15. The chemical composition of the corresponding cement pore water is listed in Table 8; the calculated pH is 9.75, which is reasonably consistent with the measured pH of 9.67 after six months of hydration (Breton 1996).

Table 7: Volume Fractions of the Main Minerals in LHHPC

Minerals	Formula	Vol Fraction [%]
Quartz	SiO_2	45.65
Silica (am)	SiO_2	11.00
TobII-07Mat	$(CaO)_{0.8333}SiO_2)(H_2O)_{1.3333}$	8.17
Hydrotalcite	$Mg_4Al_2(OH)_{14}{:}3H_2O$	0.34
Gypsum	$CaSO_4{:}2H_2O$	0.24
Calcite	$CaCO_3$	0.13
Gibbsite	$Al(OH)_3$	0.21
Ferrihydrite(am)	$Fe(OH)_3$	0.13
Albite(low) (Plagioclase)	$NaAlSi_3O_8$	13.44
Microcline-K (K-feldspar)	$KAlSi_3O_8$	13.27
chloriteca-1 (Clinochlore)	$Mg_5Al_2Si_3O_{10}(OH)_8$	0.50
Phlogopite_k (Biotite)	$KMg_3Si_3AlO_{10}(OH)_2$	1.69
Total		**94.76**

Table 8: Calculated Component Concentrations of the LHHPC Pore Water

Component	Concentration [mol L^{-1} H_2O]*
Al^{3+}	5.77×10^{-6}
CO_3^{2-}	4.76×10^{-5}
Ca^{2+}	9.87×10^{-3}
Fe^{2+}	2.15×10^{-10}
K^{+}	2.11×10^{-1}
Mg^{2+}	1.28×10^{-4}
Na^{+}	1.51×10^{-1}
SO_4^{2-}	1.90×10^{-1}
H_4SiO_4	4.03×10^{-3}
Charge balance [-]	-3.16×10^{-17}
Ionic strength [mol L^{-1}]	0.46
pH [-]	9.75

*Concentration was calculated using GEMS-selector v.3 (Kulik et al. 2013)

The transport parameters assigned to LHHPC are shown in Table 9 (Quintessa and Geofirma 2011).

Table 9: Transport Parameters for LHHPC

Parameters	Value
Porosity [%]	5.0
Dry bulk density [kg m^{-3}]	2425
Grain density [kg m^{-3}]	2560
Effective diffusion coefficient [m^2 s^{-1}]	3.0×10^{-13}

Data from Quintessa and Geofirma (2011)

It is important to note that after emplacement, LHHPC is only partially saturated (i.e., 50% water saturation; Quintessa and Geofirma 2011). However, for the simulations undertaken here it was assumed that the LHHPC was fully saturated due to the uptake of pore water from the repository host rocks. The initial component concentrations of the LHHPC pore water were calculated by mixing LHHPC pore water (Table 8) with an equal volume of granite, or limestone pore water (see sections 3.1 and 3.2) and then using PHREEQC to equilibrate that mixture with the LHHPC minerals. The resulting pore water compositions are given in Table 10. The slight increase of pH when saturated with granite pore water is because of the dissolution of TobII-07Mat and hydrotalcite in small amounts.

Table 10: Initial Component Concentrations of the LHHPC Pore Water after Mixing with Granite and Limestone Pore Water

Component	Concentration [mol L^{-1} H_2O]	
	Granite Host Rock	**Limestone Host Rock**
Al^{3+}	2.65×10^{-9}	2.42×10^{-12}
CO_3^{2-}	1.96×10^{-5}	2.00×10^{-5}
Ca^{2+}	1.41×10^{-2}	1.13×10^{-1}
Cl^-	1.55×10^{-1}	3.34
Fe^{2+}	9.06×10^{-6}	3.69×10^{-4}
K^+	1.09×10^{-1}	3.29×10^{-1}
Mg^{2+}	1.34×10^{-3}	6.64×10^{-1}
Na^+	1.20×10^{-1}	1.58
SO_4^{2-}	5.19×10^{-2}	3.32×10^{-2}
H_4SiO_4	8.84×10^{-4}	7.38×10^{-4}
Charge balance [-]	-3.40×10^{-5}	5.64×10^{-3}
Ionic strength	0.30	3.28
pH [-]	10.25	9.77

3.4 BENTONITE

Bentonite is widely considered as a barrier material for nuclear waste repositories due to its superior properties, including extremely low permeability, high cation exchange capacity, high swelling potential, and low effective diffusion coefficient (Push 1992; Sellin and Leupin 2013). Two forms of MX-80 sodium bentonite are often considered: HCB (highly compacted bentonite blocks) with a dry density of 1700 kg m^{-3}, and GFM (gap filling material in the form of bentonite pellets) with a dry density of 1400 kg m^{-3} (NWMO 2017). It is assumed that the initially unsaturated HCB and GFM will become saturated with water from the host rock. Due to the difference in the initial dry density of HCB and GFM, the pressure generated due to swelling can be different. Consequently, the dry density of HCB will decrease after saturation, while that of GFM will increase. At equilibrium, a homogenized bentonite (HB) with a uniform density of 1600 kg m^{-3} is assumed to form and its main properties are given in Table 11 (NWMO 2017, 2018).

In the reactive transport simulations only HB was considered, with the initial mineral volume fractions presented in Table 11. Careful comparison of the mineral compositions of HB (Karnland et al. 2006) and HCB (Wilson et al. 2012) reveals small discrepancies between the percentages of individual minerals in the solid phase (not shown in Table 11). The data from Karnland et al. (2006) has been selected. The initial saturations and densities of HCB and GFM are also listed in Table 11 (based on Table 6.4 in Gobien et al. 2016). The initial saturation of HB was determined in two steps: 1. Calculate the mixing ratio of HCB and GFM based on the dry densities of HCB, GFM and HB; 2. Use the mixing ratio and the initial water content to calculate the initial water saturation of HB, which is 42.7% (Table 11). The chemical composition of the corresponding bentonite pore water after mixing with granite or limestone pore water is

listed in Table 12. Because subsequent simulations of radionuclide migration focus on the anion I^-, the effective diffusion coefficients for HB were set to the peak values for anions in the host rocks as suggested by Gobien et al. (2016, 2018), which is 1.11×10^{-11} m^2 s^{-1} in granite (Table 6.13 in Gobien et al. 2016), and 1.40×10^{-10} m^2 s^{-1} in limestone (Table 6.12 in Gobien et al. 2018), respectively. The effective diffusion coefficient of HB in limestone host rock is about one order of magnitude higher than that in granite (Table 12).

Table 11: Initial Mineral Volume Fractions of MX-80 Bentonite (Wilson et al. 2012) and Initial Physical Properties of HCB, GFM and HB (Based on Gobien et al. 2016, 2018)

Mineral	Formula	Volume Fractions [%]		
		HCB*	GFM#	HB$
Smectite-MX80	$Na_{0.409}K_{0.024}Ca_{0.009}(Si_{3.738}Al_{0.262})(Al_{1.598}Mg_{0.214}Fe_{0.173}Fe_{0.035})O_{10}(OH)_2$	56.2	46.7	51.7
Quartz	SiO_2	1.9	1.6	2.0
Cristobalite/Tridymite	SiO_2	2.3	1.9	3.8
Calcite	$CaCO_3$	0.6	0.5	0.1
Gypsum	$CaSO_4{:}2H_2O$	0.7	0.6	0.7
Porosity [%]		38.2	48.6	41.6
Bulk dry density [kg m^{-3}]		1700	1410	1600
Saturation [%]		67.0	6.0	42.7
Effective diffusion coefficient [m^2 s^{-1}]	In granite host rock			1.11×10^{-11}
	In limestone host rock			1.40×10^{-10}

*from Wilson et al. (2012); #calculated based on the volume fractions of minerals in HCB; $mineral volume fractions from Karnland et al. (2006), Table 5-6

MX-80 bentonite has a high specific surface area and CEC (cation exchange capacity); the CEC of the bentonite is set to 79.0 meq/100 g soil (Bradbury and Baeyens 2003).

Table 12: Initial Component Concentrations of the HB Pore Water Saturated with 57.3% of Pore Water in Granite or Limestone

Component	Concentration [mol L^{-1} H_2O]		
	Original*	**In Granite**	**In Limestone**
Al^{3+}	-	1.43×10^{-8}	3.11×10^{-9}
CO_3^{2-}	7.79×10^{-4}	1.04×10^{-3}	1.37×10^{-3}
Ca^{2+}	1.01×10^{-2}	1.16×10^{-2}	1.56×10^{-1}
Cl^-	1.08×10^{-1}	1.47×10^{-1}	3.81
Fe^{2+}	-	1.04×10^{-5}	4.23×10^{-4}
K^+	1.32×10^{-3}	1.53×10^{-3}	5.37×10^{-2}
Mg^{2+}	7.69×10^{-3}	2.74×10^{-3}	7.26×10^{-1}
Na^+	2.61×10^{-1}	3.03×10^{-1}	2.05
SO_4^{2-}	9.45×10^{-2}	9.29×10^{-2}	2.72×10^{-2}
H_4SiO_4	1.83×10^{-4}	1.82×10^{-4}	1.45×10^{-4}
Ionic strength	0.33	0.42	2.37
pH [-]	8.0	7.89	6.81

*Component concentrations are for compacted MX-80 bentonite with dry density of 1600 kg m^{-3} based on Bradbury and Baeyens (2003), Table 5.

4. NUMERICAL SIMULATIONS

4.1 CONCEPTUAL MODELS

In the Canadian concept for a DGR for used nuclear fuel waste, in either sedimentary or crystalline host rocks, Highly-Compacted Bentonite (HCB), bentonite pellets as Gap Fill Material (GFM) and LHHPC are potential engineered barrier materials (EBM) (Figure 1 and Figure 2, NWMO 2017, 2018). Chemical alterations are expected at the interfaces between these low permeability materials, which could potentially lead to modifications of the diffusive transport properties of the barrier system. Reactive transport simulations have been performed with MIN3P-THCm V1.0.690 to investigate: (a) long-term chemical interactions driven by diffusive transport across the interfaces plus the associated solution – mineral interactions; and (b) the impact of material alteration on the migration of radionuclides (represented by I^-). Because of the very low permeability of the EBM and host rocks, advective transport has not been considered. Heat generation and transport have not been included; all simulations assume a spatially and temporally constant temperature of 25 ^oC.

According to the current conceptual design (Figure 1 and Figure 2), waste canisters will be encapsulated in HCB buffer boxes, separated by HCB buffer blocks, and gaps filled with bentonite pellets. LHHPC will only be placed at the bottom of the placement tunnels as a floor smoothing treatment with a thickness of about 0.10 to 0.25 m (Figure 1) (NWMO 2017, 2018). For the current simulations it is assumed that when the bentonite buffer boxes, spacer blocks and gap filling material (Figure 1 and Figure 2) become saturated, these materials can be represented as a homogenized bentonite (HB).

The basic scenarios for the reactive transport simulations can be summarized as follows:

1. Two arrangements of materials were considered:
   a. Type 1: HB/LHHPC/host rock (Figure 3 and Figure 4). Depending on the type of host rock (granite or limestone), the simulation cases are distinguished as Case 1 - HB/LHHPC/Granite and Case 3 - HB/LHHPC/Limestone.
   b. Type 2: HB/host rock (Figure 5 and Figure 6). The corresponding cases are Case 2 – HB/Granite and Case 4 – HB/Limestone.

   Figure 3 and Figure 5 depict the cases without consideration of EDZs, while Figure 4 and Figure 6 depict the models with consideration of EDZs.

2. The 1D reactive transport models were developed by considering locations with the minimum thickness of EBM (red arrows in Figure 1 and Figure 2). The total length of both the Type 1 and Type 2 models was 50.0 m. The domain discretization was: Δx=0.005 m from 0 to 1.5 m; Δx=0.01 m from 1.5 m to 5.0 m; and Δx=0.2 m for the rest of the domain.

3. Ten observation points (OPs) were placed to track the temporal evolution of transport properties, mineral compositions or component concentrations. The locations of these OPs are depicted in Figure 3 and Figure 4 (for Type 1 models) and Figure 5 and Figure 6 (for Type 2 models), and the coordinates are given in Table 13. One or two additional OPs were added as V11 or V12 to record the pore clogging positions. The coordinates of pore clogging positions (V11 or V12) vary with the types of model and host rocks, which will be described in the Section 5. In principle, for Type 1 models, V11 is in LHHPC adjacent to the HB/LHHPC interface, while V12 is located in the host rock adjacent to the LHHPC/host rock interface. For the Type 2 models, V11 is in the host rock adjacent to the interface between HB and host rocks. Time step size was controlled automatically by the adaptive time stepping scheme based on the change in aqueous concentrations and the number of Newton-Raphson iterations (Mayer 1999).

Table 13: The X-coordinates [in m] of the Observation Points

Model	V1	V2	V3	V4	V5	V6	V7	V8	V9	V10	V11	V12
Type 1	0	0.35	0.38	0.48	0.50	1.48	1.50	3.48	3.50	50.0	0.370	0.488
Type 2	0	0.19	0.20	0.34	0.35	1.34	1.40	3.48	3.50	50.0	0.346	-

Although the simulations include many components and minerals, and their interactions during reactive-diffusive transport, there are several processes that have not been considered due to computational or theoretical limitations. Some of these include: swelling during the saturation of bentonite and LHHPC, hydration of LHHPC, heat generation due to radionuclide decay and its effect on reactive transport, and advective transport in fractures in the host rocks.

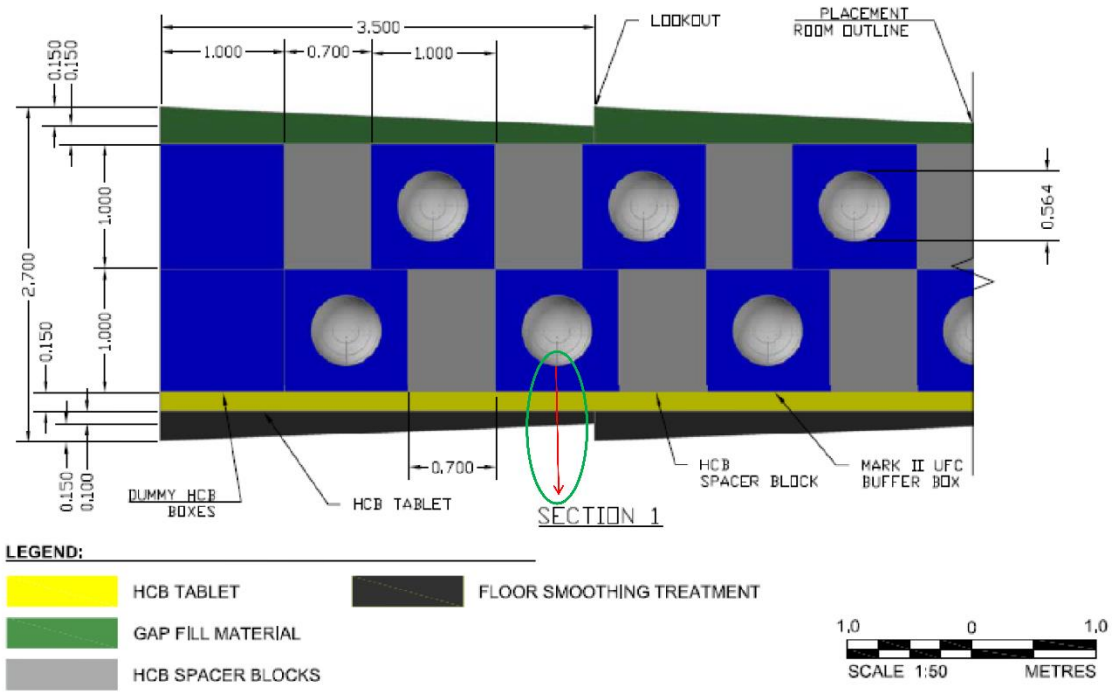

Figure 1: NWMO APM DGR Conceptual Design – Section 1 (from NWMO 2018). The Red Arrow Indicates the Position and Direction of the 1D Model for Case 1 and Case 3

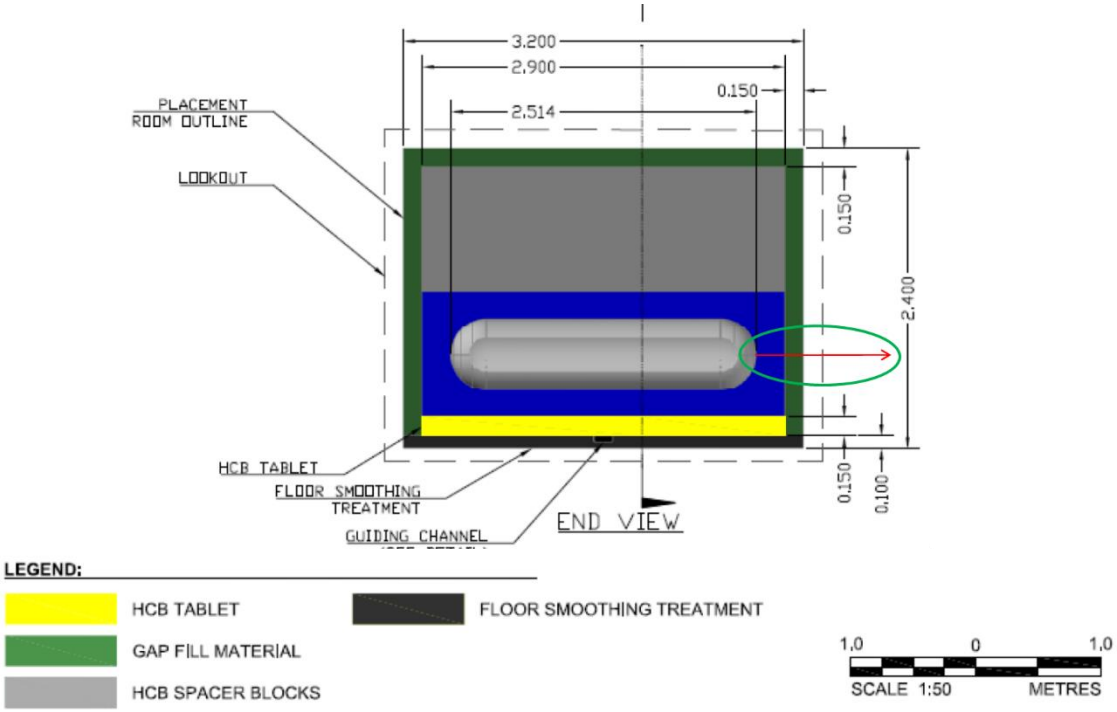

Figure 2: NWMO APM DGR Conceptual Design – End View (from NWMO 2018). The Red Arrow Indicates the Position and Direction of the 1D Model for Case 2 and Case 4

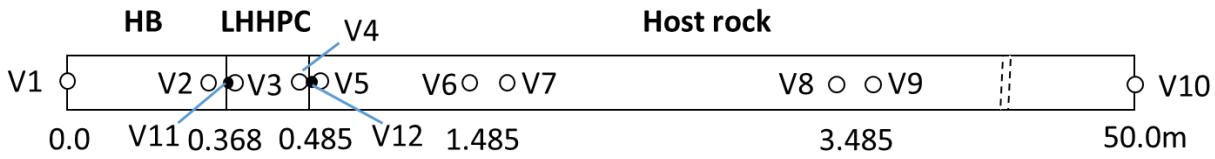

Figure 3: Conceptual Model of the Type 1 Geometry and Observation Points without Consideration of EDZ, V1 - V12 are the Observation Points

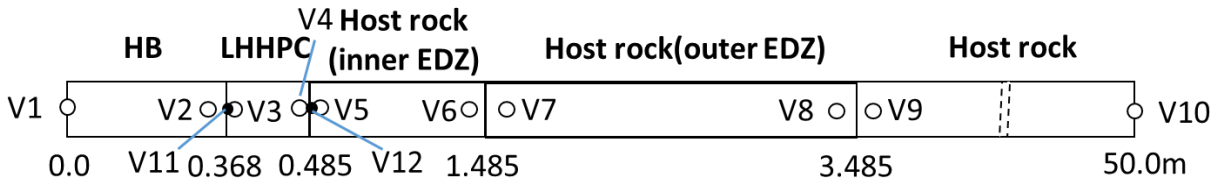

Figure 4: Conceptual Model of the Type 1 Geometry and Observation Points with Inner and Outer EDZs, V1 - V12 are the Observation Points

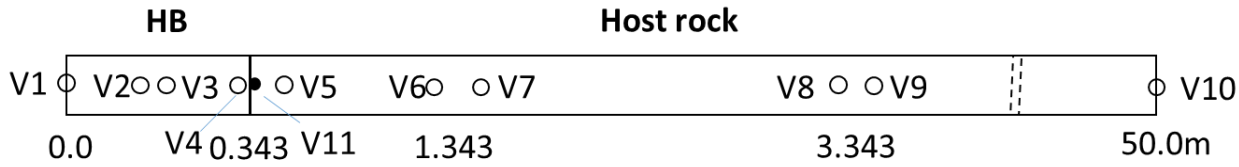

Figure 5: Conceptual Model of the Type 2 Geometry and Observation Points without Consideration of EDZ, V1 - V11 are the Observation Points

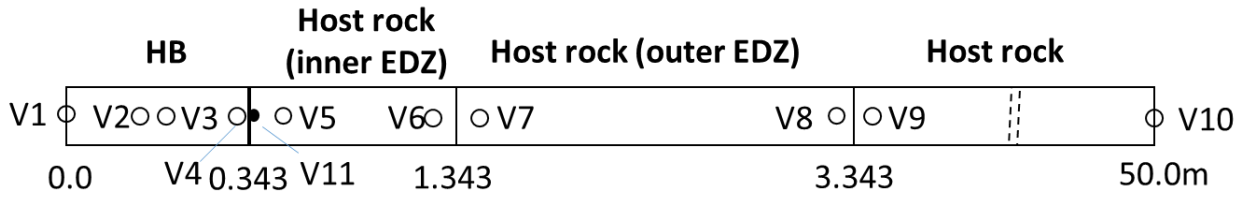

Figure 6: Conceptual Model of the Type 2 Geometry and Observation Points with Inner and Outer EDZs, V1 - V11 are the Observation Points

4.2 SIMULATED CASES

Table 14 provides an overview of the simulated cases. Two types of reactive transport simulations were undertaken: (1) reactive transport of the pore water components through the various combinations of materials, and (2) reactive transport combined with radionuclide migration (RM). The geochemical and mineralogical evolution of the materials was simulated by assuming either: (a) constant porosity and effective diffusion coefficient (CP – constant porosity), which is equivalent to conservative mass transport for inert components; or (b) temporal variations of porosity and effective diffusion coefficient due to mineral dissolution/precipitation reactions (UP – updated porosity, Table 14). Simulations were also conducted with and without consideration of EDZs.

Radionuclide migration was represented by iodine (I^-), which was assumed to be generated by canister failure resulting from either a small or large defect occurring at 1,000 years or 10,000 years. Therefore, each of the simulated cases with radionuclide migration (i.e. cases with "+ RM", Table 14) implies four canister failure scenarios – large defect at 1,000 or 10,000 years, and small defect at 1,000 or 10,000 years. At the time of canister failure, I^- is assumed to be released at V1 (x= 0.0 m) (e.g. Figure 3). The transient concentration boundary conditions at V1 were provided by NWMO (T. Yang, personal communication) and are depicted for the large defect in Figure 7, and for the small defect in Figure 8. For the large defect canister failure, the failure is assumed to result in a sudden release of radionuclides and thus a rapid increase of the I^- relative concentration from 0.0 to 1.0 (Figure 7). The relative concentration of I^- is assumed to be constant for one year and then drops to 6.2×10^{-4}, followed by a more gradual decline.

Table 14: Summary of the Simulated Cases

Host rock	EDZ	Description	Constant porosity – CP	Updated porosity - UP
Granite	No EDZ	HB/LHHPC/granite	Case 1CP	Case 1UP
		HB/LHHPC/granite + RM	Case 1rCP	Case 1rUP
		HB/granite	Case 2CP	Case 2UP
		HB/granite + RM	Case 2rCP	Case 2rUP
	With EDZ	HB/LHHPC/granite	Case 1EDZCP	Case 1EDZUP
		HB/LHHPC/granite + RM	Case 1rEDZCP	Case 1rEDZUP
		HB/granite	Case 2EDZCP	Case 2EDZUP
		HB/granite + RM	Case 2rEDZCP	Case 2rEDZUP
Limestone	No EDZ	HB/LHHPC/limestone	Case 3CP	Case 3UP
		HB/LHHPC/limestone + RM	Case 3rCP	Case 3rUP
		HB/Limestone	Case 4CP	Case 4UP
		HB/Limestone + RM	Case 4rCP	Case 4rUP
	With EDZ	HB/LHHPC/limestone	Case 3EDZCP	Case 3EDZUP
		HB/LHHPC/limestone + RM	Case 3rEDZCP	Case 3rEDZUP
		HB/Limestone	Case 4EDZCP	Case 4EDZUP
		HB/Limestone + RM	Case 4rEDZCP	Case 4rEDZUP

Notes: EDZ – excavation damage zone; HB – homogenized bentonite; LHHPC – low-heat high-performance concrete; RM – radionuclide migration.

For the small defect canister failure, the I^- relative concentration is assumed to increase from 0.0 to about 0.4 at the time of failure (Figure 8). After that, the concentration increases gradually for a long period of time and reaches the peak value of 1.0 at about 67,000 years, followed by a gradual drop until 10^7 years (i.e. the maximum simulation time). For canister failure scenarios at 10,000 years, the evolution of the I^- relative concentrations, for both the large and small defects, is the same as the canister failure scenarios at 1,000 years as depicted in Figure 7 and Figure 8, but with the start time shifted from 1,000 to 10,000 years.

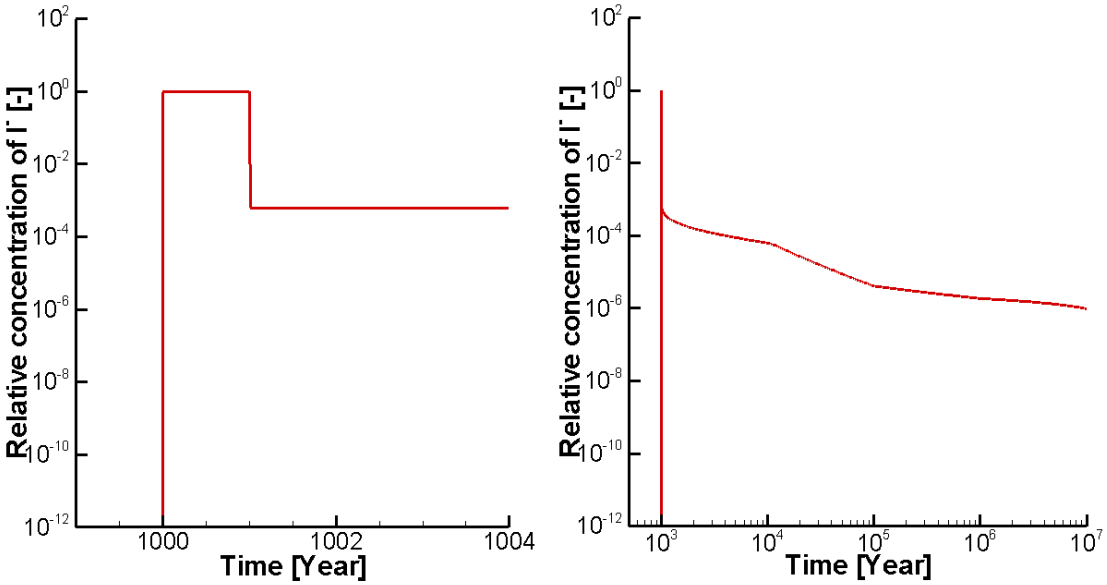

Figure 7: Evolution of I^- Concentration at the Canister Assuming a Large Defect at 1,000 Years (Left – from 999 to 1004 years, Right – Full Evolution)

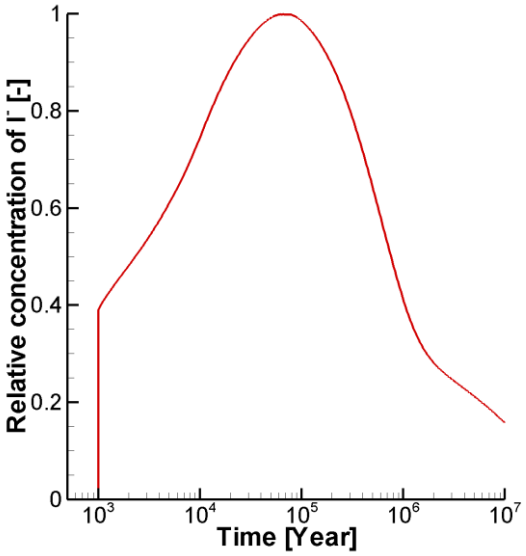

Figure 8: Evolution of I^- Concentration at the Canister Assuming a Small Defect at 1,000 Years

4.3 OTHER CONSIDERATIONS

4.3.1 Geochemical Networks

The geochemical processes considered in the reactive transport simulations are: hydrolysis, complex formation, precipitation/dissolution of minerals and cation exchange. The number of components is 12 (for the cases without consideration of radionuclide migration <RM>) or 13 (for cases with RM). The components are H^+, Al^{3+}, Fe^{2+}, H_4SiO_4, K^+, Mg^{2+}, Ca^{2+}, SO_4^{2-}, Na^+, Cl^-, CO_3^{2-}, H_2(aq) and I^- (for cases with radionuclide migration). One hundred and eight secondary species are also included, with the sorbed species being NaX, KX, CaX_2 and MgX_2.

The number of minerals is between 22 and 30 depending on the materials included in the model (see Section 3) and the potential secondary minerals (see 4.3.2).

For simulations including LHHPC and granite, the reactions and potential alteration phases are listed in Table 15. Table 16 presents the reactions for the simulations including bentonite.

Table 15: Chemical Reactions for Minerals and Potential Alteration Phases in LHHPC and Granite

Mineral	Reaction	Log_K
Primary minerals Quartz	$SiO_2 + 2\ H_2O = H_4SiO_4$	-3.74
Silica (am)	$SiO_2 + 2\ H_2O = H_4SiO_4$	-2.71
TobII-07Mat	$(CaO)_{0.8333}SiO_2)(H_2O)_{1.3333} + 1.6666H^+ = 0.8333\ Ca^{2+} + H_4SiO_4 + 0.1666\ H_2O$	11.14
Hydrotalcite	$Mg_4Al_2(OH)_{14}{:}3H_2O + 14\ H^+ = 4\ Mg^{2+} + 2\ Al^{3+} + 17\ H_2O$	75.11
Gypsum	$CaSO_4{:}2H_2O = Ca^{2+} + SO_4^{2-} + 2\ H_2O$	-4.61
Calcite	$CaCO_3 = Ca^{2+} + CO_3^{2-}$	-8.48
Gibbsite	$Al(OH)_3 + 3H^+ = Al^{3+} + 3\ H_2O$	7.74
Ferrihydrite(am)	$Fe(OH)_3 + 3\ H^+ = Fe^{3+} + 3\ H_2O$	2.54
Albite(low) (Plagioclase)	$NaAlSi_3O_8 + 4\ H^+ + 4\ H_2O = Na^+ + Al^{3+} + 3\ H_4SiO_4$	82.81
Microcline-K (K-feldspar)	$KAlSi_3O_8 + 4\ H^+ + 4\ H_2O = K^+ + Al^{3+} + 3\ H_4SiO_4$	0.05
Clinochlore (chlorite)	$Mg_5Al_2Si_3O_{10}(OH)_8 + 16H^+ = 5\ Mg^{2+} + 2\ Al^{3+} + 3\ H_4SiO_4 + 6\ H_2O$	62.72
Phlogopite_k (Biotite)	$KMg_3Si_3AlO_{10}(OH)_2 + 10H^+ = 3\ Mg^{2+} + K^+ + Al^{3+} + 3\ H_4SiO_4$	41.10

(Table 15, continued)

Secondary minerals		
Saponite-Ca	$Ca_{0.17}Mg_3Al_{0.34}Si_{3.66}O_{10}(OH)_2 + 7.36H^+ + 2.64H_2O \leftrightarrow 0.17Ca^{2+} + 3\ Mg^{2+} + 0.34Al^{3+} + 3.66\ H_4SiO_4$	29.34
Saponite-K	$K_{0.34}Mg_3Al_{0.34}Si_{3.66}O_{10}(OH)_2 + 7.36H^+ + 2.64H_2O \leftrightarrow 3\ Mg^{2+} + 0.34K^+ + 0.34Al^{3+} + 3.66H_4SiO_4$	28.17
Saponite-Mg	$Mg_{0.17}Mg_3Al_{0.34}Si_{3.66}O_{10}(OH)_2 + 7.36H^+ + 2.64H_2O \leftrightarrow 3.17Mg^{2+} + 0.34Al^{3+} + 3.66\ H_4SiO_4$	28.79
Saponite-Na	$Na_{0.34}Mg_3Al_{0.34}Si_{3.66}O_{10}(OH)_2 + 7.36H^+ + 2.64H_2O \leftrightarrow 3\ Mg^{2+} + 0.34Na^+ + 0.34Al^{3+} + 3.66H_4SiO_4$	28.67
epiolite	$Mg_4Si_6O_{15}(OH)_{2:6}H_2O + 8H^+ + H_2O \leftrightarrow 4Mg^{2+} + 6H_4SiO_4$	31.42
Ettringite	$Ca_6Al_2(SO_4)_3(OH)_{12}{:}26H_2O + 12\ H^+ \leftrightarrow 6\ Ca^{2+}\ + 2\ Al^{3+} + 3\ SO_4^{2-} + 38\ H_2O$	56.97
Friedel's salt	$Ca_4Al_2Cl_2O_6{:}10H_2O + 12H^+ \leftrightarrow 2Al^{3+} + 4Ca^{2+} + 2Cl^- + 16H_2O$	74.95
Phillipsite_Ca	$Ca_{0.5}AlSi_3O_8{:}3H_2O + 4\ H^+ + H_2O \leftrightarrow 0.50Ca^{2+} +\ Al^{3+} + 3\ H_4SiO_4$	2.32
Phillipsite_K	$KAlSi_3O_8{:}3H_2O + 4\ H^+ + H_2O \leftrightarrow K^+\ +\ Al^{3+} + 3\ H_4SiO_4$	0.04
Phillipsite_Na	$NaAlSi_3O_8{:}3H_2O + 4\ H^+ + H_2O \leftrightarrow Na^+\ +\ Al^{3+} + 3\ H_4SiO_4$	1.45
CSH0.8k	$Ca_{0.8}SiO_{2.8}{:}1.54H_2O + 1.6H^+ \leftrightarrow 0.80Ca^{2+} + H_4SiO_4\ + 0.340H_2O$	11.05
CSH1.2	$Ca_{1.2}SiO_{3.2}{:}2.06H_2O + 2.4H^+ \leftrightarrow 1.2Ca^{2+} + H_4SiO_4\ + 1.26H_2O$	19.30
CSH1.6	$Ca_{1.6}SiO_{3.6}{:}2.58H_2O + 3.2\ H^+\ \leftrightarrow 1.6Ca^{2+} + H_4SiO_4\ + 2.18H_2O$	28.00
Chamosite	$Fe_5Al_2Si_3O_{10}(OH)_8 \leftrightarrow 5\ Fe{+}2\ + 2\ Al^{3+} - 16\ H^+ + 3\ H_4SiO_4 + 6\ H_2O$	47.60
Analcime	$Na_{0.99}Al_{0.99}Si_{2.01}O_6{:}H_2O + 3.96H^+ + 1.04H_2O \leftrightarrow 0.99Na^+ + 0.99Al^{3+} + 2.01H_4SiO_4$ -	6.65
Tobermorite-14a	$Ca_5Si_6O_{16.5}(OH){:}10H_2O + 10H{+} \leftrightarrow 5\ Ca^{2+} + 6H_4SiO_4 + 3.50H_2O$	62.94

Table 16: Chemical Reactions of the Minerals and Potential Alteration Phases in HB

Mineral	Reaction	Log_K
Primary minerals		
Smectite-MX80	$Na_{0.409}K_{0.024}Ca_{0.009}(Si_{3.738}Al_{0.262})(Al_{1.598}Mg_{0.214}Fe_{0.173}Fe_{0.035})O_{10}(OH)_2 \leftrightarrow 0.009Ca^{2+} + 0.214Mg^{2+} + 0.024K^{+} + 0.409Na^{+} + 0.173Fe^{3+} + 1.860Al^{3+} + 3.738H_4SiO_4 + 0.035Fe{+}2 - 2.952H_2O - 7.048H^{+}$	5.270
Quartz	$SiO_2 + 2\ H_2O \leftrightarrow H_4SiO_4$	-3.740
Gypsum	$CaSO_4{:}2H_2O \leftrightarrow Ca^{2+} + SO_4^{2-} + 2\ H_2O$	-4.610
Calcite	$CaCO_3 \leftrightarrow Ca^{2+} + CO_3^{2-}$	-8.480
Secondary minerals		
Sepiolite*	$Sepiolite + 8\ H_2O \leftrightarrow 4\ Mg^{2+} + 6\ H_4SiO_4 + H_2O$	31.419
Illite_Imt-2	$Illite\_Imt\text{-}2 \leftrightarrow 0.241Mg^{2+} + 0.762K^{+} + 0.044Na^{+} + 0.292Fe^{3+} + 0.084Fe{+}2 + 2.040Al^{3+} - 8.452H^{+} + 3.387H_4SiO_4 - 1.548H_2O$	15.789
Kaolinite	$Al_2(Si_2O_5)(OH)_4 \leftrightarrow 2.0Al^{3+} - 6.0H^{+} + 2.0H_4SiO_4 + 1.0H_2O$	6.510

*potential secondary phase in the bentonite- cement system,

4.3.2 Secondary Minerals

The type and number of secondary minerals included in reactive transport simulations can have a substantial influence on the predictions of mineral alterations (Gaucher and Blanc 2006; Savage et al. 2007). This is because the secondary minerals will define the reaction pathways. Ideally, simulations should include all thermodynamically possible secondary phases that are associated with the components considered, and exclude those shown by experiments to be unimportant (e.g. some silicate minerals that only form under high pressures and high temperatures). In practice; however, including a large number of secondary minerals might pose numerical challenges (e.g. over 260 minerals are possible for Case 1 described in Section 5.2).

In MIN3P-THCm it is possible to run test simulations including only a limited number of secondary minerals and denoting other possible secondary minerals as “excluded minerals”. “Excluded minerals” will not be included in the reactions, but their saturation indices (SI) will be computed. If the SI of excluded minerals indicates that those minerals can form in the chemical system, then they may be included in subsequent simulations. The SI information from such test simulations helped to identify potential secondary minerals; however, the final set of secondary minerals applied for the simulations listed in Table 15 and Table 16 were selected after also considering experimental and/or theoretical predictions in the state-of-the-art literature (De La Villa et al. 2001; Metcalfe and Walker 2004; Gaucher and Blanc 2006; Savage et al. 2007, 2018; Wilson et al. 2012; Marty et al. 2010, 2015; Fernández et al. 2009, 2016; Cuevas et al. 2006, 2016, 2018; Jackson et al. 2017; González-Santamaría et al. 2018).

4.3.3 Kinetic Parameters

The kinetic model employed for the simulations is the transition state theory (TST) based approach (Marty et al. 2015):

$$r_n = \pm 10^3 s_n \rho_n \varphi_n k_n |1 - \Omega_n^{\theta}|^{\eta}$$ Equation 4-1

where r_n [mol (L bulk)$^{-1}$ s^{-1}] denotes the dissolution/precipitation rates of a mineral (n) (positive r_n indicates dissolution), s_n is the reactive specific surface area of mineral n in [m^2 g^{-1}], ρ_n is the density of mineral n in [g cm^{-3}], 10^3 is a conversion factor (1 dm^3= 10^3 cm^3), φ_n is the volumetric fraction of mineral n in [dm^3 mineral dm^{-3} bulk], k_n is the rate constant in [mol m^{-2} s^{-1}]. Ω_n is the mineral saturation ratio [-]. Parameters θ and η are dimensionless coefficients to describe the rate dependency on the saturation ratio, which are equal to 1.0 for the simulations.

Table 17: Specific Surface Areas for Minerals and Cement Phases

Mineral	Specific Surface Area [m^2 g^{-1}]	Reference/Notes
Quartz	0.001	Wilson et al. (2012)
Silica (am)	22.6	Wilson et al. (2012)
Smectite	8.0	Wilson et al. (2012)
Cristobalite/Tridymite	2.24	Bustillo et al. (1993)
TobII-07Mat	41	Wilson et al. (2012)
Hydrotalcite	11.94	Wilson et al. (2012)
Calcite	0.022	geometric calculation: 100 µm diameter sphere
Gibbsite	32	Karamalidis and Dzombak (2010)
Ferrihydrite	220	Carlson and Schwertmann (1981)
Albite(low) (Plagioclase)	0.01	Dubois (2011) (BET data)
Microcline-K (K-feldspar)	0.01	Dubois (2011) (BET data)
Chlorite (Clinochlore)	0.1	Dubois (2011) (BET data)
Phlogopite (Biotite)	0.1	Dubois (2011) (BET data)
Ettringite	9.8	Baur et al. (2004) (BET data)
Sepiolite	9.8	Wilson et al. (2012)
Brucite	10.0	Wilson et al. (2012)
Saponite	8.0	Wilson et al. (2012)
Kaolinite	8.16	Huertas et al. (1999) (BET data)
Illite-al	1.05	Watson et al. (2013)
Phillipsite	19.81	Notario et al. (1995)
Tobermorite	9.8	Ettringite used as analogue
Thaumasite	9.8	Wilson et al. (2012)
Dolomite	0.021	geometric calculation: 100 µm diameter sphere

The accessible reactive surface area is a crucial parameter for kinetically controlled reactions involving minerals (Marty et al. 2009, 2015). Marty et al. (2009, 2015) carried out sensitivity analysis regarding the potential effect of decreasing reactive surface areas by four orders of

magnitude. The results showed that higher reactive surface areas (i.e. faster reaction rates) resulted in faster pore clogging. However, the reactive surface area is difficult to determine and thus is associated with high uncertainties. This is because the surface areas of minerals measured under standard conditions using dispersed material might not be applicable to the natural system, especially in highly compacted bentonite. Yamaguchi et al. (2007) studied the alteration of clay in a compacted bentonite-sand mixture submerged in alkaline solution and found that the measured dissolution rates of montmorillonite were 1-2 orders of magnitude lower than those measured in a dispersed clay system (Yamaguchi et al. 2007; Savage and Cloet 2018). The comparison of laboratory-derived mineral reaction rates to field scale studies is even more difficult because most laboratory-derived rates are 2-5 orders of magnitude higher than field-derived rates (White and Brantley 2003; Navarre-Sitchler and Brantley 2007). The pore network and heterogeneity of the mineral distributions can further complicate the fluid accessible surface area of minerals in a rock (Lai et al. 2015; Beckingham et al. 2016, 2017).

The specific surface areas for the minerals and cement phases included in this work are listed in Table 17, and are mostly based on the Thermochimie database (Marty et al. 2015a) and Wilson et al. (2012). The rate constants of the minerals are from the Thermochimie database (Marty et al. 2015a). For the reactive transport simulations, the reactive surface areas for kinetically-controlled mineral reactions were determined by dividing the values in Table 17 by 100 for bentonite and LHHPC, and by 1000 for the host rocks. All mineral reactions, except those involving gypsum, were treated as kinetically controlled. This approach provides a high level of conservativism regarding mineral reactivity and potential for pore clogging.

4.3.4 Interfacial Diffusion Flux Calculation

A reduction in the porosity of materials due to chemical reactions will in turn lead to a reduction in the effective diffusion coefficient (D_e) of the components being transported through the domain (Chagneau et al. 2015). Numerically, the interfacial flux between two connected control volumes is calculated using Fick's law, using an averaged effective diffusion coefficient (D_{e_ev}) based on the effective diffusion coefficients of both control volumes (e.g. D_{e_1} and D_{e_2}). There are several different methods to calculate D_{e_ev}: arithmetic, harmonic and geometric means (Crank 1975; Patanker 1980; Liu et al. 2014; Kadioglu et al. 2008):

arithmetic mean:

$$D_{e\_ev} = \frac{D_{e\_1} + D_{e\_2}}{2} \qquad \text{Equation 4-2}$$

geometric mean:

$$D_{e\_ev} = \sqrt{D_{e\_1} * D_{e\_2}} \qquad \text{Equation 4-3}$$

harmonic mean:

$$D_{e\_ev} = \frac{2}{\frac{1}{D_{e\_1}} + \frac{1}{D_{e\_2}}} \qquad \text{Equation 4-4}$$

A comparison between using arithmetic and harmonic means was conducted by Kadioglu et al. (2008), with the conclusion that the harmonic mean is not necessarily more accurate than other methods when simulating conductive heat transport. The accuracy is highly dependent on how the physical problem is modelled (Kadioglu et al. 2008). In a thermal radiation diffusion problem with two regions at two different temperatures, and a much lower D_e in the colder region, Olson and Morel (1999) demonstrated that geometric averaging is more suitable than harmonic averaging.

If pore clogging (i.e. porosity reaches zero) occurs in a 1D domain, the overall diffusion of components will be limited by the clogged volume. In such a case, the arithmetic mean of the D_e values between the clogged volume and an adjacent unclogged volume will be nonzero and thus diffusion will continue, which contradicts the physical conditions. The harmonic mean will favor the smaller D_e value and can be proven to be the smallest value among the aforementioned three methods if $D_{e\_1} > 0$, $D_{e\_2} > 0$ and $D_{e\_1} \neq D_{e\_2}$ (Arbogast 2013). If one of the diffusion coefficients is zero, Equation 4-4 is not valid. On the other hand, the correctness of the harmonic mean for diffusion problems has often been questioned (Liu and Ma 2001; Arbogast 2013). Selvadurai and Selvadurai (2014) demonstrated through experiments that the geometric mean is a good proxy of the permeability for a heterogeneous limestone, with the conclusion that the geometric mean is more suitable for heterogeneous porous media.

Considering the complex properties of natural host rocks, and the potential for complete pore clogging to halt diffusive transport, for the current simulations the geometric mean (Equation 4-3) has been used to calculate the average effective diffusion coefficient (D_{e_ev}) between two connected control volumes. This approach again provides a level of conservativism with respect to solute mobility under conditions of pore clogging.

5. SIMULATION RESULTS

5.1 OVERVIEW OF CASES 1UP (HB/LHHPC/GRANITE) AND 3UP (HB/LHHPC/LIMESTONE)

Case 1UP and Case 3UP consider the combination of HB and LHHPC, with the LHHPC in contact with either undamaged granite (1UP) or limestone (3UP) host rock (Table 14). The simulation results show significant mineral alteration in the LHHPC in both cases, which arises due to differences in the pH and chemical composition of the LHHPC and host rock pore waters, and in the mineral compositions of LHHPC with respect to the other materials. Figure 9 depicts the porosity and mineral volume fraction evolution at observation point V4 (located in LHHPC close to the LHHPC/host rock interface, see Figure 3 and Table 13 in Section 4.1). The results for both cases show the same trend of dissolution for the main cementitious phases (i.e. TobII-07mat, hydrotalcite and SiO_2(am)), with the former two phases disappearing within 1,000 years, while SiO_2(am) dissolves until about 1,000 years. At that time secondary minerals begin to form. However, the main secondary minerals in the LHHPC differ substantially in the case of granite compared to the limestone (Figure 9), which leads to differences in porosity evolution at V4. Up to 100,000 years, only small porosity changes occur in the LHHPC adjacent to granite, while a significant increase of the LHHPC porosity is simulated in the limestone host rock case.

In the granite host rock, tobermorite is the dominant secondary phase followed by phillipsite and saponite, all of which are fairly stable thereafter. Tobermorite dissolves slightly after about 100,000 years due to the diffusion of granite pore water components into the LHHPC (Figure 9

left). In addition, gypsum precipitation leads to the slow increase of gypsum volume fraction up to about one million years. Apart from that, SiO_2(am) dissolves substantially after about 30,000 years, which is the main contribution to the increase of the porosity from the initial 0.05 to 0.1 at V4 in the LHHPC. The amount of SiO_2(am) dissolved at V4 is the maximum amount predicted in the whole domain, and the amount of dissolution of SiO_2(am) decreases sharply away from the LHHPC/granite interface (Figure 17 to Figure 19).

In limestone host rock, the simulation results show no precipitation of tobermorite (Figure 9 right). Instead, saponite and sepiolite precipitate and remain stable up to approximately two million years. A small amount of phillipsite precipitation occurs at about 40 years, with subsequent dissolution after 500 years due to the interaction with the pore water from the adjacent limestone host rock. The porosity at V4 reaches a maximum of slightly less than 0.08 after about 1000 years, and remains constant up to about 10^6 years (Figure 9 right).

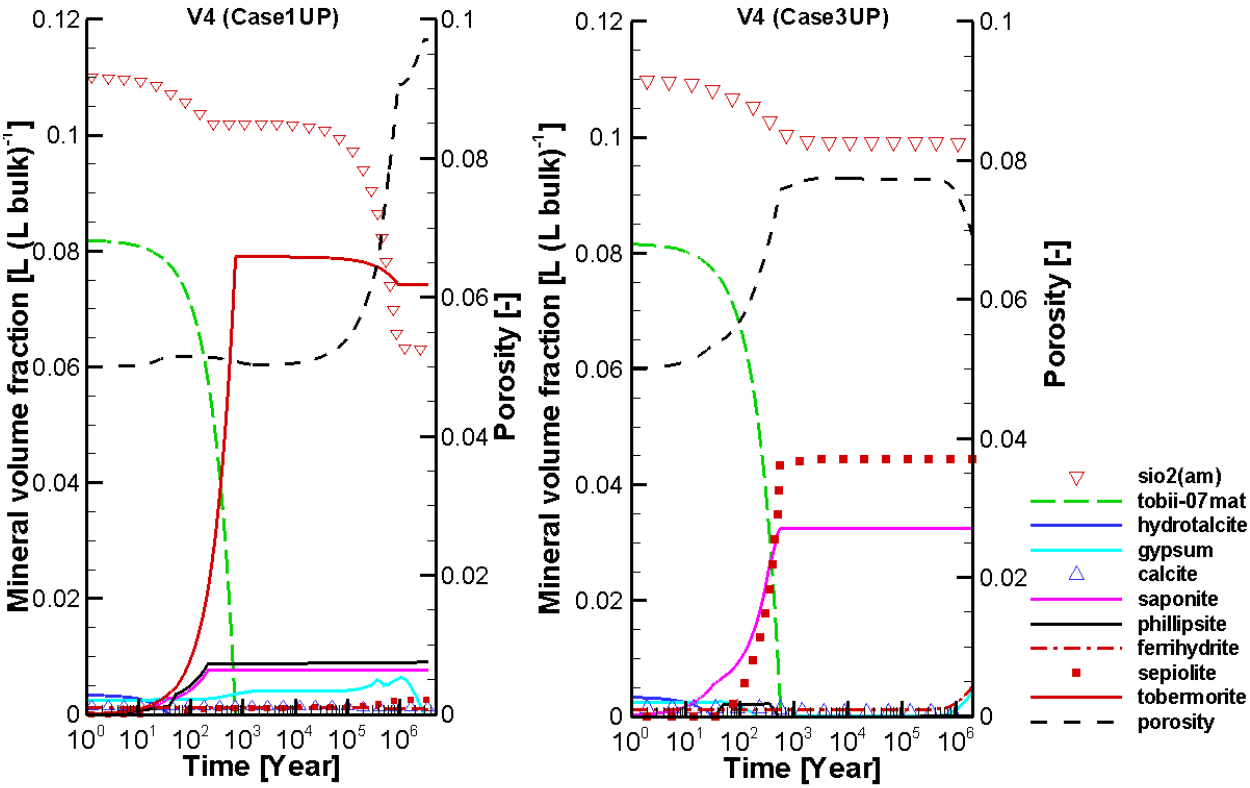

Figure 9: Evolution of Porosity and the Volume Fractions of Selected Minerals at Observation Point V4 (LHHPC; Figure 3) in Granite (Case 1UP; Left) and in Limestone (Case 3UP; Right)

It is noteworthy that local clogging is simulated for all the cases in Table 14 that included LHHPC and porosity updating (e.g. Case 1UP, Case 3UP; Figure 10). This finding is consistent with earlier simulation studies (e.g., Gaucher and Blanc 2006; Savage and Cloet 2018) and experimental observations (e.g. Torres et al. 2013; Yamaguchi et al. 2016). Generally, pore clogging will restrict the diffusive migration of solutes including radionuclides. However, the

timing of clogging relative to the release of radionuclides is an important factor to consider when assessing the consequences of pore clogging on radionuclide migration, and this will be considered in detail in the following sections. For all cases that did not include LHHPC, no clogging was predicted, indicating that the main minerals in bentonite are geochemically stable when in contact with either granite or limestone.

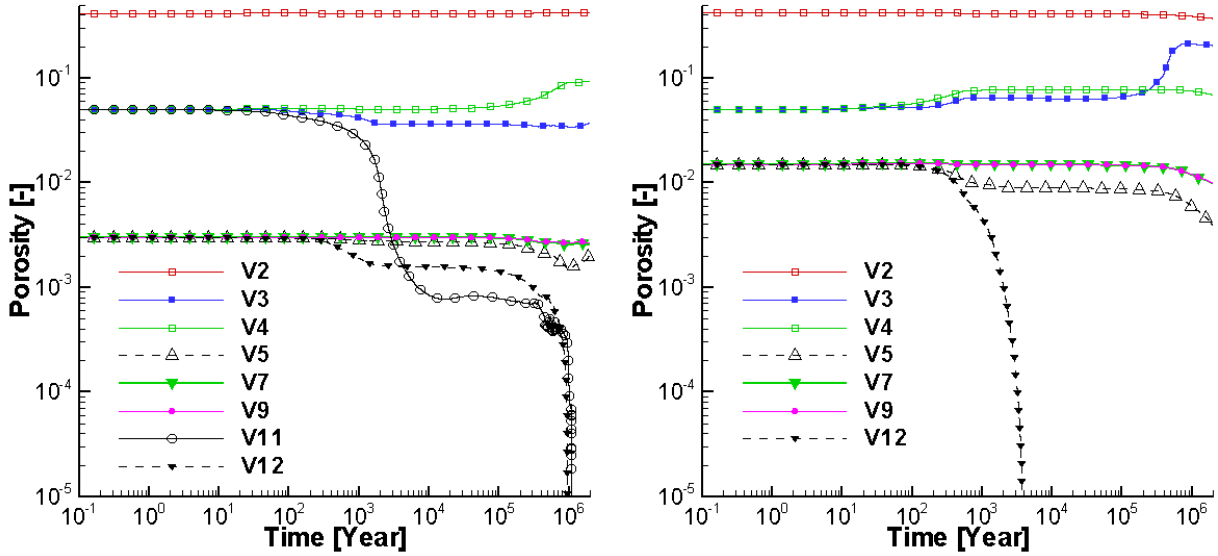

Figure 10: Evolution of Porosity at Observation Points V2 to V12 (Figure 3 and Table 13) in Granite (Case 1UP; Left) and in Limestone (Case 3UP; Right). V2 (HB), V3, V4 and V11 (LHHPC), V5, V7, V9 and V12 (Host Rock)

5.2 GRANITE HOST ROCK CASES

Two main cases were simulated for the granite host rock, i.e., Case 1 (HB/LHHPC/granite) and Case 2 (HB/granite) (see Table 14 in Section 4.2). In subsection 5.2.1, the results of the simulations for Case 1 without consideration of EDZs (i.e. Case 1CP and Case 1UP, Table 14) are discussed, including reactive transport (Subsection 5.2.1.1), and the impact of different canister failure scenarios on radionuclide migration (Subsection 5.2.1.2).

Simulation results for Case 1 considering EDZs (i.e. Case 1EDZCP and Case 1EDZUP, Table 14) are discussed in Section 5.2.2. These results will be compared to Case 1CP and Case 1UP to show the impact of EDZs on reactive transport and on radionuclide migration.

5.2.1 Case 1 – Without Consideration of EDZs

5.2.1.1 Reactive Transport – Case 1CP (HB/LHHPC/Granite) and 1UP (HB/LHHPC/Granite)

The early-time diffusive transport of solutes in the domain is driven by the initial concentration gradients of the components; the initial spatial distributions of the components, pH and porosity

are shown in Figure 11. For all three materials (HB, LHHPC, granite) in Case 1, the main components in the pore water are Na^+, Cl^-, SO_4^{2-} and Ca^{2+}. The initial sorbed species are dominated by NaX and CaX_2 (Figure 11). The sorbed species exist only in the HB because the sorption capacities of LHHPC and granite are relatively low and currently not taken into consideration. The initial volume fractions of minerals in the HB, LHHPC and granite are the same for both cases 1CP and 1UP as depicted in Figure 12; the exact fractions of each mineral in HB, LHHPC and granite are given in Table 11, Table 7 and Table 2 in Section 3, respectively.

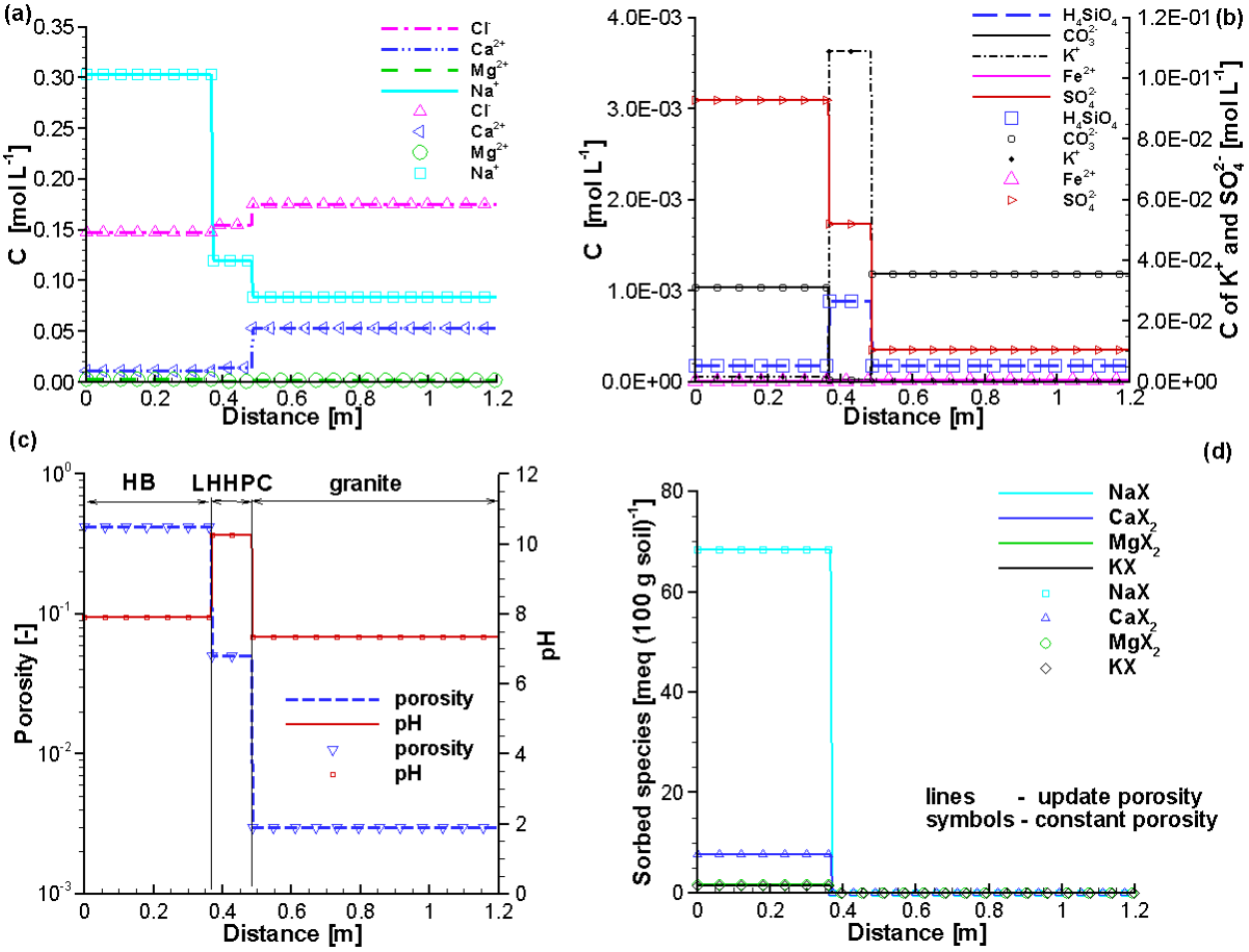

Figure 11: Profiles of Initial Component Concentrations (a and b), pH and Porosity (c) and Sorbed Species (d) for Case 1CP (Symbols) and Case 1UP (Lines)

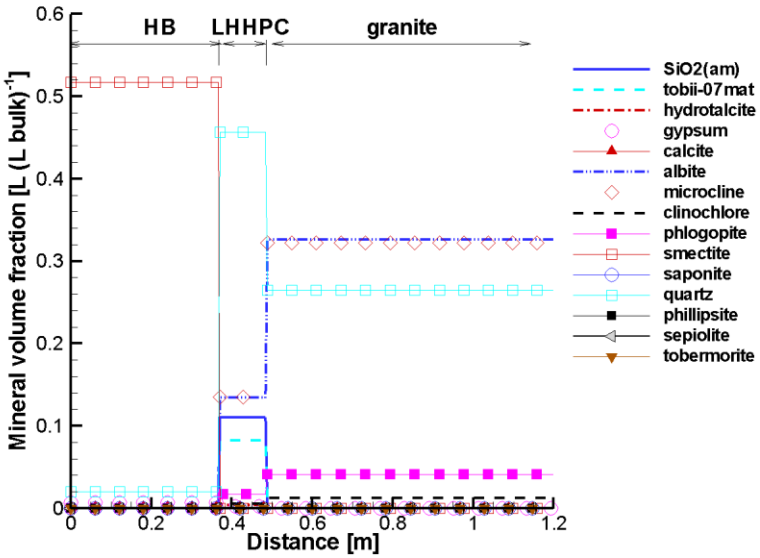

Figure 12: Profiles of Initial Mineral Volume Fractions for Case 1CP and Case 1UP (the Same for Both Cases)

The initial concentrations of Na^+ and SO_4^{2-} are highest in the bentonite, while those in the granite are the lowest, leading to the diffusion of both components from HB towards the granite (Figure 13 to Figure 15). On the contrary, the concentrations of Ca^{2+}, Cl^- and Fe^{2+} in HB are the lowest in the domain, and thus diffusion of these occurs toward the HB (Figure 13 to Figure 15). The concentrations of K^+ and H_4SiO_4 and the pH are highest in the LHHPC, which leads to the diffusion of both K^+ and H_4SiO_4 towards bentonite and granite. Additional simulation results are provided in Appendix A.3.1.

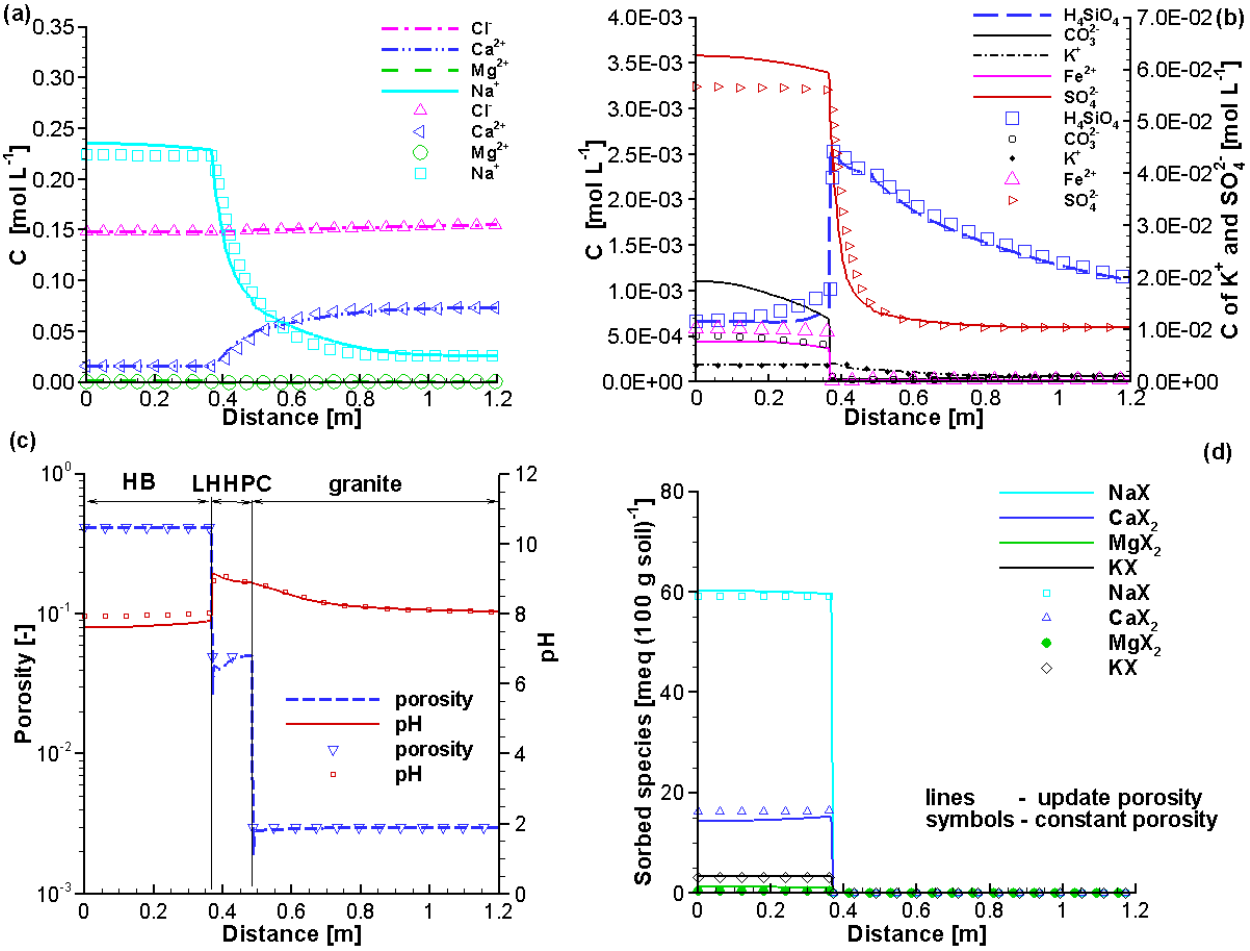

Figure 13: Comparison of Component Concentration Profiles (a and b), pH and Porosity (c) and Sorbed Species (d) at 1,000 Years for Case 1CP (Symbols) and Case 1UP (Lines)

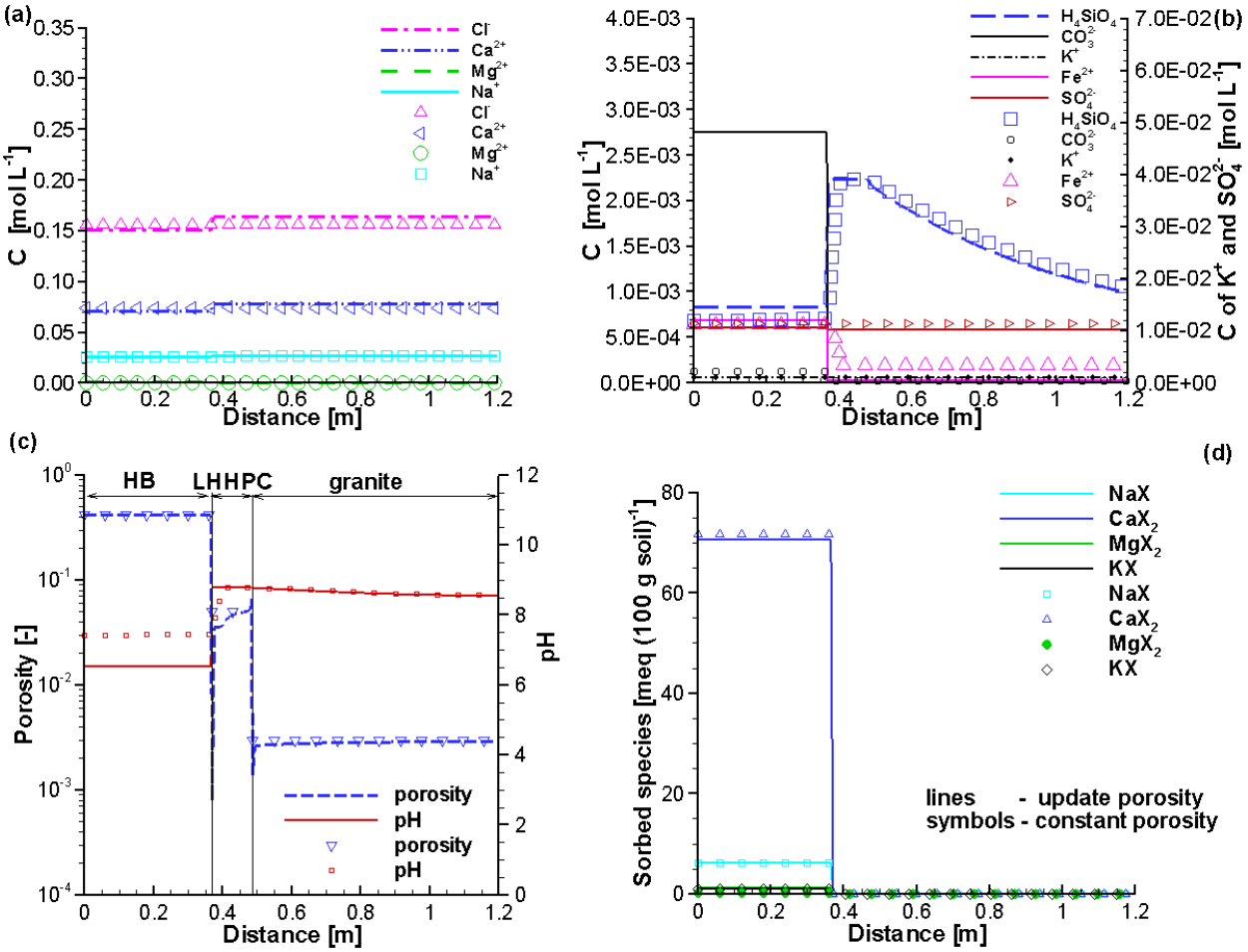

Figure 14: Comparison of Component Concentration Profiles (a and b), pH and Porosity (c) and Sorbed Species (d) at 100,000 Years for Case 1CP (Symbols) and Case 1UP (Lines)

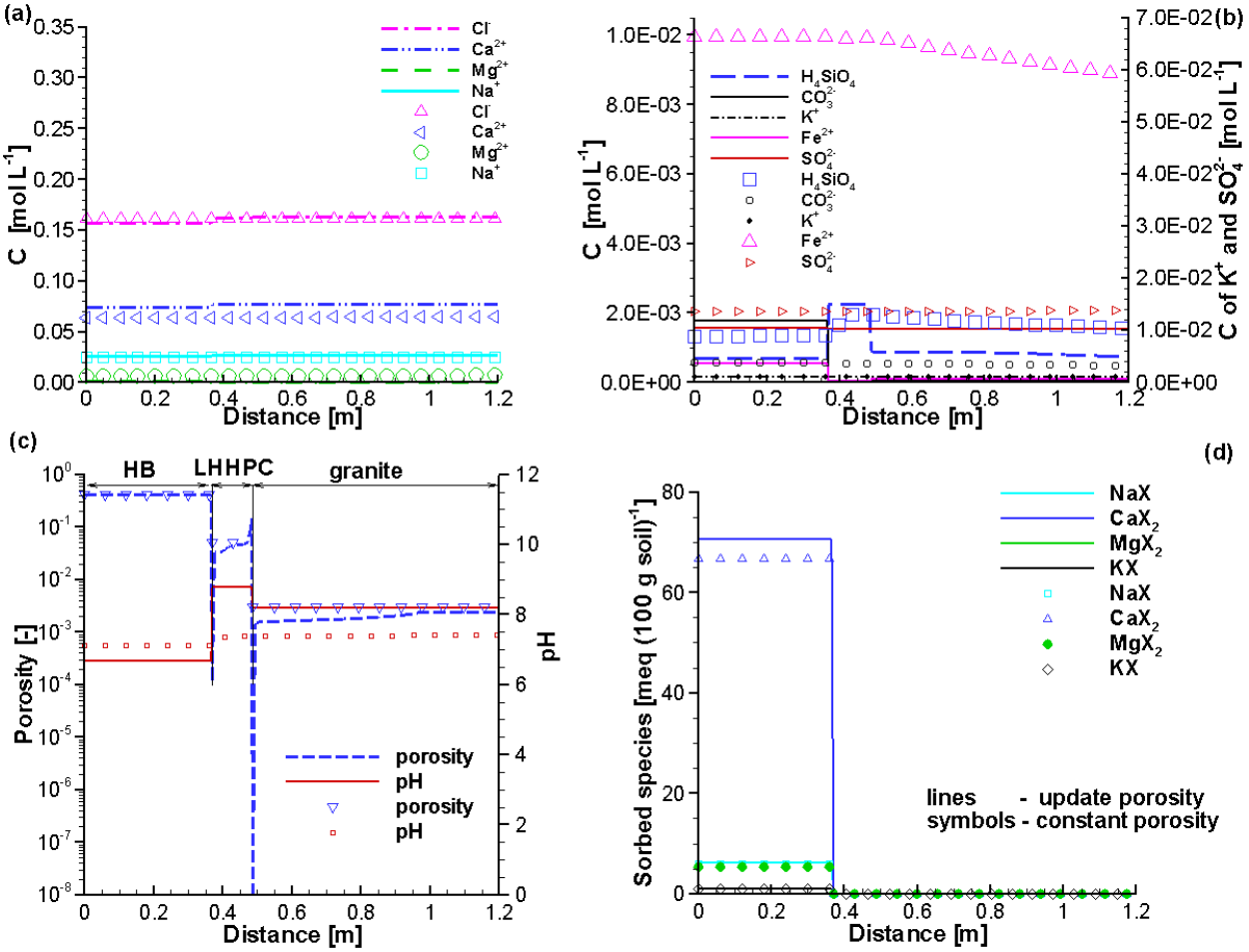

Figure 15: Comparison of Component Concentration Profiles (a and b), pH and Porosity (c) and Sorbed Species (d) at 1,000,000 Years for Case 1CP (Symbols) and Case 1UP (Lines)

Figure 16 depicts the evolution of the mineral volume fractions that are associated with pore clogging at V11 in LHHPC adjacent to the HB/LHHPC interface and V12 in granite adjacent to the LHHPC/Granite interface. At V11, porosity decreases significantly from 100 to 3,000 years, mainly due to the precipitation of gypsum, saponite, sepiolite, tobermorite, calcite, phillipsite and ferrihydrite. The volume fraction of tobermorite increases after 100 years and reaches a peak value at about 1,000 years, followed by a gradual decline. The porosity at V12 begins to decrease from 0.003 to 0.0018 after about 300 years until about 2,000 years due to the precipitation of gypsum. After about 70,000 years, the porosity decreases further until clogging after more than one million years due to the additional precipitation of sepiolite and phillipsite.

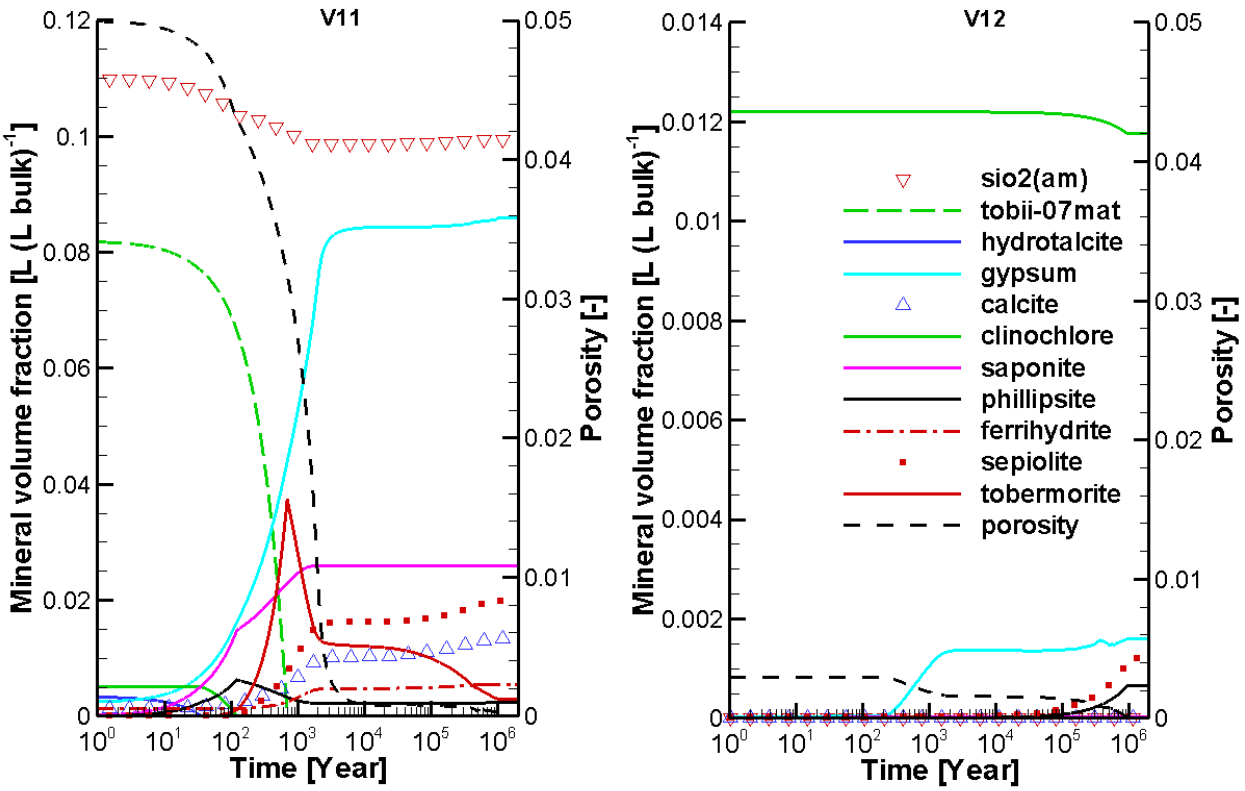

Figure 16: Evolution of the Volume Fractions and Porosity of Selected Minerals at Observation Points V11 (LHHPC, Left) and V12 (Granite, Right) for Case 1UP

The reactions in the HB and LHHPC can be better understood from the profiles of mineral volume fractions at different times (Figure 17 to Figure 19). Simulation results show that mineral alteration in LHHPC is significant, while that in HB is less significant (Figure 17 to Figure 19). The main chemical reactions are: (a) in LHHPC, transformation of the tobermorite-like CSH phase TobII-07mat into tobermorite; dissolution of hydrotalcite plus SiO_2(am) and precipitation of gypsum, phillipsite, saponite and sepiolite; (b) in HB, dissolution of smectite, gypsum and calcite, and precipitation of phillipsite; precipitation of gypsum, calcite, phillipsite, sepiolite at the interface between HB/LHHPC; and (c) a small amount of precipitation of phillipsite and sepiolite in granite near the interface between LHHPC/granite. The excess of silica fume in LHHPC cement provides high concentrations of H_4SiO_4, which is a key component to form zeolites represented by phillipsite (Savage et al. 2007; Donahoe and Liou 1985) and saponite (Shao and Pinnavaia 2010; Besselink et al. 2019).

Tobermorite, phillipsite and saponite are the main minerals in LHHPC after 1,000 years (Figure 17), and remain fairly stable thereafter according to the results for Case 1UP (compare Figure 18 and Figure 19 to Figure 17). In addition, dissolution of SiO_2(am) intensifies in LHHPC close to the LHHPC/granite interface. In contrast, if the feedback of porosity reduction due to mineral dissolution/precipitation is not included (i.e., Case 1CP), tobermorite dissolves from the left hand side at 100,000 years (Figure 18) and disappears at 1,000,000 years (Figure 19). At the same time, volume fractions of sepiolite and calcite increase, while dissolution and precipitation of SiO_2(am) can be observed within LHHPC at 100,000 years (Figure 18). In HB, generally, phillipsite precipitates, while smectite and gypsum dissolves. However, for the constant porosity

case (1CP), the intensity differs substantially compared to Case 1UP. At the interface between HB/LHHPC, the changes in volume fractions are the highest in the domain, no matter whether the porosity is treated as constant or is updated (compare lines to symbols in Figure 17 to Figure 19). It is interesting to note; however, that the change in mineral volume fractions at the interface between LHHPC/granite is relatively small, but that the net porosity reduction in granite adjacent to LHHPC leads to pore clogging after 1,000,000 years due to the very low initial porosity of granite of 0.3% (Case 1UP, and V12 in Figure 20).

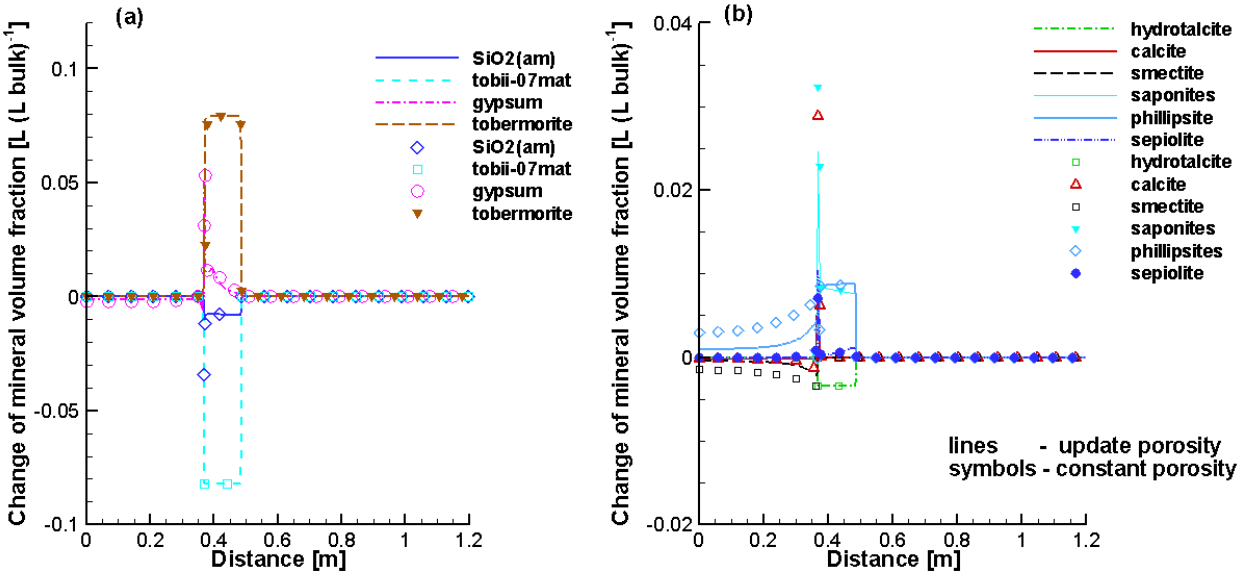

Figure 17: Comparison of Profiles of Mineral Volume Fraction Changes at 1,000 Years for Case 1CP (Symbols) and Case 1UP (Lines)

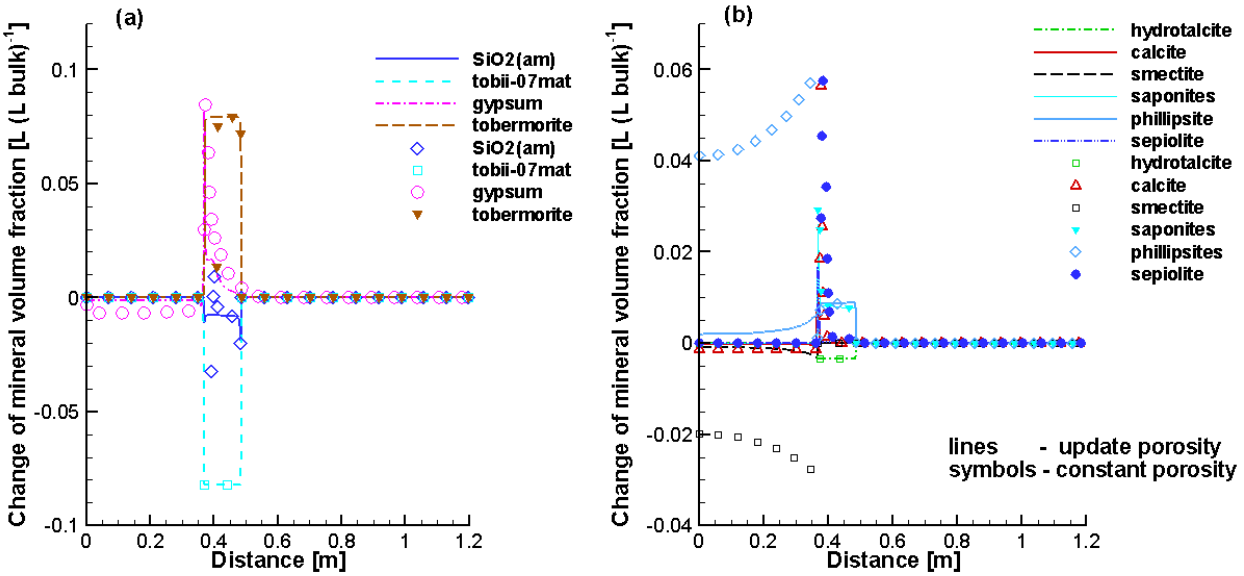

Figure 18: Comparison of Profiles of Mineral Volume Fraction Changes at 100,000 Years for Case 1CP (Symbols) and Case 1UP (Lines)

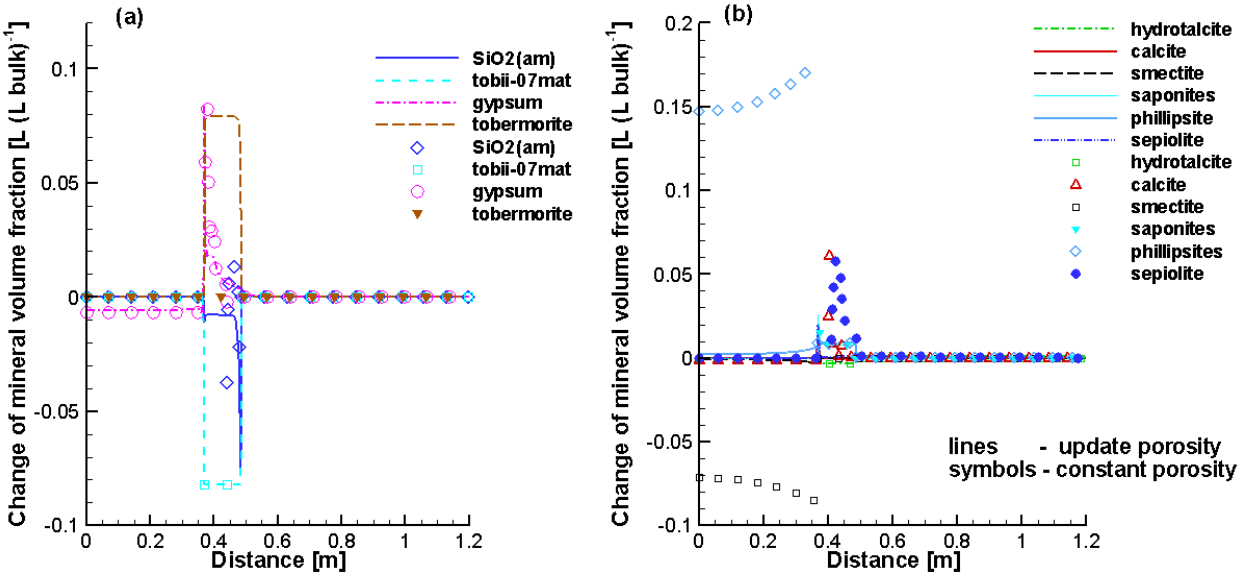

Figure 19: Comparison of Profiles of Mineral Volume Fraction Changes at 1,000,000 Years for Case 1CP (Symbols) and Case 1UP (Lines)

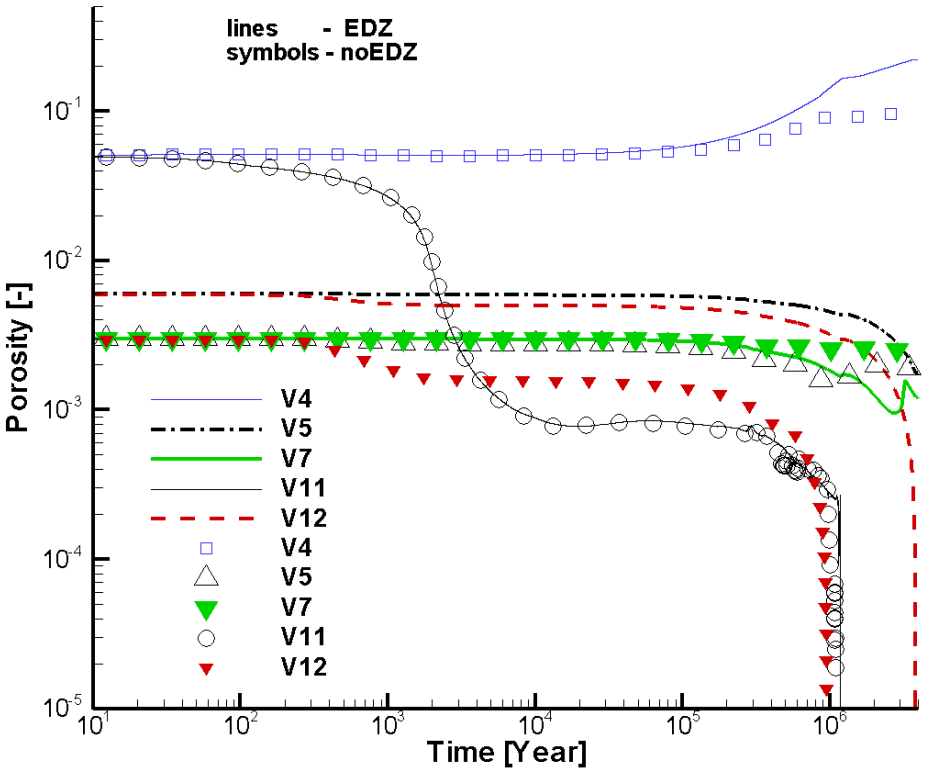

Figure 20: Comparison of Porosity Evolution at Observation Points (Case 1EDZUP – Lines vs. Case 1UP - Symbols). V4 and V11 (LHHPC), V5 and V12 (inner EDZ), V7 (outer EDZ)

Component concentration and pH distributions reflect the chemical interactions as well (Figure 13 to Figure 15). Concentrations of Na^+ decrease in general due to the precipitation of phillipsite and saponite. The dissolution of SiO_2(am) in LHHPC is responsible for the increase of H_4SiO_4 in the domain. Precipitation of gypsum and calcite leads to the decrease of the concentrations of SO_4^{2-} and Ca^{2+}, while smectite dissolution results in the increase of iron concentrations.

After approximately 1,000 years, the pH value in the LHHPC and HB decreases, while the pH in granite increases. This is mainly because of the diffusion of OH^- from the LHHPC into bentonite and granite. In the bentonite, smectite can partially dissolve and form phillipsite, which will further buffer the pH (Figure 17). These reactions are consistent with the literature findings (e.g. Savage et al. 2007).

5.2.1.2 Impact of Reactive Transport on Radionuclide Diffusion – Case 1rCP and 1rUP

Mineral dissolution/precipitation will induce porosity changes that in turn will affect the effective diffusion coefficients. The initial effective diffusion coefficients for I^- in intact granite, LHHPC, and HB are 1.11×10^{-12}, 3.0×10^{-13} and 1.11×10^{-11} $m^2\ s^{-1}$ as given in Table 1, Table 9 and Table 11, respectively.

For the case assuming constant porosity (Case 1rCP) the D_e values of all three materials remain constant. For the small defect canister failure at 1,000 years (see Figure 8), the simulated profiles for I^- concentrations at selected times are shown in Figure 21. After the canister failure, the relative concentration of I^- increases at the left boundary and by 500,000 years the profile is almost flat up to about 40 metres, approaching an equilibrium condition (Figure 21). It is important to note that in all simulations I^- is treated as a conservative tracer.

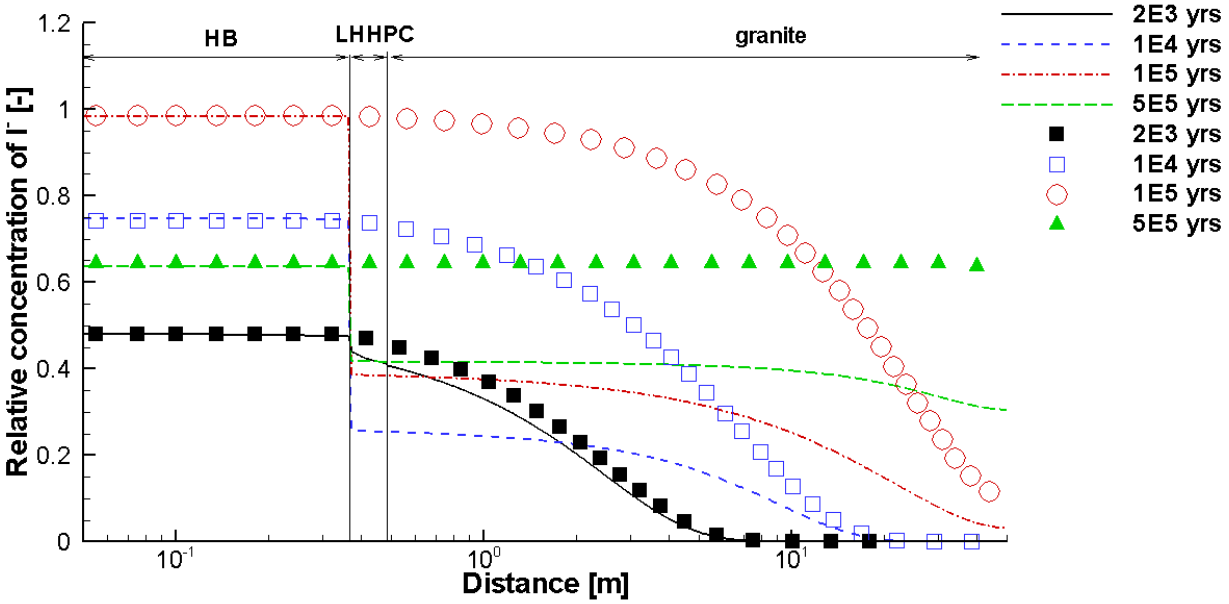

Figure 21: Concentration Profiles of I^- for a Small Defect Occurring at 1,000 Years for Case 1rCP (Symbols) and Case 1rUP (Lines)

For Case 1rUP (updated porosity), the concentration profiles are distinctly different than those for Case 1rCP (Figure 21). At 10,000 years, the sharp drop of the relative concentrations of I^- is due to the substantial porosity reduction from 0.05 to 0.0008 at observation point V11 (in LHHPC adjacent to the HB/LHHPC interface) (Figure 21 and see Figure 20). At 500,000 years, the I^- relative concentration of 0.64 in HB is still much higher than that of 0.42 in LHHPC, indicating an effective retardation due to the clogging position V11.

The comparison of the breakthrough (BT) curves at selected observation points for both Case 1rCP and Case 1rUP is shown in Figure 22. One of the most significant differences in the BT curves occurs at observation point V7, where for Case 1rUP the relative concentration reaches a maximum value of about 0.45 at a time of 364,000 years. On the other hand, for Case 1rCP the maximum I^- relative concentration of 0.97 is simulated at 79,000 years. Relatively large differences in the BT curves also are simulated for observation points V5, V9 and V10 (Figure 22).

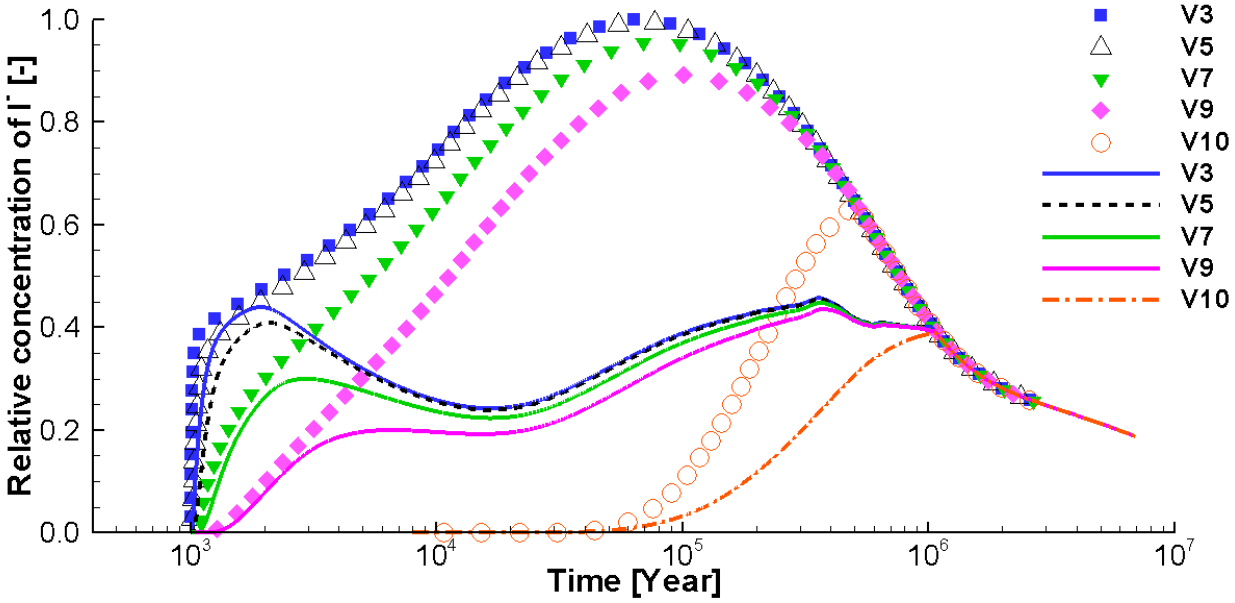

Figure 22: Breakthrough Curves at Selected Observation Points for a Small Defect Occurring at 1,000 Years for Case 1rCP (Symbols) and Case 1rUP (Lines). V3 (LHHPC), V5 to V10 (granite)

The BT curves for selected observation points for a small canister defect occurring at 10,000 years are depicted in Figure 23. The increase in I^- relative concentration at points V3 to V9 is more gradual than for the failure time of 1,000 years because of the significant porosity reduction that takes place near V11 between 2,000 and 10,000 years (Figure 20). This porosity reduction limits the diffusion of I^- across the HB/LHHPC interface. Nevertheless, a peak I^- relative concentration of 0.42 is reached at V7 at about 415,000 years (Figure 23), which is similar to the peak value of 0.45 for a canister failure scenario at 1,000 years (Figure 22). However, the time required to reach the peak concentration is about 50,000 years greater for a canister failure at 10,000 years in comparison to a failure time of 1,000 years.

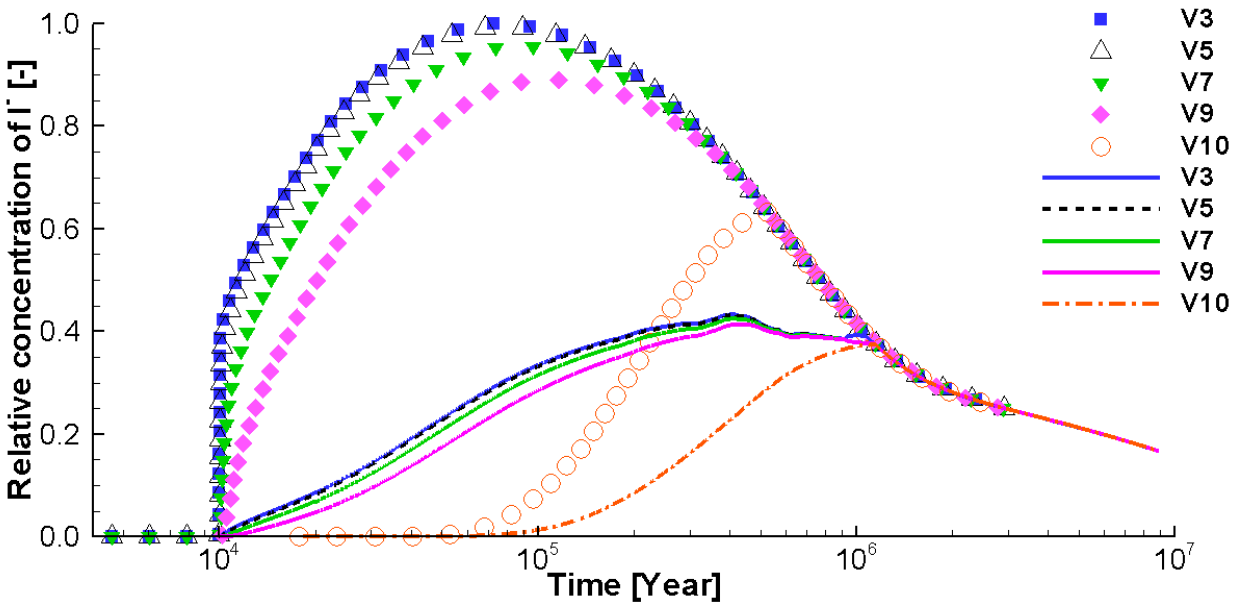

Figure 23: Breakthrough Curves at Selected Observation Points for a Small Defect Occurring at 10,000 Years for Case 1rCP (Symbols) and Case 1rUP (Lines). V3 (LHHPC), V5 to V10 (granite)

For the large defect canister failure at 1,000 years, the I^- relative concentration is assumed to remain at 1.0 for the first year and then abruptly drop to 6.3×10^{-4} (Figure 7 left) and then gradually drop to 1.0×10^{-6} (Figure 7 right). For Case 1rCP, this sudden impulse of I^- at the boundary results in a rapid concentration increase at observation point V3, which is located in LHHPC close to the HB/LHHPC interface (Figure 24). For observation points V5-V9, the concentrations of I^- gradually increase with time and show relatively small differences between Case 1rCP and Case 1rUP (Figure 24).

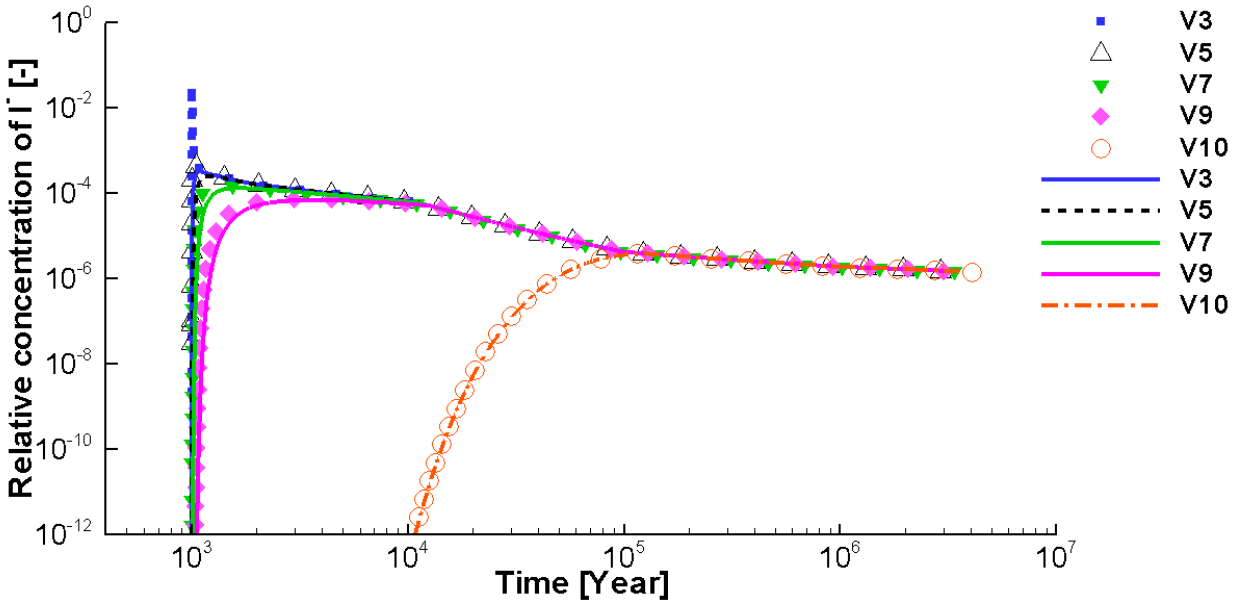

Figure 24: Breakthrough Curves at Selected Observation Points for a Large Defect Occurring at 1,000 Years for Case 1rCP (Symbols) and Case 1rUP (Lines). V3 (LHHPC), V5 to V10 (Granite)

For a large defect occurring at 10,000 years, the BT curves for I^- are depicted in Figure 25 for both Case 1rCP (symbols) and Case 1rUP (lines). The relative concentrations of I^- at all observation points for Case 1rUP are lower than those for Case 1rCP (Figure 25) due to the porosity reduction near the observation point V11 (Figure 20).

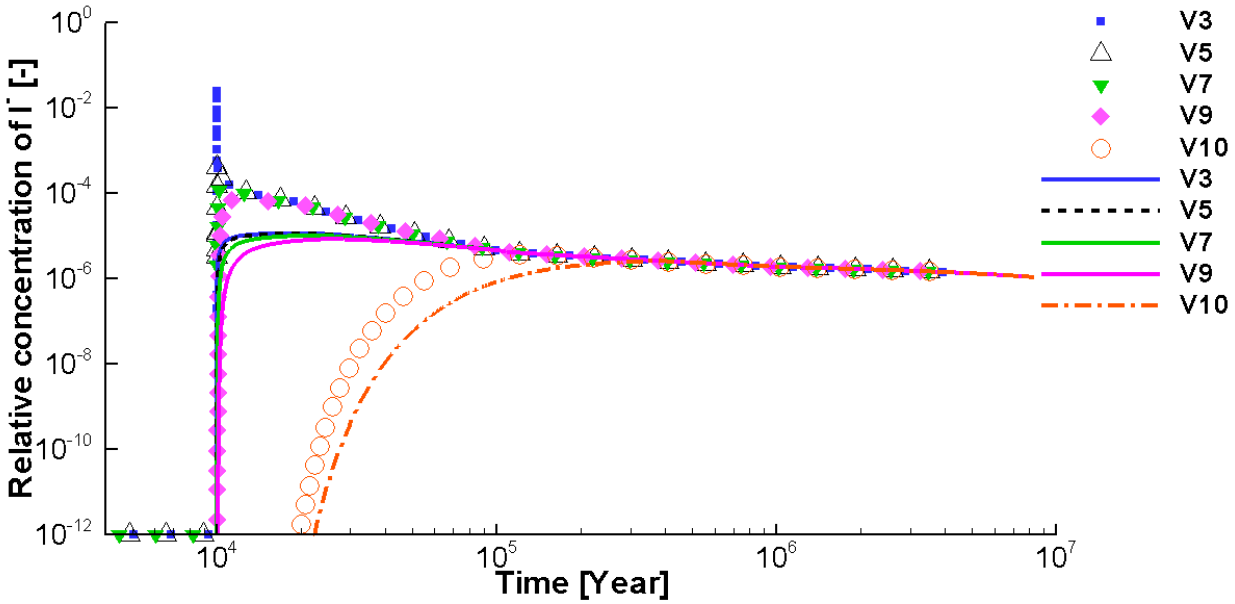

Figure 25: Breakthrough Curves at Selected Observation Points for a Large Defect Occurring at 10,000 Years for Case 1rCP (Symbols) and Case 1rUP (Lines). V3 (LHHPC), V5 to V10 (Granite)

5.2.2 Case 1 (HB/LHHPC/Granite) - With Consideration of EDZs

The initial conditions for the simulations including EDZs are the same as the aforementioned cases in Section 5.2.1 with the additional consideration of the increased porosity and diffusion coefficients in the EDZs. The simulated results for mass transport and chemical reactions for the cases including EDZs are very similar to those for the cases without consideration of EDZs, and in the following subsections emphasis will be put on the differences. Additional simulation results including EDZs are provided in Appendix A.3.2.

5.2.2.1 Impact of EDZs on Reactive Transport – Case 1UP and 1EDZUP

Figure 26 to Figure 28 present the profiles of component concentrations, porosity, pH and the concentrations of sorbed species at 1,000, 100,000 and 1,000,000 years, respectively. The results show that all parameters within the HB are very similar for both Case 1UP and 1EDZUP, indicating that the EDZs have little impact on the reactive transport processes within the HB. At the HB/LHHPC interface, however, the porosity at one million years for Case 1UP is lower than that of Case 1EDZUP (Figure 28c). The difference in porosity at the interface between LHHPC/granite is even larger. At one million years, the simulation results show complete pore clogging when EDZs are not considered (Case 1UP), but only a slight decrease in porosity is predicted if EDZs are taken into consideration (Figure 28 and compare the porosity evolution curves at the observation points V11 and V12 in Figure 20). The increased porosity in the inner EDZ enhances ion diffusion and thus more granite pore water components will react with the LHHPC. This enhances SiO_2(am) dissolution in the LHHPC close to the interface in Case 1EDZUP in comparison to that for Case 1UP (Figure 29c lines). Consequently, the products of the dissolution diffuse into the granite (Figure 28) and cause greater precipitation within the inner EDZ – greater phillipsite and sepiolite precipitation are predicted in the granite for Case 1EDZUP compared to Case 1UP (Figure 29 b and d).

Overall, the impact of EDZs in granite is not significant in terms of the main component concentrations and the volume fractions of most of the minerals. This is because significant porosity reduction occurs primarily in the LHHPC at the HB/LHHPC interface, which limits solute migration. However, due to the very low initial porosity of granite, small amounts of precipitation result in significant porosity reduction at the interfaces, and ultimately causing effective or full clogging at certain positions within the domain (Figure 29 and Figure 20).

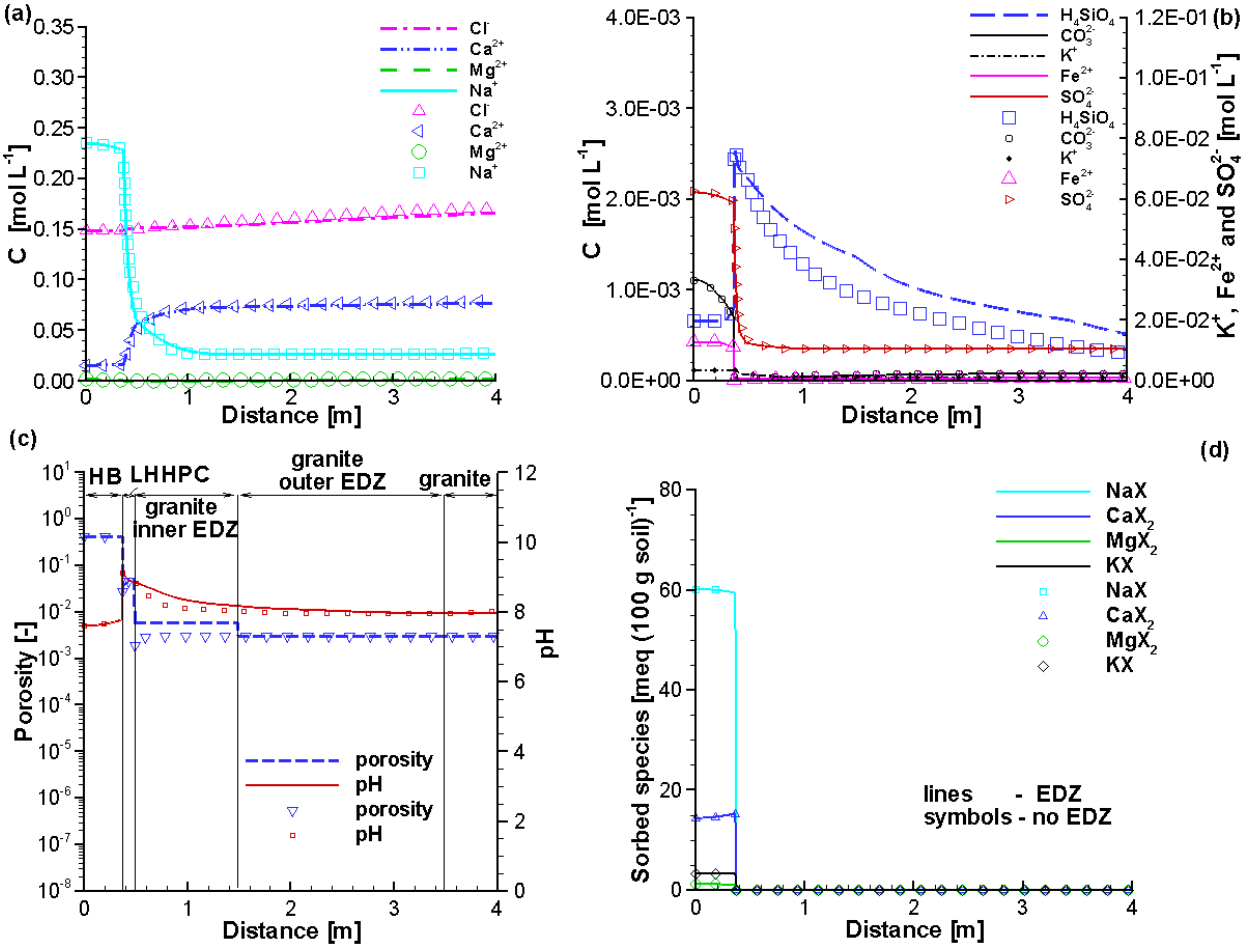

Figure 26: Comparison of Component Concentration Profiles (a and b), pH and Porosity (c) and Sorbed Species (d) at 1,000 Years for Case 1UP (Symbols) and Case 1EDZUP (Lines)

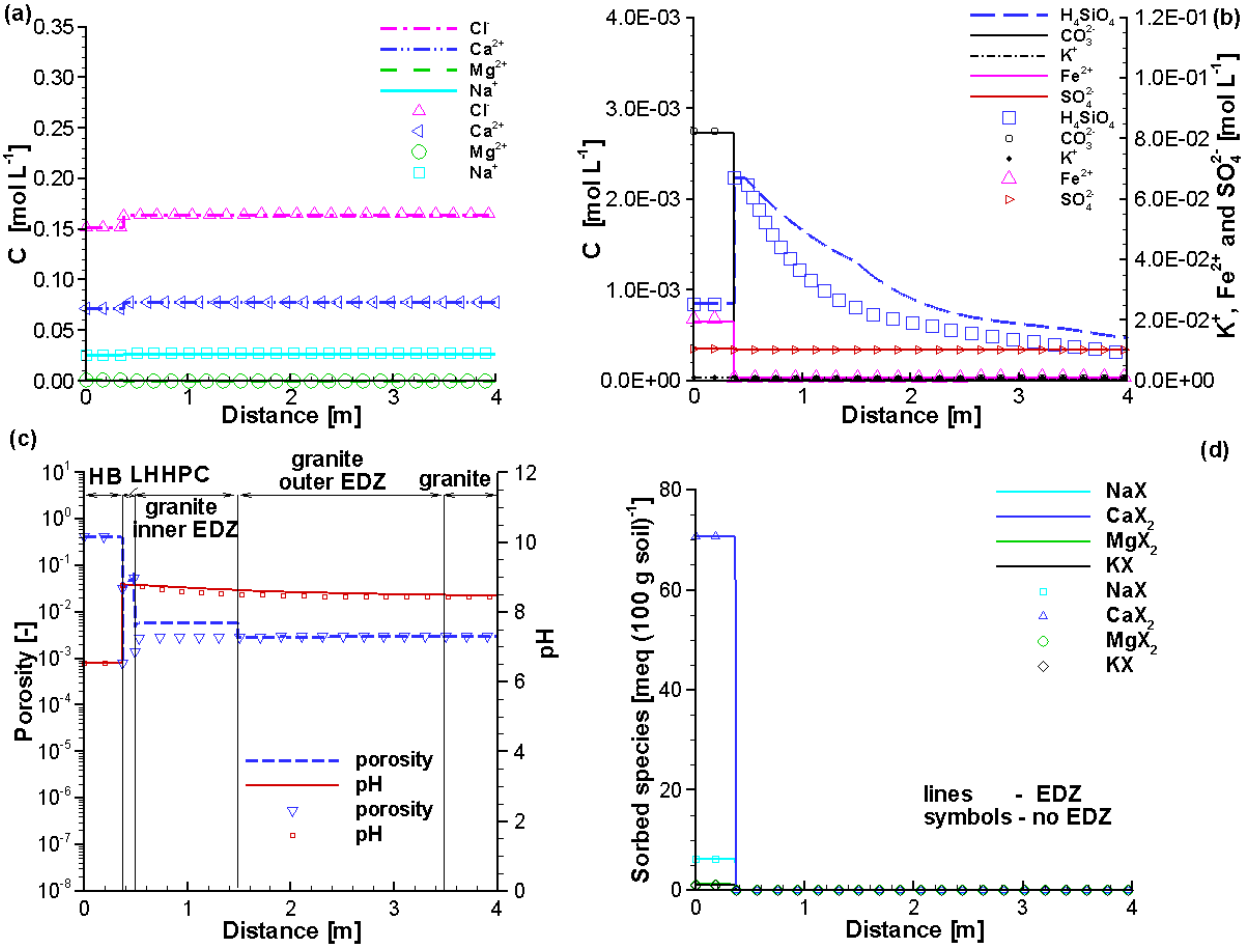

Figure 27: Comparison of Component Concentration Profiles (a and b), Porosity and pH (c) and Sorbed Species (d) at 100,000 Years for Case 1UP (Symbols) and Case 1EDZUP (Lines)

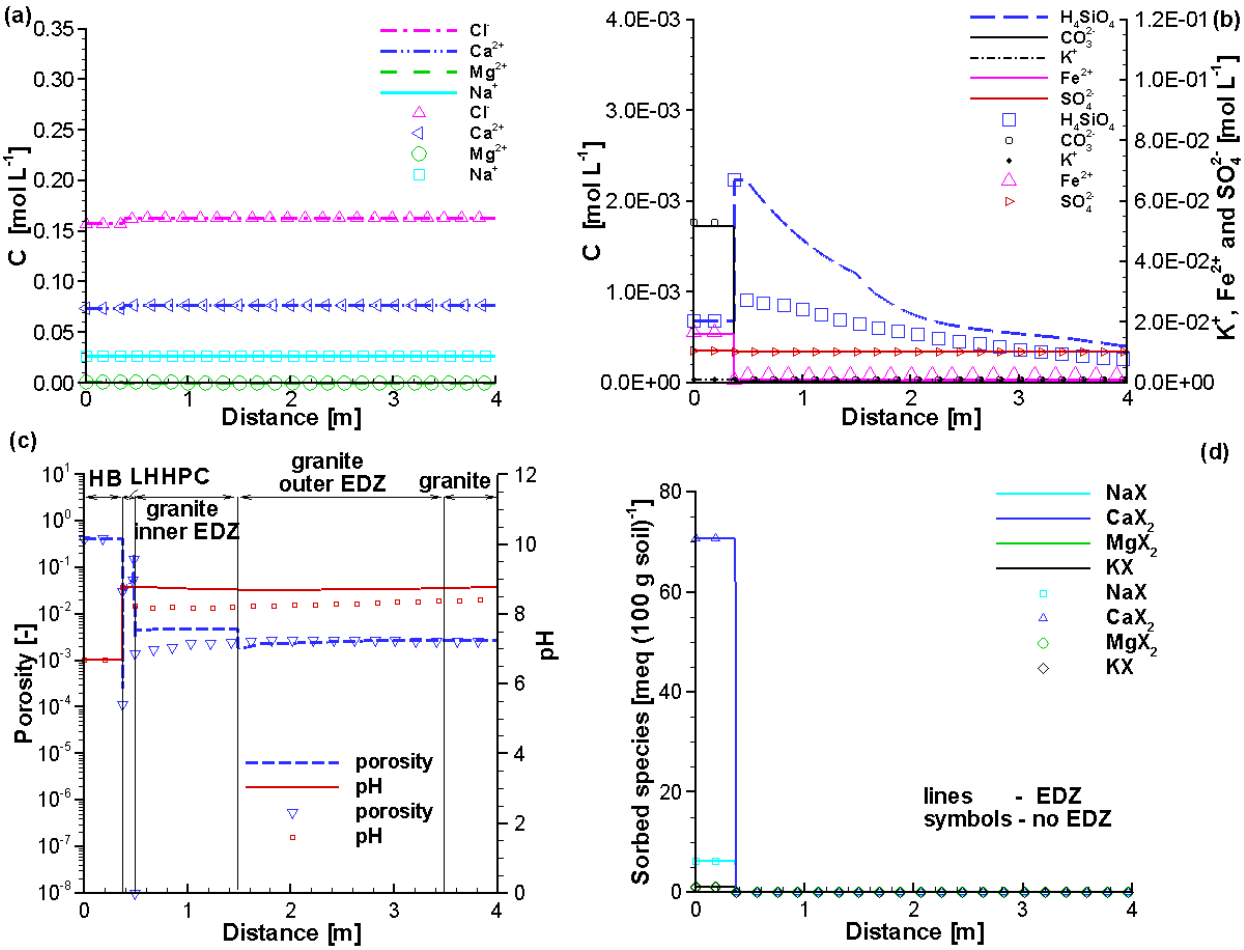

Figure 28: Comparison of Component Concentration Profiles (a and b), Porosity and pH (c) and Sorbed Species (d) at 1,000,000 Years for Case 1UP (Symbols) and Case 1EDZUP (Lines)

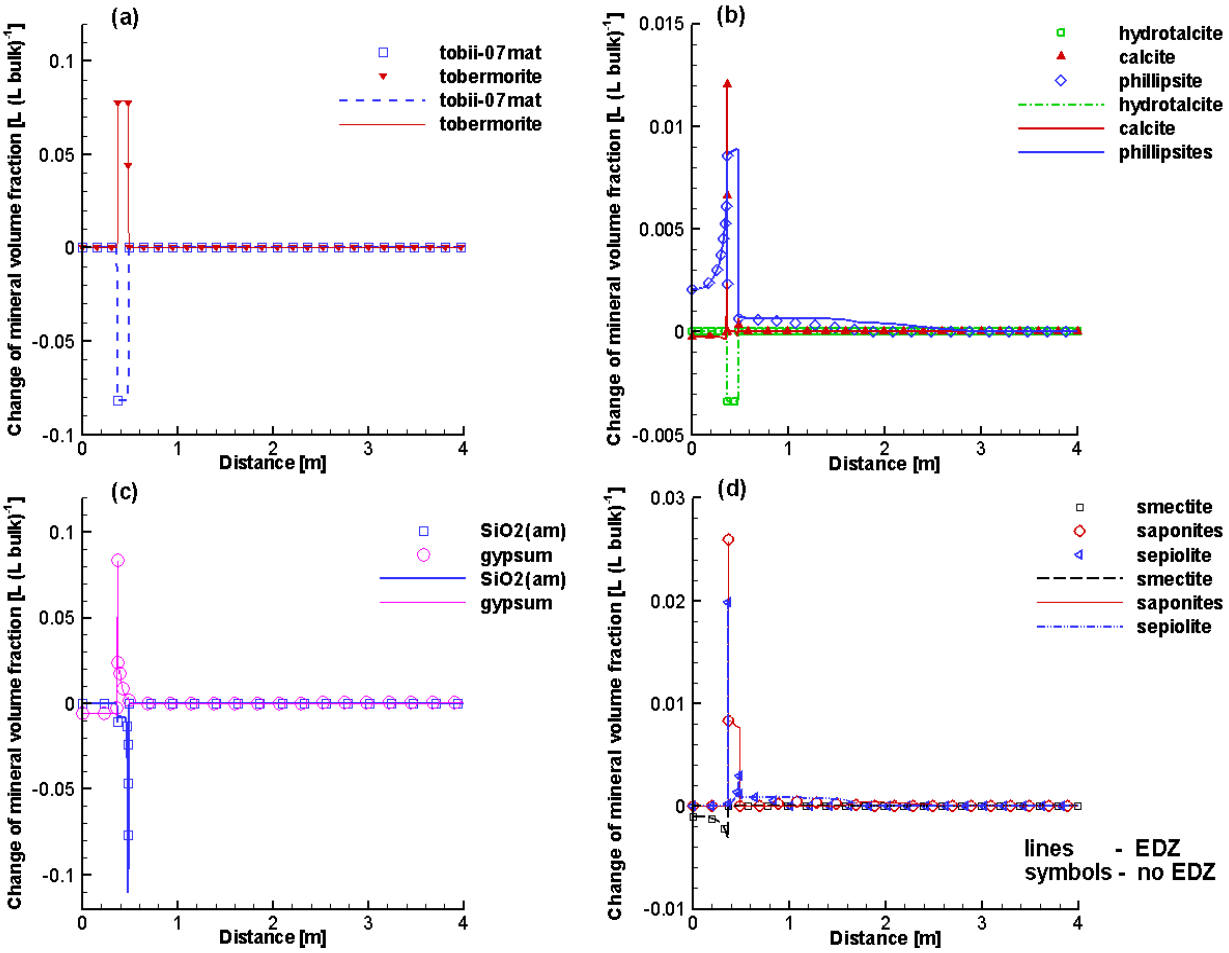

Figure 29: Comparison of Profiles of Mineral Volume Fraction Changes at 1,000,000 Years for Case 1UP (Symbols) and Case 1EDZUP (Lines)

5.2.2.2 Impact of EDZs on Radionuclide Diffusion – Case 1rEDZCP and 1rEDZUP

The impact of EDZs on radionuclide migration is illustrated by comparing results for cases with and without consideration of EDZs. For conciseness, only the results for the cases associated with the small defect scenario occurring at 1,000 years are described in detail here. The simulation results for this scenario are depicted in Figure 30 to Figure 32. Figure 30 shows that when the porosity and effective diffusion coefficients are held constant, the I^- profiles are very similar for simulations that ignore (Case 1rCP) or include (Case 1rEDZCP) EDZs. The maximum difference in I^- concentration is only about 11% at 10,000 years for locations close to the interface between the outer EDZ and intact granite.

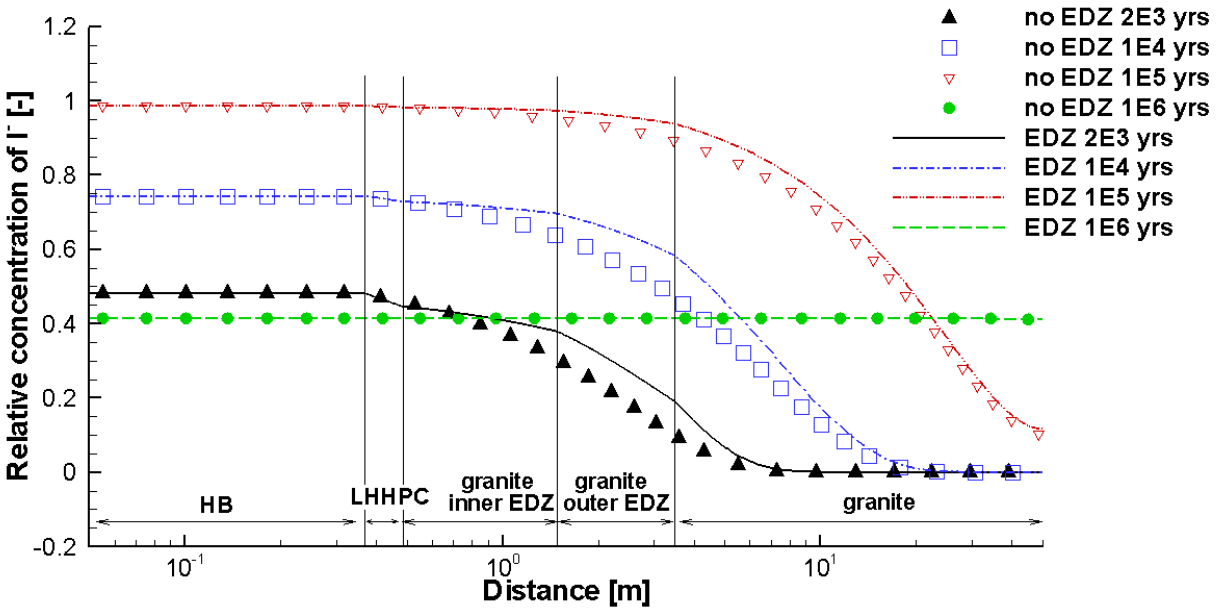

Figure 30: Concentration Profiles of I^- at Selected Times for a Small Defect Occurring at 1,000 Years for Case 1rCP (Symbols) and Case 1rEDZCP (Lines)

The simulated profiles of I^- for cases in which reaction-induced porosity change and its feedback are included are depicted in Figure 31. There are abrupt changes in I^- concentrations at the HB/LHHPC interface due to the aforementioned significant porosity reduction near observation point V11 (Figure 20). In the HB, the relative concentrations of I^- profiles at various times for both cases are nearly flat, and no differences between the two cases are observed. At 2,000 years, the relative concentrations of I^- in the LHHPC and in the inner EDZ up to about 1.0 m for Case 1rEDZUP (Figure 31 black line) are lower than those for Case 1rUP (Figure 31 black symbols). This is because of the higher effective diffusion coefficients in the EDZs. A maximum I^- concentration difference, of about 7%, is observed between Case 1rEDZUP and Case 1rUP at 2,000 years in outer EDZ.

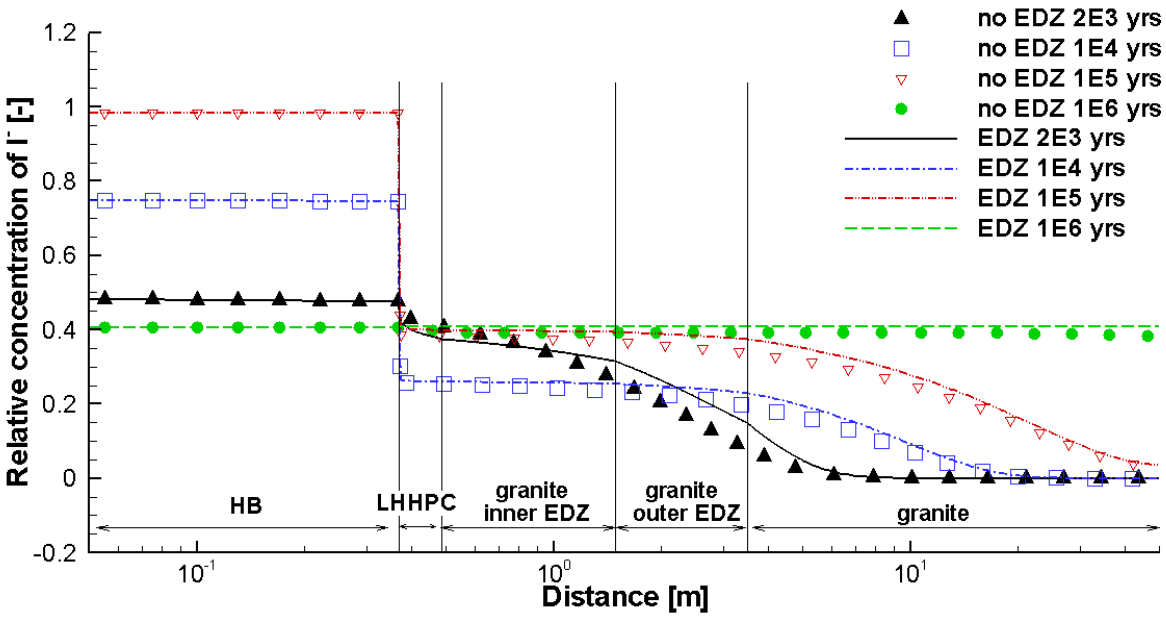

Figure 31: Concentration Profiles of I^- at Selected Times for a Small Defect Occurring at 1,000 Years for Case 1rUP (Symbols) and Case 1rEDZUP (Lines)

Breakthrough curves for I^- at selected observation points for the small defect occurring at 1,000 years for the cases assuming constant and updated porosity, and/or considering EDZs are depicted in Figure 32. By comparing these results it is seen that:

a) The peak values of I^- for cases assuming constant porosity can be up to 65% higher than the cases with updated porosity and diffusion coefficients (Figure 32). For the constant porosity cases (i.e. 1rCP and 1rEDZCP), there is only one peak for each BT curve; however, for the updated porosity and diffusion coefficient cases, two peaks are predicted. The first peak reflects the impact of porosity reduction near V11 (Figure 20), while the second peak corresponds to the transient I^- boundary condition (Figure 8).

b) Generally, the predicted I^- concentrations for the cases considering EDZs are higher than those without consideration of EDZs at all observation points except V3 and V5 before about 7,000 years. This is because of the location of V3 and V5 (Figure 3 and Figure 4), both of which are to the right of V11. In comparison to the cases without EDZs, higher diffusion coefficients in the EDZs, lower the I^- concentration gradient. Therefore, the relative concentrations of I^- at the interface between LHHPC/granite are lower with respect to the corresponding case without EDZs.

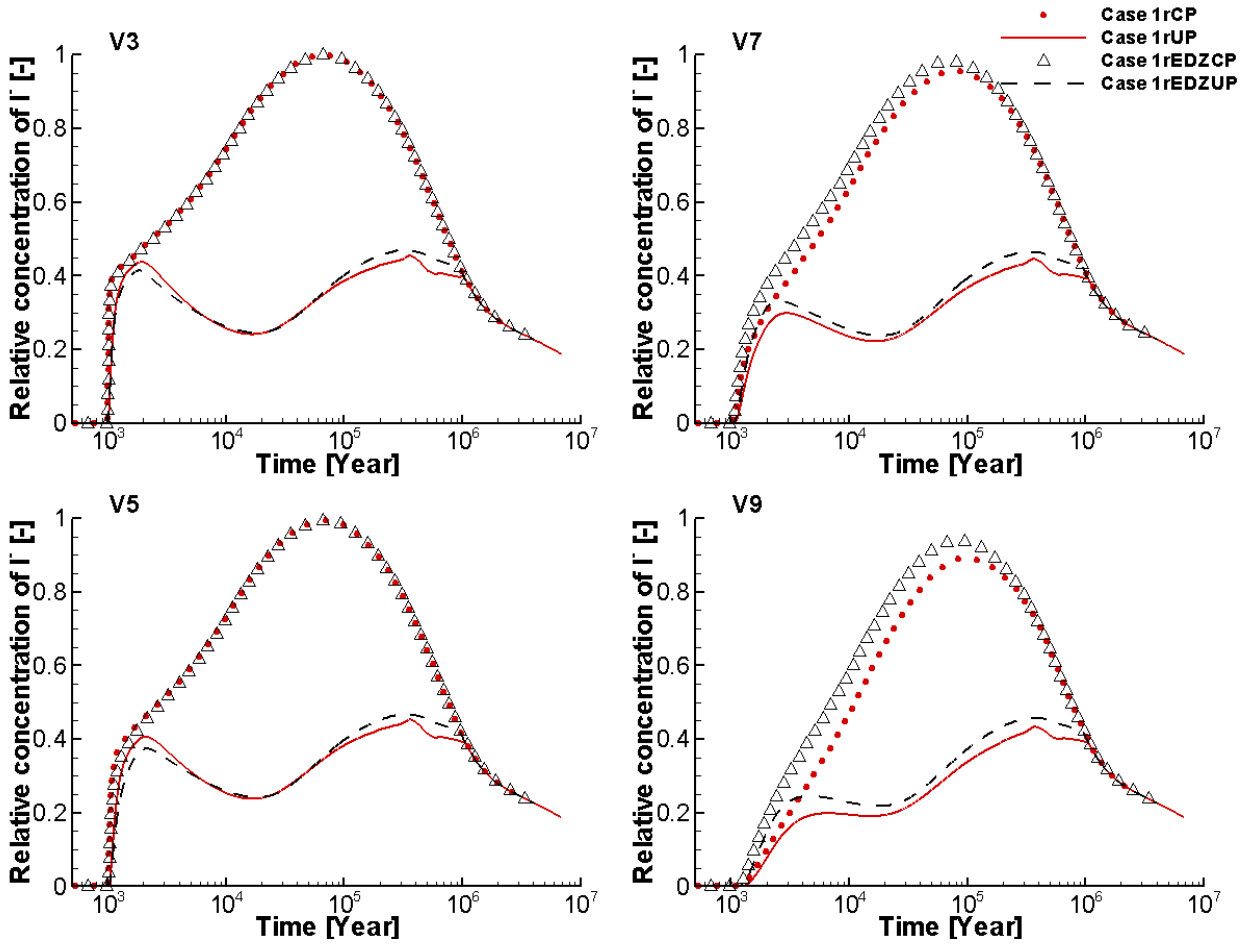

Figure 32: Breakthrough Curves at Selected Observation Points for a Small Defect Occurring at 10,000 Years for Cases 1rCP, 1rUP, 1rEDZCP and 1rEDZUP. V3 (LHHPC), V5 (Inner EDZ), V7 (Outer EDZ) and V9 (Intact Granite)

The impact of EDZs on I^- transport for the other canister failure scenarios (i.e. small defect at 10,000 years; large defect at 1,000 or 10,000 years) produced results similar to those discussed above. Selected results for these simulations are provided in Appendix A.3.2.

5.2.3 Case 2 (HB/Granite) – Without Consideration of EDZs

Case 2 includes homogenized bentonite (HB) and granite, both of which are natural materials with nearly neutral initial pH values. The initial concentrations of components and sorbed species, pH, porosity (Figure 33) and initial volume fractions of primary minerals (Figure 34) in HB and granite are the same as in Case 1 (Figure 11). In this subsection the results of the simulations for Case 2 without EDZs (i.e. Case 2CP and Case 2UP, Table 14) are discussed, including reactive transport (Subsection 5.2.3.1), and the impact of different canister failure scenarios on radionuclide migration (Subsection 5.2.3.2).

Simulation results for Case 2 considering EDZs (i.e. Case 2EDZCP and Case 2EDZUP, Table 14) are discussed in Section 5.2.4. These results will be compared to Case 2CP and Case 2UP to show the impact of EDZs on reactive transport and on radionuclide migration.

5.2.3.1 Reactive Transport – Case 2CP and 2UP

After 100,000 years, the concentration of Na^+ within the HB drops slightly from the initial 0.30 to 0.29 mol L^{-1} water, while that of Ca^{2+} increases from 0.011 to 0.014 mol L^{-1} water (Figure 33 and Figure 36), which differs substantially from the results for Case 1 (compare Figure 36 to Figure 14). This is mainly due to the dissolution of gypsum in the HB (Figure 37). Due to ion exchange, sorbed sodium can be released into the solution as well. Consequently, NaX remains the dominant sorbed species with a slight drop in concentration from 68.3 to 66.2 meq (100 g soil)$^{-1}$.

Precipitation of small amount of gypsum and calcite is simulated at the interface between HB and granite (Figure 37). However, the amount of mineral dissolution/precipitation is very small. As a result, the profiles of component concentrations, pH, sorbed species, and porosity for Case 2CP (constant porosity and effective diffusion coefficients) show no noticeable difference to those for Case 2UP (updated porosity) (Figure 35 to Figure 36). Simulated profiles of mineral volume fractions also exhibit very small differences for both cases (Figure 37), indicating that bentonite is geochemically stable when in contact with the granite host rock. The small amount of gypsum precipitation at V11 results in a small porosity decrease at that location (Figure 38).

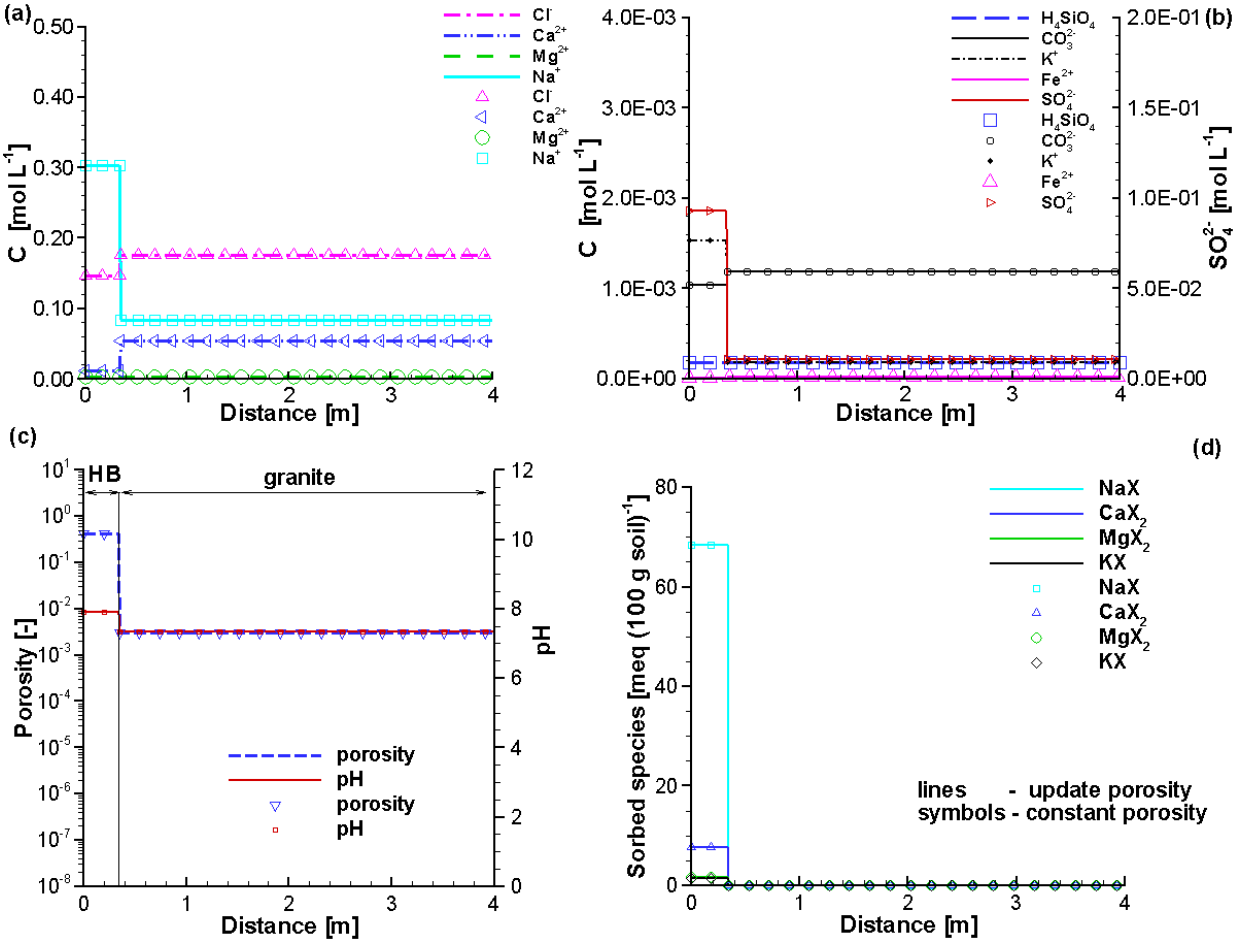

Figure 33: Profiles of Initial Component Concentrations (a and b), pH and Porosity (c) and Sorbed Species (d) for Case 2CP (Symbols) and Case 2UP (Lines)

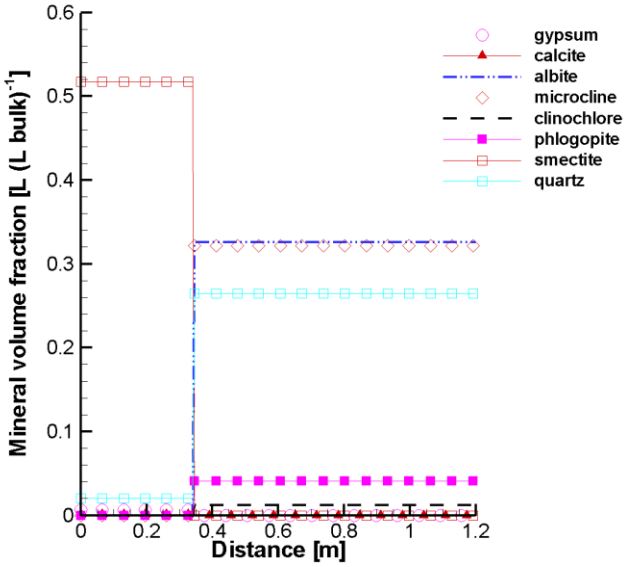

Figure 34: Profiles of Initial Mineral Volume Fractions for Case 2CP and Case 2UP (the Same Fraction of Each Mineral for Both Cases)

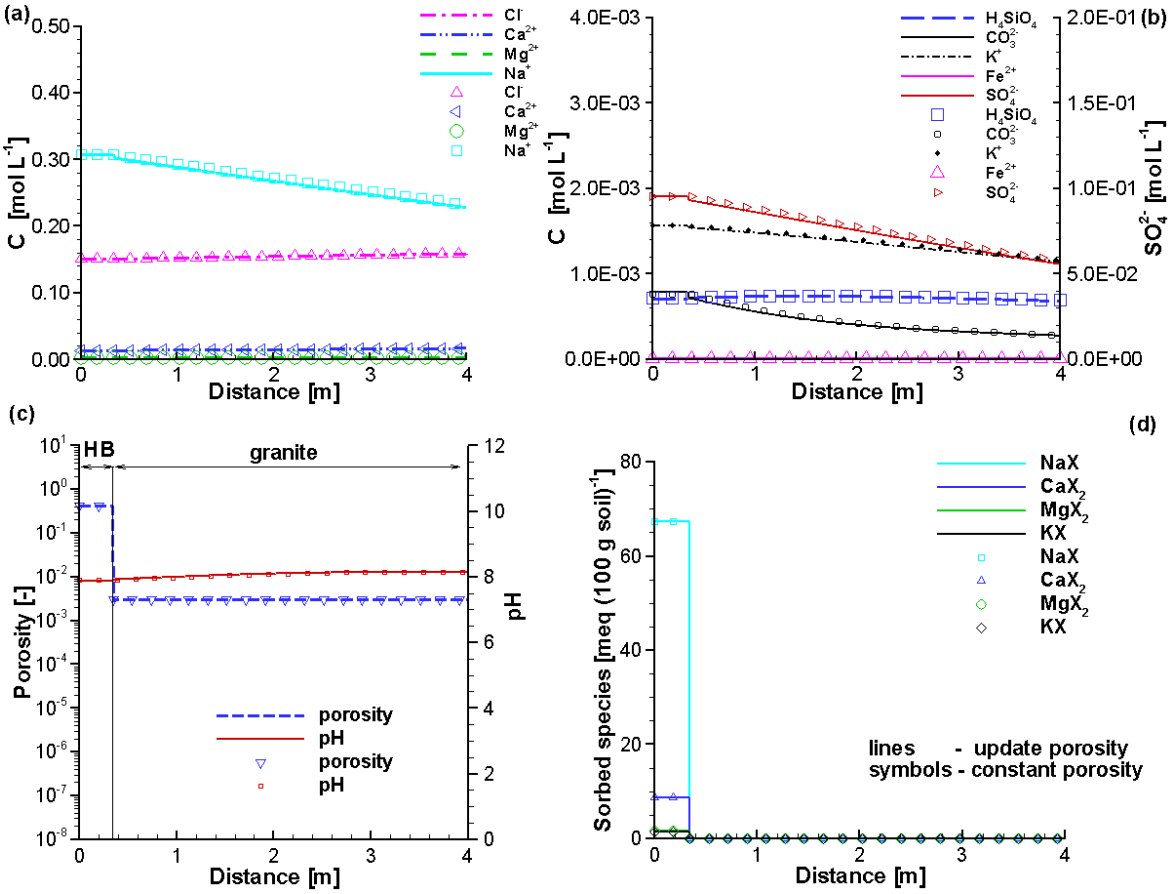

Figure 35: Comparison of Component Concentration Profiles (a and b), pH and Porosity (c) and Sorbed Species (d) at 10,000 Years for Case 2CP (Symbols) and Case 2UP (Lines)

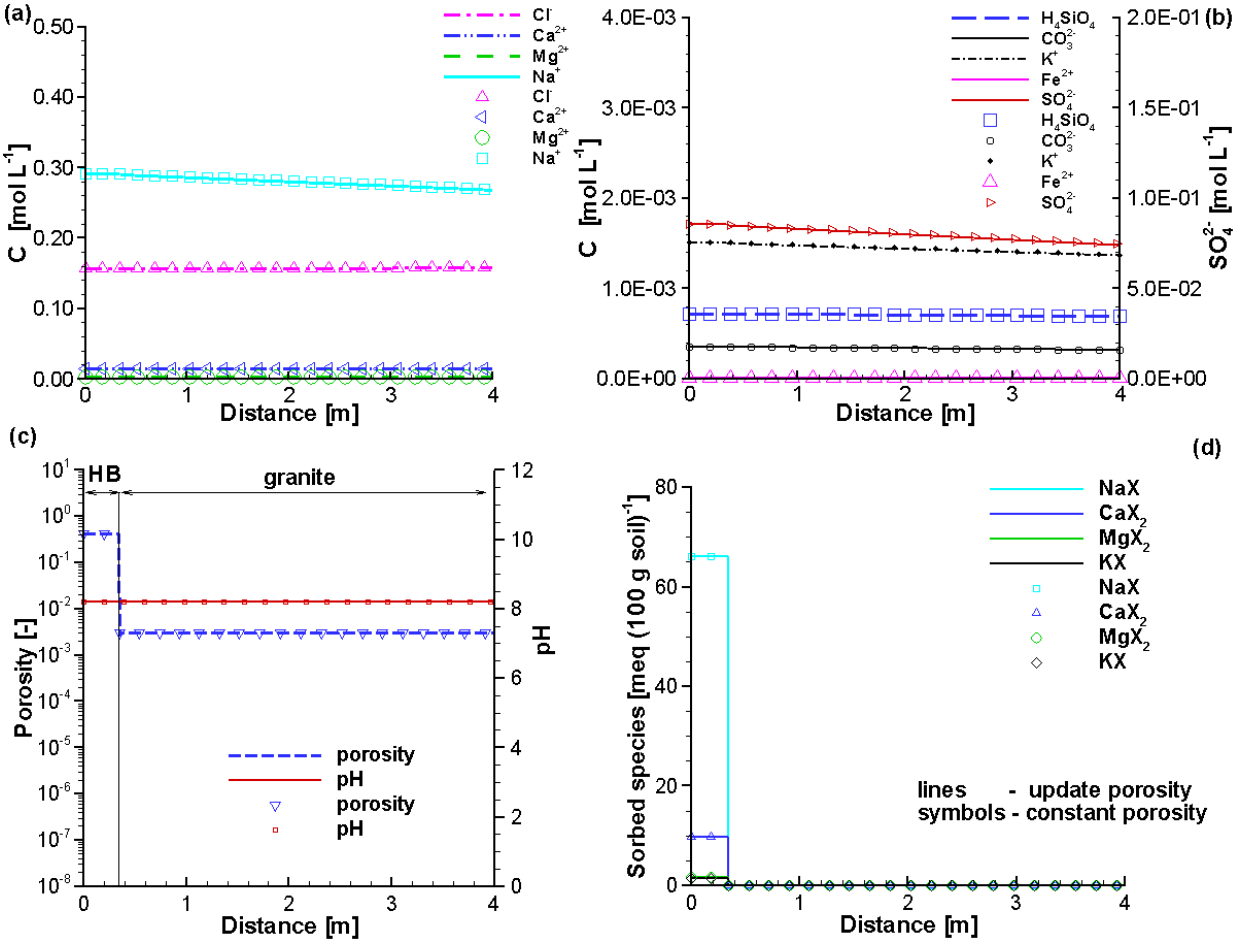

Figure 36: Comparison of Component Concentration Profiles (a and b), pH and Porosity (c) and Sorbed Species (d) at 100,000 Years for Case 2CP (Symbols) and Case 2UP (Lines)

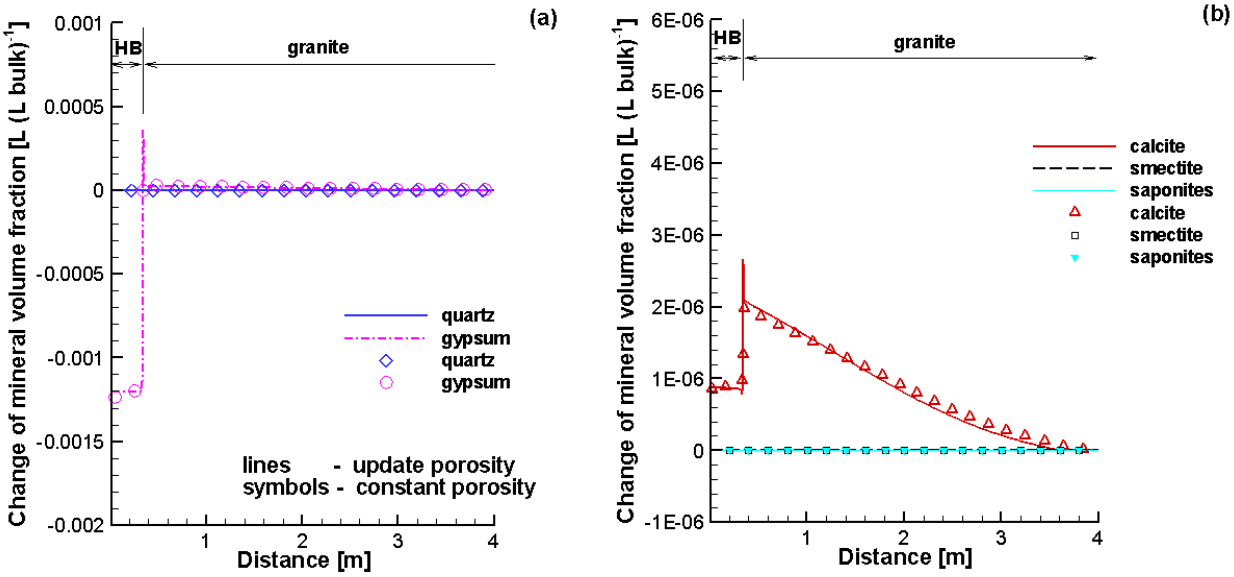

Figure 37: Comparison of Profiles of Mineral Volume Fraction Changes at 100,000 Years for Case 2CP (Symbols) and Case 2UP

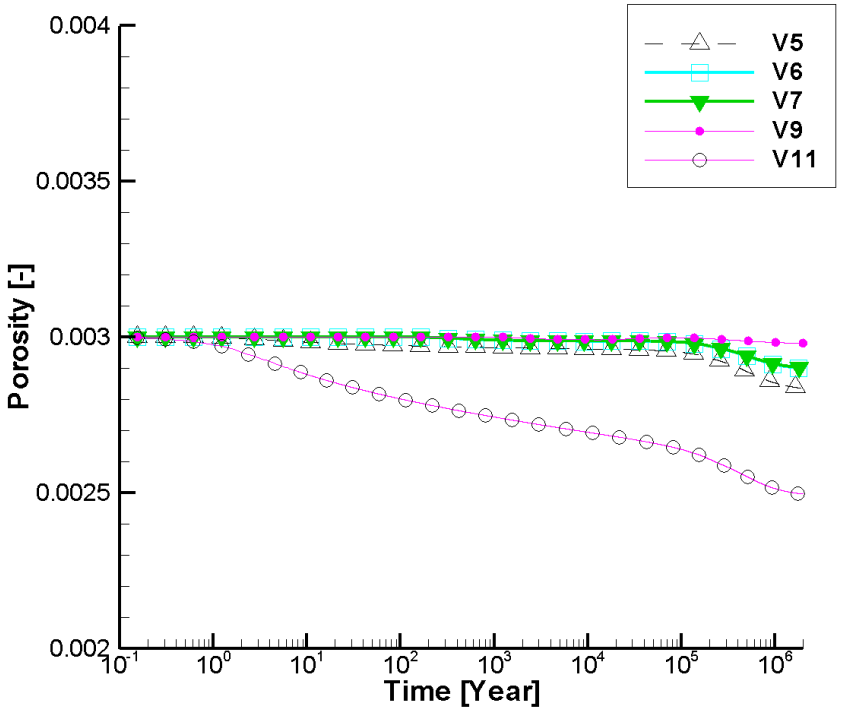

Figure 38: Porosity Evolution at Selected Observation Points V5 to V11 (Granite) for Case 2UP

5.2.3.2 Impact of Reactive Transport on Radionuclide Diffusion – Case 2rCP and 2rUP

As expected, the small amount of gypsum dissolution/precipitation has very limited impact on radionuclide migration. Figure 39 (red symbols and lines) presents the breakthrough curves at selected observation points for a small canister defect occurring at 1,000 years. There are only small differences in simulated relative concentrations of I^- for Case 2rCP (red symbols) and Case 2rUP (red solid lines), mostly at the early times after the canister failure. The simulated relative concentrations of I^- for Case 2rCP are either higher or equal to those for Case 2rUP. At V3 (in HB close to the HB/granite interface, Figure 5), there is a small difference in I^- concentration between both cases for a short time period after the canister failure occurring at 1,000 years (Figure 39). At V5 (in granite, close to the interface), the difference in I^- concentration between both cases is larger than that at V3, especially within 1,000 years after the canister failure. At V7 and V9 in granite, the simulated I^- concentrations for Case 2rCP is slightly higher than those for Case 2rUP.

Figure 40 depicts the simulated I^- concentration profiles at selected times for the small canister failure scenario for Case 2rCP and Case 2rUP. The results for Case 2rCP (symbols) show slightly higher concentrations than those for Case 2rUP (lines), with the differences decreasing with time. At 2,000 years, the maximum difference in I^- concentration between both cases is about 4.0% close to the interface between HB and granite (Figure 40).

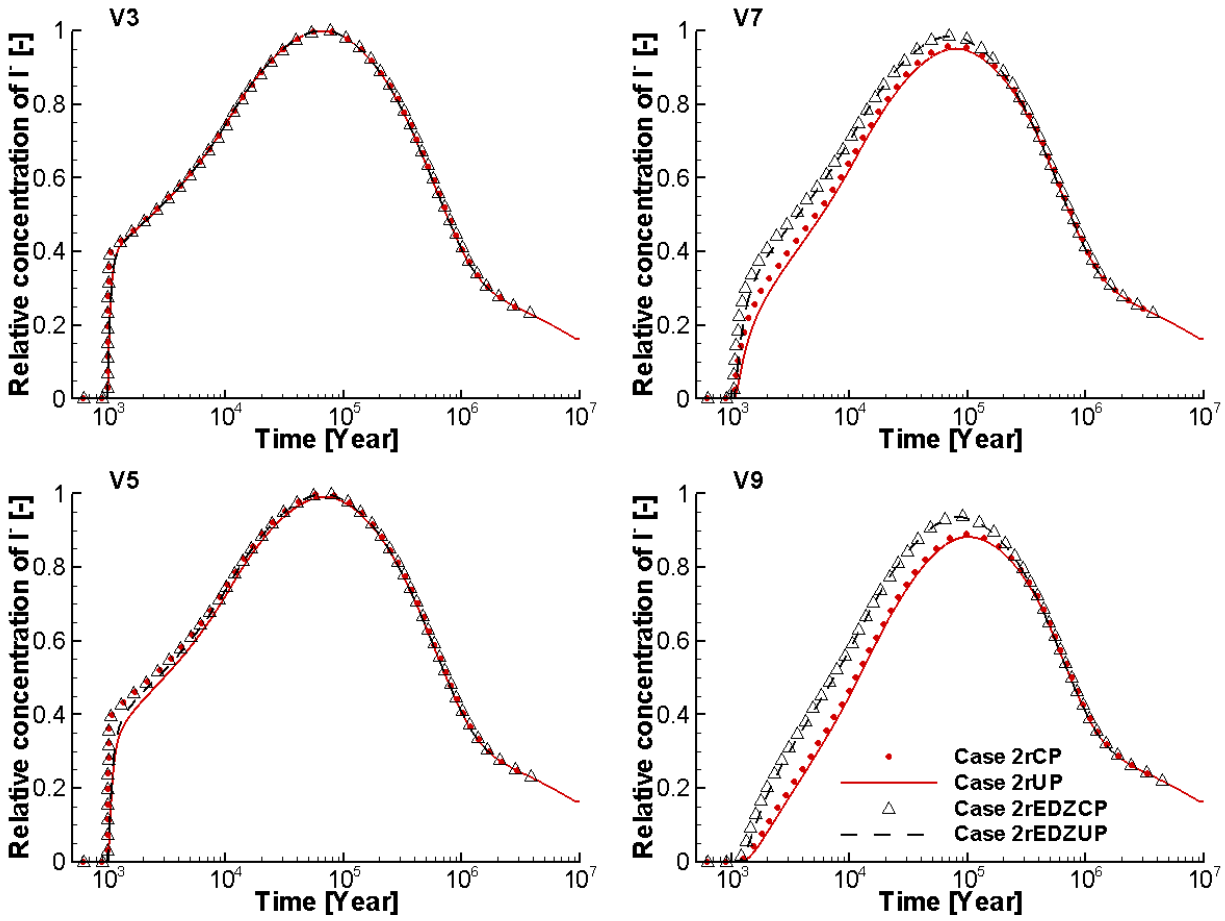

Figure 39: Breakthrough Curves at Selected Observation Points for a Small Defect Occurring at 1,000 Years for Cases 2rCP, 2rUP, 2rEDZCP and 2rEDZUP. V3 (HB), V5 (Inner EDZ), V7 (Outer EDZ) and V9 (Intact Granite)

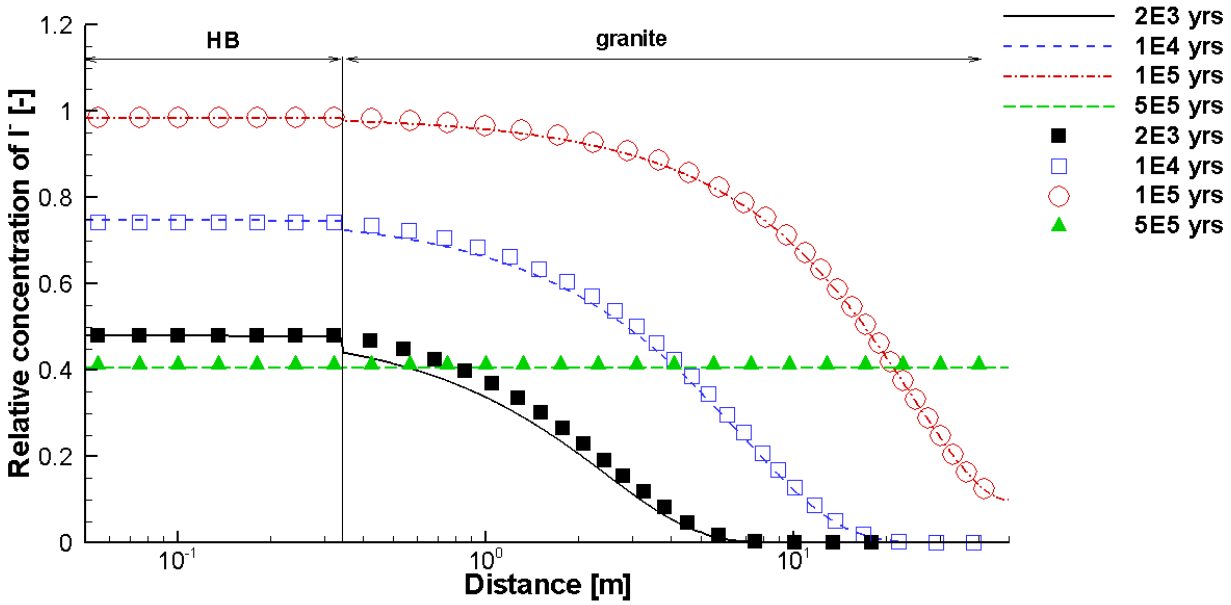

Figure 40: Comparison of Relative Concentration Profiles of I^- at Selected Times for a Small Defect Occurring at 1,000 Years for Case 2rCP (Symbols) and Case 2rUP (Lines)

As shown in Appendix A.4.1, for all other canister failure scenarios the breakthrough curves of I^- at selected observation points show very small differences between Case 2rCP and Case 2rUP.

5.2.4 Case 2 (HB/Granite) with Considerations of EDZs

The initial conditions for the simulations considering EDZs are the same as the aforementioned cases in Section 5.2.3, with the additional consideration of the increased porosity and diffusion coefficients in the EDZs. The simulated results for mass transport and chemical reactions for the cases including EDZs are very similar to those for the cases without EDZs, and in the following subsections only the most significant differences will be discussed. Additional EDZ simulation results are provided in Appendix A.4.2.

5.2.4.1 Impact of EDZs on Reactive Transport

Figure 41 and Figure 43 present the profiles of component concentrations, pH, porosity and sorbed species concentrations for both Case 2UP (symbols) and Case 2EDZUP (lines) at 1,000 and 100,000 years, respectively. The initial porosity in the inner EDZ is 0.6% for Case 2EDZUP, and 0.3% for Case 2UP. After 1,000 years, the concentration profiles of most components exhibit differences between the two cases in the granite, but little or no difference in the HB (Figure 41). Pore water – mineral interactions are also relatively weak (Figure 42). After 100,000 years, the differences in all parameters between Case 2UP and Case 2EDZUP are again very small. Figure 45 demonstrates that a small decrease of porosity is simulated at observation point V11 (located in granite adjacent to the HB/granite interface) and V5 for Case 2UP and 2EDZUP.

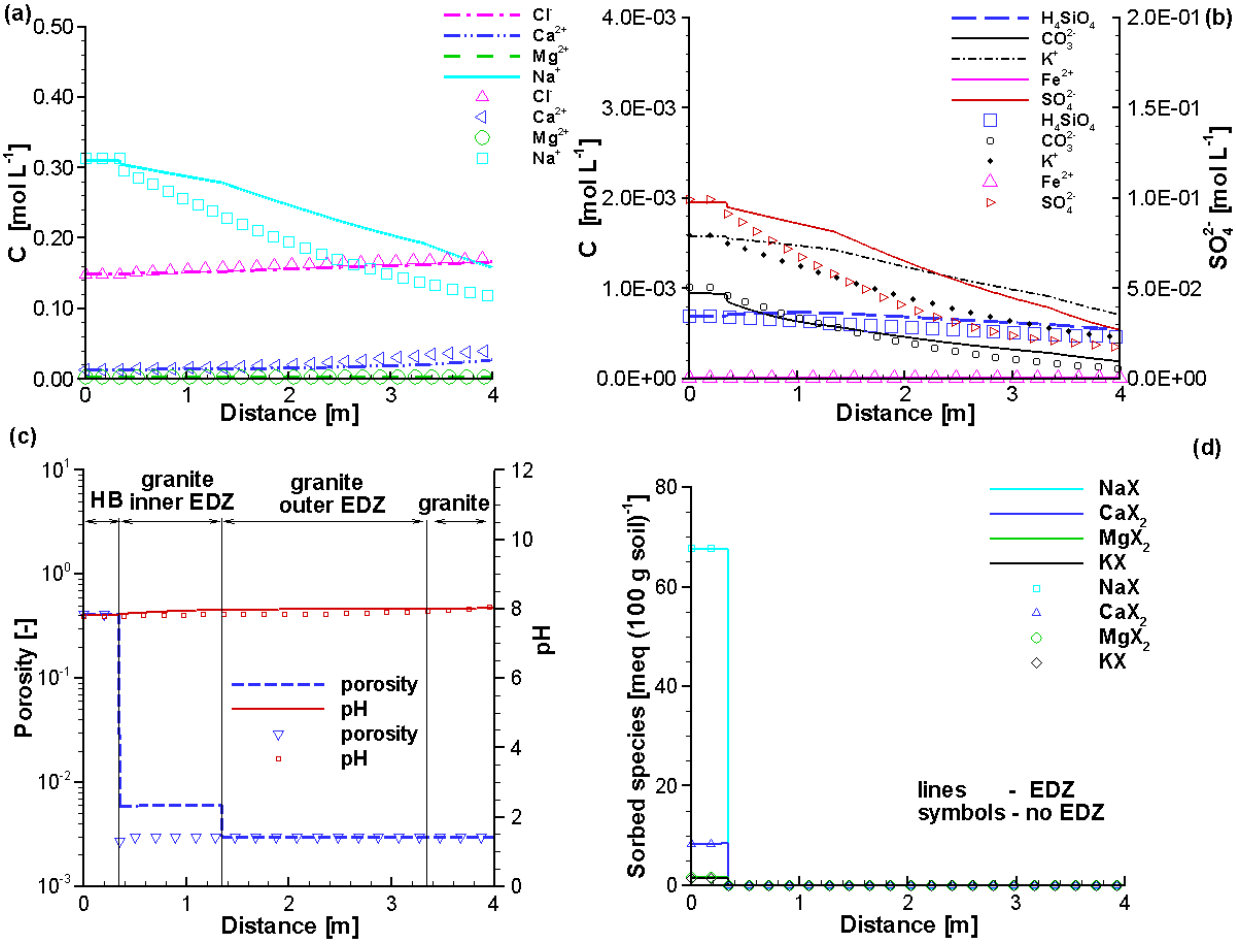

Figure 41: Profiles of Component Concentrations (a and b), Porosity and pH (c) and Sorbed Species (d) at 1,000 Years for Case 2UP (Symbols) and Case 2EDZUP (Lines)

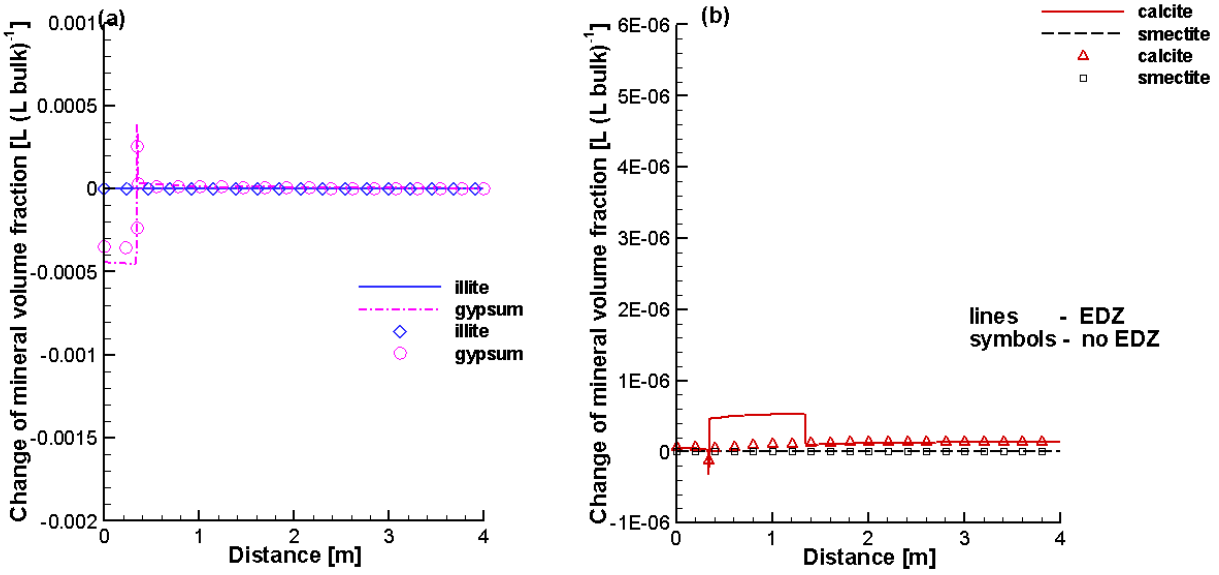

Figure 42: Comparison of Profiles of Mineral Volume Fraction Changes at 1,000 Years for Case 2UP (Symbols) and Case 2EDZUP (Lines)

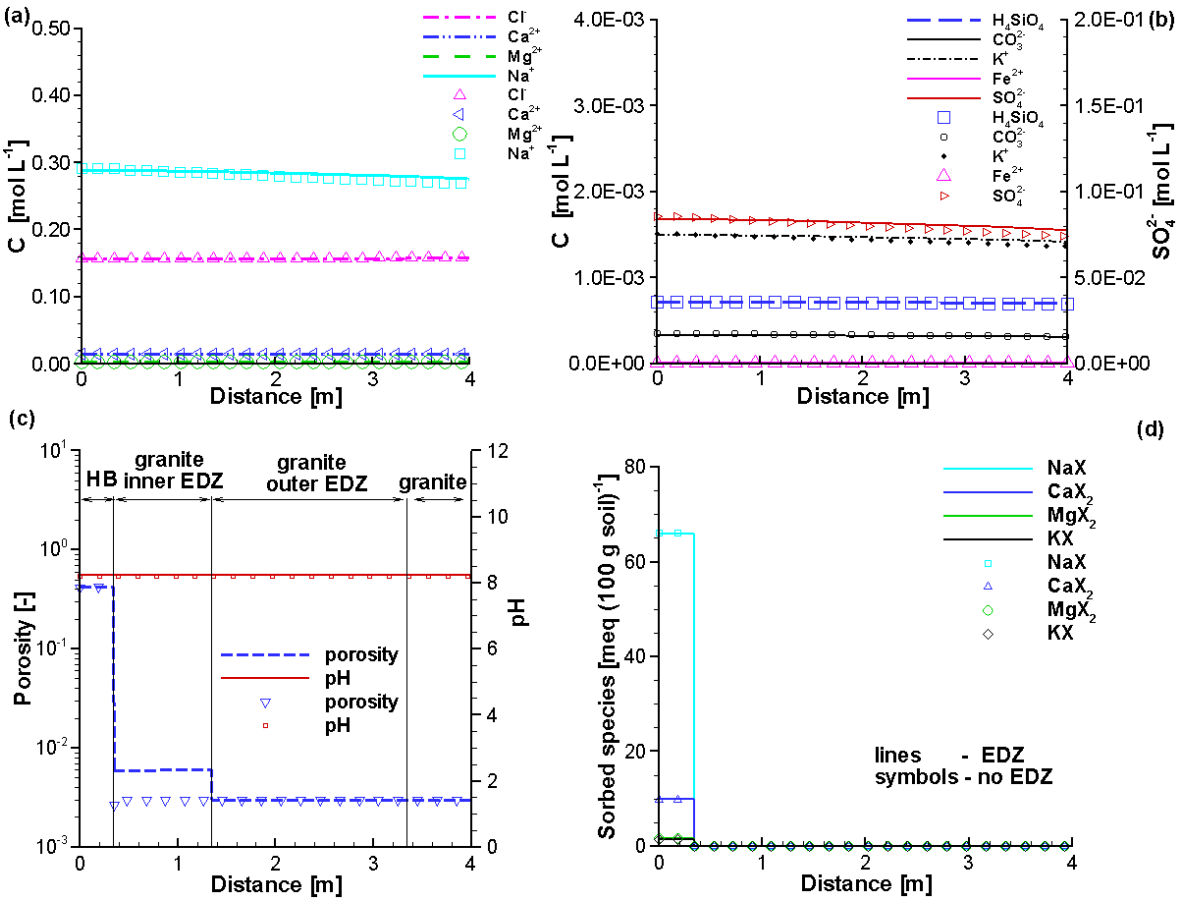

Figure 43: Profiles of Component Concentrations (a and b), Porosity and pH (c) and Sorbed Species (d) at 100,000 Years for Case 2UP (Symbols) and Case 2EDZUP (Lines)

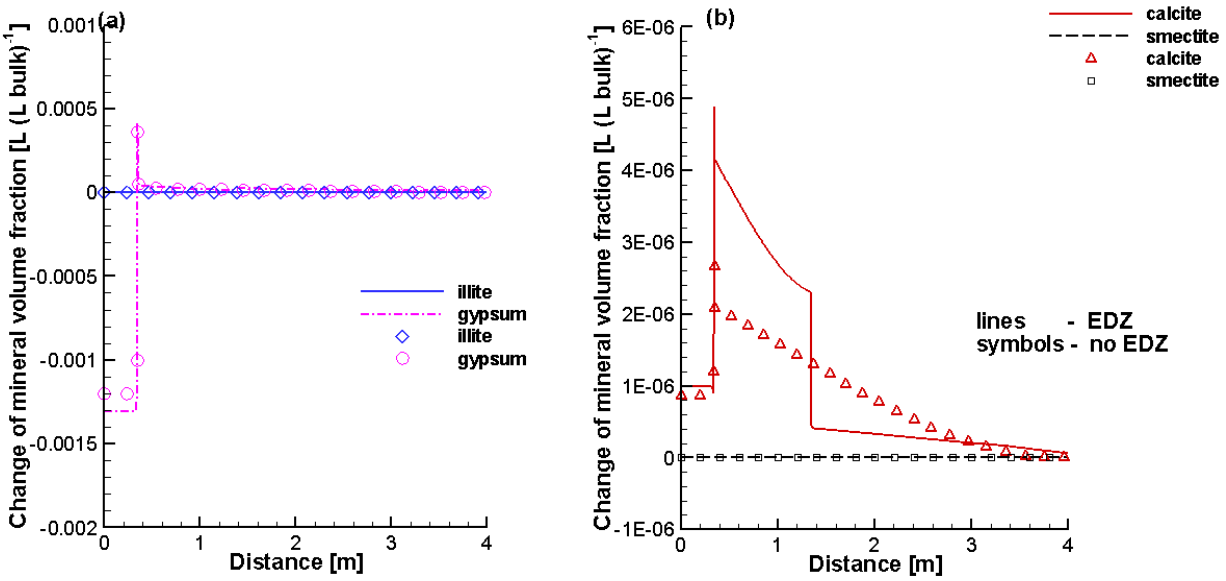

Figure 44: Comparison of Profiles of Mineral Volume Fraction Changes at 100,000 Years for Case 2UP (Symbols) and Case 2EDZUP (Lines)

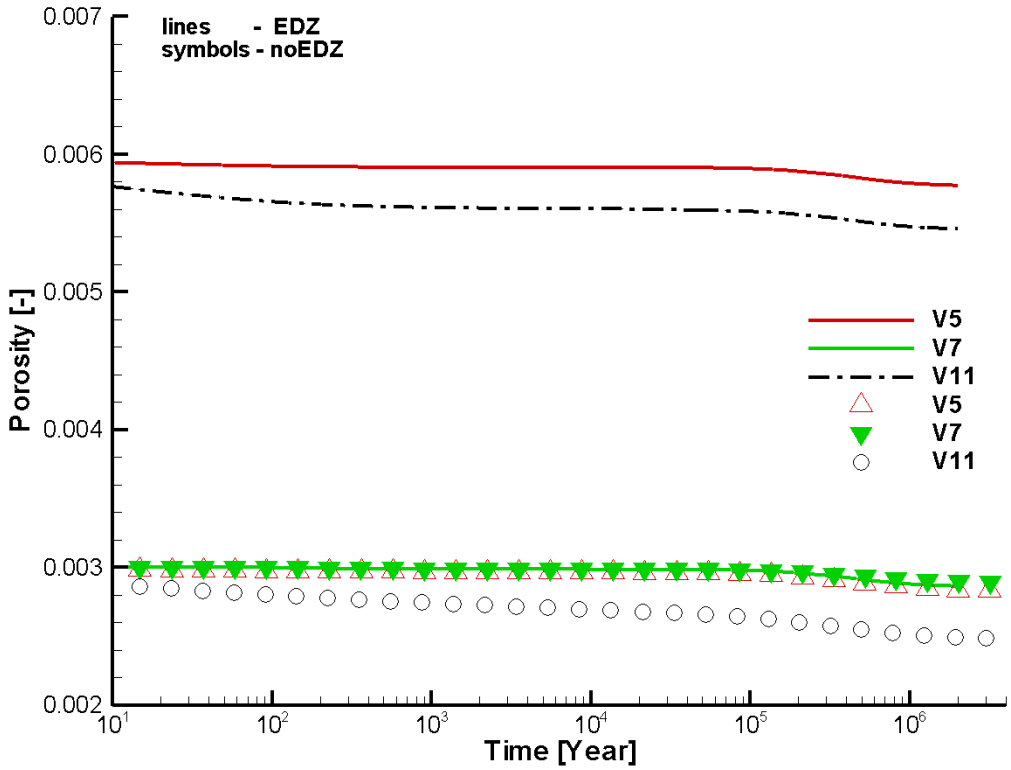

Figure 45: Evolution of Porosity at Selected Observation Points for Case 2UP (Symbols) and Case 2EDZUP (Lines). V5 and V11 (Inner EDZ), V7 (Outer EDZ)

5.2.4.2 Impact of EDZs on Radionuclide Diffusion – Case 2rEDZCP and 2rEDZUP

The impact of EDZs on radionuclide migration is illustrated by comparing results for cases with and without EDZs. For conciseness, only the results for the cases associated with the small defect scenario occurring at 1,000 years are described in detail here. Simulated results for all other canister defect scenarios are presented in Appendix A.4.2.

Figure 39 in section 5.2.3.2 presents the simulated breakthrough curves of I^- at selected observation points for Cases 2rCP, 2rUP, 2rEDZCP and 2rEDZUP. The results show very small differences in the relative concentrations between Case 2rCP and 2rUP, and Case 2rEDZCP and 2rEDZUP. Figure 46 shows the concentration profiles of I^- at selected times for Case 2rEDZCP (lines) and Case 2rCP (symbols). Simulated concentrations for Case 2rEDZCP are higher in the granite, especially in EDZs and the intact granite close to the outer EDZ at 2,000, 10,000 and 100,000 years in comparison to those for Case 2rCP. The differences between the two cases diminish over time and are negligible at 1,000,000 years.

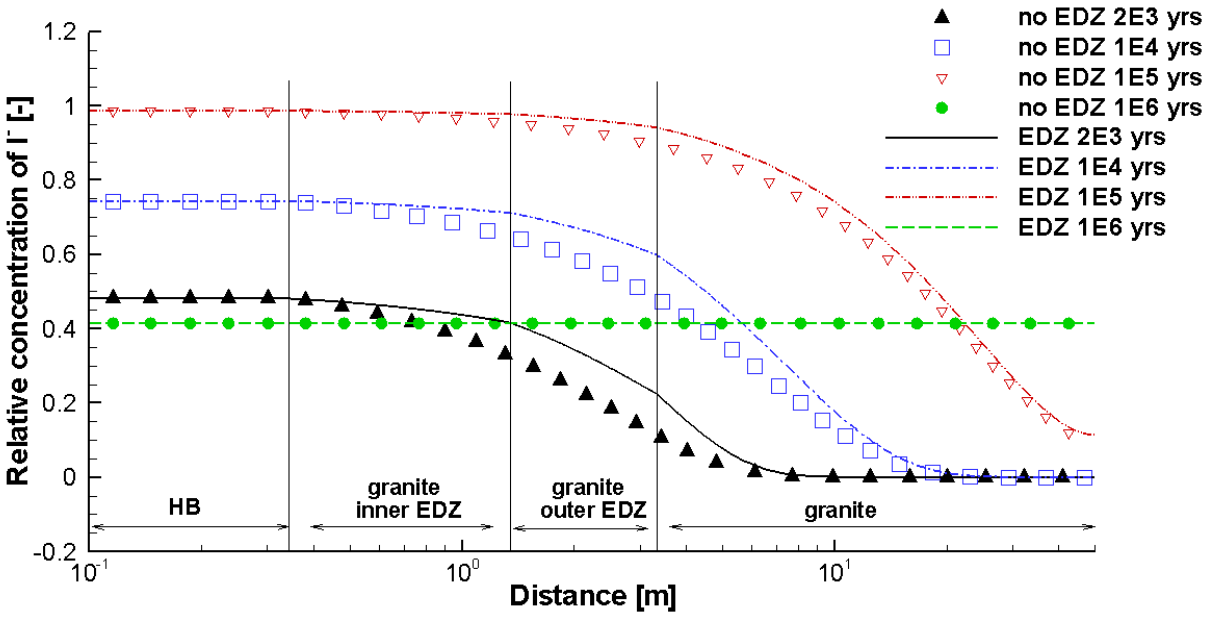

Figure 46: Comparison of Relative Concentration Profiles of I^- at Selected Times for a Small Defect Occurring at 1,000 Years for Case 2rCP (Symbols) and Case 2rEDZCP (Lines)

The simulated concentration profiles of I^- for Case 2rEDZUP (lines) and Case 2rUP (symbols) are depicted in Figure 47. At 2,000 years there is a small change in the I^- concentration at the HB/granite interface for both cases, with the relative concentrations of I^- in granite for Case 2rEDZUP being higher than those for Case 2rUP. The differences in the I^- concentration profiles decrease over time.

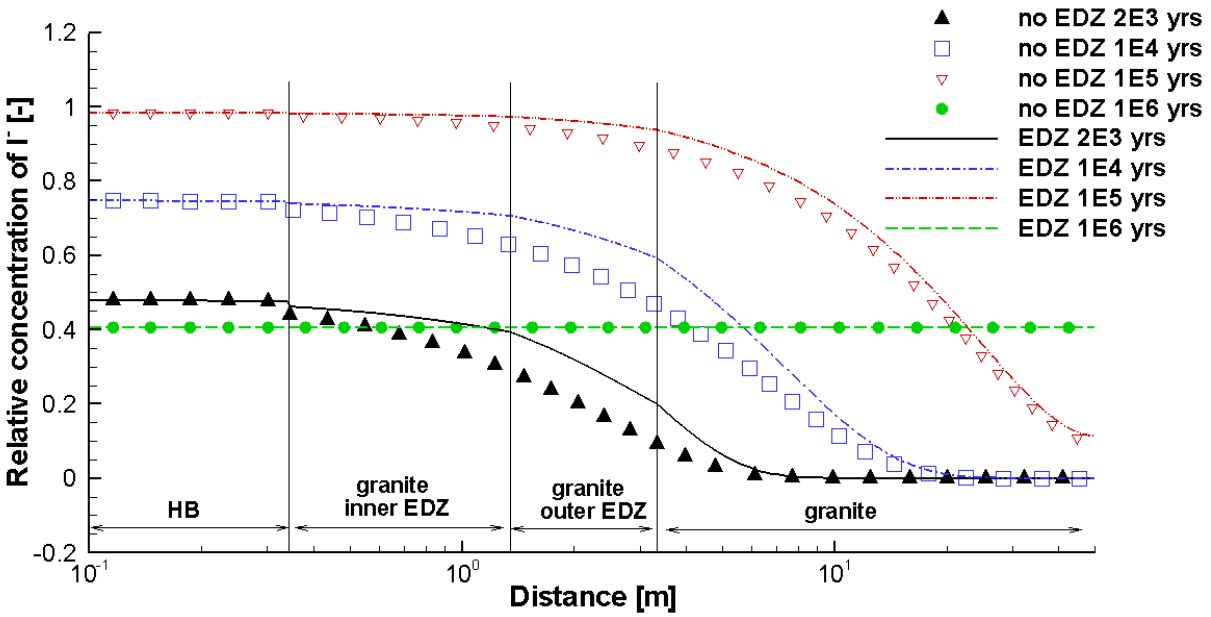

Figure 47: Comparison of Relative Concentration Profiles of I^- at Selected Times for a Small Defect Occurring at 1,000 Years for Case 2rUP (Symbols) and Case 2rEDZUP (Lines)

5.3 LIMESTONE HOST ROCK CASES

The simulation results for cases associated with the interfaces between bentonite/LHHPC/limestone (i.e., Case 3 discussed in Section 5.3.1) and bentonite/limestone (i.e., Case 4 in Section 5.3.2) are described in the following subsections (see Table 14 in Section 4.2 for the related simulation cases).

5.3.1 Case 3 (HB/LHHPC/Limestone) Without Consideration of EDZs

5.3.1.1 Reactive Transport – Case 3CP and 3UP

The initial component concentrations (Figure 48) and mineral compositions (Figure 49) are the same for both Case 3CP (constant porosity) and Case 3UP (updated porosity and effective diffusion coefficient). In general, the concentrations of all the main components, except SO_4^{2-}, in the limestone are initially higher than those in the HB and LHHPC, which leads to the diffusion of all components except SO_4^{2-} towards the HB. The higher concentration of SO_4^{2-} is due to the existence of gypsum in HB (Table 11) and LHHPC (Table A- 5), but not in the limestone. The pH of the pore water in the LHHPC is the highest in the domain (Figure 48).

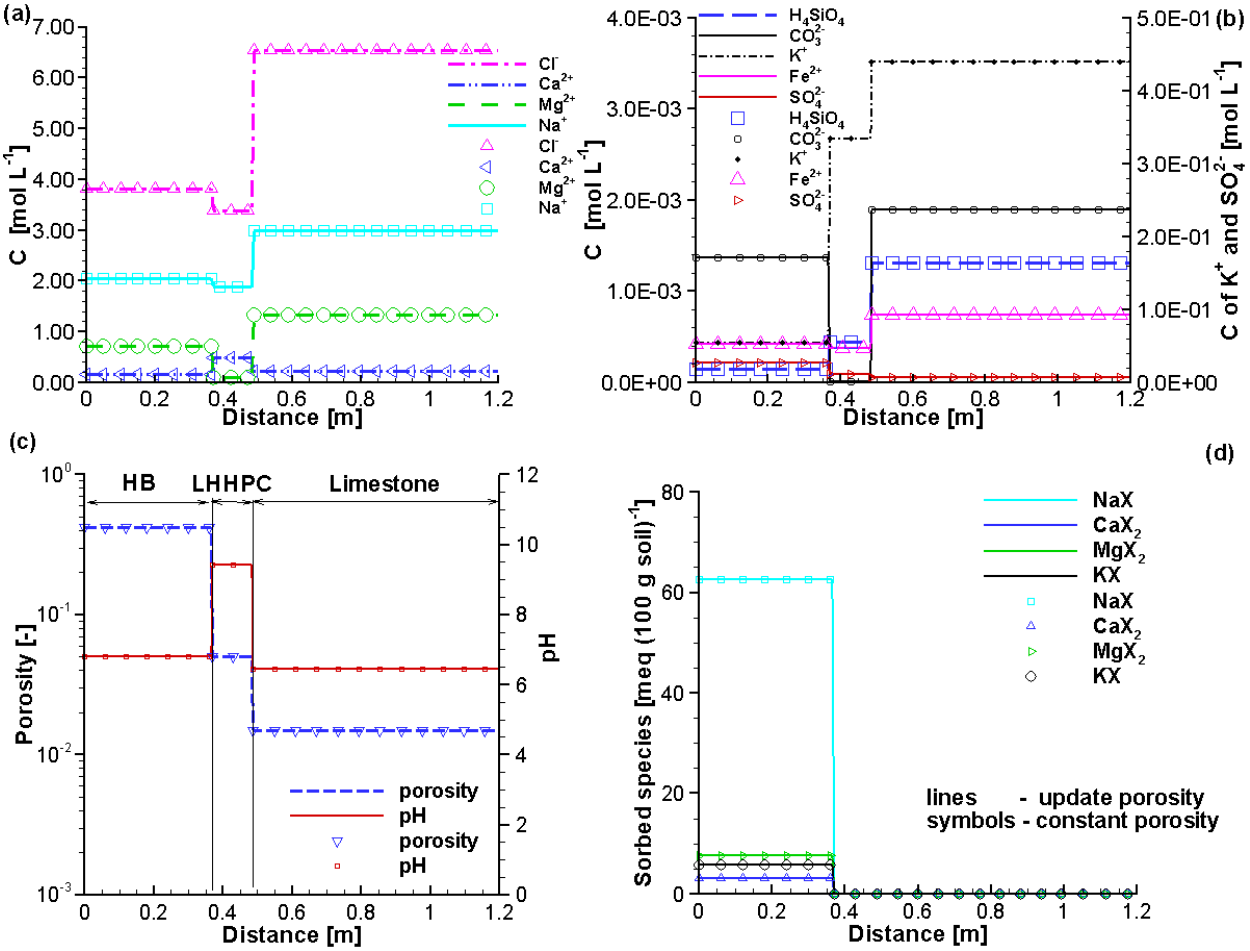

Figure 48: Profiles of Initial Component Concentrations (a and b), pH and Porosity (c) and Sorbed Species (d) for Case 3CP (Symbols) and Case 3UP (Lines)

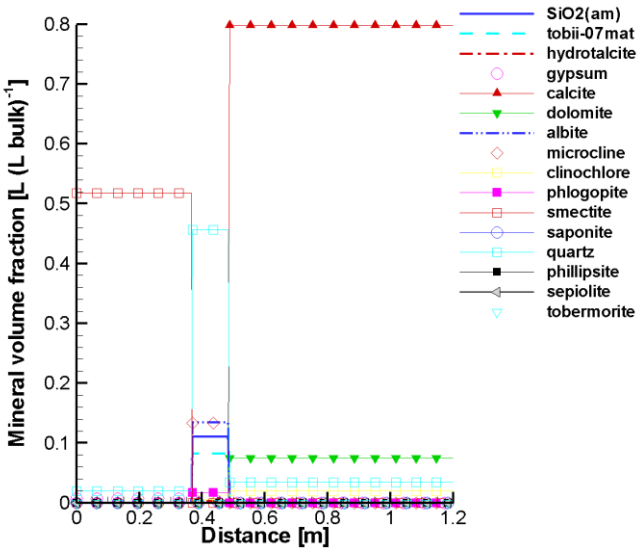

Figure 49: Profiles of Initial Mineral Volume Fractions for Case 3CP (Symbols) and Case 3UP (Lines)

Figure 50 depicts the evolution of porosity at selected observation points for Case 3UP. At observation points V3 and V4 (both located in LHHPC), porosities begin to increase after about 100 years due to the dissolution of the cementitious substances (i.e. TobII-07mat, hydrotalcite and SiO_2(am), Figure 9 right). At observation point V12, the porosity begins to decrease significantly after 1,000 years, leading to pore clogging at about 3,800 years. Significant porosity changes only occur close to the interfaces, for example less than 10 cm from the interface between LHHPC/limestone at 100,000 years as shown in Figure A- 41. The porosity decrease at V12 is mainly due to the precipitation of calcite, phillipsite, sepiolite and saponite (Figure 51 and Figure 52). Small amounts of smectite dissolve and phillipsite precipitate in HB after 100,000 years (Figure 52). For most reactive minerals, the changes of mineral volume fractions for Case 3CP are higher than those for Case 3UP (Figure 51 and Figure 52).

The interactions between minerals and solutes, together with diffusive transport and cation exchange, result in the profiles of component concentrations, pH, sorbed species concentrations and porosity depicted in Figure 53 (at 1,000 years) and Figure 54 (at 100,000 years). At 100,000 years for Case 3UP, the abrupt concentration changes of components (e.g. Cl^-, Ca^{2+} etc.) at the interface between LHHPC/limestone (Figure 54) is due to the pore clogging at V12. Due to ion exchange reactions in HB, sodium smectite is converted to calcium bentonite (compare Figure 48d to Figure 53d and Figure 54d).

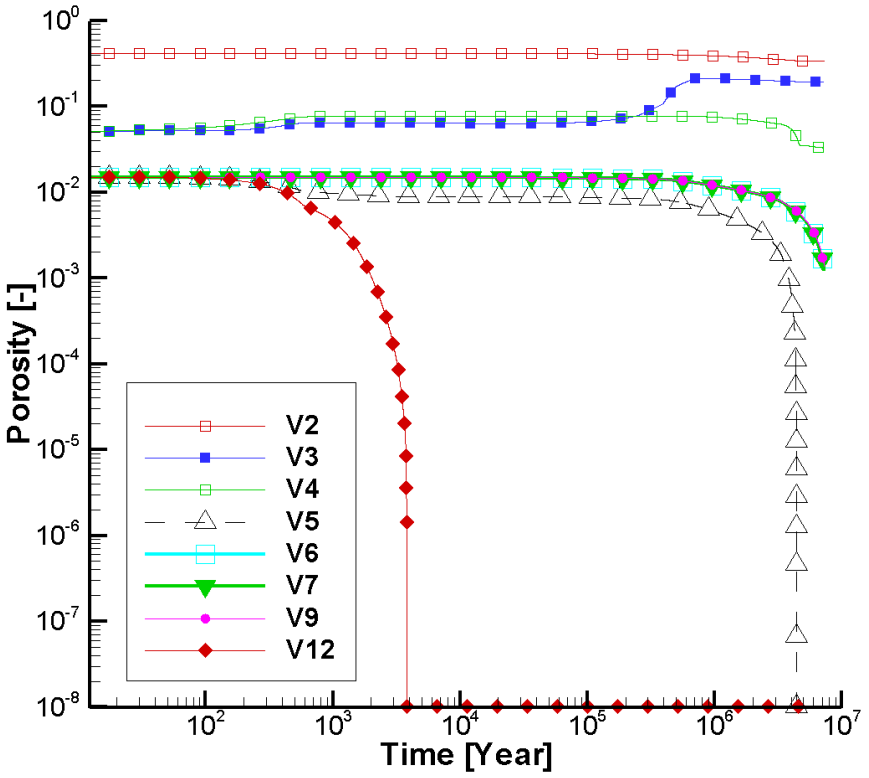

Figure 50: Evolution of Porosity at Selected Observation Points for Case 3UP. V2 (HB), V3 and V4 (LHHPC), V5 to V12 (Limestone)

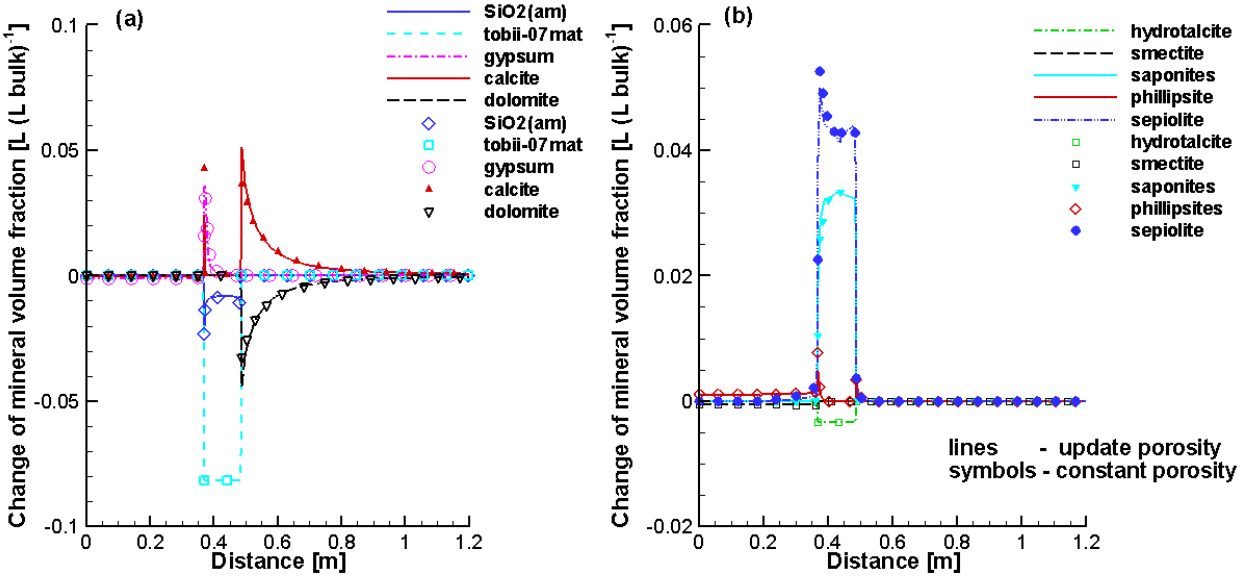

Figure 51: Comparison of Profiles of Mineral Volume Fraction Changes at 1,000 Years for Case 3CP (Symbols) and Case 3UP (Lines)

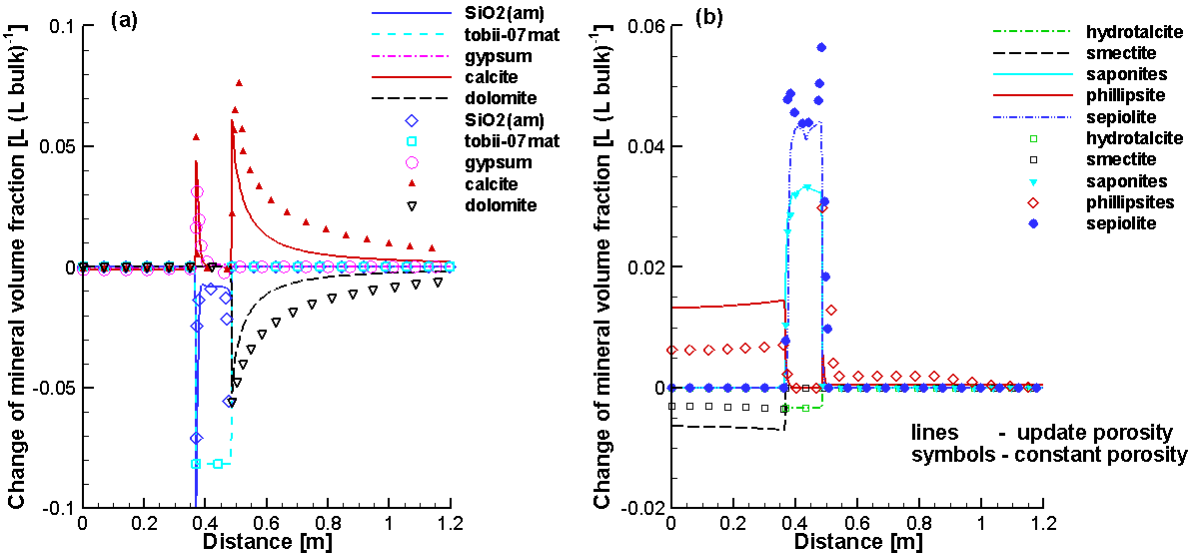

Figure 52: Comparison of Profiles of Mineral Volume Fraction Changes at 100,000 Years for Case 3CP (Symbols) and Case 3UP (Lines)

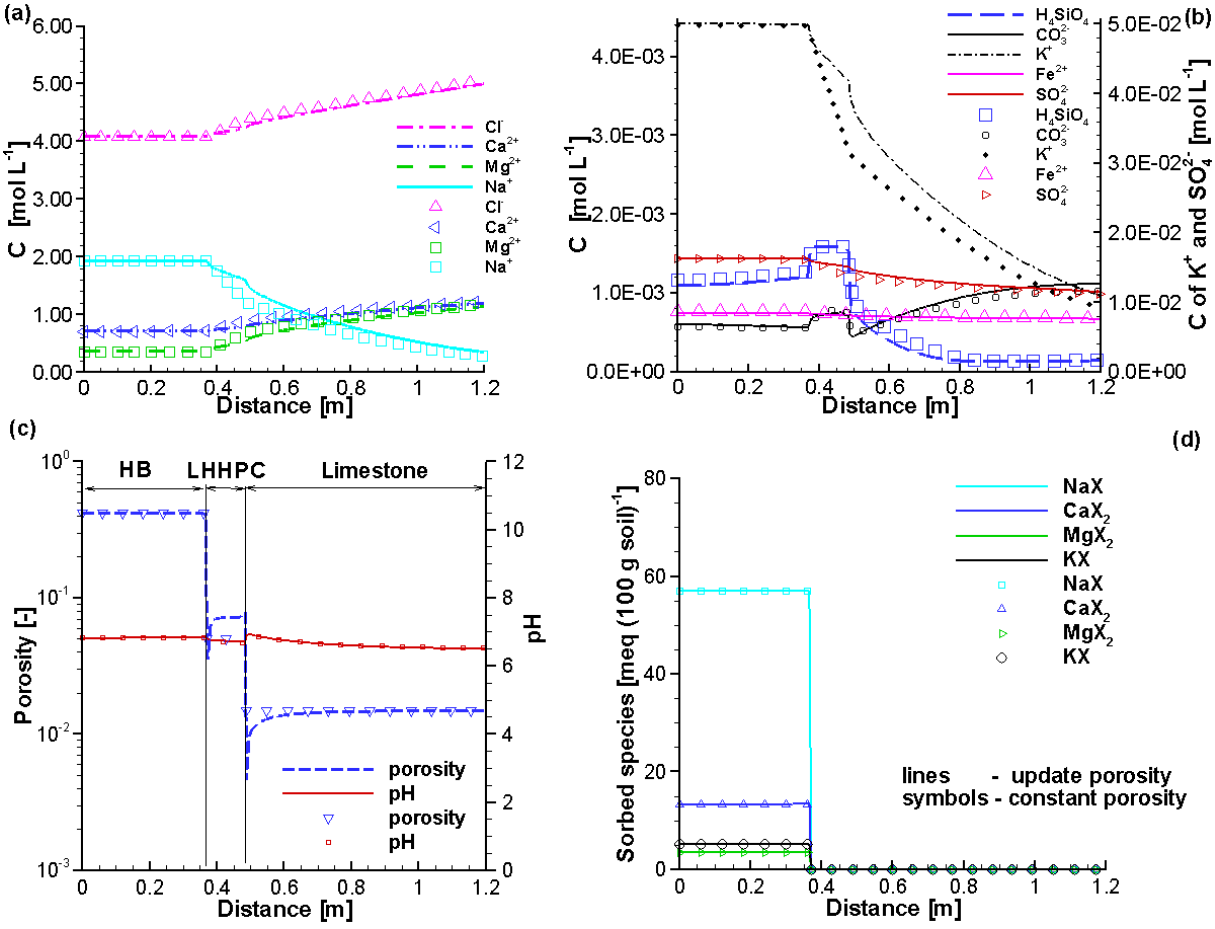

Figure 53: Profiles of Component Concentrations (a and b), Porosity and pH (c), and Sorbed Species (d) at 1,000 Years for Case 3CP (Symbols) and Case 3UP (Lines)

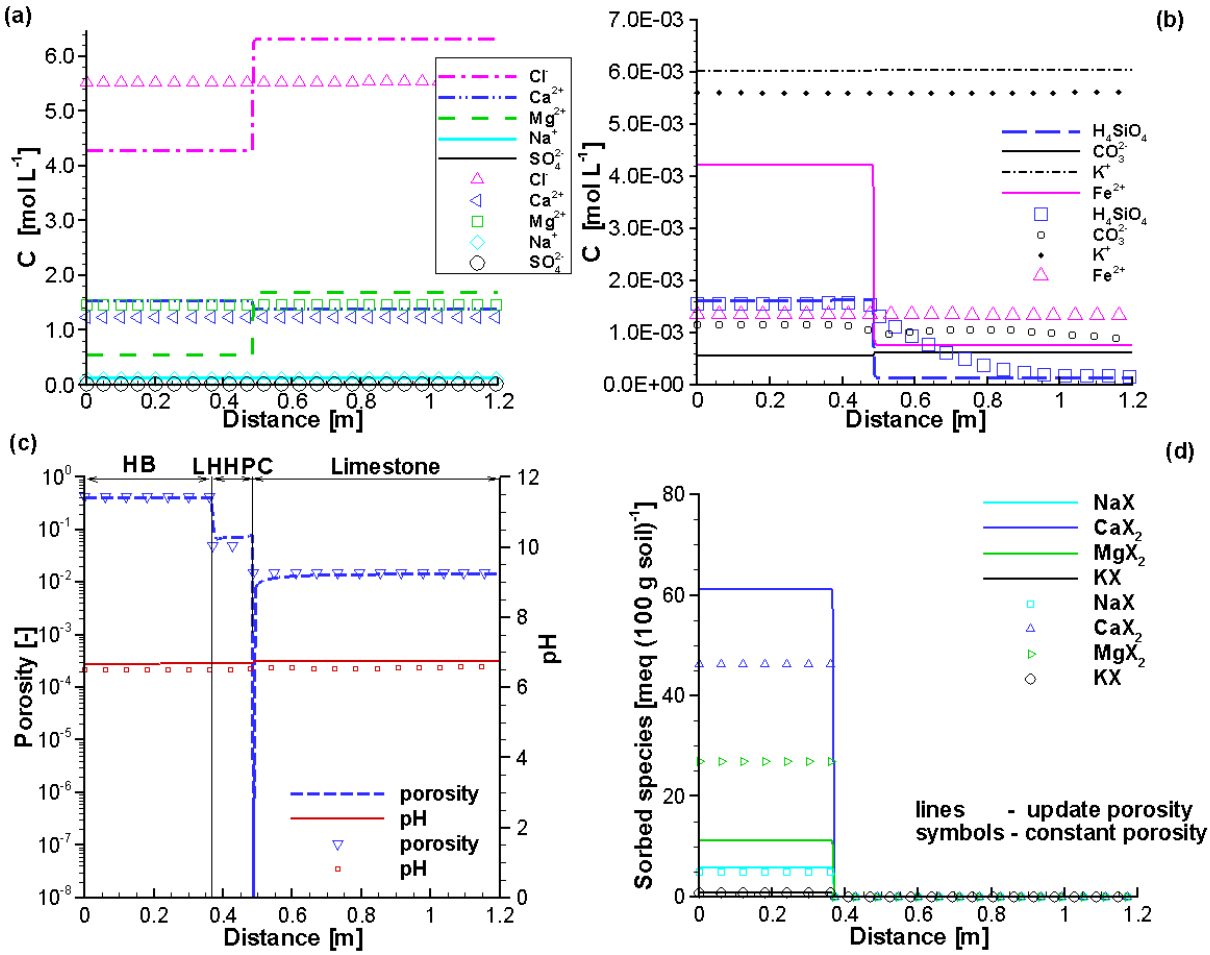

Figure 54: Comparison of Component Concentration Profiles (a and b), Porosity and pH (c), and Sorbed Species (d) at 100,000 Years for Case 3CP (Symbols) and Case 3UP (Lines)

5.3.1.2 Impact of Reactive Transport on Radionuclide Diffusion – Case 3rCP and 3rUP

The simulated concentration profiles of I^- for a small defect occurring at 1,000 years are depicted in Figure 55 for both Case 3rCP (symbols) and Case 3rUP (lines). For the case assuming constant porosity (Case 3rCP), the simulated concentration profiles for I^- are typical of conservative solute diffusion. For the simulation with porosity updating (Case 3rUP), the concentration profiles for I^- at 10,000 years and later show abrupt changes at the interface between LHHPC and limestone due to the porosity reduction at V12 (Figure 50). The maximum difference in I^- concentration between Case 3rCP and 3rUP at 100,000 years is up to 94% in the limestone close to the LHHPC/HB interface.

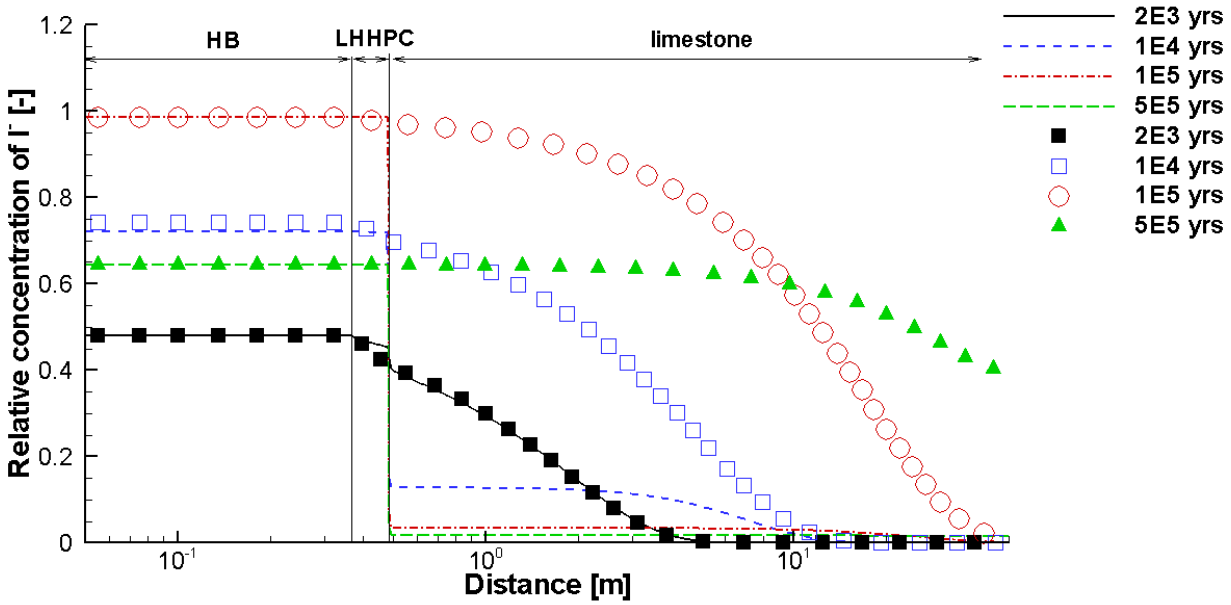

Figure 55: Comparison of Relative Concentration Profiles of I^- at Selected Times for a Small Defect Occurring at 1,000 Years for Case 3rCP (Symbols) and Case 3rUP (Lines)

Similar results were simulated for a small defect occurring at 10,000 years (Figure 56). The maximum difference in I^- concentrations for both cases at 100,000 years is up to 97%. The effect of pore clogging on radionuclide diffusion for all other canister failure scenarios is also significant (see Appendix A.5.1).

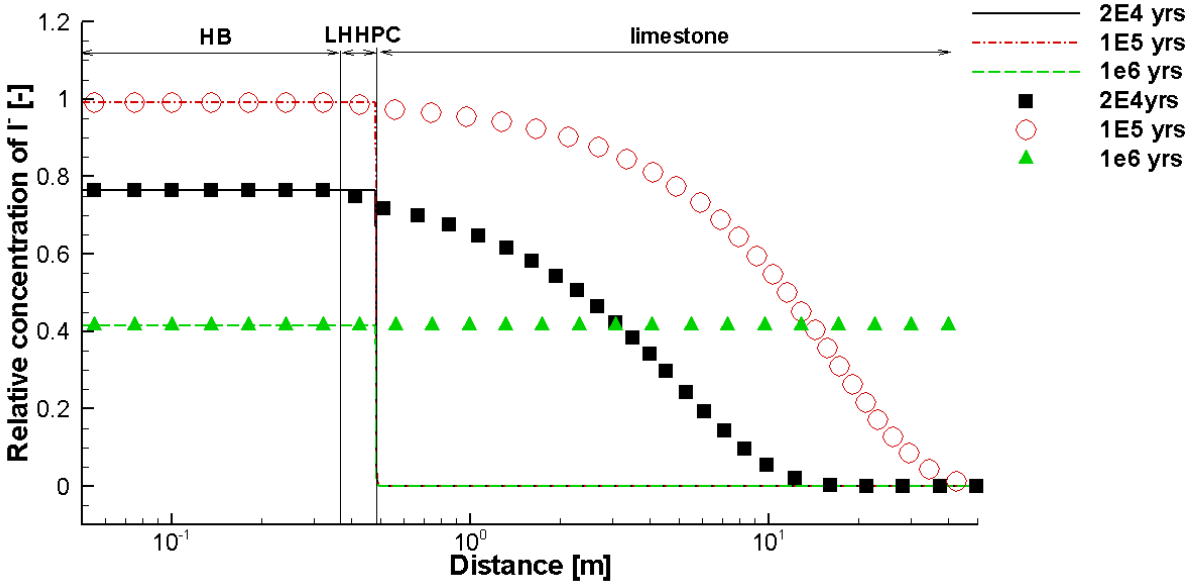

Figure 56: Comparison of Relative Concentration Profiles of I^- at Selected Times for a Small Defect Occurring at 10,000 Years for Case 3rCP (Symbols) and Case 3rUP (Lines)

5.3.2 Case 3 (HB/LHHPC/Limestone) With Consideration of EDZs

The simulated results for Case 3 with EDZs are similar in many ways to the results obtained for Case 3 without EDZs. For conciseness, the following subsections focus only on Case 3EDZUP and the comparison of the results to Case 3UP. More results for Case 3EDZCP can be found in Appendix A.5.2.

5.3.2.1 Impact of EDZs on Reactive Transport – Case 3UP and 3EDZUP

The most significant difference between Case 3UP and Case 3EDZUP is the time to reach pore clogging at observation point V12 (Figure 57). The time to reach pore clogging at V12 is 122,000 years for Case 3EDZUP (initial porosity of 0.030), which is much longer than the 3,800 years for Case 3UP (initial porosity of 0.015). Figure 58 and Figure 59 depict the profiles of the volume fraction changes of the most reactive minerals for both cases at 1,000 and 100,000 years, respectively. The results show that the patterns of mineral dissolution/precipitation are the same for both cases, but the intensities differ especially near the interface between LHHPC and limestone. The amount of SiO_2(am) dissolution in LHHPC close to LHHPC/limestone interface is more for Case 3EDZUP than for Case 3UP (Figure 59 c). Within the EDZs, larger amounts of calcite precipitation and dolomite dissolution are simulated for Case 3EDZUP than for Case 3UP. As the initial porosity in the outer EDZ is higher for Case 3EDZUP than for Case 3UP, more precipitation is required, and thus a longer time is needed, for clogging to occur for Case 3EDZUP.

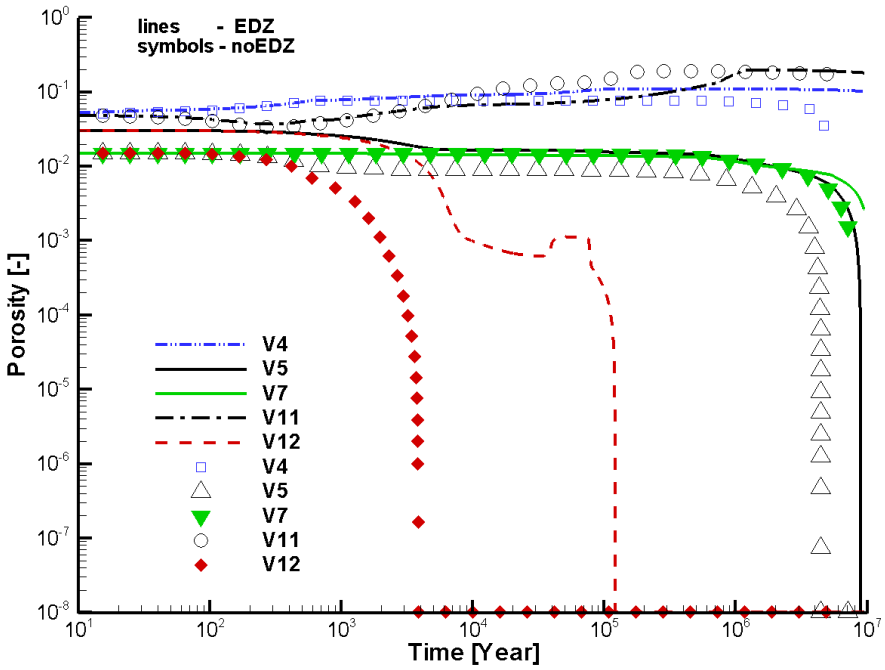

Figure 57: Comparison of Porosity Evolution at Selected Observation Points (Lines – Case 3EDZUP, Symbols – Case 3UP) . V4 and V11 (LHHPC), V5 and V12 (Inner EDZ) and V7 (Outer EDZ in Limestone)

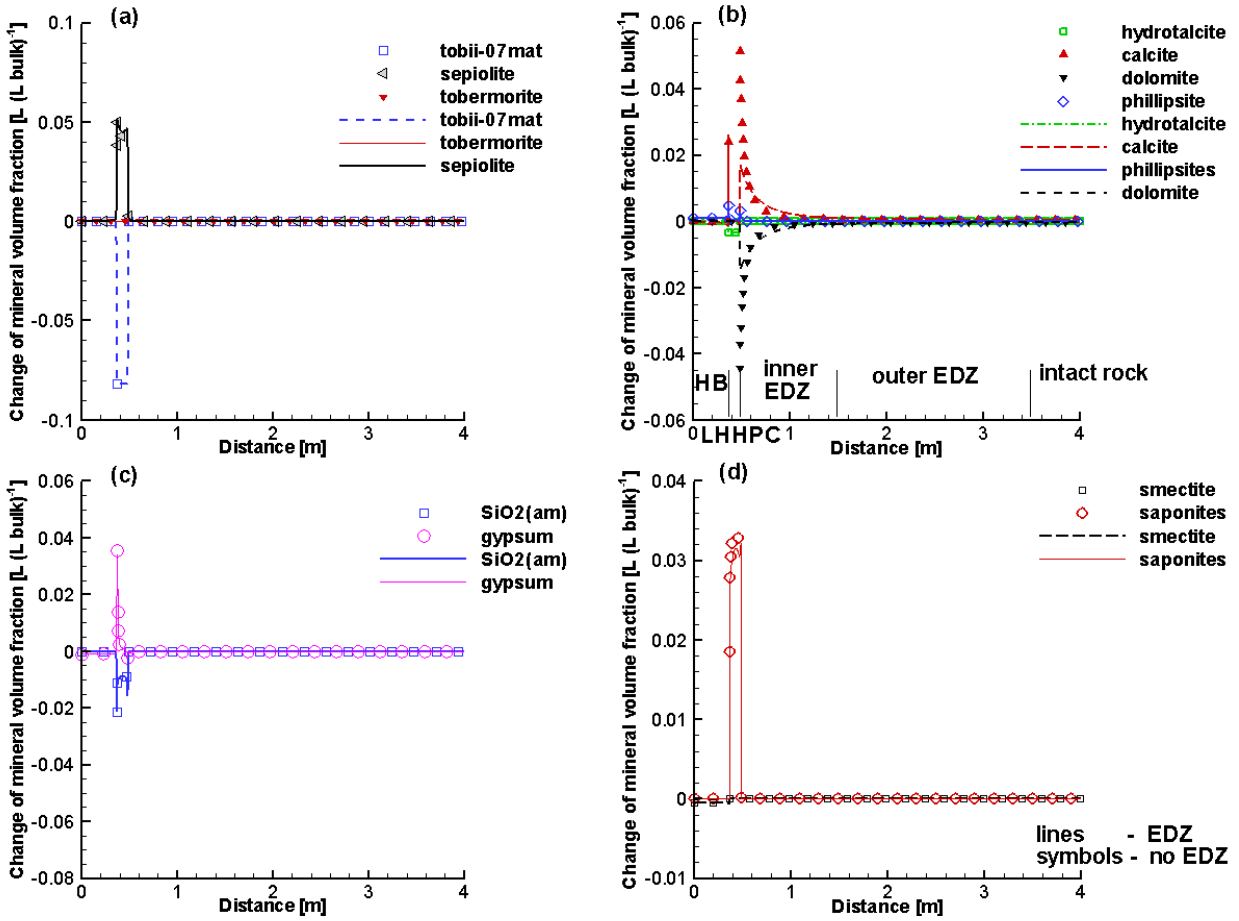

Figure 58: Comparison of Profiles of Mineral Volume Fraction Changes at 1,000 Years for Case 3UP (Symbols) and Case 3EDZUP (Lines)

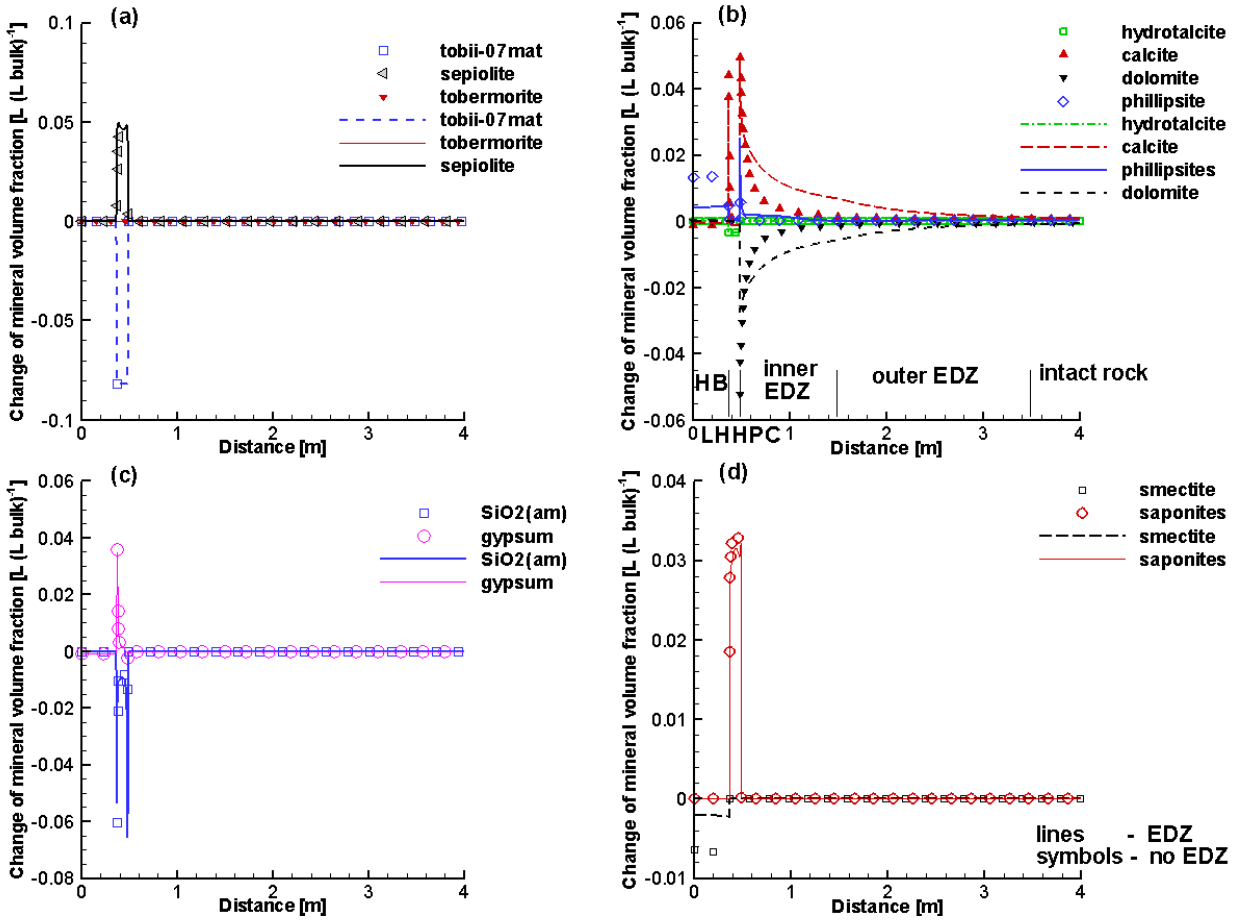

Figure 59: Comparison of Profiles of Mineral Volume Fraction Changes at 100,000 Years for Case 3UP (Symbols) and Case 3EDZUP (Lines)

5.3.2.2 Impact of EDZs on Radionuclide Diffusion – Case 3rUP and 3rEDZUP

The simulation results for a small canister defect occurring at 1,000 years are shown in Figure 60 to Figure 62. Figure 60 shows that when the porosity and effective diffusion coefficients are held constant, the I^- profiles are very similar for simulations that ignore (Case 3rCP) or include (Case 3rEDZCP) EDZs. The maximum difference in I^- concentrations is only about 15% at 10,000 years for locations close to the interface between the outer EDZ and intact limestone.

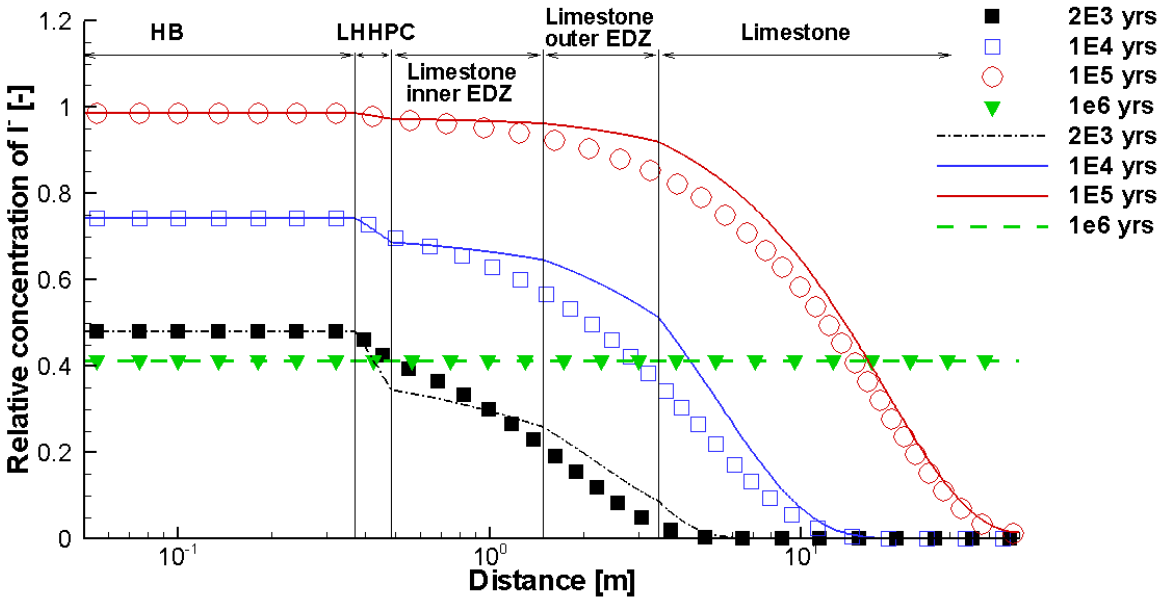

Figure 60: Comparison of Relative Concentration Profiles of I^- at Selected Times for a Small Defect Occurring at 1,000 Years for Case 3rCP (Symbols) and Case 3rEDZCP (Lines)

The concentration profiles of I^- for cases in which reaction-induced porosity change and its feedback are included are presented in Figure 61. The relative concentrations at the LHHPC/limestone interface show abrupt changes for Case 3rUP (Figure 61 symbols) due to the aforementioned significant porosity reduction near observation point V12 (i.e. clogging at about 3,800 years). The relative concentrations of I^- for Case 3rEDZUP and 3rUP at 1,000 years show almost no differences within the HB; however significant differences are simulated in the limestone, especially at 10,000 years and thereafter due to the clogging at V12.

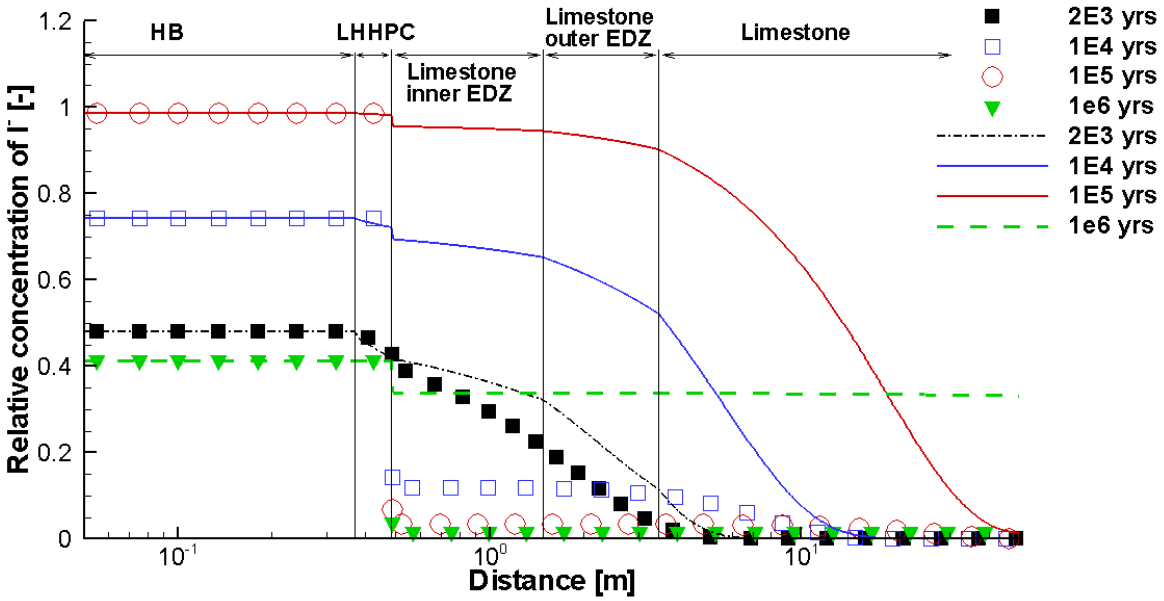

Figure 61: Comparison of Relative Concentration Profiles of I^- at Selected Times for a Small Defect Occurring at 1,000 Years for Case 3rUP (Symbols) and Case 3rEDZUP (Lines)

Breakthrough curves for I^- at selected observation points for the small defect occurring at 1,000 years for the cases assuming constant and updated porosity, and/or considering EDZs are depicted in Figure 62. By comparing these results, it is seen that:

a) The peak values of I^- for cases assuming constant porosity can be up to 96% higher than the cases in which the porosity and diffusion coefficients are updated (Figure 62). For the constant porosity cases (i.e. 3rCP and 3rEDZCP), the difference in the peak values of I^- is small and mainly within the EDZs and outwards. The peak values of I^- for Case 3rEDZUP at V5, V7 and V9 (locate in limestone to the right of V12) are much higher than those for Case 3rUP due to the difference in the timing of clogging (at 3,800 and 122,000 years for Case 3rUP and 3rEDZUP, respectively).
b) There is only one peak in each breakthrough curve for all cases except for Case 3rUP at V5. For that case and location, the first peak reflects the impact of porosity reduction at V12 (Figure 50), while the second peak corresponds to the pore clogging at V5 (Figure 50), which strongly limits diffusion of I^- further into the limestone (Figure 61).
c) Generally, the predicted I^- concentrations for the cases considering EDZs are higher than those without EDZs at all observation points except V3 and V5 before about 2,000 years. This is because of the location of V3 and V5 (Figure 3 and Figure 4), both of which are to the left of V12, where the porosity increases in LHHPC (V4 in Figure 50 and Figure A- 58 in the Appendix A.4.2).

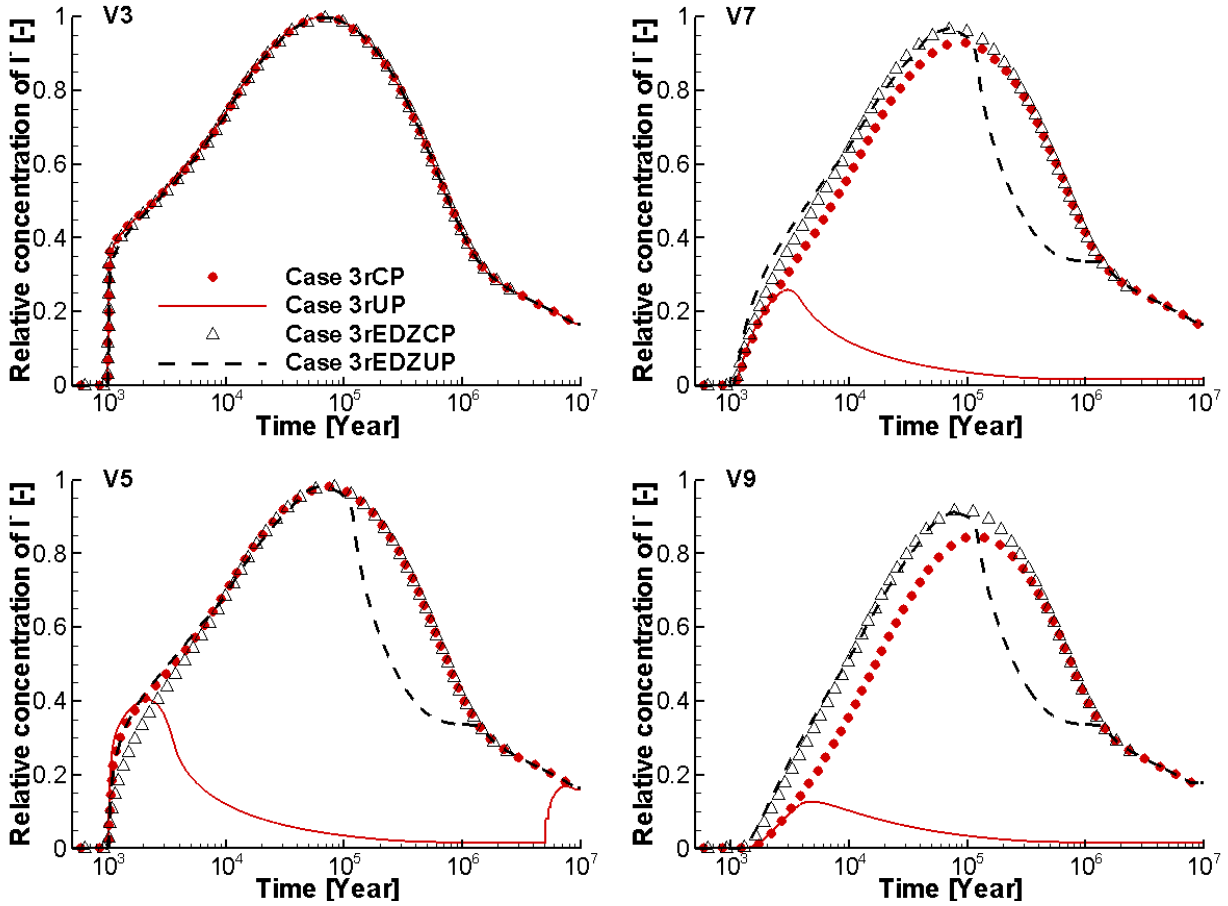

Figure 62: Breakthrough Curves at Selected Observation Points for a Small Defect Occurring at 10,000 Years for Cases 3rCP, 3rUP, 3rEDZCP and 3rEDZUP. The Observation Point Locations are shown in Figure 4. V3 (HB), V5 (Inner EDZ), V7 (Outer EDZ) and V9 (Intact Limestone)

For all other canister failure scenarios, the simulated results are presented in Appendix A.5.2.

5.3.3 Case 4 (HB/Limestone) Without Consideration of EDZs

5.3.3.1 Reactive Transport – Case 4CP and 4UP

The initial conditions for Case 4CP and Case 4UP are depicted in Figure 63 and Figure 64, and these are the same as those for Cases 3CP and 3UP. As the two materials (HB and limestone) are natural substances with close to neutral pH values, similar to Case 2, mineral alterations due to fluid-rock interactions are limited and only small changes in porosity occur near the interface (Figure 65). At the interface between HB/limestone (V11), the porosity decreases from 0.015 (initial) to approximately 0.013 by 1,000 years, but then increases up to 0.023 at 100,000 years (Figure 65). After 300,000 years, the porosity at V11, V5, V7 and V9 decreases due to the

precipitation of calcite (Figure 68). At 1,000 years, gypsum has accumulated in the limestone close to the HB/limestone interface (Figure 66), but thereafter is dissolved as shown in Figure 67. Simulated component concentration profiles for Case 4CP and Case 4UP (results not shown) show little difference.

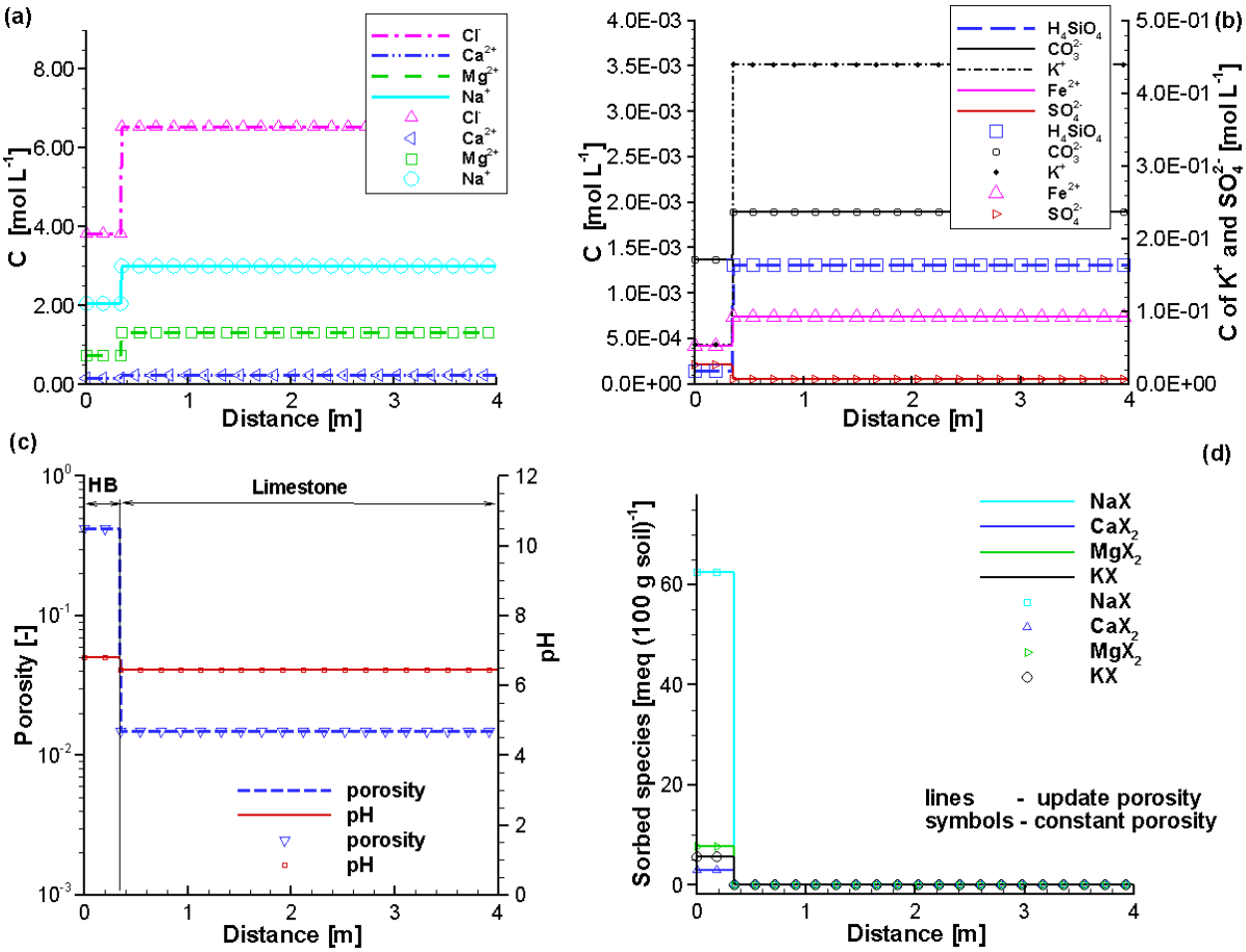

Figure 63: Profiles of Initial Component Concentrations (a and b), pH and Porosity (c) and Sorbed Species (d) for Case 4CP (Symbols) and Case 4UP (Lines)

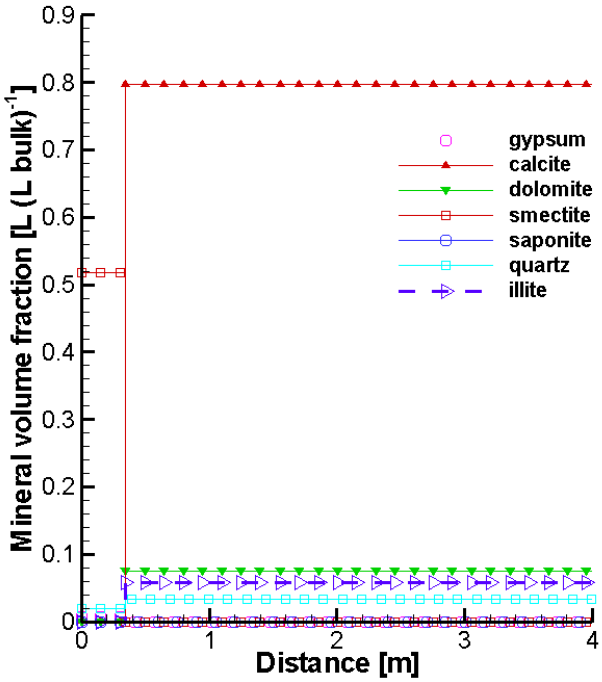

Figure 64: Profiles of Initial Mineral Volume Fractions for Case 4CP (Symbols) and Case 4UP (Lines)

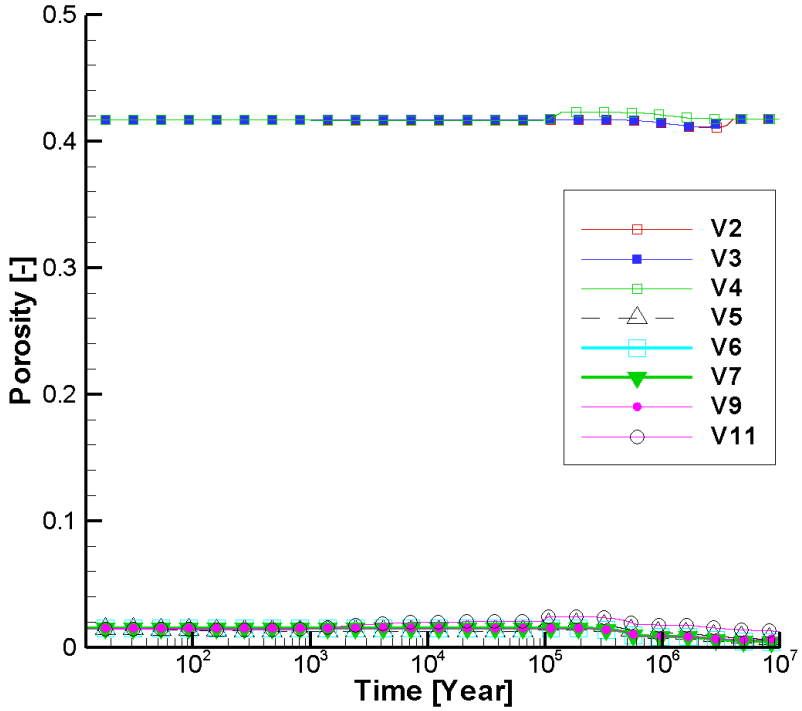

Figure 65: Porosity Evolution at Selected Observation Points for Case 4UP. V2 and V3 (HB), V5 to V11 (Limestone)

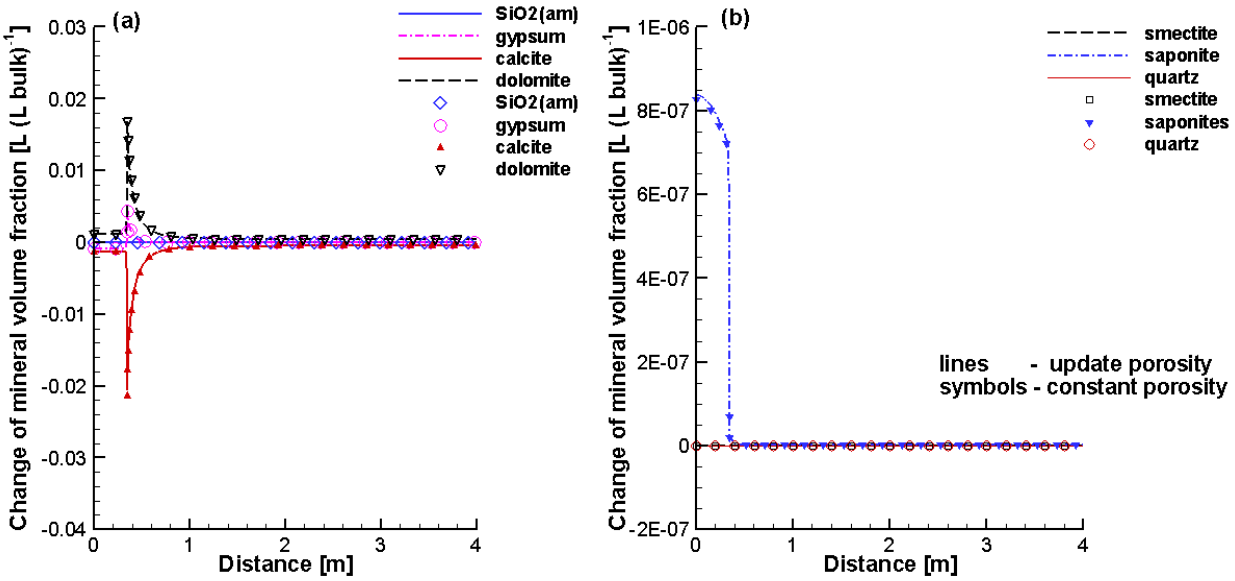

Figure 66: Comparison of Profiles of Mineral Volume Fraction Changes at 1,000 Years for Case 4CP (Symbols) and Case 4UP (Lines)

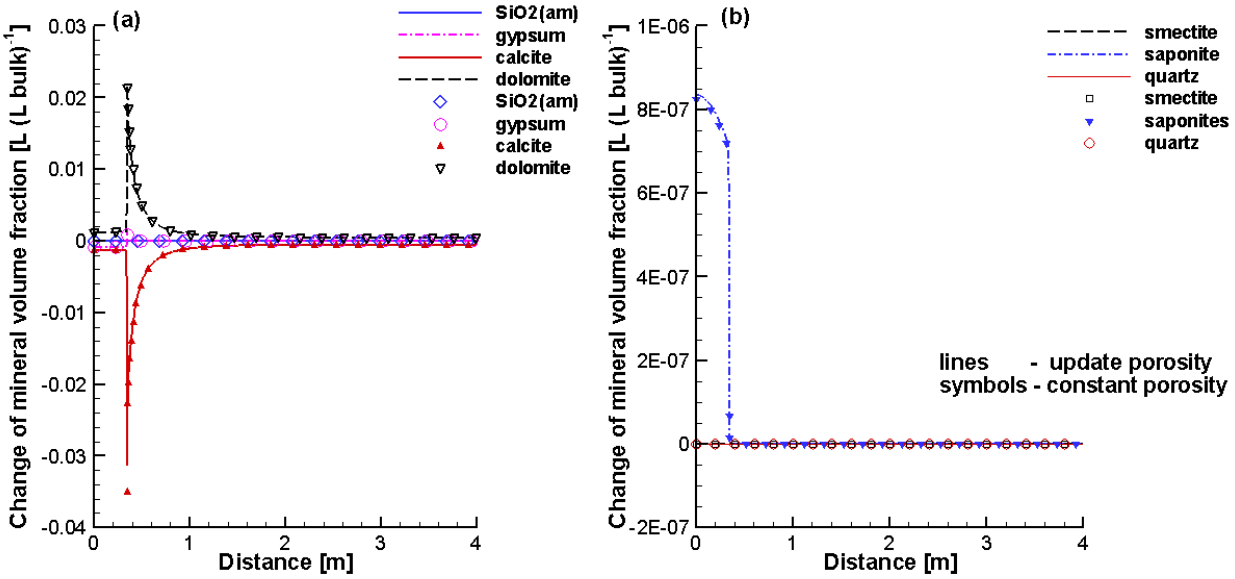

Figure 67: Comparison of Profiles of Mineral Volume Fraction Changes at 100,000 Years for Case 4CP (Symbols) and Case 4UP (Lines)

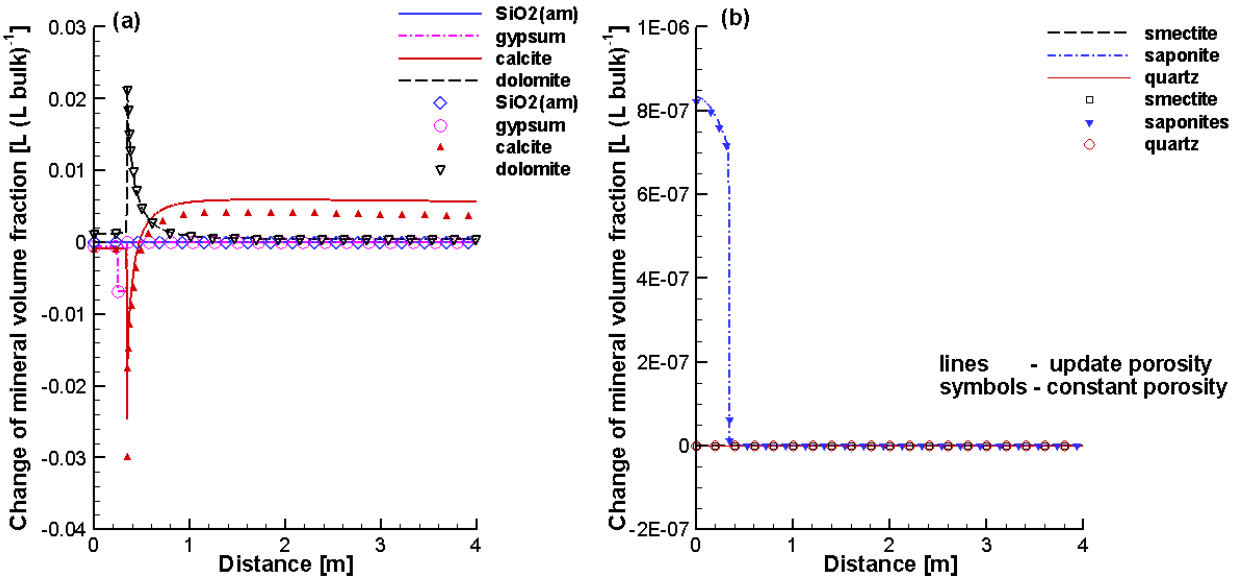

Figure 68: Comparison of Profiles of Mineral Volume Fraction Changes at 1,000,000 Years for Case 4CP (Symbols) and Case 4UP (Lines)

5.3.3.2 Impact of Reactive Transport on Radionuclide Diffusion – Case 4rCP and 4rUP

As a consequence of the small changes of porosity simulated for Case 4, the impact of reactive transport on radionuclide migration is also small. For a small defect occurring at 1,000 years, the simulated concentration profiles of I^- at selected times are depicted in Figure 69 for both Case 4rCP (symbols) and Case 4rUP (lines). The profiles for Case 4rCP are almost identical to the corresponding profiles for Case 4rUP. For all other canister failure scenarios, similar trends are observed (see Appendix A.6.1).

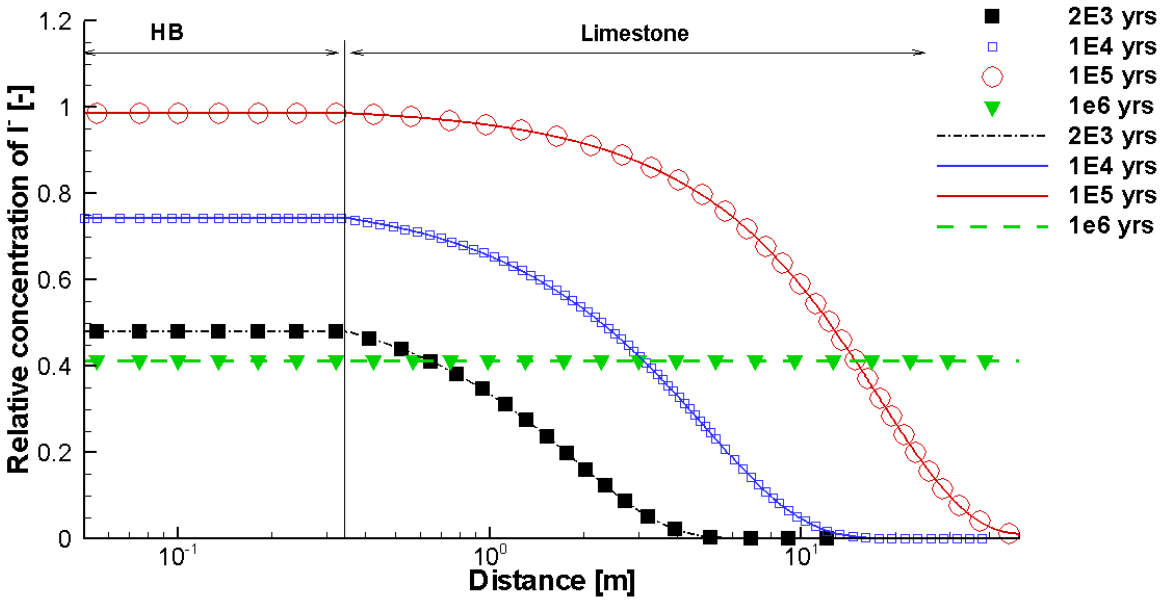

Figure 69: Relative Concentration Profiles of I^- at Selected Times for Case 4rCP (Symbols) and Case 4rUP (Lines) for the Canister Failure Scenario – Small Defect at 1,000 Years

5.3.4 Case 4 (HB/Limestone) With Consideration of EDZs

5.3.4.1 Impact of EDZs on Reactive Transport – Case 4UP and 4EDZUP

Comparisons of the volume fraction changes of minerals for Case 4UP (lines) and Case 4EDZUP (symbols) are presented in Figure 70 (at 1,000 years), Figure 71 (at 100,000 years), and Figure 72 (1,000,000 years), respectively. The results show that the change of the volume fractions of calcite and dolomite for Case 4rUP are slightly higher than the corresponding values for Case 4EDZUP, but in the limestone close to the interface HB/limestone the opposite is observed. In the HB, the changes of the volume fractions of calcite, dolomite and saponite for Case 4UP are all slightly higher than those for Case 4EDZUP. Consequently, the porosity change at the interface for Case 4EDZUP (Figure 73) is slightly lower than that for Case 4UP (Figure 65). Overall, the impact of EDZs on the porosity change is very low (Figure 73).

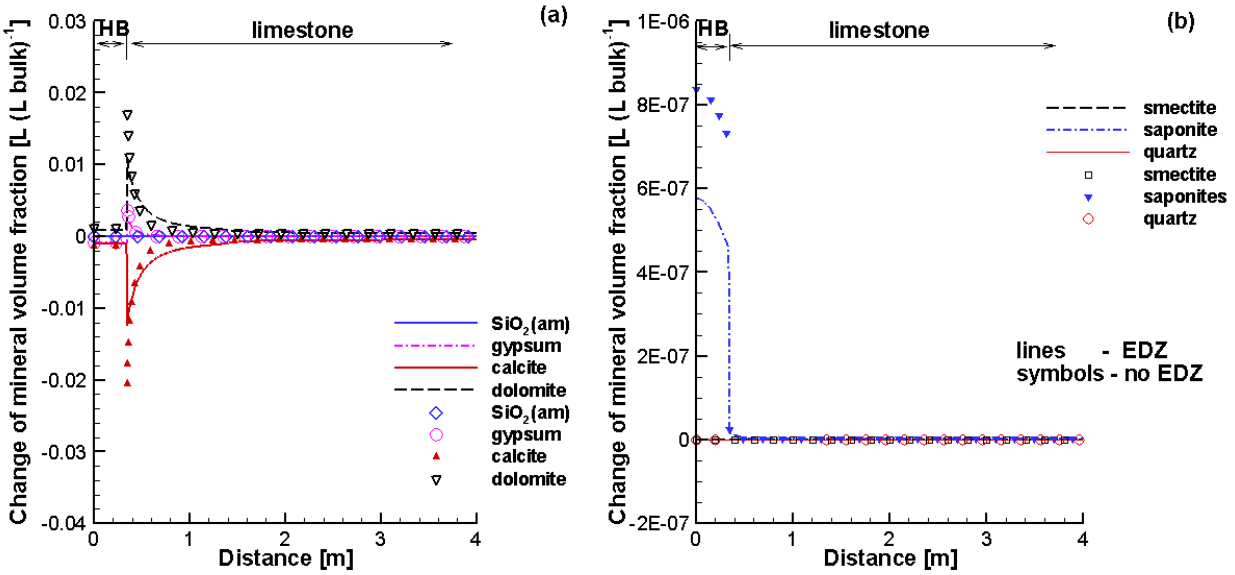

Figure 70: Comparison of Profiles of Mineral Volume Fraction Changes at 1,000 Years for Case 4UP (Symbols) and Case 4EDZUP (Lines)

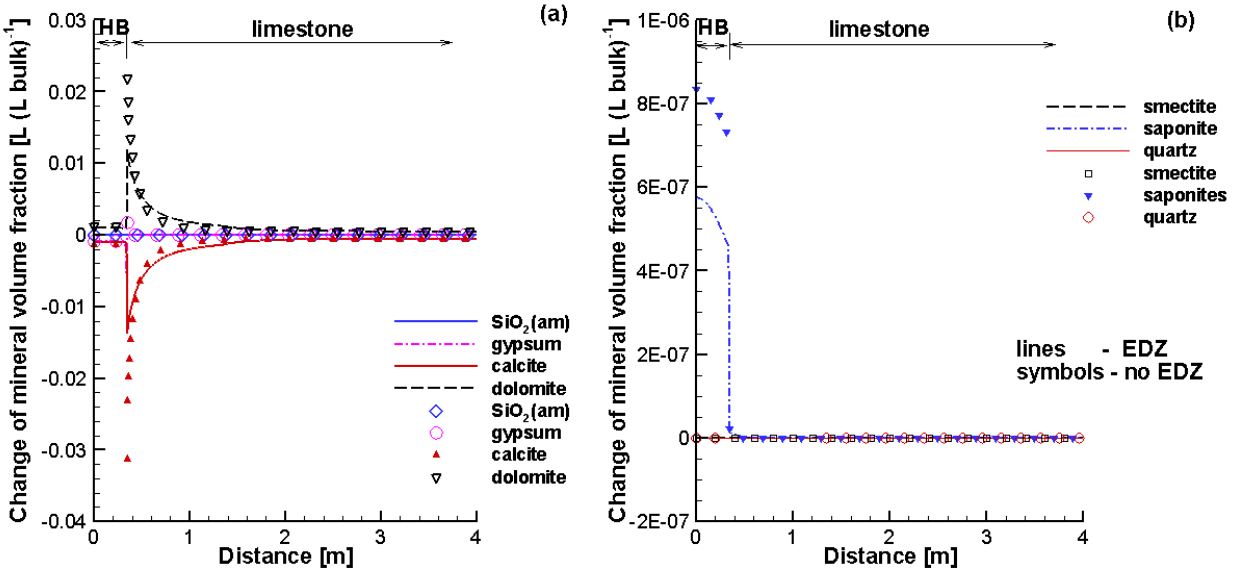

Figure 71: Comparison of Profiles of Mineral Volume Fraction Changes at 100,000 Years for Case 4UP (Symbols) and Case 4EDZUP (Lines)

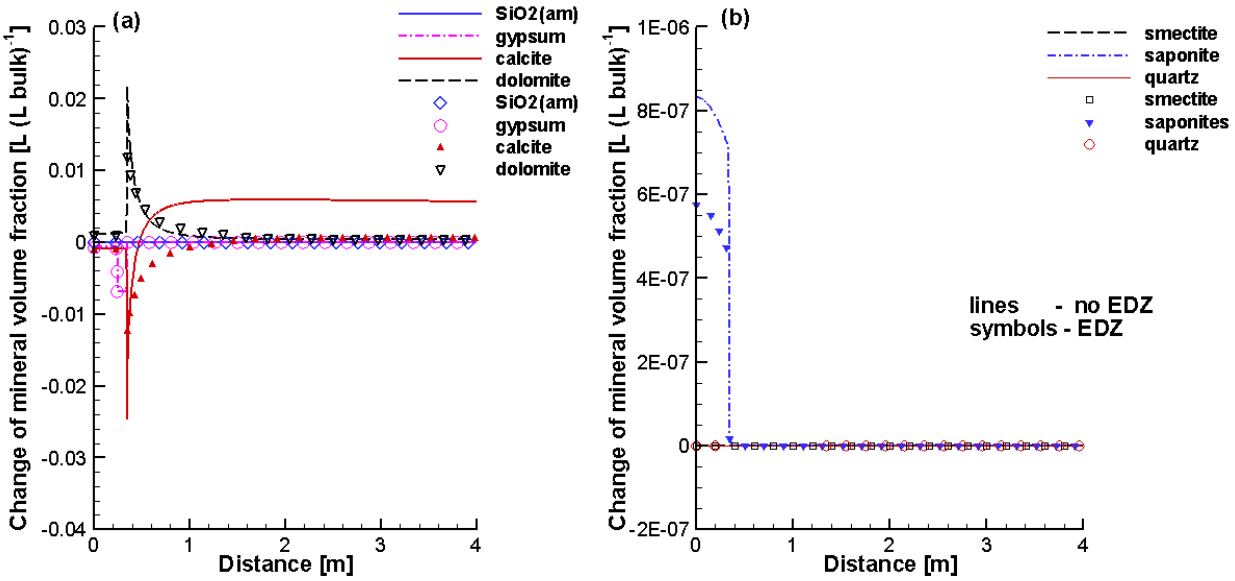

Figure 72: Comparison of Profiles of Mineral Volume Fraction Changes at 1,000,000 Years for Case 4UP (Symbols) and Case 4EDZUP (Lines)

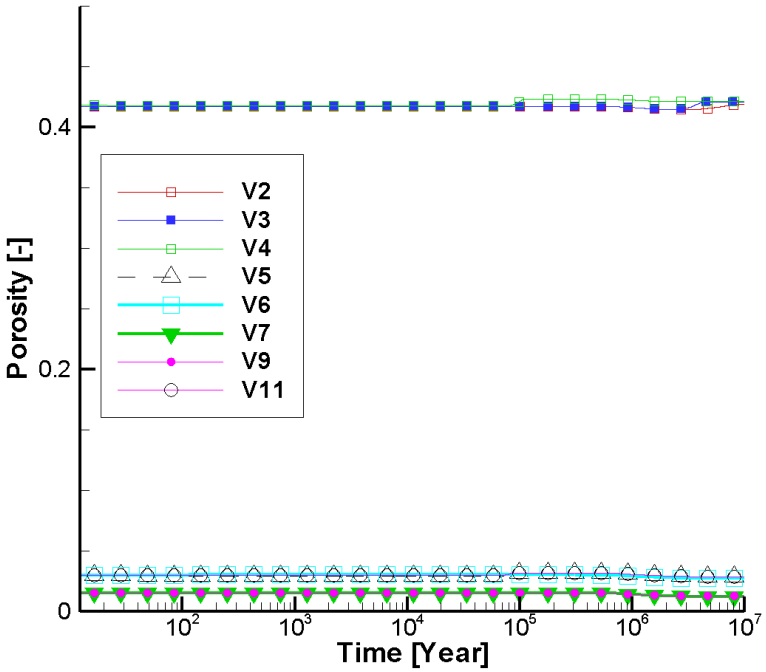

Figure 73: Porosity Evolution at Selected Observation Points for Case 4EDZUP. V2 and V3 (HB), V5 and V11 (Inner EDZ), V7 (Outer EDZ) and V9 (Intact Limestone)

5.3.4.2 Impact of EDZs on Radionuclide Diffusion – Case 4rUP and 4rEDZUP

Figure 74 shows the simulated breakthrough curves of I^-, for a small canister defect occurring at 1,000 years, at observation points V3, V5, V7 and V9 (see Figure 5 and Figure 6 for their locations) for Case 4rCP, 4rUP, 4rEDZCP and 4rEDZUP. Comparison of the results show that:

a) There is little difference in the I^- breakthrough curves for the cases assuming either constant porosity or updated porosity (i.e. Case 4rCP and 4rUP, or Case 4rEDZCP and 4rEDZUP).
b) Small differences in I^- concentrations exist at V7 (in the outer EDZ) and V9 (Figure 6) between the cases with or without consideration of EDZs (i.e. Case 4rCP and 4rEDZCP, or Case 4rUP and 4rEDZUP).

For all other canister failure scenarios, simulated results can be found in the Appendix A.6.2.

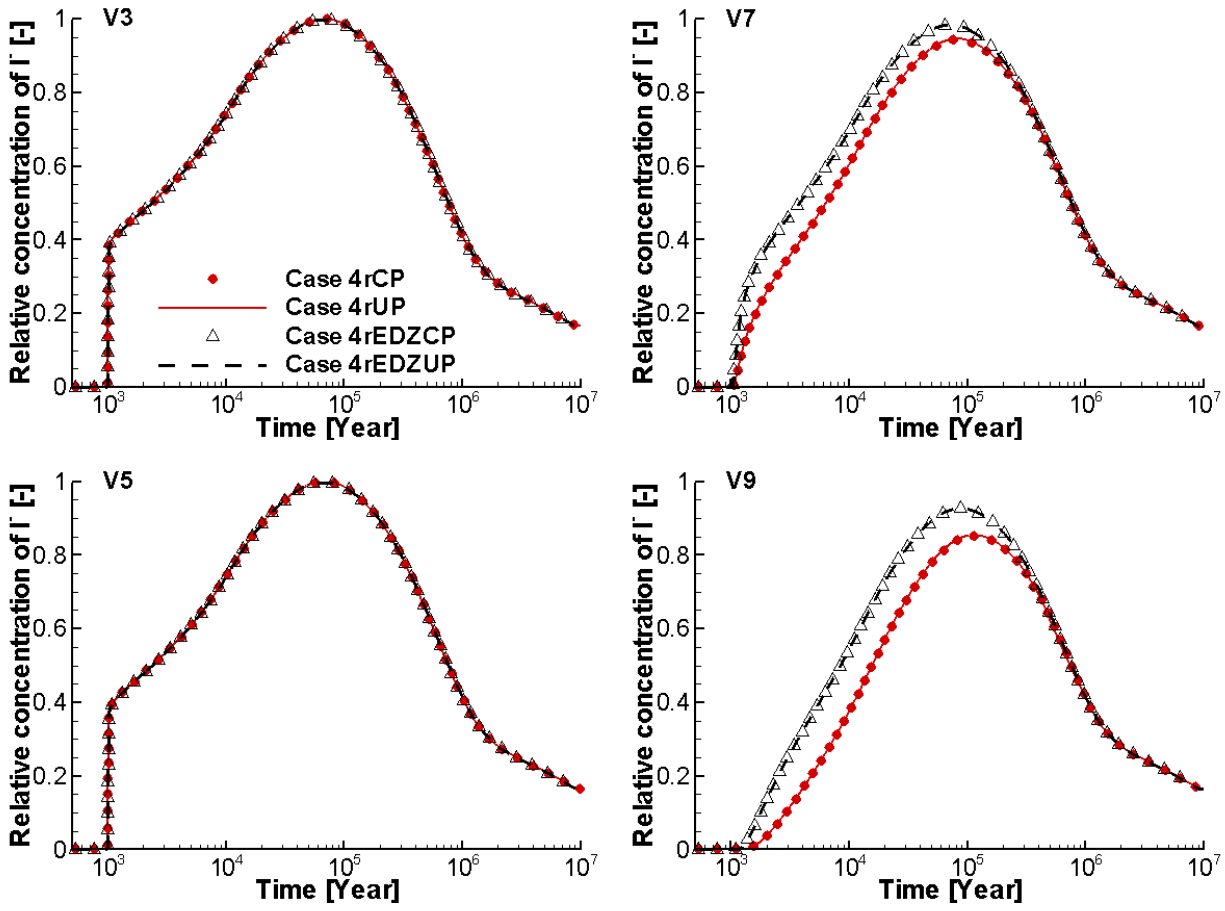

Figure 74: Breakthrough Curves of I^- at the Observation Points for a Small Defect Occurring at 1,000 Years for Case 4rCP, 4rUP, 4rEDZCP and 4rEDZUP. V3 (HB), V5 (Inner EDZ), V7 (Outer EDZ) and V9 (Intact Limestone)

6. DISCUSSION

Reactive transport simulations of cases including Low-Heat High-Performance Concrete (LHHPC), and including porosity updating, show pore clogging near the interfaces with the host rocks due to the degradation of the cementitious minerals. However, the major reactions driving the clogging are different in granite and in limestone host rock. In the granite host rock, porosity reduction occurs due to the interaction of bentonite and LHHPC, resulting in the precipitation of gypsum, saponite, calcite, tobermorite, and phillipsite in the LHHPC adjacent to the bentonite. The pore space in the concrete at the HB/LHHPC interface thus tends to become clogged. At the other interface with the granite, LHHPC tends to be dissolved, but the dissolved materials migrate into the granite and result in precipitation in granite adjacent to the LHHPC/granite interface, leading to clogging owing to the very low initial porosity of granite. In the limestone host rock; however, clogging only occurs in the limestone adjacent to the LHHPC/limestone interface due to the precipitation of calcite, phillipsite, saponite and sepiolite. The simulated clogging at the LHHPC/limestone interface is consistent with the predictions for LHHPC used as shaft seal in contact with limestone by Wilson et al. (2012), but the clogging position differs. Wilson et al. (2012) predicted the clogging to occur in the concrete adjacent to the interface mainly due to the precipitation of sepiolite, while the current simulations predict the clogging to occur in limestone due to the precipitation of sepiolite, saponite, phillipsite and calcite. The main reason for the differences in the results might be the inclusion of bentonite in the current Case 3 model, which provides additional pH buffering capacity. In addition, the thickness of the LHHPC in the current simulations is very small in comparison to the simulations conducted by Wilson et al. (2012). Apart from that, different accessible mineral surface areas were used for the current simulations. The reactive surface areas for kinetically-controlled mineral reactions were determined by dividing the values in Table 17, which were mostly based on Wilson et al. (2012), by 100 for bentonite and LHHPC, and by 1000 for the host rocks. All mineral reactions, except those involving gypsum, were treated as kinetically controlled. These differences show the importance of the conceptual models and highlight the role of laboratory and in situ experiments for verifying secondary minerals, and kinetic parameters.

The temporal evolution of porosity in the LHHPC also differs as a function of the host rock. In the granite, the porosity of LHHPC remains almost unchanged up to 100,000 years, while the porosity of LHHPC in limestone host rock increases from the initial value of 0.05 to 0.08 within 1,000 years (Figure 9). This is because of the high salinity of the limestone pore water that enhances the concrete degradation, which is consistent with the observations from laboratory experiments on the effect of salinity on concrete degradation by Jang and Iwasaki (1993). The excessive amount of silica fume was assumed to be converted to SiO_2(am), which might be partially dissolved when in contact with the pore waters from both granite or limestone host rocks, especially in the regions close to the interfaces. If temperature increase due to the decay of radionuclides in the canisters had also been considered, the dissolution of SiO_2(am) may have been further intensified. The same general results are expected at elevated temperatures, but likely over shorter time scales (Gaucher and Blanc 2006; Savage et al. 2007; Fernández et al. 2006; Lalan et al. 2016; Gaboreau et al. 2020).

All simulations that produced porosity reductions, especially pore clogging (i.e. including LHHPC), also had an impact on solute migration. Having higher initial porosities within the EDZs required more precipitates to fill the pore space, which in turn increased the predicted time needed to reach pore clogging in both the granitic and limestone host rocks. Reaction-induced porosity changes had a more significant impact on radionuclide (i.e. I^-) transport in the granite than the presence of EDZs, while for the limestone host rock simulations, both porosity updating

and EDZs had an impact on the simulated radionuclide transport. The results showed that porosity reductions were limited to a distance of less than 2 cm from the interfaces within a simulated period of 100,000 years. If substantial porosity reduction occurred before radionuclide release, the impact of porosity reduction on the radionuclide transport was significant even though the porosity reduction was localized (see porosity evolution at observation point V5 for the case 1EDZUP in Figure 20, and the concentration profiles of I^- in Figure 31). In the one-dimensional simulations conducted here, pore clogging in one control volume acted as a “bottle neck” to diffusive transport, a result which might be different if 2D or 3D models were considered.

Unlike the results for simulations involving LHHPC, the results for cases including HB and host rocks showed no pore clogging. Because of the low reactivity of bentonite compared to LHHPC, only minor mineral volume fraction and porosity changes were predicted for the HB-granite and HB-limestone host rock cases. Radionuclide transport in the HB-host rock cases was not significantly affected by porosity changes or the presence of EDZs.

It is important to point out that for the simulations in the sedimentary rocks with highly saline pore water (i.e. Case 3 and 4), Pitzer model should be more accurate to calculate the activity coefficients. However, reliable Pitzer parameters required for the complex geochemical system of the current project were unavailable, especially the aqueous components associated with the element Al (Prentice 2018). Therefore, the Brönsted–Guggenheim–Scatchard SIT model was employed for all reactive transport simulations.

7. CONCLUSIONS

Isothermal reactive transport simulations were undertaken to investigate the processes and alterations occurring within several metres of bentonite/LHHPC/host rock interfaces and their potential impact on diffusive radionuclide migration. Material properties and 1D domain geometries were selected to represent generic conditions near a repository in either crystalline or sedimentary rocks. Nonreactive radionuclide transport was represented by I^-, which was assumed to be released due to canister failure.

Among the investigated materials, the cementitious substances in LHHPC (i.e. tobermorite-like TobII-07mat, hydrotalcite and SiO_2(am)) were the most reactive in comparison to the natural materials such as bentonite, granite and limestone. Cases including LHHPC (i.e. Case 1 (HB/LHHPC/Granite) and Case 3 (HB/LHHPC/Limestone)) thus showed substantial mineral alterations close to the interfaces of HB/LHHPC and LHHPC/host rock in comparison to the models that did not include LHHPC (i.e. HB/host rock; Cases 2 and 4). Consequently, porosity reduction to the point of complete clogging was simulated for all cases in which LHHPC was included and porosity updating was implemented. Due to the higher initial porosities assumed within the inner EDZs, simulations including inner EDZs required more time to reach complete pore clogging at the interface between LHHPC and the host rocks.

The simulation results indicate that due to the relatively high pH of pore water in LHHPC (pH = 9.7), substantial mineral dissolution/precipitation occurs at the interfaces of bentonite/LHHPC. However, after 100,000 years the alteration remains restricted to a distance of 2 cm from the interfaces. In the case of granitic host rock, Calcium Silicate Hydrate (CSH) phases present in LHHPC are predicted to transform into tobermorite, phillipsite and saponite within 1000 years. The simulations indicate that a substantial reduction in porosity occurs after about 1,500 years

in the concrete adjacent to bentonite due to the precipitation of tobermorite, sepiolite, saponite, phillipsite, gypsum and calcite. In the case of limestone host rock, saponite and sepiolite are the dominant minerals formed in the LHHPC within a time frame of 1000 years. In this case, complete pore clogging is predicted after about 3,800 years in the limestone adjacent to the LHHPC, mainly due to the precipitation of saponite, sepiolite, calcite and phillipsite.

The impact of porosity reduction/pore clogging on I^- diffusion was shown to be significant depending on the timing of clogging relative to the canister failure scenarios. If the canister failure occurred after the pore clogging, then the impact was most significant.

In contrast, for the simulations dealing with interfaces between bentonite and host rocks (i.e. Case 2 HB/granite, and 4 HB/limestone), porosity reduction was very small for both the granite and limestone host rocks, and no clogging was predicted. As a result, there were relatively small differences in radionuclide transport between simulations assuming constant porosity and reaction-induced porosity changes. However, the inclusion of EDZs slightly increased the mobility of I^- across the EDZs.

ACKNOWLEDGEMENTS

This study was funded by the NWMO, Canada. Valuable discussions with Tammy Yang (NWMO) and Monique Hobbs (NWMO) helped to improve this report. Mark Gobien (NWMO) provided the data for the canister failure scenarios.

REFERENCES

Alexander, W.R., A.E. Milodowski and A.F. Pitty (Eds.). 2012. Cyprus Natural Analogue Project (CNAP) Phase III Final Report, Posiva Working Report WR 2011-77. Posiva, Eurajoki, Finland.

Alexander, W.R., A.E. Milodowski, A.F. Pitty, S.M.L. Hardy, S.J. Kemp, J.C. Rushton, A. Siathas, A. Siathas, A.B. Mackenzie, P. Korkeakoski, S. Norris, P. Sellin and M. Rigas. 2013. Bentonite reactivity in alkaline solutions: interim results of the Cyprus Natural Analogue Project (CNAP). Clay Mineral., 48, pp. 235-249

Alonso, M.C., J.L.G. Calvo, J. Cuevas, M.J. Turrero, R. Fernández, E. Torres and A.I. Ruiz. 2017. Interaction processes at the concrete-bentonite interface after 13 years of FEBEX-Plug operation. Part I: Concrete alteration. Physics and Chemistry of the Earth, Parts A/B/C, 99, pp.38-48.

Arbogast, T. 2013. Flow through heterogeneous porous rocks: What average is the correct average? Mathematics of Planet Earth. http://mpe.dimacs.rutgers.edu/2013/04/29/flow-through-heterogeneous-porous-rocks-what-average-is-the-correct-average/

Baur, I., P. Keller, D. Mavrocordatos, B. Wehrli and A. Johnson. 2004. Dissolution-precipitation behaviour of ettringite, monosulfate and calcium silicate hydrate. Cement and Concrete Research 34, 341-348.

Bea, S.A., K.U. Mayer and K.T.B. MacQuarrie. 2011. Modelling Reactive Transport in Sedimentary Rock Environments - Phase II MIN3P code enhancements and illustrative simulations for a glaciation scenario. Nuclear Waste Management Organization Technical Report NWMO TR-2011-13.

Bea, S.A., K.U. Mayer and K.T.B. MacQuarrie. 2012. Modelling of reactive transport in a hypothetical sedimentary basin affected by a glaciation/deglaciation event. 39th IAH Congress, Niagara Falls, Canada: September 16-21.

Beckingham, L.E., E.H. Mitnick, C.I. Steefel, S. Zhang, M. Voltolini, A.M. Swift, L. Yang, D.R. Cole, J.M. Sheets, J.B. Ajo-Franklin and D.J. DePaolo. 2016. Evaluation of mineral reactive surface area estimates for prediction of reactivity of a multi-mineral sediment. Geochimica et Cosmochimica Acta, 188, pp.310-329.

Beckingham, L.E., C.I. Steefel, A.M. Swift, M. Voltolini, L. Yang, L.M. Anovitz, J.M. Sheets, D.R. Cole, T.J. Kneafsey, E.H. Mitnick and S. Zhang. 2017. Evaluation of accessible mineral surface areas for improved prediction of mineral reaction rates in porous media. Geochimica et Cosmochimica Acta, 205, pp. 31-49

Besselink, R., T.M. Stawski, H. M. Freeman, J. Hövelmann, D. J. Tobler and L. G. Benning. 2019. Mechanism of saponite crystallization from a rapidly formed amorphous intermediate. https://arxiv.org/abs/1906.07479v1.

Bertettti, F.P. 2016. Determination of sorption properties for sedimentary rocks under saline reducing conditions-key radionuclides (No. NWMO-TR--2016-08). Nuclear Waste Mangement Organization (NWMO).

Blanc, P., V. Philippe, H. Gailhanou, S. Gaboreau, N. Marty, F. Claret, B. Made, E. Giffaut. 2015. ThermoChimie Database Developments in the Framework of Cement/Clay Interactions. Applied Geochemistry. 10.1016/j.apgeochem.2014.12.006.

Bradbury, M.H. and B. Baeyens. 2003. Pore water chemistry in compacted re-saturated MX-80 bentonite. Journal of Contaminant Hydrology, 61(1–4), pp 329-338.

Breton, D. 1996. Atomic Energy of Canada Ltd (AECL), Low-heat high-performance concrete. U.S. Patent 5,531,823.

Brønsted, J.N., 1922. Studies on solubility. IV. The principle of the specific interaction of ions. Journal of the American Chemical Society, 44(5), pp.877-898.

Bustillo, M.A., R. Fort and M. Bustillo. 1993. Specific surface area and ultramicroporosity in polymorphs of silica. European Journal of Mineralogy. 5(6): 1195 – 1204.

Calvo, JL García, A. Hidalgo, C. Alonso and L.F. Luco. 2010. Development of low-pH cementitious materials for HLRW repositories: Resistance against ground waters aggression. Cement and Concrete Research, 40(8), pp.1290-1297.

Calvo, JL García, M.C. Alonso, A. Hidalgo, L. Fernández Luco, and V. Flor-Laguna. 2013. Development of low-pH cementitious materials based on CAC for HLW repositories: Long-term hydration and resistance against groundwater aggression. Cement and concrete research, 51, pp.67-77.

Carlson, L. and U Schwertmann. 1981. Natural ferrihydrites in surface deposits from Finland and their association with silica Geochim. Cosmochim. Acta, 45, pp. 421-429

Cassagnabère, A., J.C. Parneix, S. Sammartino and A.E. Milodowski. 2001. Mineralogical evolution of bituminous marl adjacent to an alkaline water conducting feature at the Maqarin analogue site. Pp. 367-370 in: Water-Rock Interaction (R. Cidu, editor). Balkema, Liss, Tokyo

Chagneau, A., F. Claret, F. Enzmann, M. Kersten, S. Heck, B. Madé and Th. Schäfer. 2015. Mineral precipitation‐induced porosity reduction and its effect on transport parameters in diffusion‐controlled porous media. Geochemical Transactions. 16:13. DOI 10.1186/s12932-015-0027-z

Ciavatta, L. 1990. The specific interaction theory in equilibrium-analysis-some empirical rules for estimating interaction coefficients of metal-ion complexes. Annali di Chimica, 80(5-6), pp.255-263.

Crank, J. 1979. The mathematics of diffusion. Oxford university press.

Cuevas, J., R. Vigil de la Villa, S. Ramírez, L. Sánchez, R. Fernández and S. Leguey. 2006. The alkaline reaction of FEBEX bentonite: a contribution to the study of the performance of bentonite/concrete engineered barrier systems. Journal of Iberian Geology, 32(2), 151–174.

Cuevas, J., A.I. Ruiz, R. Fernández, E. Torres, A. Escribano, M. Regadío and M. J. Turrero. 2016. Lime mortar-compacted bentonite–magnetite interfaces: An experimental study

focused on the understanding of the EBS long-term performance for high-level nuclear waste isolation DGR concept. Applied Clay Science, 124-125: 79–93.

Cuevas, J., A.I. Ruiz, R. Fernández, D. González-Santamaría, M. Angulo, A. Ortega, E. Torres, and M. J. Turrero. 2018. Authigenic ClayMinerals from Interface Reactions of Concrete-Clay Engineered Barriers: A New Perspective on Mg-Clays Formation in Alkaline Environments. Minerals, 8: 362.

Dauzeres, A., G. Achiedo, D. Nied, E. Bernard, S. Alahrache and B. Lothenbach. 2016. Magnesium perturbation in low-pH concretes placed in clayey environment—solid characterizations and modeling. Cement and Concrete Research 79: 137-150.

Debye, P. and E. Hückel. 1923. The theory of electrolytes. I. Lowering of freezing point and related phenomena. Physikalische Zeitschrift. 24: 185–206.

De La Villa, R.V.; J. Cuevas,S. Ramírez and S. Leguey. 2001. Zeolite formation during the alkaline reaction of bentonite. European Journal of Mineralogy, 13(3), p. 635 – 644.

Davies, C. W. 1962. Ion association, Butterworths, London, 190 pp

Deschner, F., F. Winnefeld, B. Lothenbach, S. Seufert, P. Schwesig, S. Dittrich, F. Goetz-Neunhoeffer and J. Neubauer. 2012. Hydration of Portland cement with high replacement by siliceous fly ash. Cement and Concrete Research, 42 (10) , pp. 1389-1400

Donahoe, R.J. and J.G. Liou. 1985. An experimental study on the process of zeolite formation. Geochimica et Cosmochimica Acta. 49(11), p. 2349-2360

Dolder, F., U. Mäder, A. Jenni and B. Münch. 2016. Alteration of MX-80 bentonite backfill material by high-pH cementitious fluids under lithostatic conditions – an experimental approach using core infiltration techniques. Geological Society, London, Special Publications, 443, 281-305

Dubois, I.E. 2011. Specific surface area of some minerals commonly found in granite, Licentiate thesis, KTH, Sweden.

Fernández, R., J. Cuevas, L. Sánchez, R.V. de la Villa and S. Leguey. 2006. Reactivity of the cement–bentonite interface with alkaline solutions using transport cells. Applied Geochemistry, 21(6), pp.977-992.

Fernández, R., U.K. Mäder, M. Rodriguez, R. Vigil de la Villa and J. Cuevas. 2009. Alteration of compacted bentonite by diffusion of highly alkaline solutions. European Journal of Mineralogy 21: 725-735.

Fernández, R., A. I. Ruiz and J. Cuevas. 2016. Formation of C-A-S-H phases from the interaction between concrete or cement and bentonite. Clay Minerals; 51 (2): 223–235. doi: https://doi.org/10.1180/claymin.2016.051.2.09

Fernández, R., E. Torres, A.I. Ruiz, J. Cuevas, M.C. Alonso, J.L.G. Calvo, E. Rodríguez and M.J. Turrero. 2017. Interaction processes at the concrete-bentonite interface after 13 years of FEBEX-Plug operation. Part II: Bentonite contact. Physics and Chemistry of the

Earth, Parts A/B/C, 99, pp.49-63.Gaucher, E. and P. Blanc. 2006. Cement/clay interactions - a review: experiments, natural analogues, and modeling. Waste Management 26: 776-788.

Giambalvo, E.R., C.I. Steefel, A.T. Fisher, N.D. Rosenberg and C.G. Wheat. 2002. Effect of fluid-sediment reaction on hydrothermal fluxes of major elements, eastern flank of the Juan de Fuca Ridge. Geochim. Cosmochim. Acta, 66 (10), 1739–1757.

Giffaut, E., M. Grivé, P. Blanc, P. Vieillard, E. Colàs, H. Gailhanou, S. Gaboreau, N. Marty, B. Madé and L. Duro. 2014. Andra thermodynamic database for performance assessment: ThermoChimie, Applied Geochemistry, 49, pp. 225-236.

Gobien, M., F. Garisto, E. Kremer and C. Medri. 2016. Sixth case study: reference data and codes. Nuclear Waste Management Organization Technical Report NWMO-TR-2016-10.

Gobien, M., F. Garisto, E. Kremer and C. Medri. 2018. Seventh case study: reference data and codes. Nuclear Waste Management Organization Technical Report NWMO-TR-2018-10.

González-Santamaría, D.E., M. Angulo, A.I. Ruiz, R. Fernández, A. Ortega and J. Cuevas. 2018. Low-pH cement mortar-bentonite perturbations in a small-scale pilot laboratory experiment. Clay Minerals, 53(2): 237-254.

Grenthe, I., F. Mompean K. Spahiu and H. Wanner. 2013. TDB-2: Guidelines for the extrapolation to zero ionic strength. OECD Nuclear Energy Agency, Data Bank Issy-les-Moulineaux (France)

Grenthe, I. and A. Plyasunov. 1997. On the use of semiempirical electrolyte theories for modeling of solution chemical data. Pure and applied chemistry, 69(5), pp.951-958.

Guggenheim, E.A. and J.C. Turgeon. 1955. Specific interaction of ions. Transactions of the Faraday Society, 51, pp.747-761.

Henderson, T., K.U. Mayer, B. Parker and T. Al. 2009. Three-dimensional density-dependent flow and multicomponent reactive transport modeling of chlorinated solvent oxidation by potassium permanganate. Journal of Contaminant Hydrology, 106, 195-211.

Herbert, H.J., J. Kasbohm, H.C. Moog and K.H. Henning. 2004. Long-term behaviour of the Wyoming bentonite MX-80 in high saline solutions. Applied Clay Science, 26(1-4), pp.275-291.

Hodgkinson, E.S. and C.R. Hughes. 1999. The mineralogy and geochemistry of cement/rock reactions: high-resolution studies of experimental and analogue materials. Geological Society, London, Special Publications, 157(1), pp.195-211.

Huertas, F.J., L. Chou and R. Wollast. 1999. Mechanism of kaolinite dissolution at room temperature and pressure Part II: kinetic study. Geochimica et Cosmochimica Acta 63, 3261-3275.

Jackson, M. D., S. R. Mulcahy, H. Chen, Y. Li, Q. Li, P. Cappelletti and H. Wenk. 2017. Phillipsite and Al-tobermorite mineral cements produced through low-temperature water-

rock reactions in Roman marine concrete. American Mineralogist ; 102 (7): 1435–1450. doi: https://doi.org/10.2138/am-2017-5993CCBY

Jang, J. and I. Iwasaki. 1993. Effect of salt additives on concrete degradation. Technical report MNIRD-93/10.

Kadioglu, S.Y., R.R. Nourgaliev and V.A. Mousseau. 2008. A Comparative Study of the Harmonic and Arithmetic Averaging of Diffusion Coefficients for Non-Linear Heat Conduction Problems, Technical report of the Idaho National Laboratory INL/EXT-08-13999

Karamalidis, A. K. and D.A. Dzombak. 2010. Surface Complexation Modeling: Gibbsite; John Wiley: New York.

Karnland O, S. Olsson and U. Nilsson.2006. Mineralogy and sealing properties of various bentonites and smectite-rich clay materials. SKB TR-06-30, Svensk Kärnbränslehantering AB.

King, F., D. S. Hall and P. G. Keech. 2017. Nature of the near-field environment in a deep geological repository and the implications for the corrosion behaviour of the container, Corrosion Engineering, Science and Technology, 52:sup1, 25-30, DOI: 10.1080/1478422X.2017.1330736

Kulik, D.A., T. Wagner, S.V. Dmytrieva, G. Kosakowski, F.F. Hingerl, K.V. Chudnenko and U. Berner. 2013. GEM-Selektor geochemical modeling package: revised algorithm and GEMS3K numerical kernel for coupled simulation codes. Computational Geosciences 17, 1-24.

Lai, P., K. Moulton and S. Krevor. 2015. Pore-scale heterogeneity in the mineral distribution and reactive surface area of porous rocks. 411: 260-273.

Lalan, P., A. Dauzeres, L. De Windt, D. Bartier, J. Sammaljarvi, J.D. Barnichon, I. Techer and V. Detilleux. 2016. Impact of a 70 degrees C temperature on an ordinary Portland cement paste/claystone interface: An in situ experiment. Cement Concr. Res., 83, pp. 164-178

Lerouge, C., S. Gaboreau, S. Grangeon, F. Claret, F. Warmont, A. Jenni, V. Cloet and U. Mäder. 2017. In situ interactions between opalinus clay and low alkali concrete. Physics and Chemistry of the Earth, Parts A/B/C, 99, pp.3-21.

Liu, Z. and C. Ma. 2001. A new method for numerical treatment of diffusion coefficients at control-volume surfaces. Numerical Heat Transfer, Part B, 47: 1–15.

Liu, H.H., L.J. Bao and E.Y. Zeng. 2014. Recent advances in the field measurement of the diffusion flux of hydrophobic organic chemicals at the sediment-water interface. Trends in Analytical Chemistry, 54: 56–64.

Lothenbach, B., G. Le Saout, M.B. Haha, R. Figi and E. Wieland. 2012. Hydration of a low-alkali CEM III/B–SiO2 cement (LAC). Cement and Concrete Research, 42(2), pp.410-423.

Lothenbach, B., T. Matschei, G. Möschner and F.P. Glasser. 2008. Thermodynamic modelling of the effect of temperature on the hydration and porosity of Portland cement. Cement and Concrete Research, 38, pp. 1-18

Lothenbach, B., D. Rentsch and E. Wieland. 2014. Hydration of a silica fume blended low-alkali shotcrete cement. Physics and Chemistry of the Earth, Parts A/B/C, 70, pp.3-16.

Lothenbach, B., K. Scrivener and R.D. Hooton. 2011. Supplementary cementitious materials. Cement and Concrete Research, 41 (12), pp. 1244-1256

MacQuarrie, K.T.B., K.U. Mayer, B. Jin and S.M. Spiessl. 2010. The importance of conceptual models in the reactive transport simulation of oxygen ingress in sparsely fractured crystalline rock. Journal of contaminant hydrology, 112(1-4), pp.64-76.

Martin, L.H., A. Leemann, A.E. Milodowski, U.K. Mäder, B. Münch and N. Giroud. 2016. A natural cement analogue study to understand the long-term behaviour of cements in nuclear waste repositories: Maqarin (Jordan). Applied Geochemistry, 71, pp.20-34.

Marty, N.C.M., O. Bildstein, P. Blanc, F. Claret, B. Cochepin, E.C. Gaucher, D. Jacques, J.-E. Lartigue, S. Liu, K.U. Mayer, J.C.L. Meeussen, I. Munier, I. Pointeau, D. Su and C.I. Steefel. 2015. Benchmarks for multicomponent reactive transport across a cement/clay interface. Computational Geosciences, 19, 635–653.

Marty, N.C.M., Claret, F., Giffaut, E., Madé, B., Tournassat, C., 2015a. A database of dissolution and precipitation rates for clay-rocks minerals. Applied Geochemistry, 55, 108-118.

Marty, N., B. Fritz, A. Clément and N.Michau. 2010. Modelling the long term alteration of the engineered bentonite barrier in an underground radioactive waste repository. Applied Clay Science 47, 82-90.

Marty, N.C., C. Tournassat, A. Burnol, E. Giffaut and E.C. Gaucher. 2009. Influence of reaction kinetics and mesh refinement on the numerical modelling of concrete/clay interactions. Journal of Hydrology, 364(1-2), pp.58-72.

Mayer, K.U. 1999. A numerical model for multicomponent reactive transport in variably-saturated porous media, Ph.D. – thesis, Department of Earth Sciences, University of Waterloo, Waterloo, Ontario, Canada.

Mayer, K.U., E.O. Frind and D.W. Blowes. 2002. Multicomponent reactive transport modeling in variably-saturated porous media using a generalized formulation for kinetically controlled reactions. Water Resources Research, 38(9).

Mayer, K.U. and K.T.B. MacQuarrie 2010. Solution of the MoMaS reactive transport benchmark with MIN3P – Model formulation and simulation results, Computational Geosciences, 14, 405 – 419, doi: 1007/s105596-009-9158-6

Metcalfe, R. and C. Walker. 2004. Proceedings of the International Workshop on Bentonite-Cement Interaction in Repository Environments, Tokyo, Posiva Working Report 2004-25, Posiva Oy, Olkiluoto, Finland.

Milodowski, A.E., S. Norris and W.R. Alexander. 2016. Minimal alteration of montmorillonite following long-term interaction with natural alkaline groundwater: Implications for geological disposal of radioactive waste. Applied Geochemistry. 66, pp184-197.

Navarre-Sitchler A. and S. Brantley 2007. Basalt weathering across scales. Earth and Planetory Sciences Letter; 261: 321-334.

Notario, J.S., J.E. Garcia, J.M. Caceres, I.J.Arteaga and M.M.Gonzalez. 1995. Characterization of natural phillipsite modified with orthophosphoric acid, Applied Clay Science, 10(3): 209-217.

NWMO. 2017. Postclose Safety Assessment of a Used Fuel Repository in Crystalline Rock. Nuclear Waste Management Organization Technical Report NWMO TR-2017-02. Toronto, Canada.

NWMO. 2018. Postclose Safety Assessment of a Used Fuel Repository in Sedimentary Rock. Nuclear Waste Management Organization Technical Report NWMO TR-2018-08. Toronto, Canada.

Olson, G. L. and J. E. Morel. 1999. Solution of the radiation diffusion equation on an AMR eulerian mesh with material interface. In Technical Report LA-UR-99-2949, 1999. Los Alamos National Laboratory.

Parkhurst, D.L. and C.A.J. Appelo. 2013. Description of input and examples for PHREEQC version 3 − A computer program for speciation, batch-reaction, one-dimensional transport, and inverse geochemical calculations: U.S. Geological Survey Techniques and Methods, book 6, chap. A43, 497 p. http://pubs.usgs.gov/tm/06/a43/.

Pitzer KS. 1991. Ion interaction approach: Theory and data correlation. In: PitzerKS (ed) Activity Coefficients in Electrolyte Solutions, 2nd edn. CRC Press, Boca Raton, Florida, pp 76-153

Preis, W. and H. Gamsjäger. 2001. Thermodynamic Investigation of Phase Equilibria in Metal Carbonate–Water–Carbon Dioxide Systems. Monatshefte fuer Chemie 132: 1327-1346. https://doi.org/10.1007/s007060170020

Prentice, D. 2018. Thermodynamic modelling of ultra-long-term durability of cementitious binders for waste immobilisation (Doctoral dissertation, University of Sheffield).

Pusch, R. 1992. Use of bentonite for isolation of radioactive waste products. Clay Minerals, 27(3), pp.353-361.

Quintessa Ltd. and Geofirma Engineering Ltd. 2011. Postclosure safety assessment: Data. Nuclear Waste Management Organization Report NWMO DGR-TR-2011-32 R000. Toronto, Canada.

Read, D., F.P. Glasser, C. Ayora, M.T. Guardiola and A. Sneyers. 2001. Mineralogical and microstructural changes accompanying the interaction of Boom Clay with ordinary Portland cement. Advances in cement research, 13(4), pp.175-183.

Savage, D. and S. Benbow. 2007. Low pH Cements, Technical report, SKI Report 2007:32.

Savage, D., S. Benbow, C. Watson, H. Takase, K. Ono. C. Oda and K. Honda. 2010. Natural systems evidence for the alteration of clay under alkaline conditions: an example from Searles Lake, California. Applied Clay Science, 47, 7281.

Savage, D., C. Walker, R.C. Arthur, C.A. Rochelle, C. Oda and H. Takase. 2007. Alteration of bentonite by hyperalkaline fluids: a review of the role of secondary minerals. Physics and Chemistry of the Earth 32: 287-297.

Savage, D. and V. Cloet. 2018. A review of cement-clay modelling. Nagra Arbeitsbericht NAB 18-24.

Scatchard, G. 1936. Concentrated solutions of strong electrolytes. Chemical reviews, 19(3), pp.309-327.

Sellin, P. and O.X. Leupin. 2013. The use of clay as an engineered barrier in radioactive-waste management – a review. Clays and Clay Minerals 61 (6): 477-498.

Selvadurai, P.A. and A.P.S. Selvadurai. 2014. On the effective permeability of a heterogeneous porous medium: the role of the geometric mean, Philosophical Magazine, 94:20, 2318-2338, DOI: 10.1080/14786435.2014.913111

Sipos, P. 2008. Application of the Specific Ion Interaction Theory (SIT) for the ionic products of aqueous electrolyte solutions of very high concentrations. Journal of Molecular Liquids, 143(1), 13-16. DOI: 10.1016/j.molliq.2008.04.003

Sipos, P., P.M. May, G.T. Heffer and I. Kron. 1994. The ultraviolet absorption spectra of synthetic bayer liquors. Journal of the Chemical Society, Chemical Communications. 0: 2355-2356. DOI:10.1039/C39940002355

Sipos, P., Hefter, G., & May and P.M. 1998. A hydrogen electrode study of concentrated alkaline aluminate solutions. Australian Journal of Chemistry, 51(6), 445-453.

Smellie, J.L. 1999. Lithostratigraphy of Miocene – Recent, alkaline volcanic fields in the Antarctic Peninsula and eastern Ellsworth Land. Antarctic Science, 11(3), pp.362-378.

Tinseau, E., D. Bartier, L. Hassouta, I. Devol-Brown and D. Stammose. 2006. Mineralogical characterization of the Tournemire argillite after in situ interaction with concretes. Waste Management, 26(7), pp.789-800.

Torres, E., M.J. Turrero, A. Escribano and P.L. Martín. 2013. Geochemical interactions at the concrete-bentonite interface of column experiments. PEBS Project Report.

Watson, C., D. Savage, J. Wilson, S. Benbow, C. Walker and S. Norris. 2013. The Tournemire industrial analogue: reactive-transport modelling of a cement–clay interface. Clay Minerals, 48, 167–184

White A.F. and S.L. Brantley. 2003. The effect of time on the weathering of silicate minerals: why do weathering rates differ in the laboratory and field? Chemical Geology; 202: 479-506.

Wilson, J., S. Benbow and R. Metcalfe. 2012. Geochemical Modelling of the Long-term Evolution of the OPG DGR Shaft Seals. Quintessa Technical report QRS-1544A-TR1.

Xie, M., P. Rasouli, K.U. Mayer and K.T.B. MacQuarrie. 2014a. Reactive Transport Modelling of In-situ Diffusion Experiments for the Mont Terri Project − MIN3P-THCm Code Enhancement and Numerical Simulations, Nuclear Waste Management Organization Technical Report NWMO-TR-2014-25.

Xie, M., P. Rasouli, K.U. Mayer and K.T.B. MacQuarrie. 2014b. Reactive Transport Modelling in Low Permeability Media – MIN3P-THCm Simulations of EBS TF-C Compacted Bentonite Diffusion Experiments, Nuclear Waste Management Organization Technical Report NWMO-TR-2014-23.

Yamaguchi, T., T., Y.Sakamoto, M.Akai, M.Takazawa, Y.Iida, T.Tanaka and S.Nakayama. 2007. Experimental and modeling study on long-term alteration of compacted bentonite with alkaline groundwater. Physics and Chemistry of the Earth, Parts A/B/C. 32(1–7): 298-310.

Yamaguchi, T., T. Sawaguchi, M. Tsukada, S. Hoshino and T. Tanaka. 2016. Mineralogical changes and associated decrease in tritiated water effective diffusion coefficient after alteration of cement–bentonite interfaces. Clay Minerals; 51 (2): 279–287. doi: https://doi.org/10.1180/claymin.2016.051.2.13

APPENDIX A: LIST OF ADDITIONAL SIMULATION RESULTS

CONTENTS

LIST OF FIGURES

Page

A.1 *VERIFICATION EXAMPLE FOR SIT MODEL IMPLEMENTATION*

A.1.1. Problem Definition

This example verifies the specific ion interaction theory (SIT) model through code comparison of MIN3P-THCm (v1.0.690) and PHREEQC v3.1.1.8288 (Parkhurst and Appelo 2013).

A.1.2. Problem Set-Up

A 1D domain, 16.0 m in length, is discretized into 201 control volumes. The domain is homogeneous and fully saturated, and contains calcite, anhydrite and halite. The initial hydraulic head is 0.0 m across the domain. The hydraulic heads at the inflow and outflow boundaries are held constant at 1.4 m and 0.0 m, respectively. Initially, the column contains highly saline water (see IC for aqueous component concentrations in Table A- 1). With the infiltration of fresh water (chemical composition according to Bea et al. 2011) from the left side of the domain (x= 0.0 m), the composition of the pore water in the column changes over time. The geochemical system includes 8 components and primary species (Ca^{2+}, Na^{+}, Mg^{2+}, K^{+}, Cl^{-}, SO_4^{2-}, H^{+} and CO_3^{2-}), forming 16 secondary species. The initial composition (IC) of pore water and the abundance of minerals and organic matter in the domain, as well as the composition of fresh water (BC), are provided in Table A- 1.

Table A- 1: Initial and Boundary Conditions (IC and BC), and Initial Mineral Abundances for the Verification Example SIT

Parameter	**IC[1]**	**BC (inflow)[2]**	**Unit**
Aqueous component concentration			
Ca^{2+}	2.40×10^{-1}	2.10×10^{-4}	[mol L^{-1} H_2O]
Na^{+}	4.63	4.63×10^{-3}	[mol L^{-1} H_2O]
Mg^{2+}	1.40×10^{-1}	3.99×10^{-6}	[mol L^{-1} H_2O]
K^{+}	6.65×10^{-2}	1.84×10^{-3}	[mol L^{-1} H_2O]
Cl^{-}	5.44	4.63×10^{-3}	[mol L^{-1} H_2O]
SO_4^{2-}	6.25×10^{-3}	1.04×10^{-15}	[mol L^{-1} H_2O]
pH	5.95	7.0	[-]
CO_3^{2-}	1.27×10^{-3}	2.73×10^{-3}	[mol L^{-1} H_2O]
Mineral volume fraction			
Mineral	**IC**		**Unit**
Calcite	0.10		[m^3 m^{-3}]
Anhydrite	0.32		[m^3 m^{-3}]
Halite	0.30		[m^3 m^{-3}]

[1] From Hobbs et al. (2011), Table A-5, Sample ID: SF-3; [2] Bea et al. (2011); mineral volume fractions are assumed data

A.1.3. Problem Parameters

The physical parameters for the homogeneous porous medium are: a porosity of 0.25; a hydraulic conductivity of 1.0×10^{-3} m s^{-1}, and a dispersivity of 0.01 m. The free water diffusion coefficients of all components are set at 1.0×10^{-9} m^2 s^{-1}.

The geochemical thermodynamic database is based on the ThermoChimie-TDB Version 9b0 including SIT parameters (Giffaut et al. 2014; Blanc et al. 2015). Some of the ion interaction coefficients between species are derived from sit.dat coming with PHREEQC (Parkhurst and Appelo 2013). The sit.dat database is used in this study for PHREEQC (Parkhurst and Appelo 2013) simulations.

Table A- 2: Ion Interaction Coefficients Used for the Verification Example SIT (from sit.dat, PHREEQC, Parkhurst and Appelo 2013)

Species 1	Species 2	Coefficient
Ca^{2+}	Cl^-	0.14
Na^+	Cl^-	0.03
Na^+	SO_4^{2-}	-0.12
Na^+	CO_3^{2-}	-0.08
Na^+	HSO_4^-	-0.01
Na^+	OH^-	0.04
Mg^{2+}	Cl^-	0.19
Cl^-	H^+	0.12

A.1.4. Results

Simulated results for total concentrations are depicted in Figure A- 1 and Figure A- 2. Figure A-1 shows comparisons of the longitudinal profiles of pH, the main component concentrations, as well as the saturation indexes of calcite, anhydrite and halite at five hours. With the infiltration of fresh water into the domain initially filled with highly saline pore water, the concentrations of all components except CO_3^{2-} decrease from the left-hand side. The increase of carbonate is due to the dissolution of calcite. After about 13 hours, the fresh water reaches the right-hand boundary as shown in the breakthrough curves (Figure A- 2). After that, the concentrations of all components except carbonate drop significantly. The results simulated by PHREEQC and MIN3P-THCm are identical, which verifies the implementation of the SIT model in MIN3P-THCm.

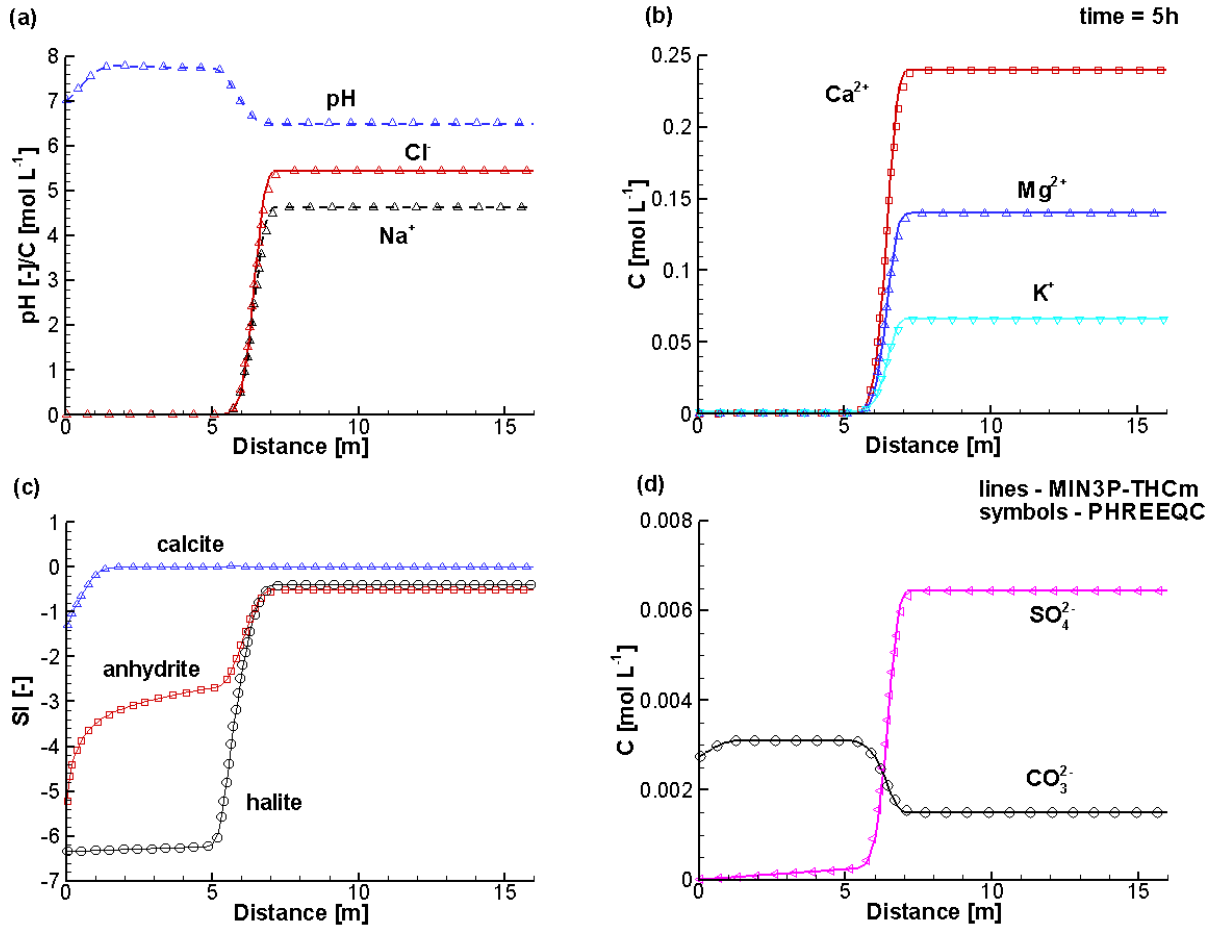

Figure A- 1: Comparison of Profiles at 5 Hours as Simulated by MIN3P-THCm (Lines) and PHREEQC (Symbols), (a) pH and Concentrations of Cl^- and Na^+, (b) Concentrations of Ca^{2+}, Mg^{2+} and K^+, (c) SI of Calcite, Anhydrite and Halite, and (d) Concentrations of SO_4^{2-} and CO_3^{2-}

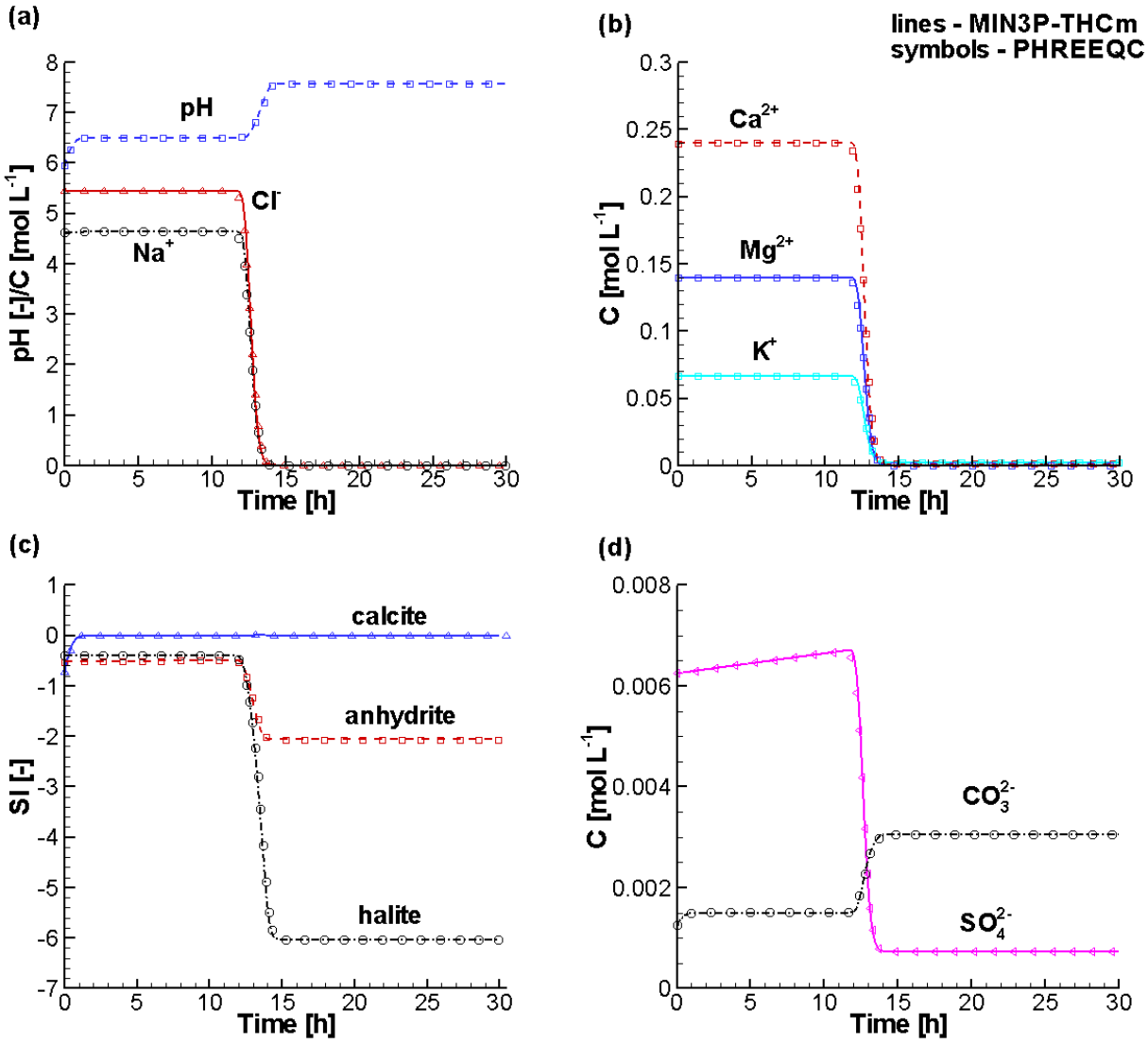

Figure A- 2: Comparison of Breakthrough Curves at 16 m as Simulated by MIN3P-THCm (Lines) and PHREEQC (Symbols), (a) pH and Concentrations of Cl^- and Na^+, (b) Concentrations of Ca^{2+}, Mg^{2+} and K^+, (c) SI of Calcite, Anhydrite and Halite, and (d) Concentrations of SO_4^{2-} and CO_3^{2-}

A.2 *THERMODYNAMIC MODELLING OF LHHPC HYDRATION*

The optimized LHHPC mix design is shown in Table A- 3 (NWMO, email communication). The main components of the concrete are: 1. Cementitious substances: Portland cement and silica fume (a pozzolanic silica) in the weight ratio 50:50; 2. Fine aggregate: silica flour (ground quartz sand); 3. Coarse aggregate: crushed granite, 4. Superplasticizer and water. Cement hydration reactions occur in a short time period following mixing of the LHHPC ingredients. As the focus of the current work are the long-term interactions across the interfaces between different materials, for simplicity, it is assumed that the LHHPC consists of thermodynamically stable phases that exist after cement hydration. These phases were calculated using the thermodynamic simulator

GEM-Selecktor v.3 (Kulik et al. 2013) together with the geochemical database for cement CEMDATA14 (Lothenbach et al. 2008).

In the hydration calculation, only Portland cement, silica fume and water were considered to be reactive, while the other ingredients were assumed to be inert. Chemical compositions of the Portland cement (St. Mary's cement) and the silica fume are listed in Table A- 4. Silica fume has a high SiO_2 content (94%) and large surface area. The simulated results show that when the Portland cement is mixed with silica fume and fresh water in a weight ratio of 1:1:1, the CSH (calcium silicate hydrate) phases form a solid solution CSHQ (Kulik 2011), which consists of four end members: CSH-TobH in 98.0%, CSH-TobD in 1.9%, CSH-JenH in 0.1% and CSH-JenD in 1.6×10^{-4}%. The former two end members totaling 99.9% of the CSH phases are tobermorite-like phases (Wilson et al. 2012). In our simulations, the solid solution model is not considered. The CSH phases were instead represented by TobII-07Mat – a tobermorite-like phase (Wilson et al. 2012). Simulation results show that the main cementitious phases of the LHHPC after cement hydration were: TobII-07Mat in 76.7 vol% and SiO_2(am) in 13.54 vol%. SiO_2(am) is formed because of the excess amount of silica fume in the system (Table A- 5). Other minor minerals are OH-hydrotalcite (in abbreviation of hydrotalcite), gypsum, calcite, gibbsite and ferrihydrite.

Table A- 3: Optimized LHHPC Mix Design

Component	Amount by mass [kg m^{-3}]	Percentage [wt%]
Cement (Type GU from St. Mary's)	95.6	4.0%
Silica fume	95.6	4.0%
Silica flour	190.9	7.9%
Concrete sand	889.4	36.9%
Coarse aggregate	1035.7	42.9%
Superplasticizer (Glenium, dry)	10.16	0.4%
Fresh water added	95.6 (for SSD* aggregate)	4.0%
Water-to-cementitious materials ratio	0.50	-

SSD* – Saturated surface dry

Table A- 4: Chemical Compositions (in wt%) of the St. Mary's Cement and Silica Fume

Component	St. Mary's Cement	Silica Fume
SiO_2	19.5	93.60
Fe_2O_3	2.92	0.32
Al_2O_3	4.8	0.28
CaO	62.9	0.77
Free CaO	1.2	-
MgO	3.0	0.24
SO_3	3.38	-
K_2O	0.53	0.44
Na_2O	0.25	0.17
TiO_2	0.23	0.01
Loss of ignition	2.5	-
Insoluble Residue	0.09	-
Total alkali as Na_2O	0.60	-
Calculated compounds		
C_2S (Belite, $2CaO \bullet SiO_2$)	14	-
C_3S (Alite, $3CaO \bullet SiO_2$)	55	-
C_3A (Tricalcium aluminate, $3CaO \bullet Al_2O_3$)	8	-
C_4AF (Calcium aluminoferrite, $3CaO \bullet Al_2O_3 \bullet Fe_2O_3$)	9	-

Data from AMEC through NWMO (Project Number TB152037, Appendix B, 2015)

Table A- 5: Mineral Volume Fractions of Hydrated Cementitious Materials in LHHPC Calculated Using GEMS-selector v.3

Minerals	Formula	Vol Fraction [vol%]
TobII-07Mat (Tobermorite-like)	$(CaO)_{0.8333}SiO_2)(H_2O)_{1.3333}$	76.72
OH-hydrotalcite (hydrotalcite)	$Mg_4Al_2(OH)_{14}{:}3H_2O$	3.19
Silica (am)	SiO_2	13.54
Gypsum	$CaSO_4{:}2H_2O$	2.23
Calcite	$CaCO_3$	1.20
Gibbsite	$Al(OH)_3$	1.94
Ferrihydrite	$Fe(OH)_3$	1.18

A.3 *CASE 1 – HB/LHHPC/GRANITE*

A.3.1. Case1CP and Case 1UP

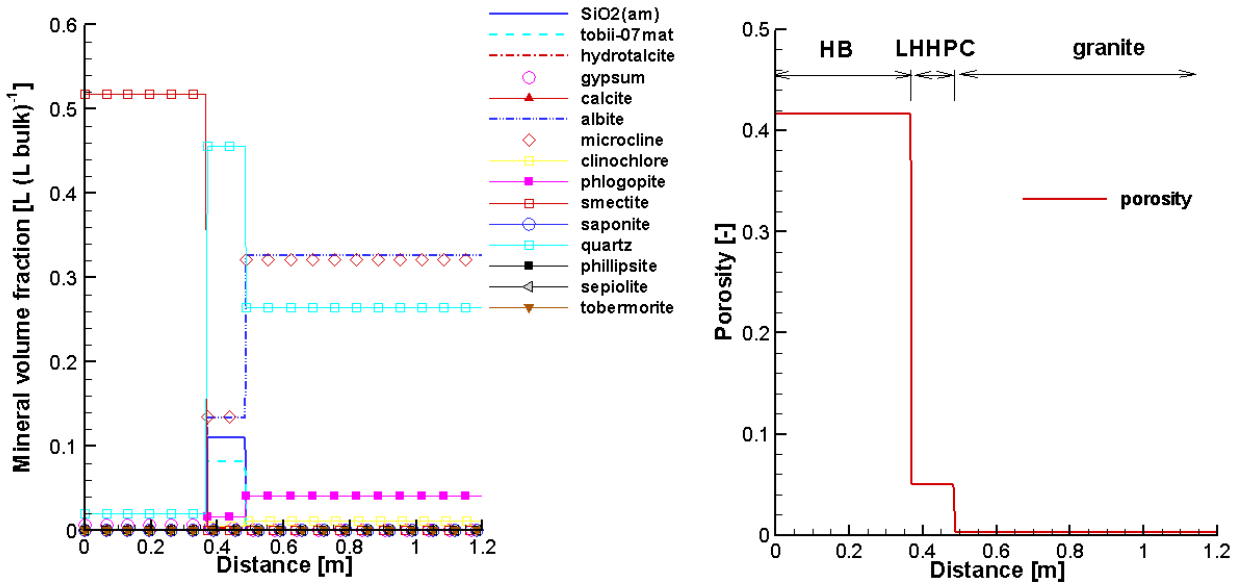

Figure A- 3: Profiles of Initial Volume Fractions of Minerals (Left) and Porosity (Right) (the Same for Case 1CP and Case 1UP)

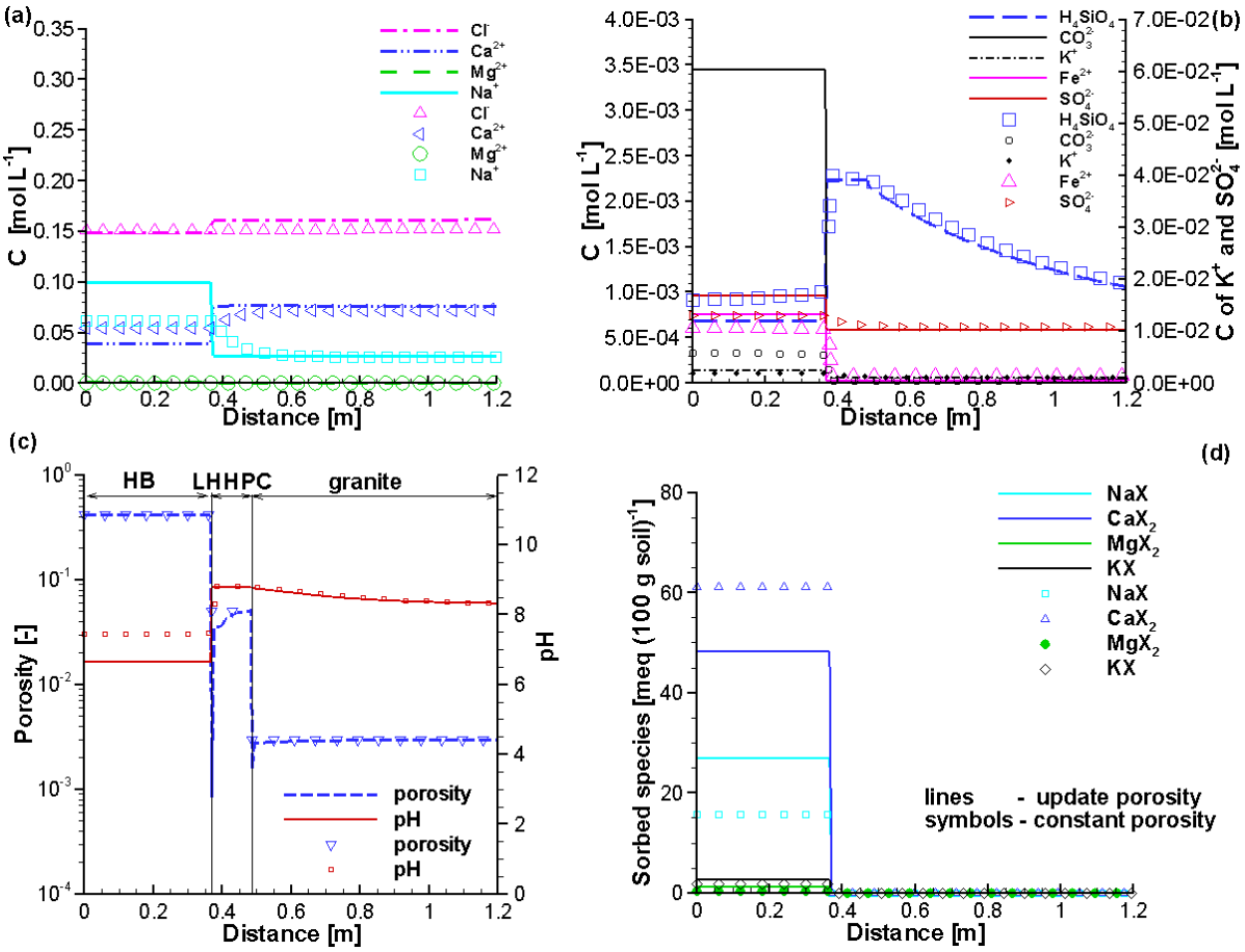

Figure A- 4: Profiles of Component Concentrations at 10,000 Years for Case 1CP (Symbols) and Case 1UP (Lines)

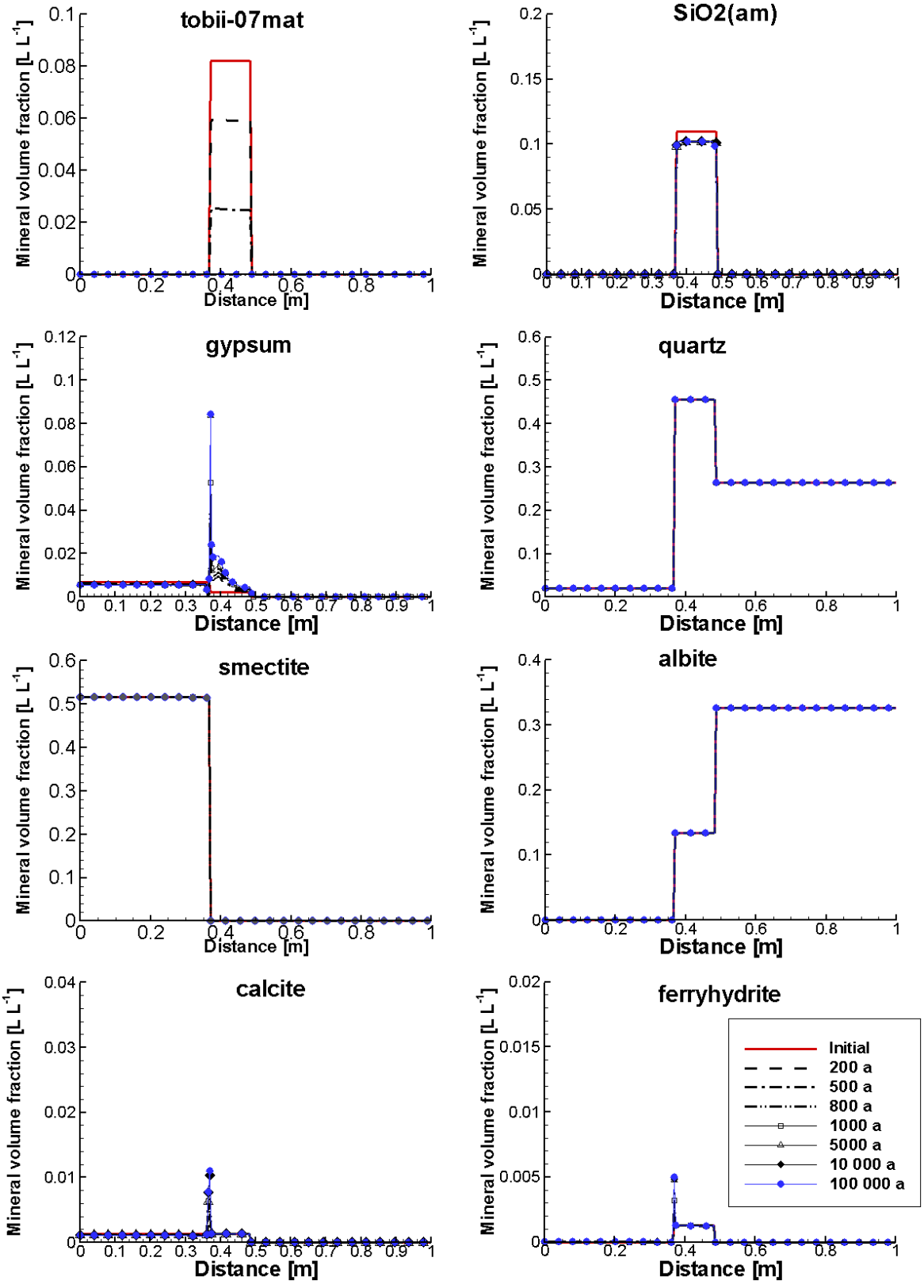

Figure A- 5: Profiles of Volume Fractions of Primary Minerals at Selected Times (Case 1UP)

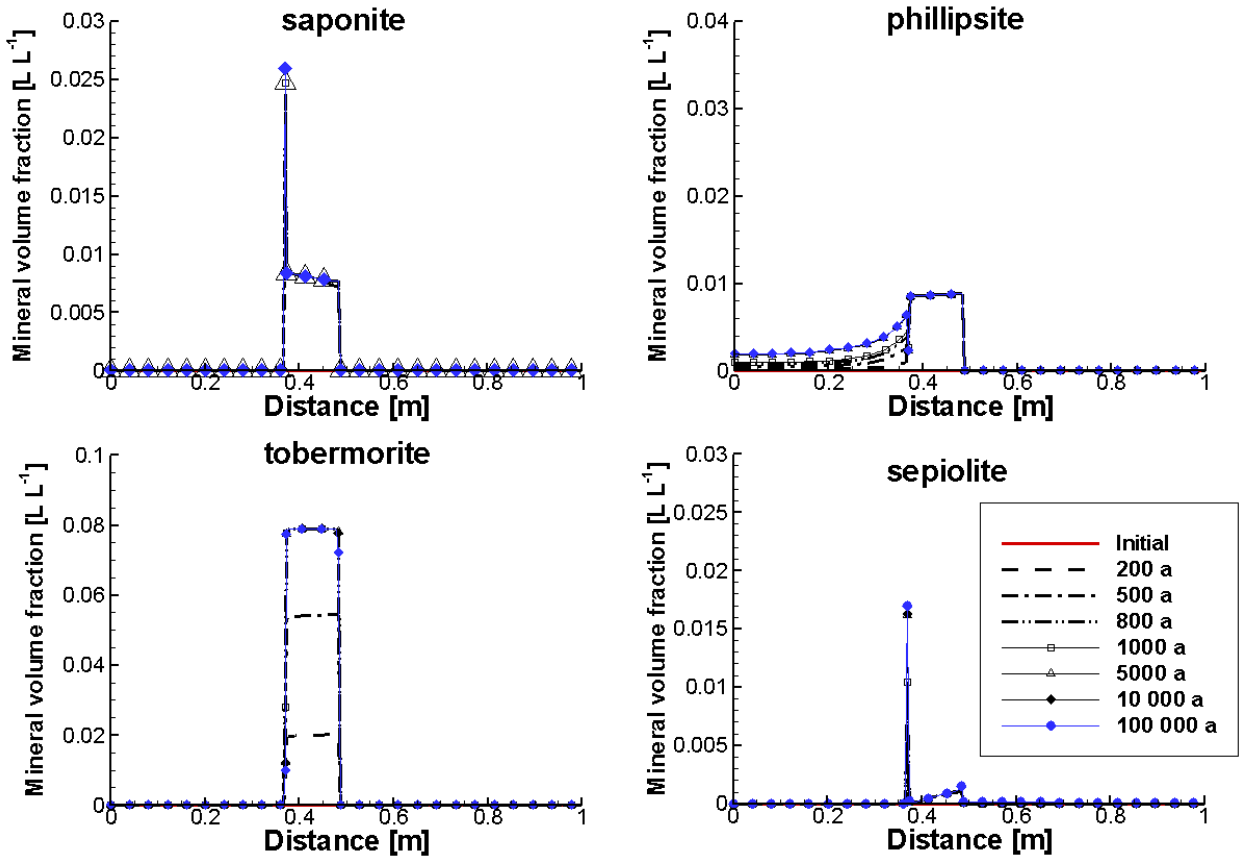

Figure A- 6: Profiles of Volume Fractions of Secondary Minerals at Selected Times (Case 1UP)

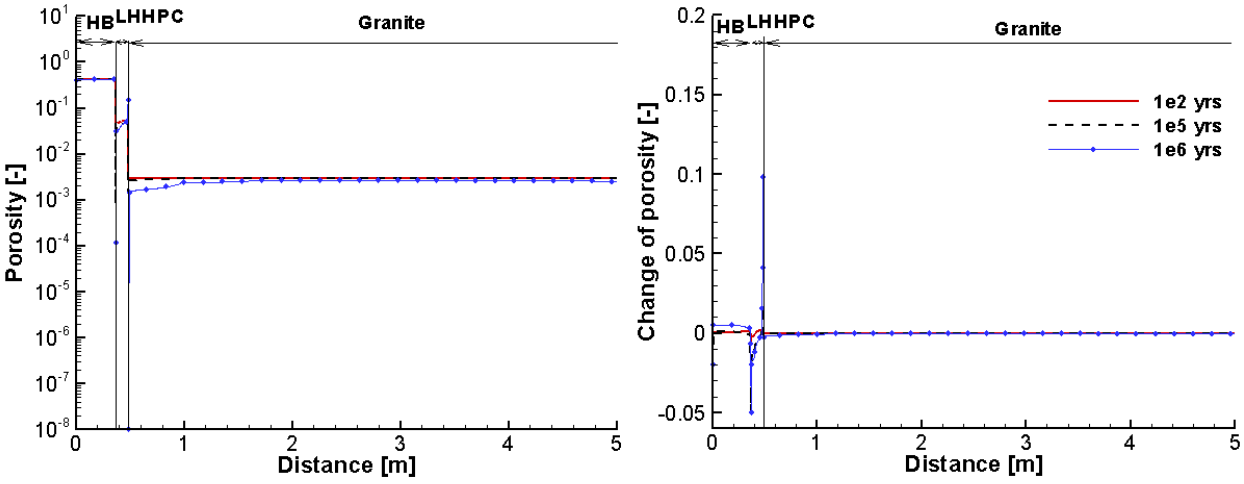

Figure A- 7: Profiles of Porosity (Left) and Porosity Change (Right) at Selected Times

A.3.2. Case 1EDZCP and Case 1EDZUP

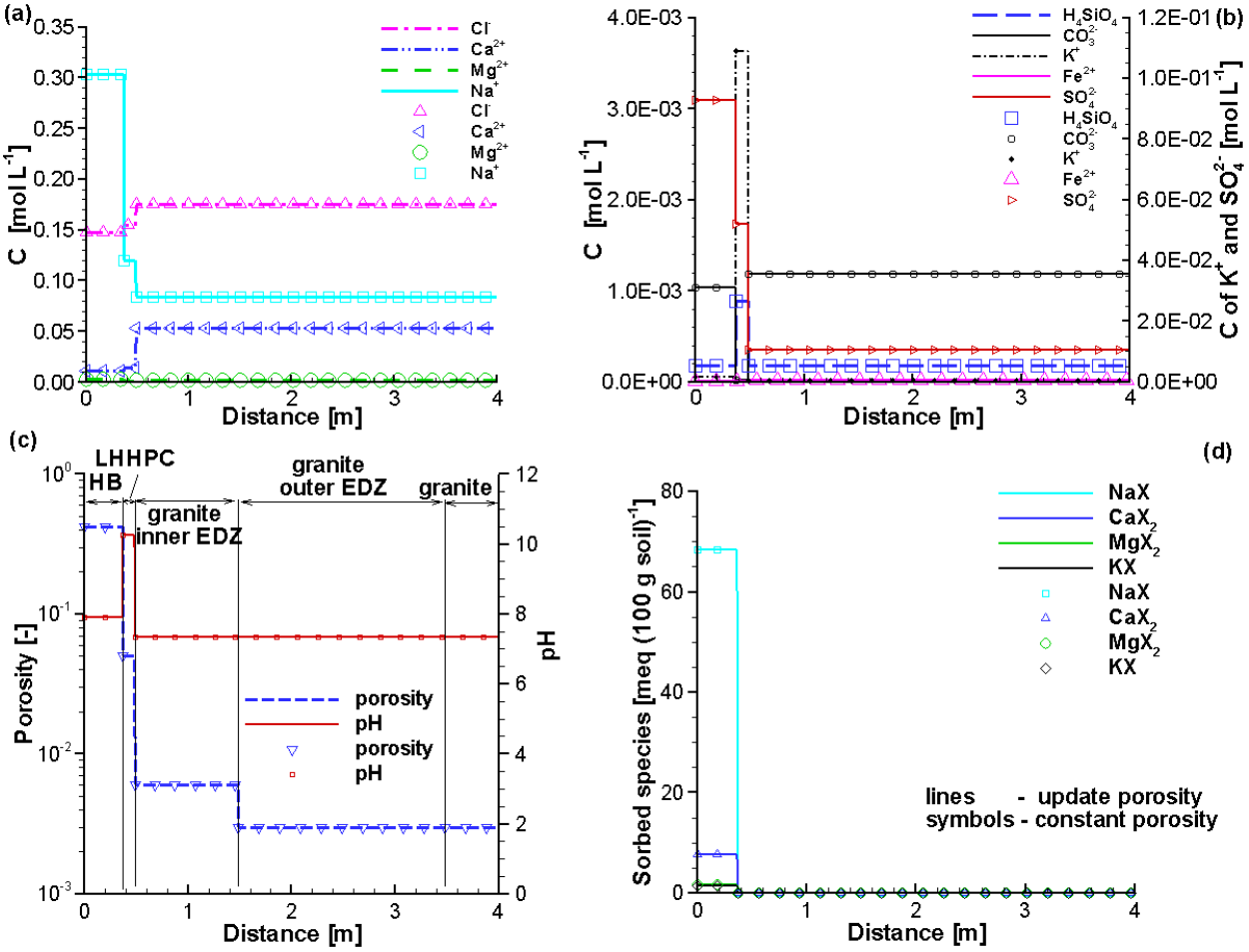

Figure A- 8: Profiles of Initial Component Concentrations for Case 1EDZCP (Symbols) and Case 1EDZUP (Lines)

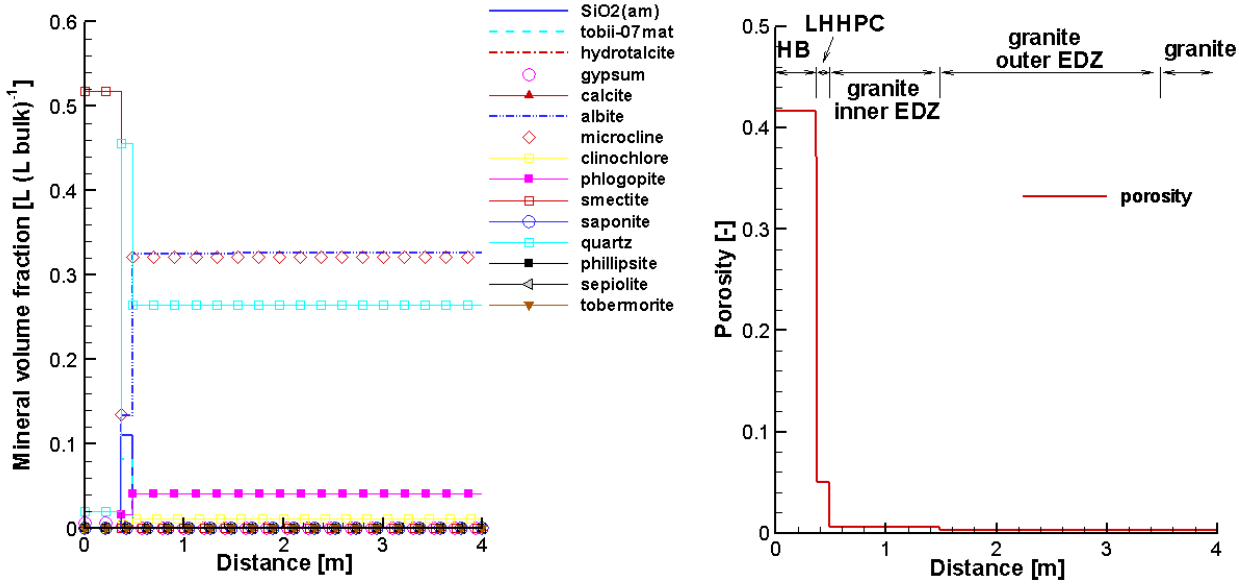

Figure A- 9: Profiles of Initial Volume Fractions of Minerals (Left) and Porosity (Right) (the Same for Case 1EDZCP and Case 1EDZUP)

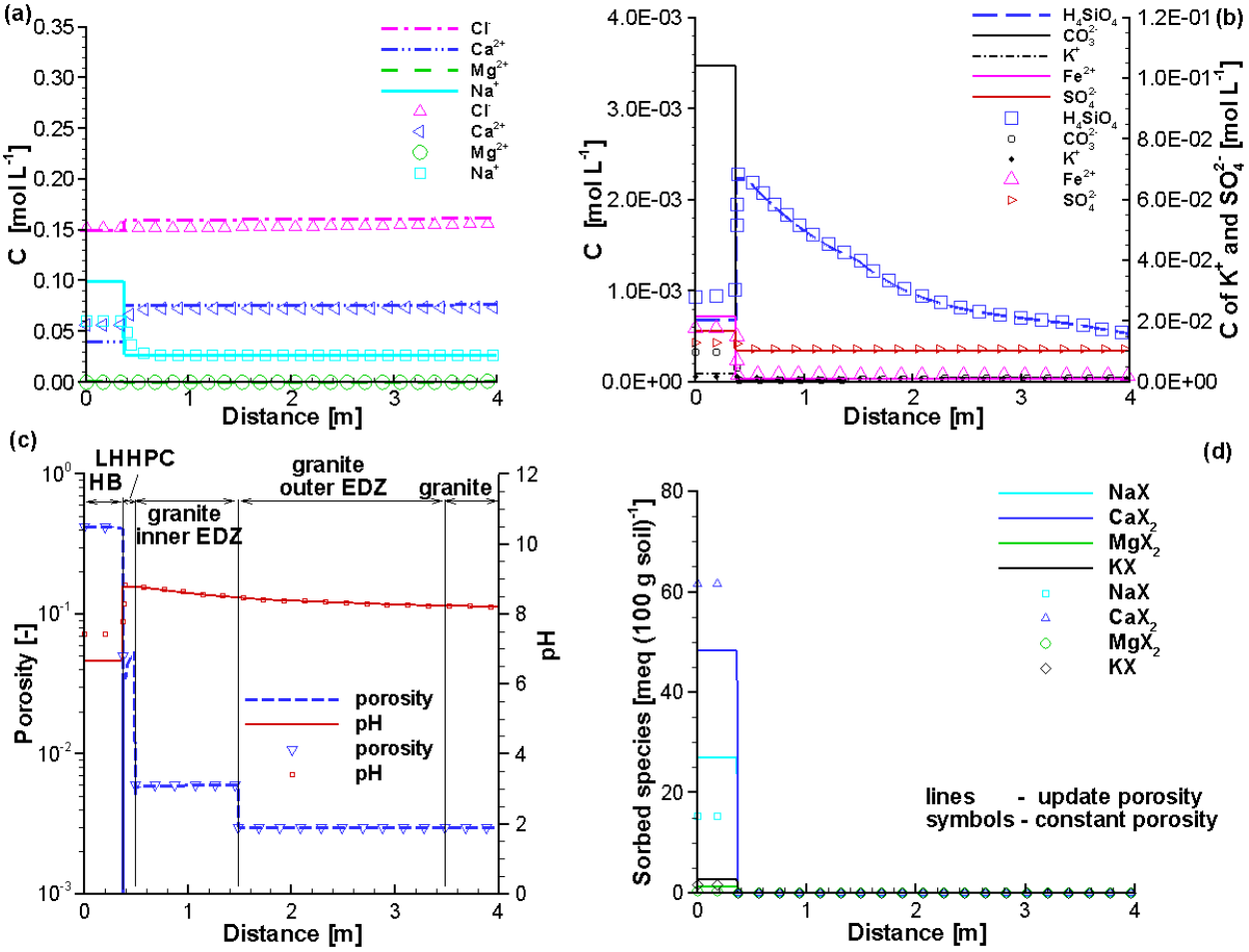

Figure A- 10: Profiles of Component Concentrations at 10,000 Years for Case 1EDZCP (Symbols) and Case 1EDZUP (Lines)

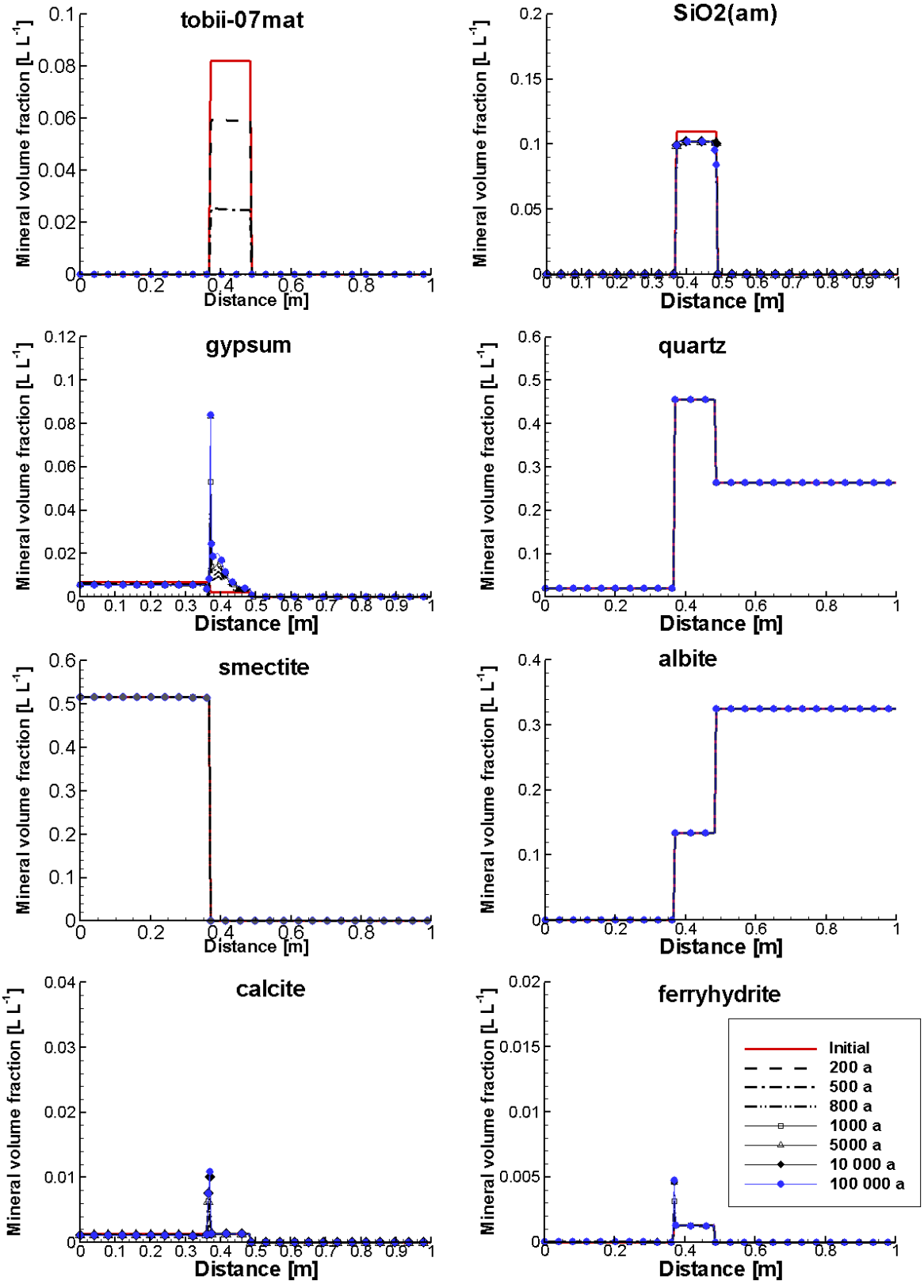

Figure A- 11: Profiles of Volume Fractions of Primary Minerals at Selected Times (Case 1EDZUP)

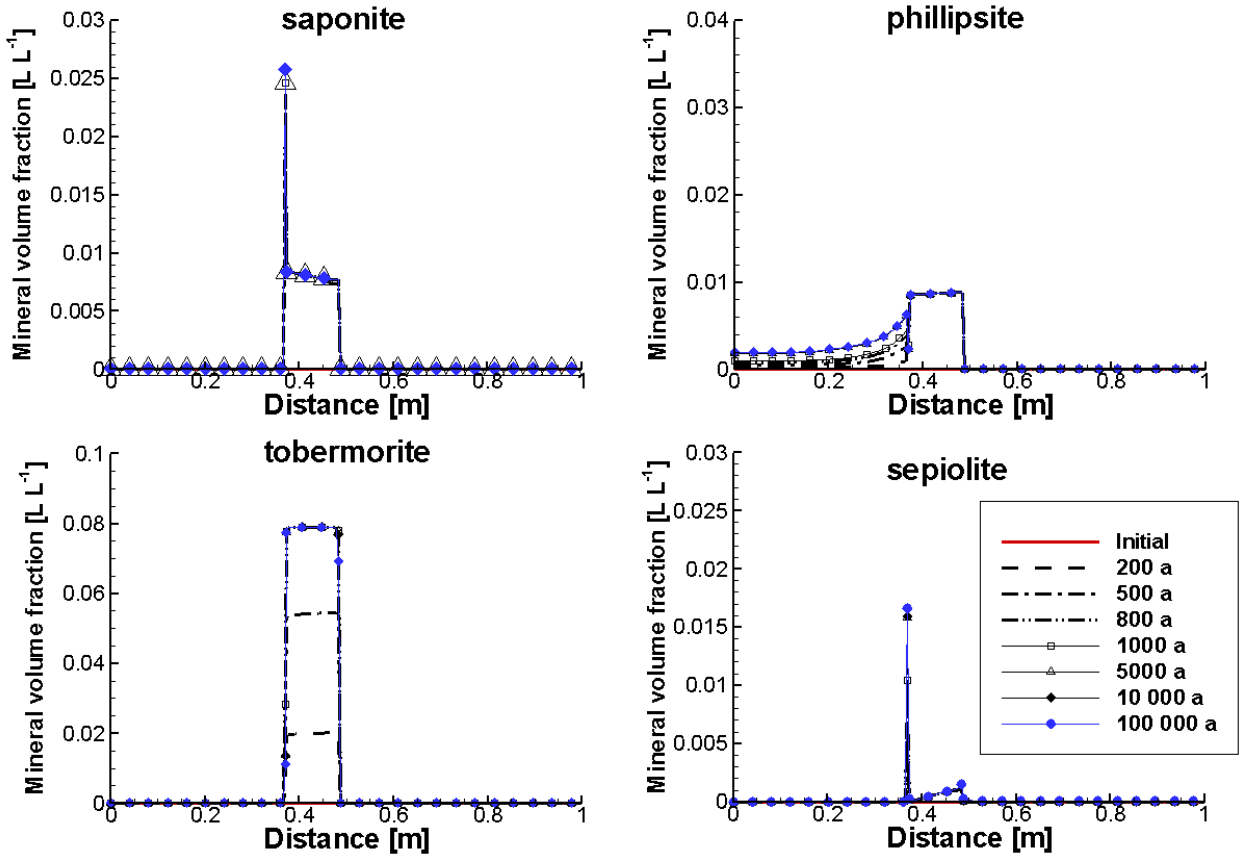

Figure A- 12: Profiles of Volume Fractions of Secondary Minerals at Selected Times (Case 1EDZUP)

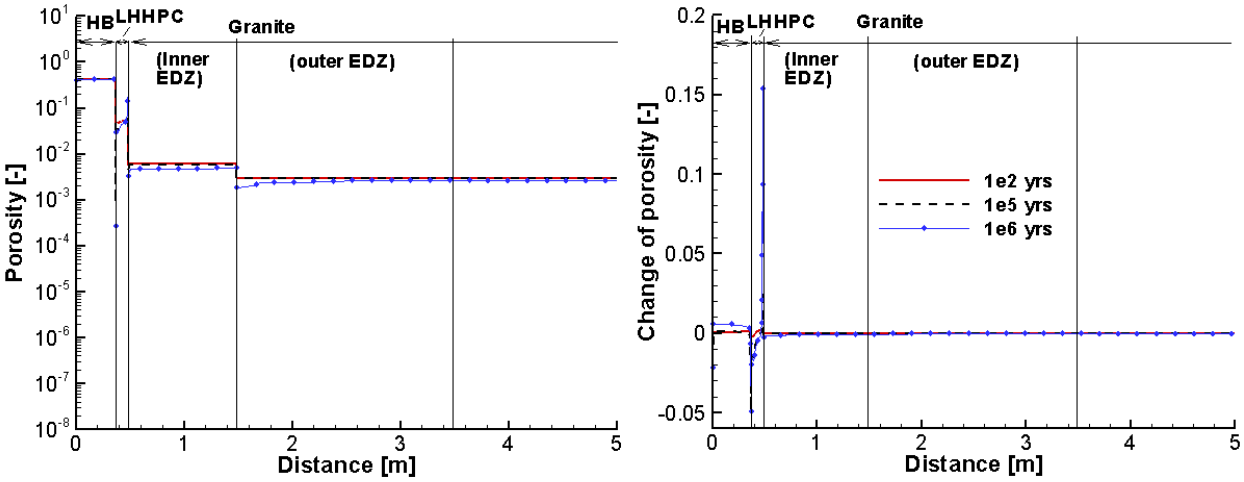

Figure A- 13: Profiles of Porosity (Left) and Porosity Change (Right) at Selected Times (Case 1EDZUP)

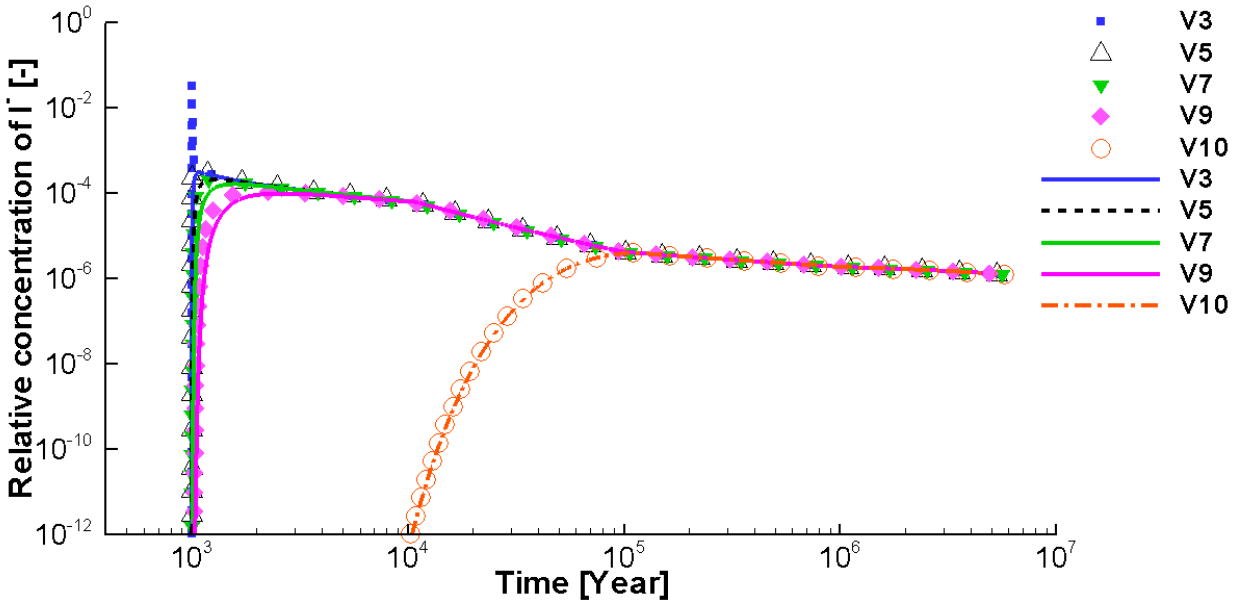

Figure A- 14: Comparison of Breakthrough Curves at Selected Observation Points for a Large Defect Occurring at 1,000 Years for Case 1EDZCP (Symbols) and Case 1EDZUP (Lines). V3 (LHHPC), V5 (inner EDZ), V7 (outer EDZ in Granite), V9 and V10 (Intact Granite)

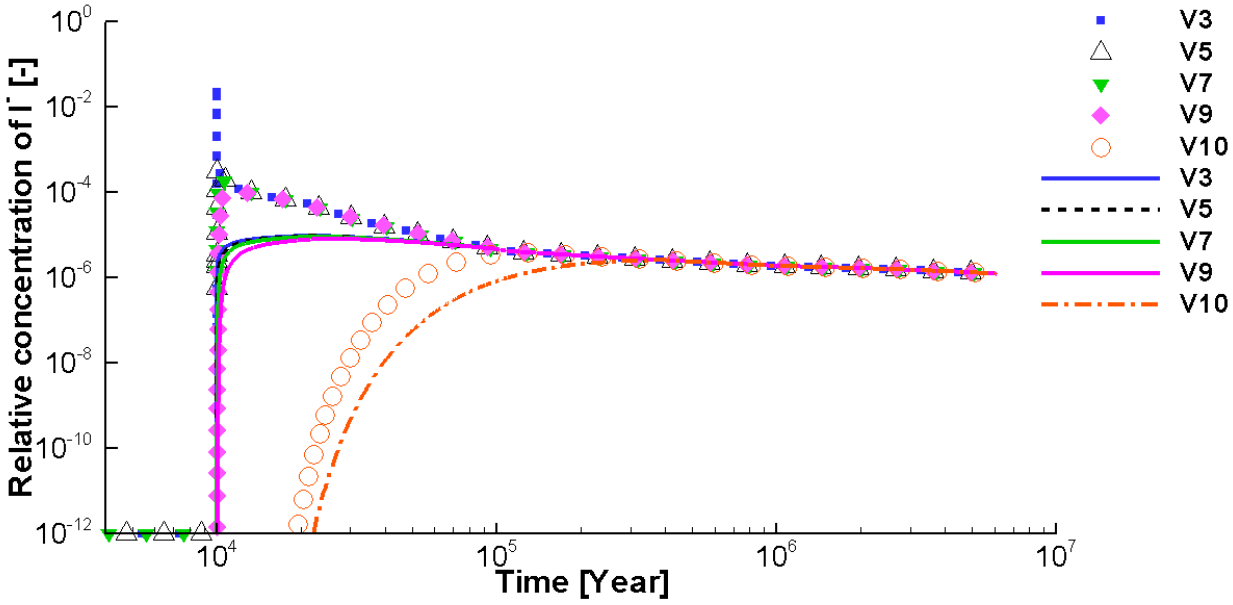

Figure A- 15: Comparison of Breakthrough Curves at Selected Observation Points for a Large Defect Occurring at 10,000 Years for Case 1EDZCP (Symbols) and Case 1EDZUP (Lines). V3 (LHHPC), V5 (inner EDZ), V7 (outer EDZ in Granite), V9 and V10 (Intact Granite)

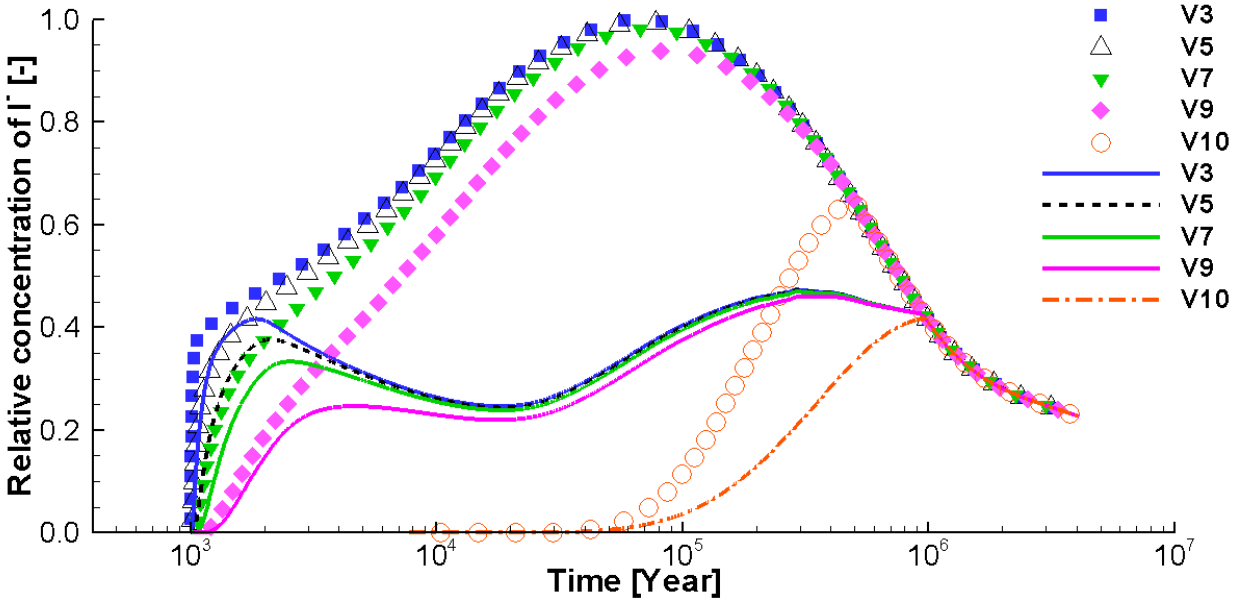

Figure A- 16: Comparison of Breakthrough Curves at Selected Observation Points for Canister Failure Scenario - Small Defect at 1,000 Years for Case 1EDZCP (Symbols) and Case 1EDZUP (Lines). V3 (LHHPC), V5 (inner EDZ), V7 (outer EDZ in Granite), V9 and V10 (Intact Granite)

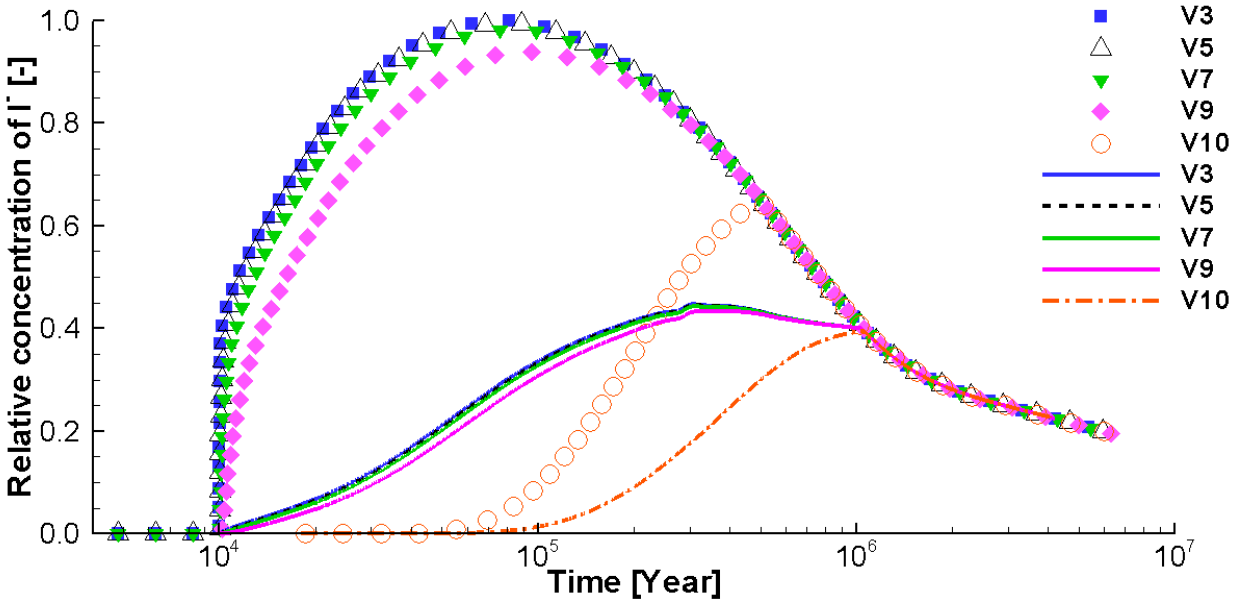

Figure A- 17: Comparison of Breakthrough Curves at Selected Observation Points for a Small Defect Occurring at 10,000 Years for Case 1EDZCP (Symbols) and Case 1EDZUP (Lines). V3 (LHHPC), V5 (inner EDZ), V7 (outer EDZ in L), V9 and V10 (Intact Granite)

Simulated concentration profiles of I^- are depicted in Figure A- 18 (small defect at 10,000 years), Figure A- 19 (large defect at 1,000 years), and Figure A- 20 (large defect at 10,000 years), respectively. EDZs, in general, enhance the mobility of radionuclides across the EDZs.

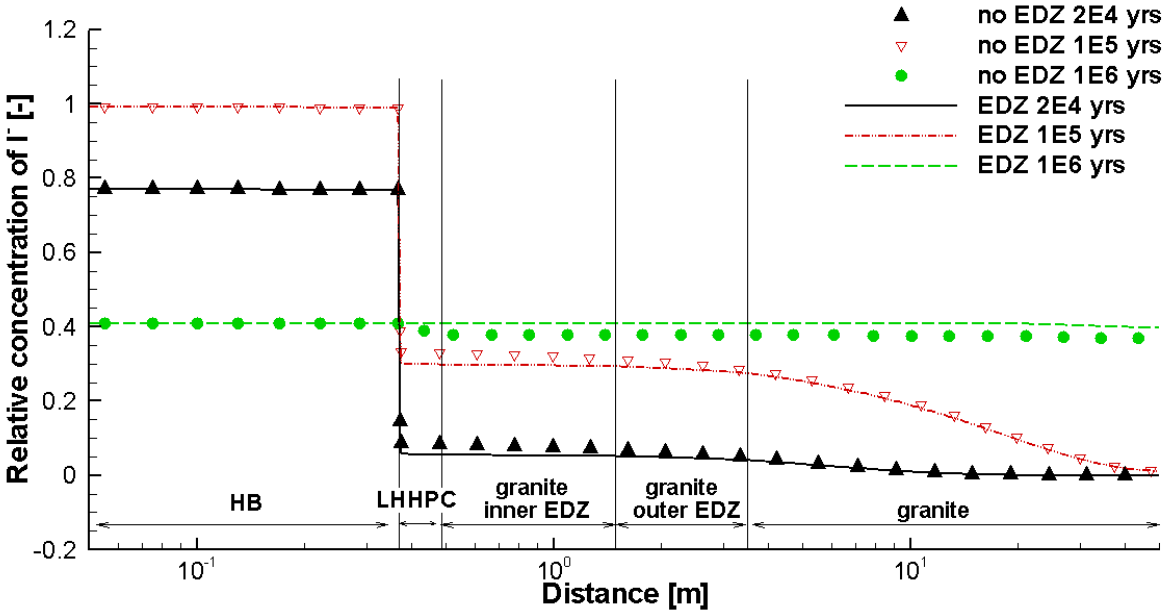

Figure A- 18: Concentration Profiles of I^- at Selected Times for a Small Defect Occurring at 10,000 Years for Case 1rUP (Symbols) and Case 1rEDZUP (Lines)

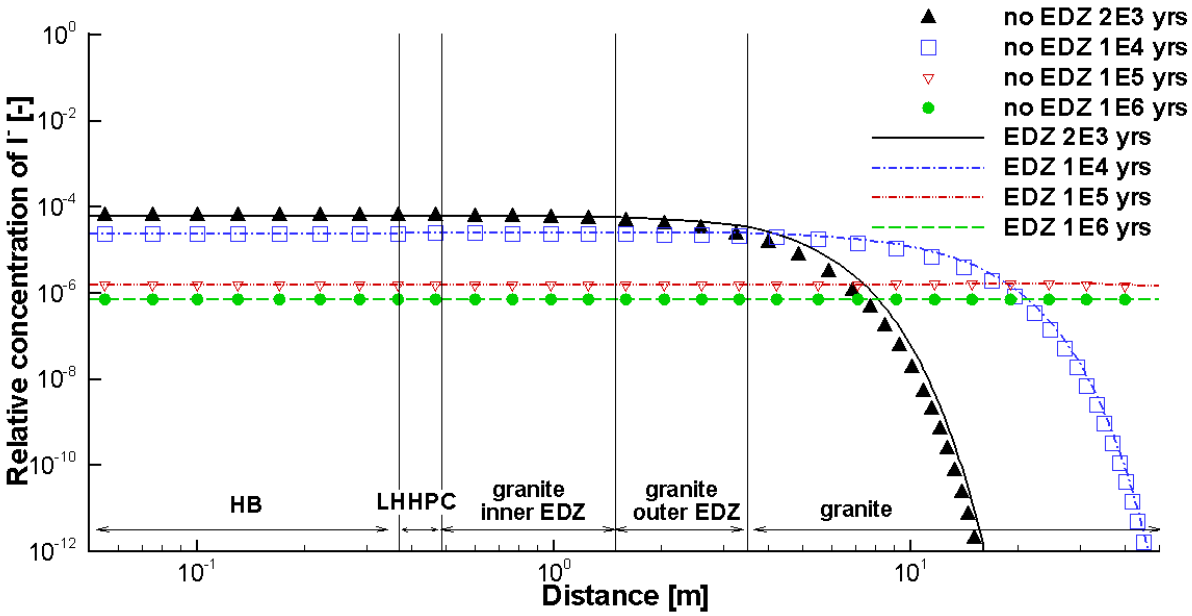

Figure A- 19: Concentration Profiles of I^- at Selected Times for a Large Defect Occurring at 1,000 Years for Case 1rUP (Symbols) and Case 1rEDZUP (Lines)

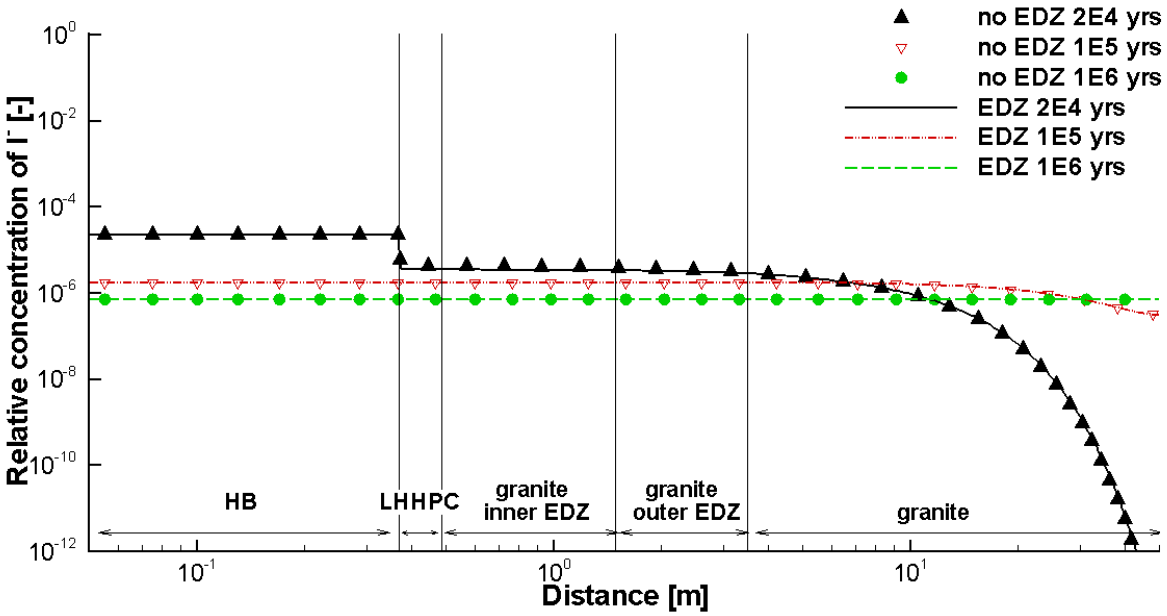

Figure A- 20: Concentration Profiles of I^- at Selected Times for a Large Defect Occurring at 10,000 Years for Case 1rUP (Symbols) and Case 1rEDZUP (Lines)

A.4 *CASE 2 – HB/GRANITE*

A.4.1. Case 2CP and Case 2UP

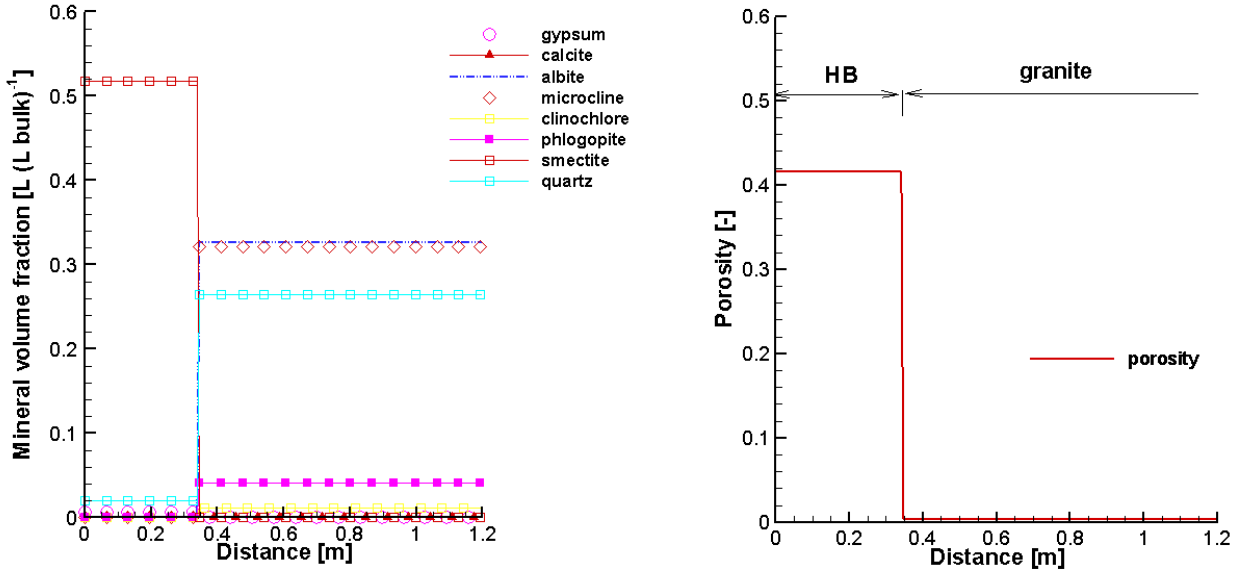

Figure A- 21: Profiles of Initial Volume Fractions of Minerals (Left) and Porosity (Right) (the Same for Case 2CP and Case 2UP)

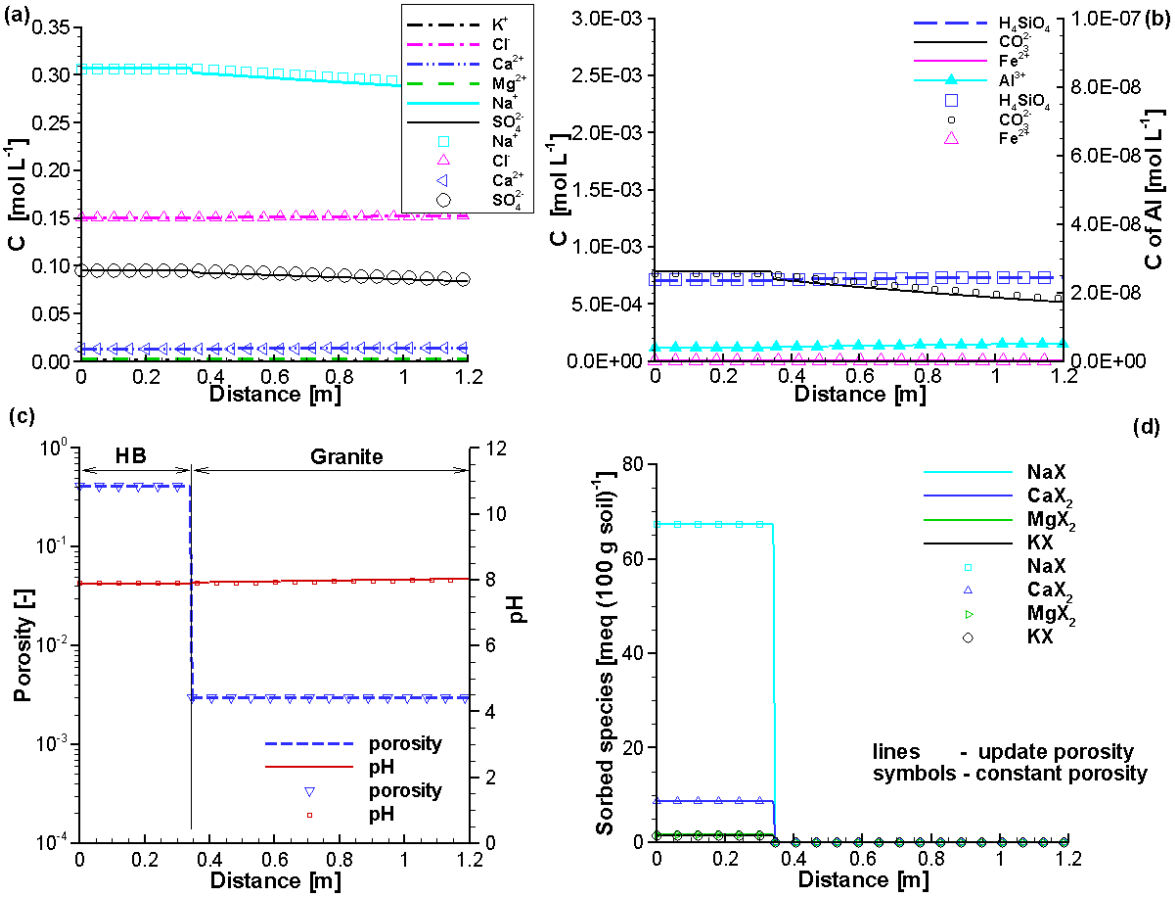

Figure A- 22: Profiles of Component Concentrations at 10,000 Years for Case 2CP (Symbols) and Case 2UP (Lines)

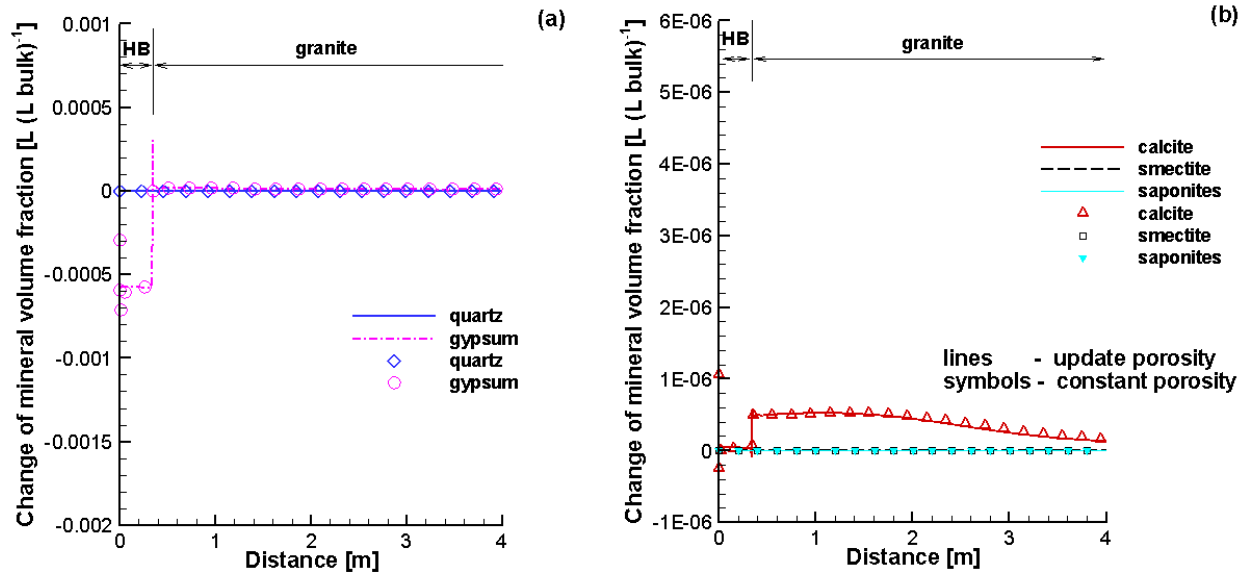

Figure A- 23: Comparison of Profiles of Mineral Volume Fraction Changes at 10,000 Years for Case 2CP (Symbols) and Case 2UP (Lines)

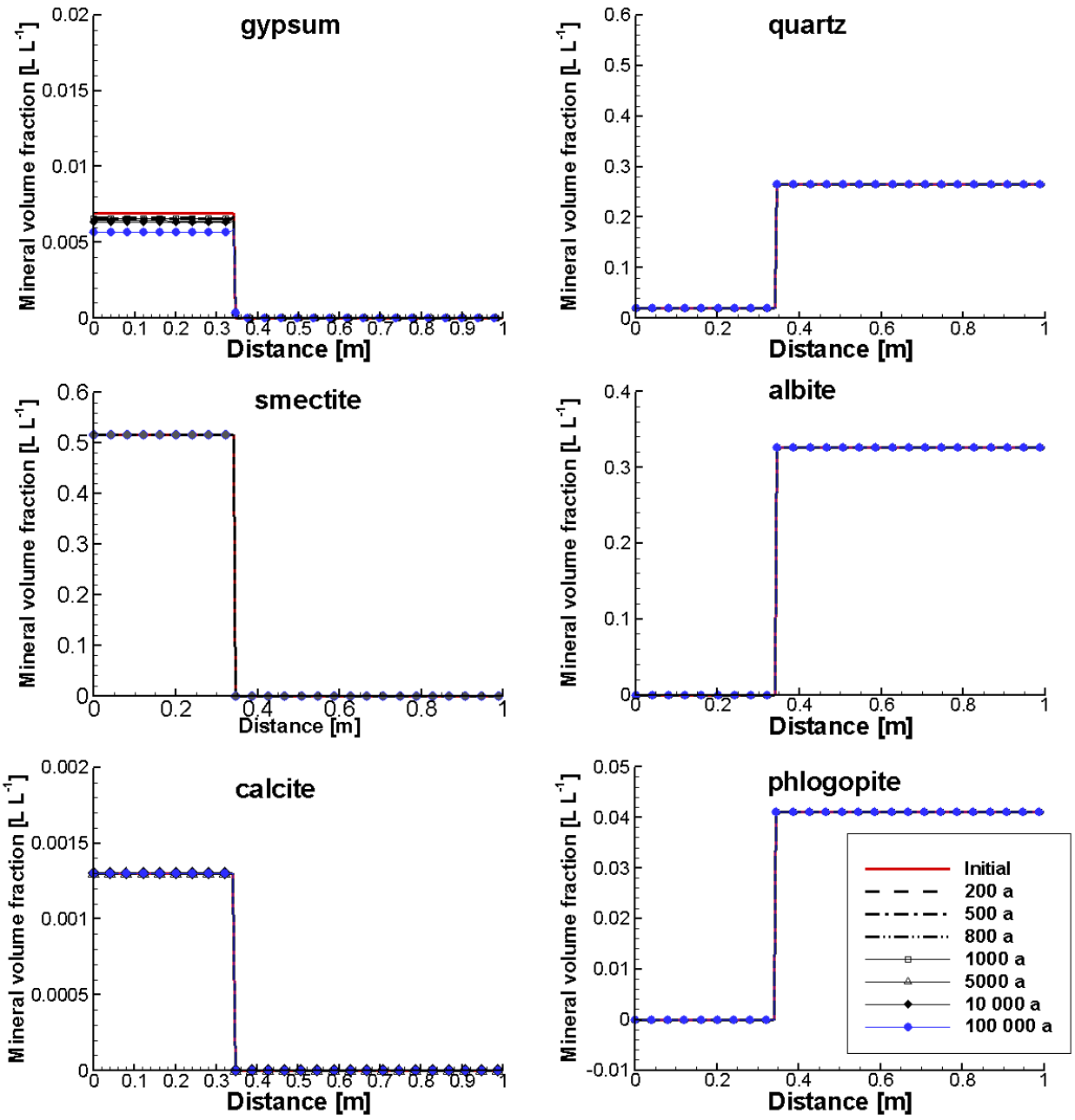

Figure A- 24: Profiles of Mineral Volume Fractions at Selected Times (Case 2UP)

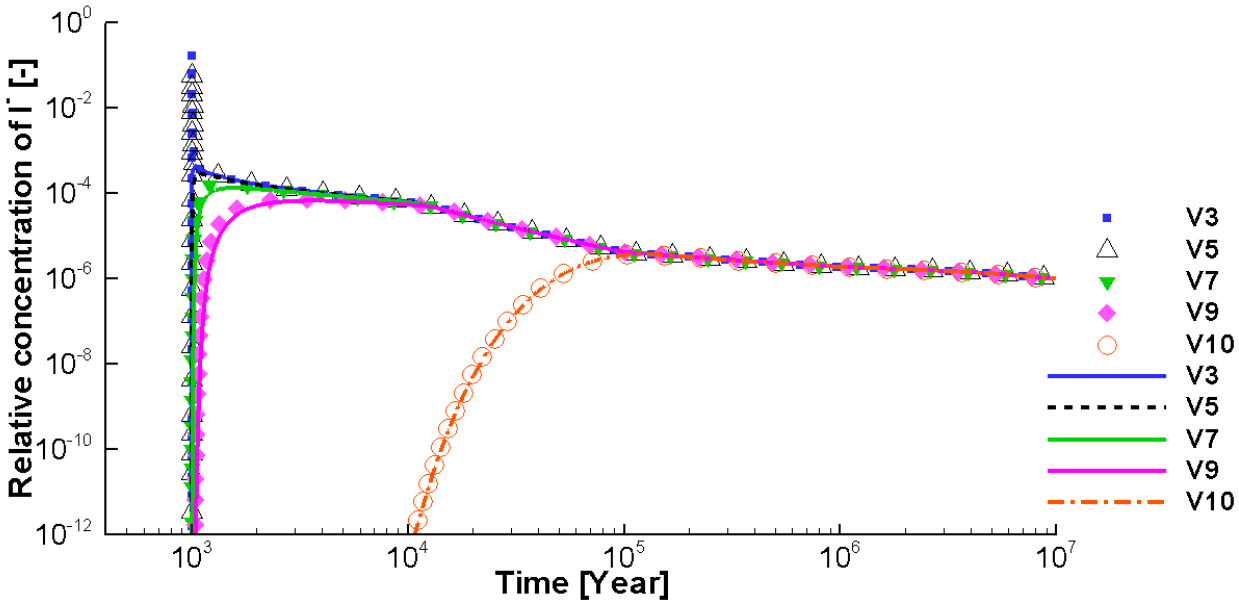

Figure A- 25: Comparison of Breakthrough Curves at Selected Observation Points for a Large Defect Occurring at 1,000 Years for Case 2rCP (Symbols) and Case 2rUP (Lines) . V3 (LHHPC), V5 to V10 (Granite)

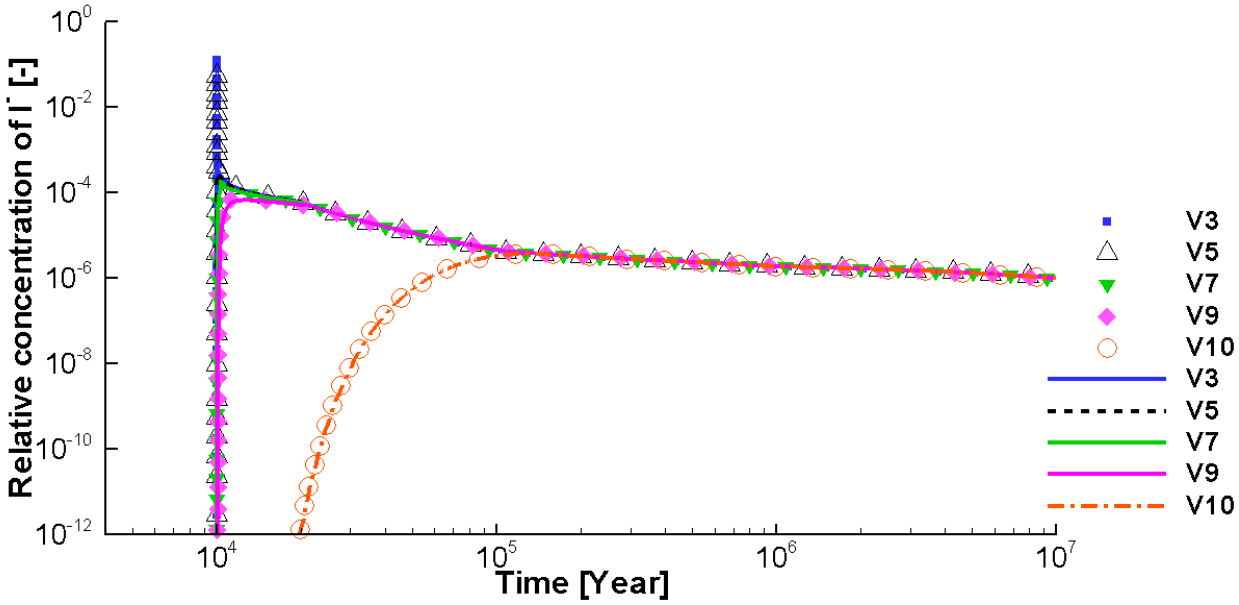

Figure A- 26: Comparison of Breakthrough Curves at Selected Observation Points for a Large Defect Occurring at 10,000 Years for Case 2rCP (Symbols) and Case 2rUP (Lines). V3 (LHHPC), V5 to V10 (Granite)

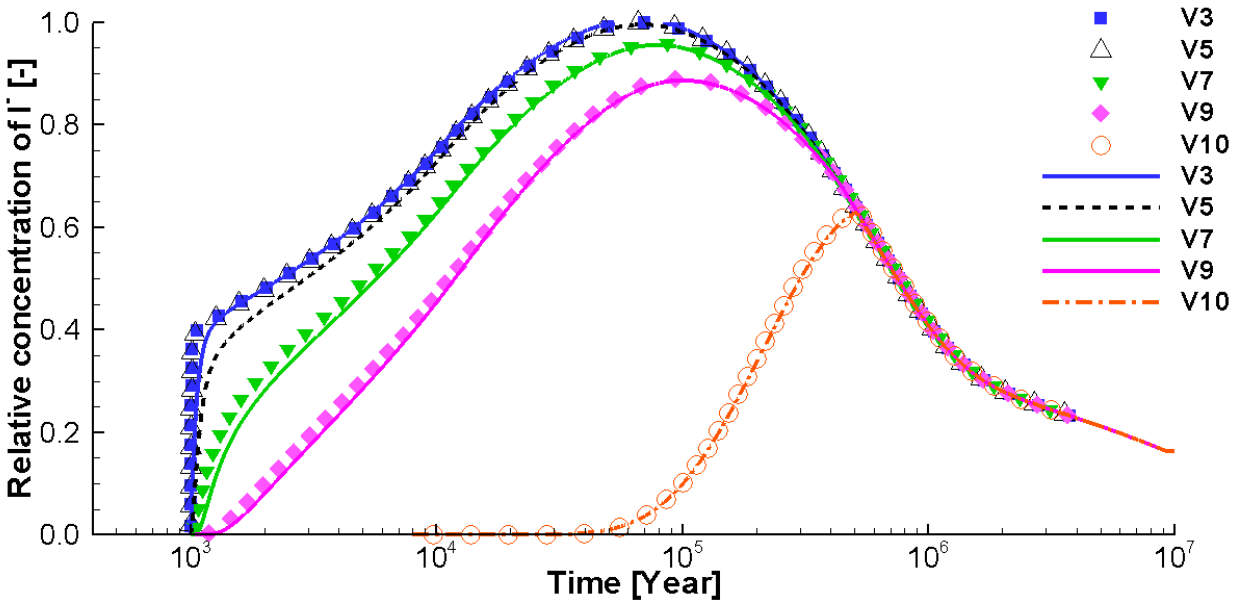

Figure A- 27: Comparison of Breakthrough Curves at Selected Observation Points for a Small Defect Occurring at 1,000 Years for Case 2rCP (Symbols) and Case 2rUP (Lines). V3 (LHHPC), V5 to V10 (Granite)

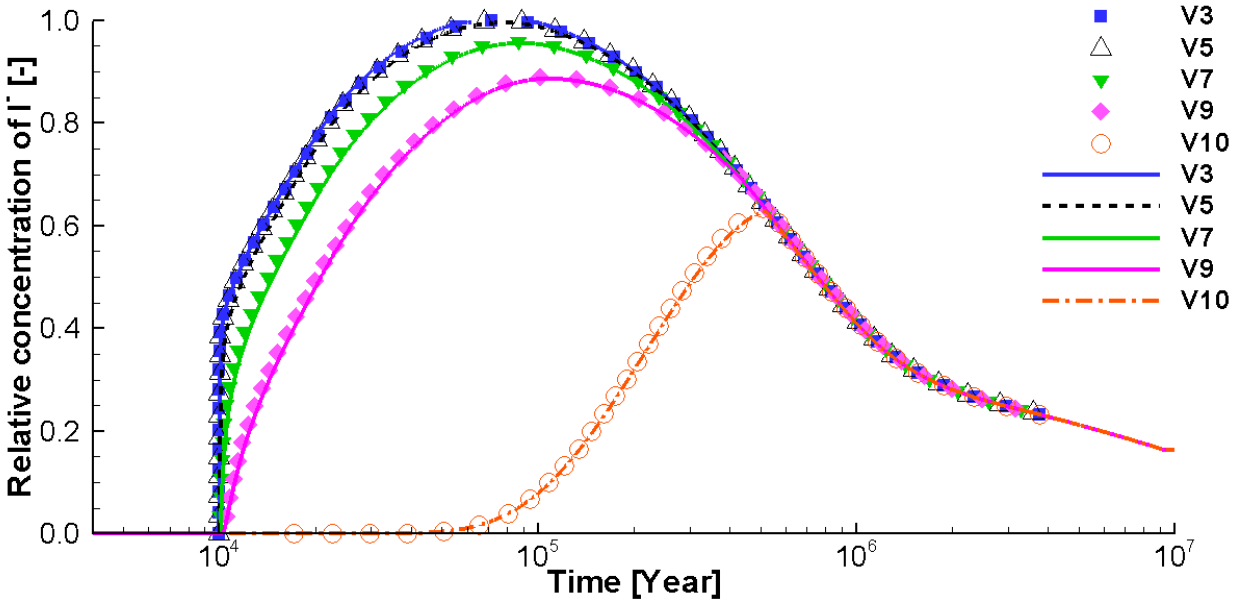

Figure A- 28: Comparison of Breakthrough Curves at Selected Observation Points for a Small Defect Occurring at 10,000 Years for Case 2rCP (Symbols) and Case 2rUP (Lines). V3 (LHHPC), V5 to V10 (Granite)

A.4.2. Case 2EDZCP and Case 2EDZUP

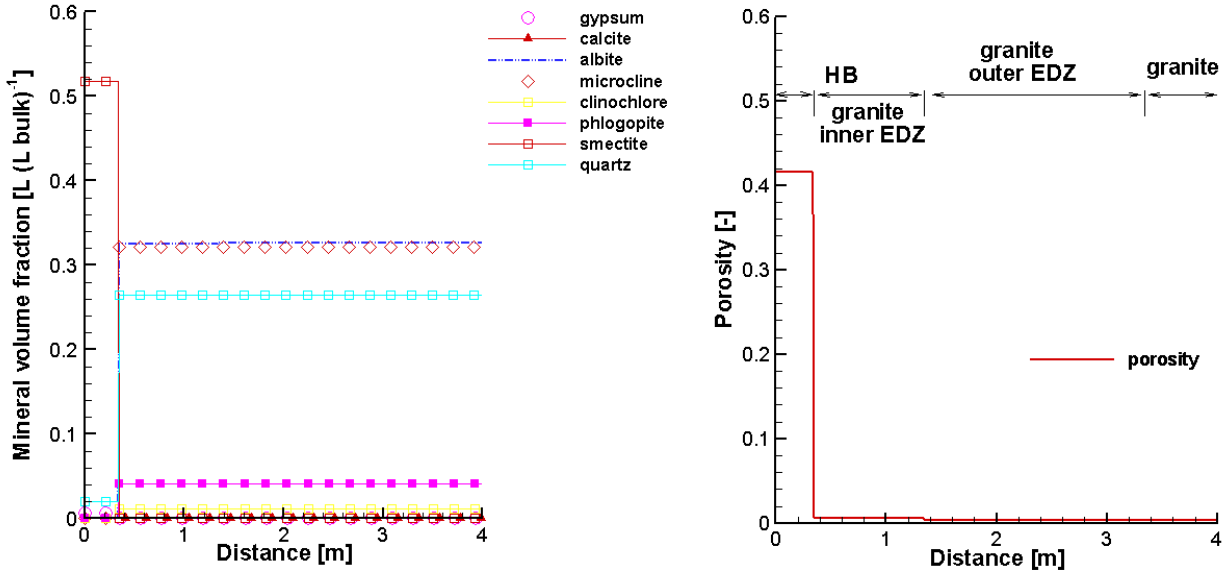

Figure A- 29: Profiles of Initial Volume Fractions of Minerals (Left) and Porosity (Right) (the Same for Case 2EDZCP and Case 2EDZUP)

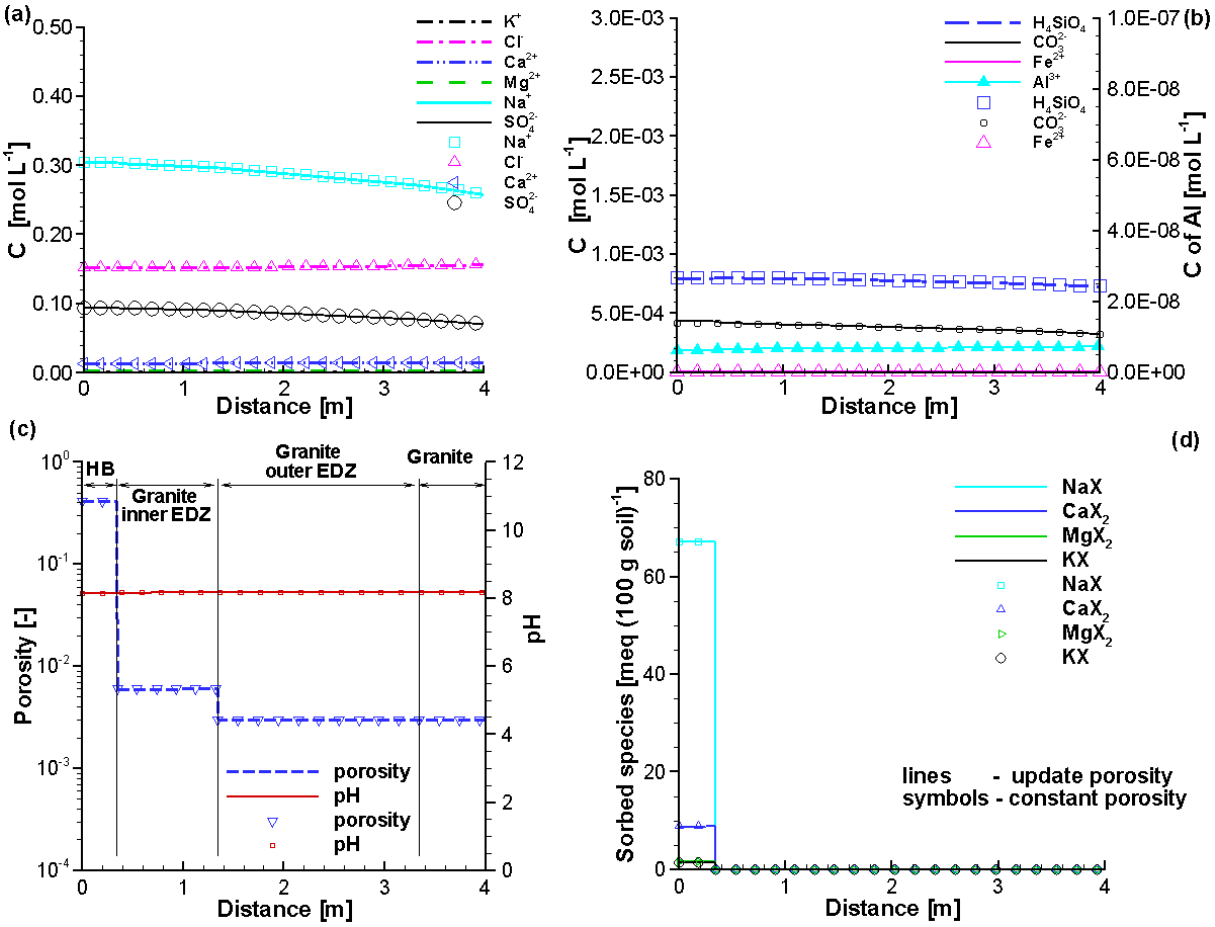

Figure A- 30: Profiles of Component Concentrations at 10,000 Years (Symbols – Case 2EDZCP, Lines – Case 2EDZUP)

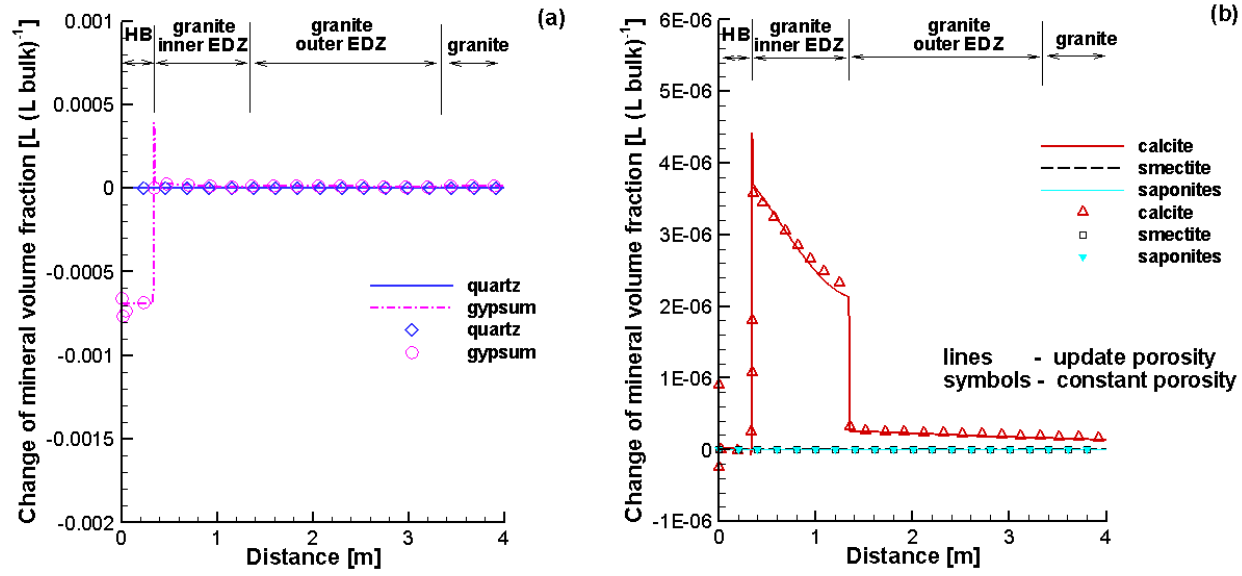

Figure A- 31: Comparison of Profiles of Mineral Volume Fraction Changes at 10,000 Years (Symbols – Case 2EDZCP, Lines – Case 2EDZUP)

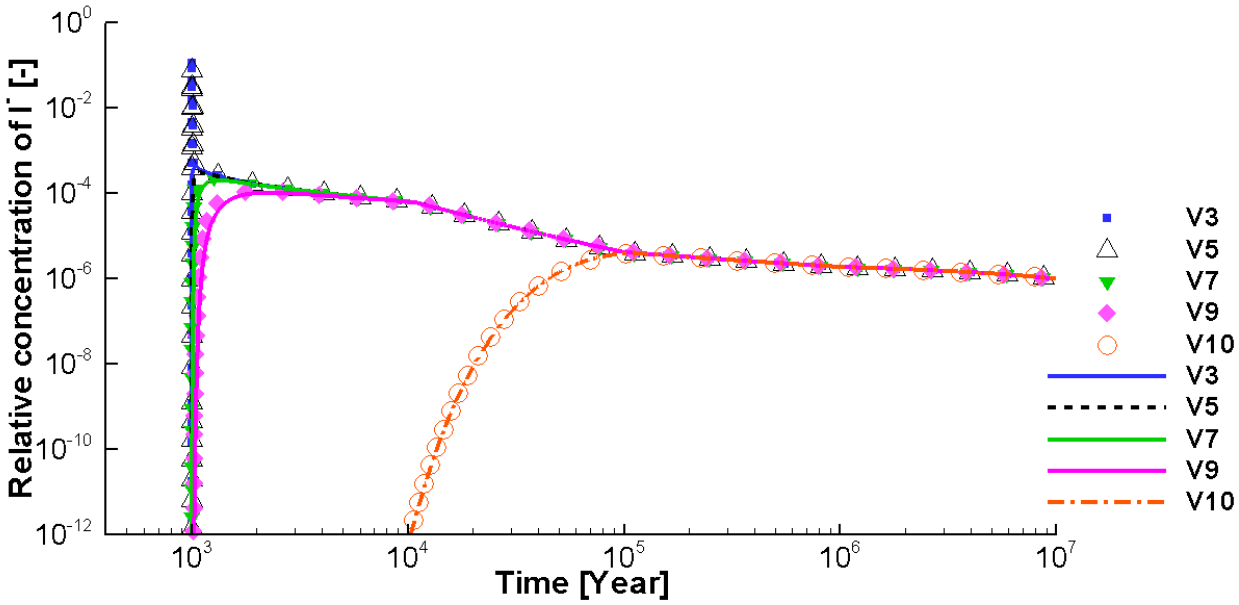

Figure A- 32: Comparison of Breakthrough Curves at Selected Observation Points for a Large Defect Occurring at 1,000 Years for Case 2rEDZCP (Symbols) and Case 2rEDZUP (Lines). V3 (HB), V5 (Inner EDZ), V7 (Outer EDZ), V9 and V10 (Intact Granite)

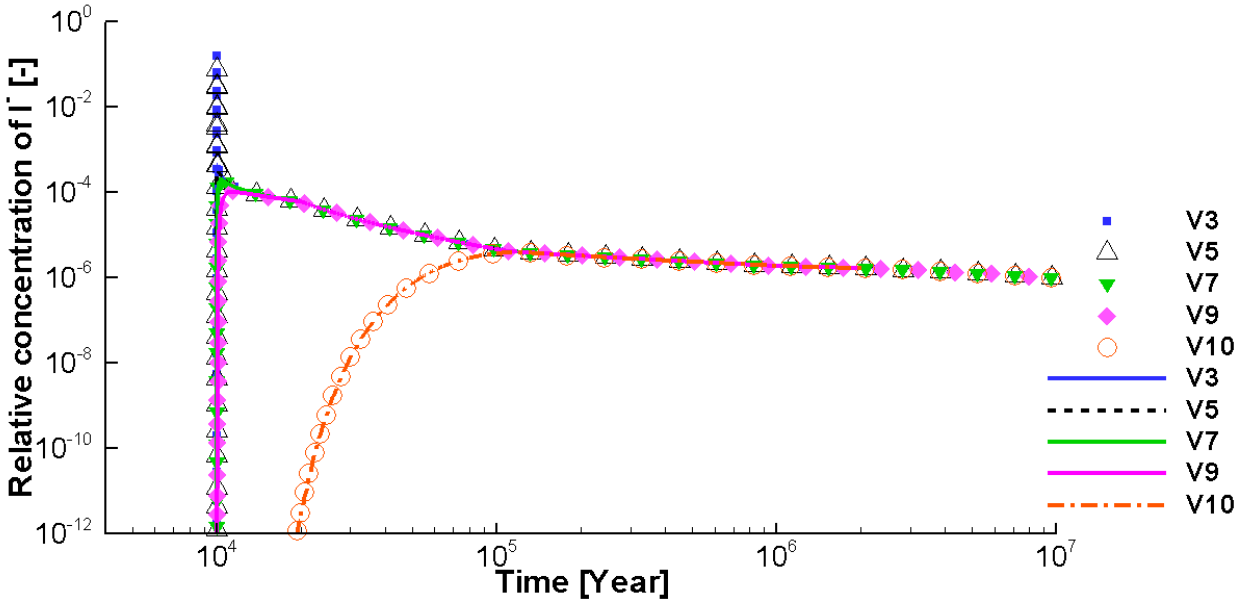

Figure A- 33: Comparison of Breakthrough Curves at Selected Observation Points for a Large Defect Occurring at 10,000 Years for Case 2rEDZCP (Symbols) and Case 2rEDZUP (Lines). V3 (HB), V5 (Inner EDZ), V7 (Outer EDZ), V9 and V10 (Intact Granite)

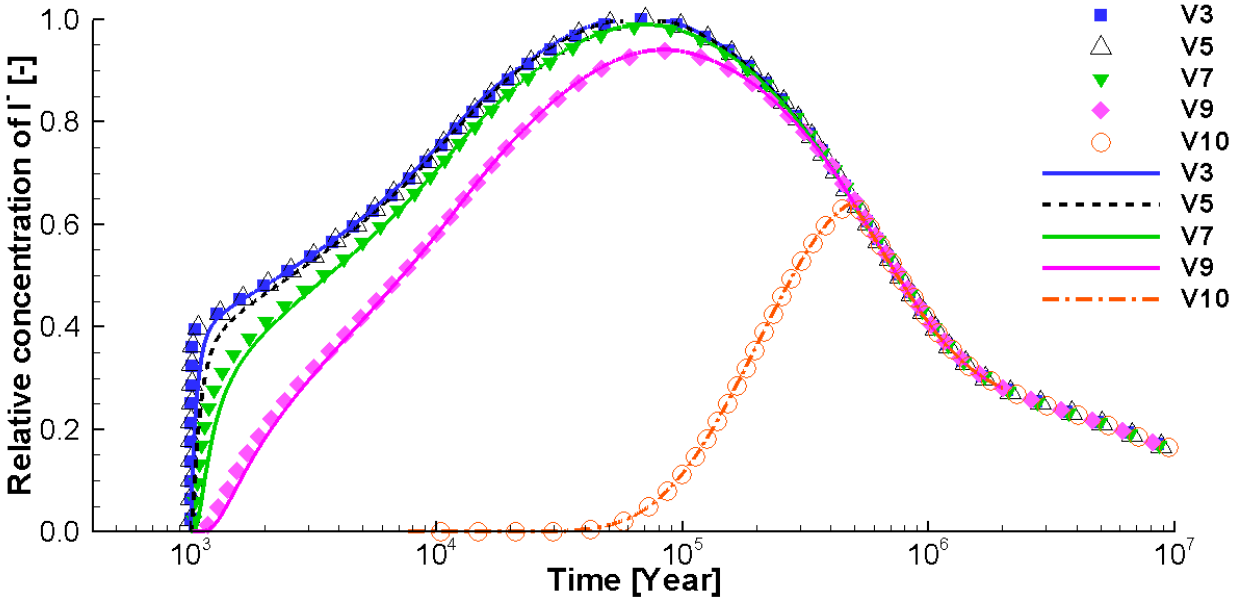

Figure A- 34: Comparison of Breakthrough Curves at Selected Observation Points for a Small Defect Occurring at 1,000 Years for Case 2rEDZCP (Symbols) and Case 2rEDZUP (Lines). V3 (HB), V5 (Inner EDZ), V7 (Outer EDZ), V9 and V10 (Intact Granite)

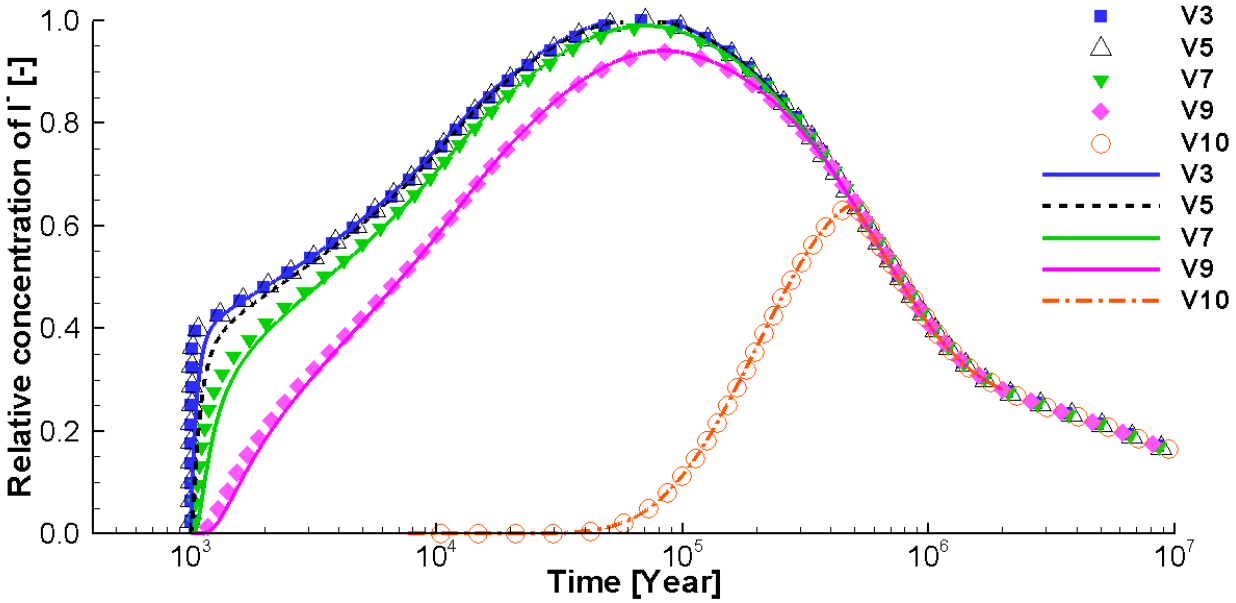

Figure A- 35: Comparison of Breakthrough Curves at Selected Observation Points for a Small Defect Occurring at 10,000 Years for Case 2rEDZCP (Symbols) and Case 2rEDZUP (Lines). V3 (HB), V5 (Inner EDZ), V7 (Outer EDZ), V9 and V10 (Intact Granite)

A.5 *CASE 3– HB/LHHPC/LIMESTONE*

A.5.1. Case 3CP and Case 3UP

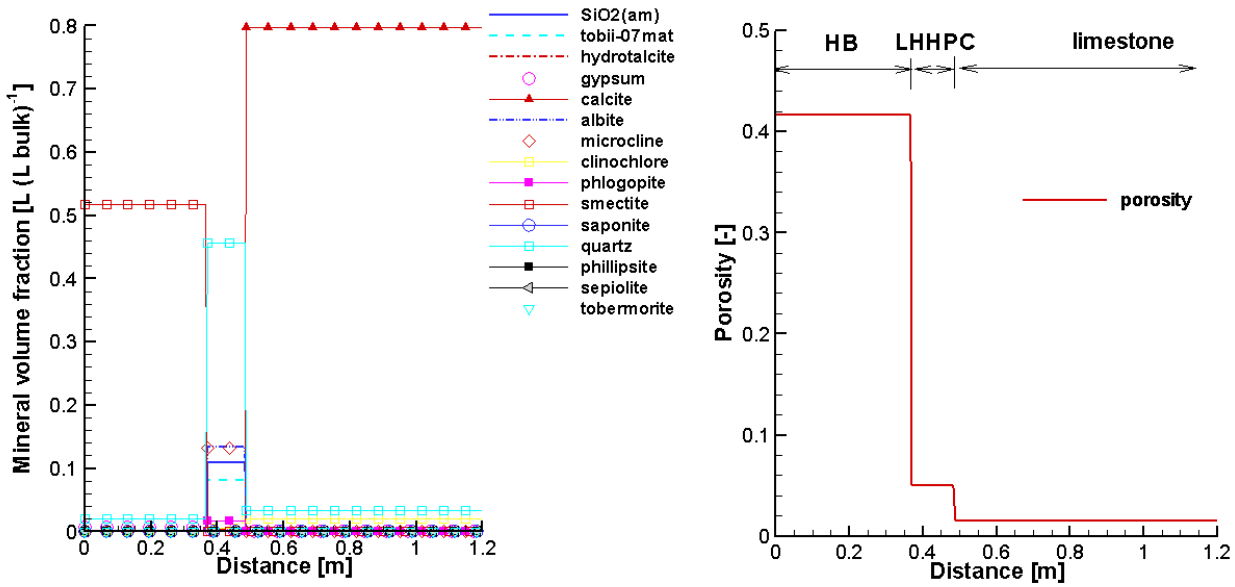

Figure A- 36: Profiles of Initial Volume Fractions of Minerals (Left) and Initial Porosity (Right) (the same for Case 3UP and Case 3CP)

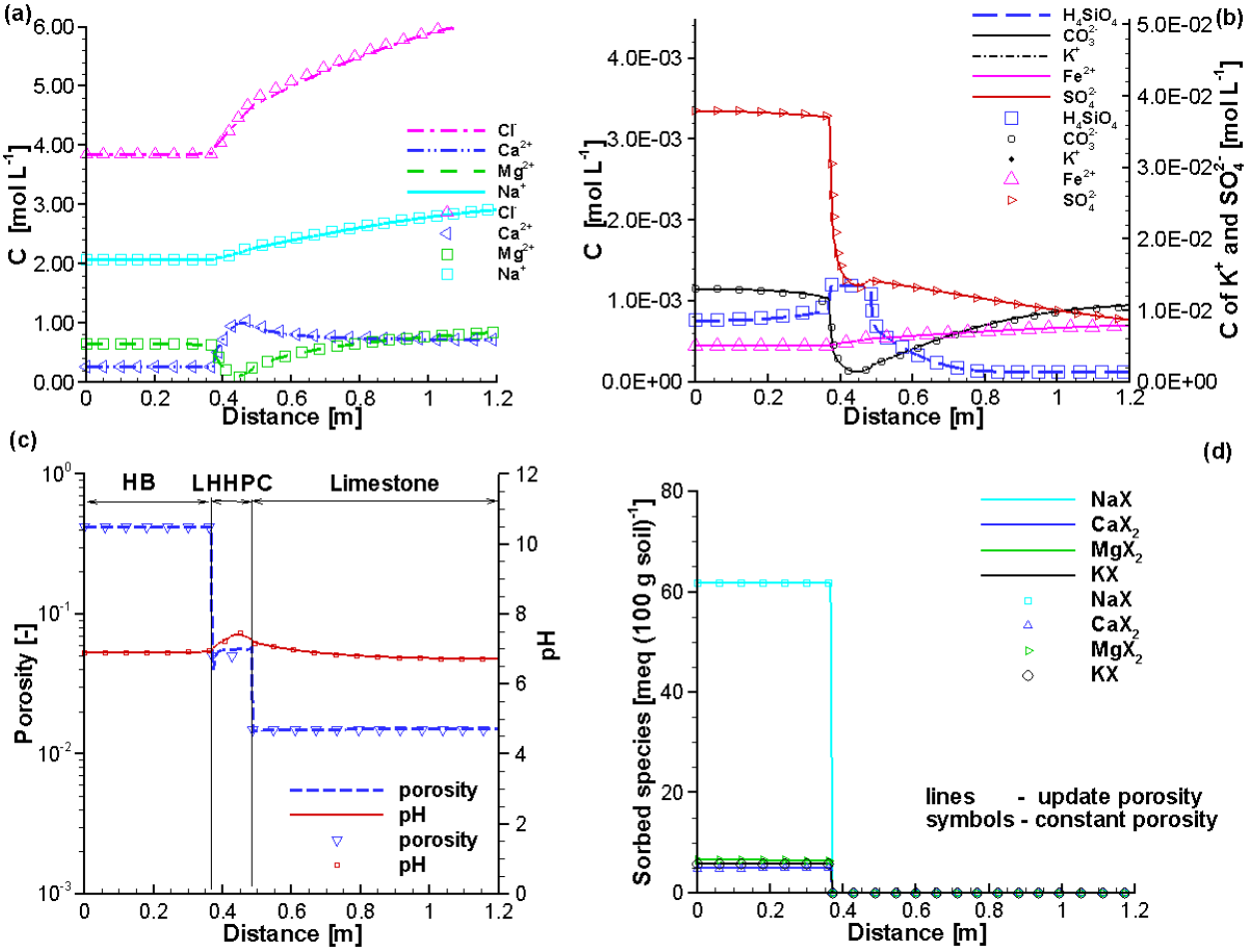

Figure A- 37: Profiles of Component Concentrations at 100 Years for Case 3CP (Symbols) and Case 3UP (Lines)

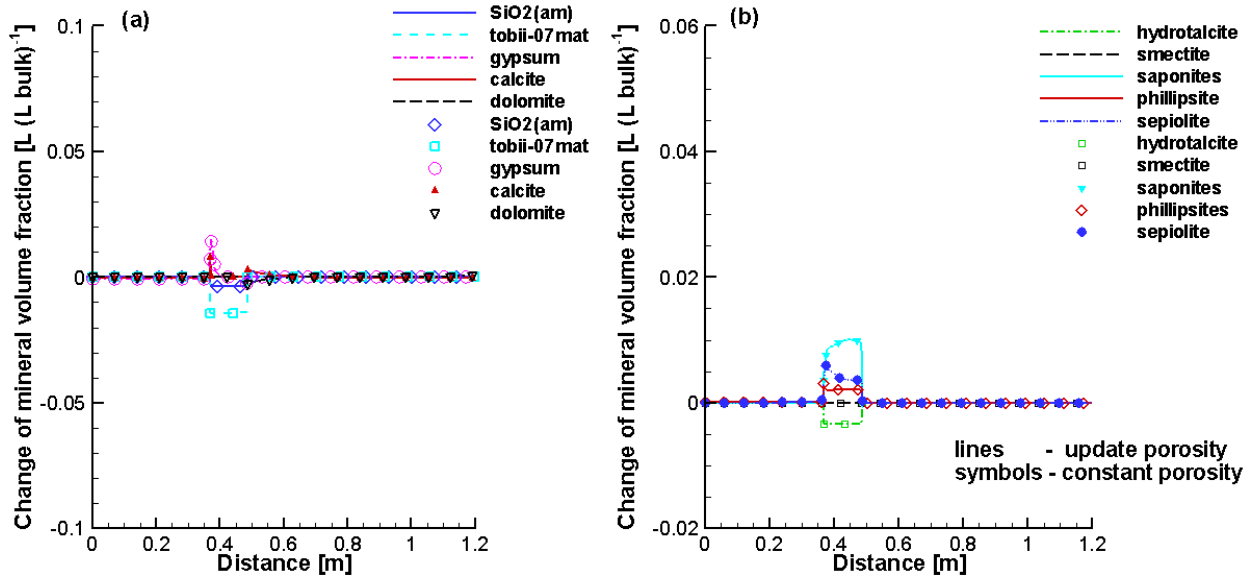

Figure A- 38: Comparison of Profiles of Mineral Volume Fraction Changes at 100 Years (Symbols – Case 3EDZCP, Lines – Case 3EDZUP)

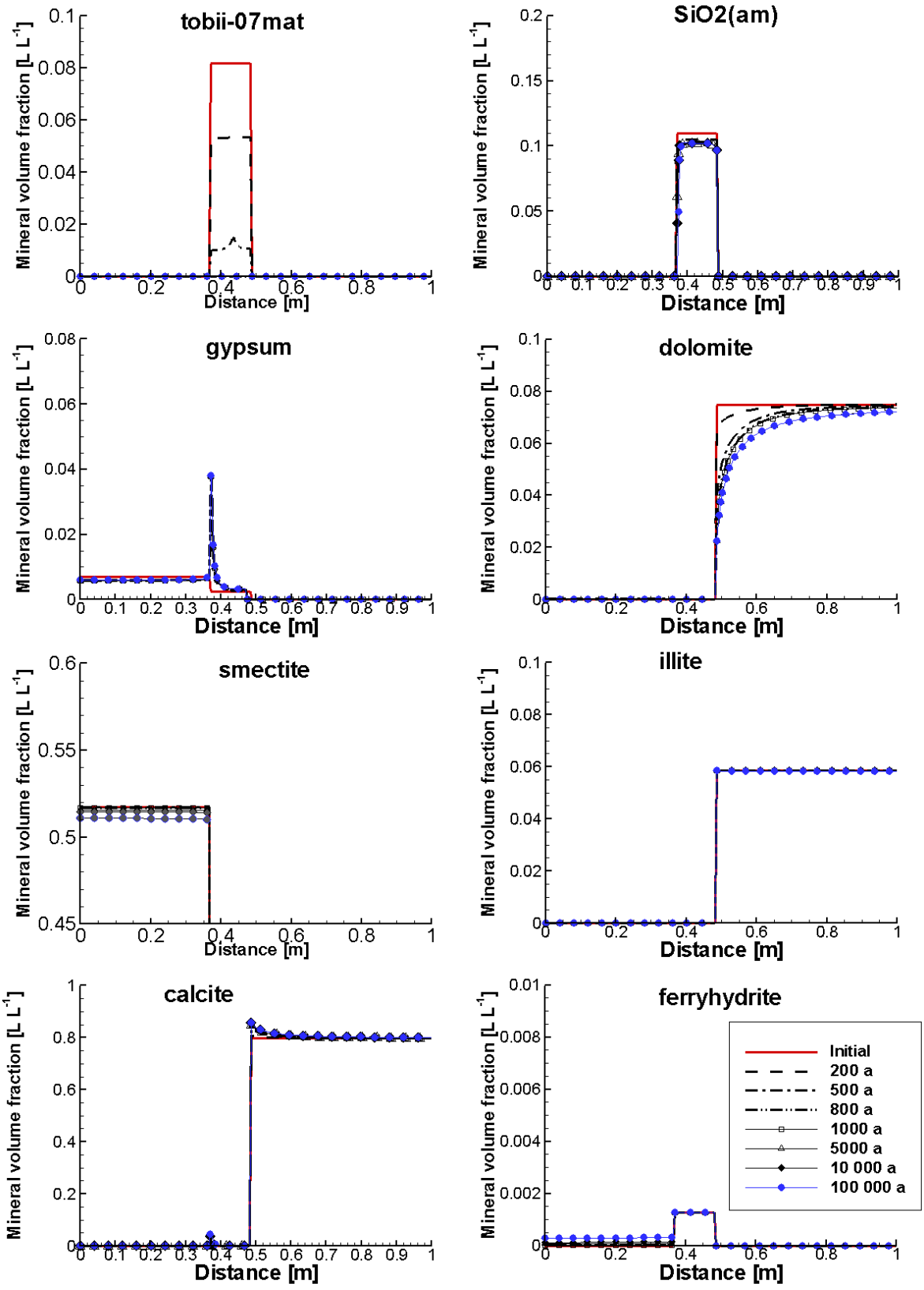

Figure A- 39: Profiles of the Volume Fractions of Primary Minerals at Selected Times (Case 3UP)

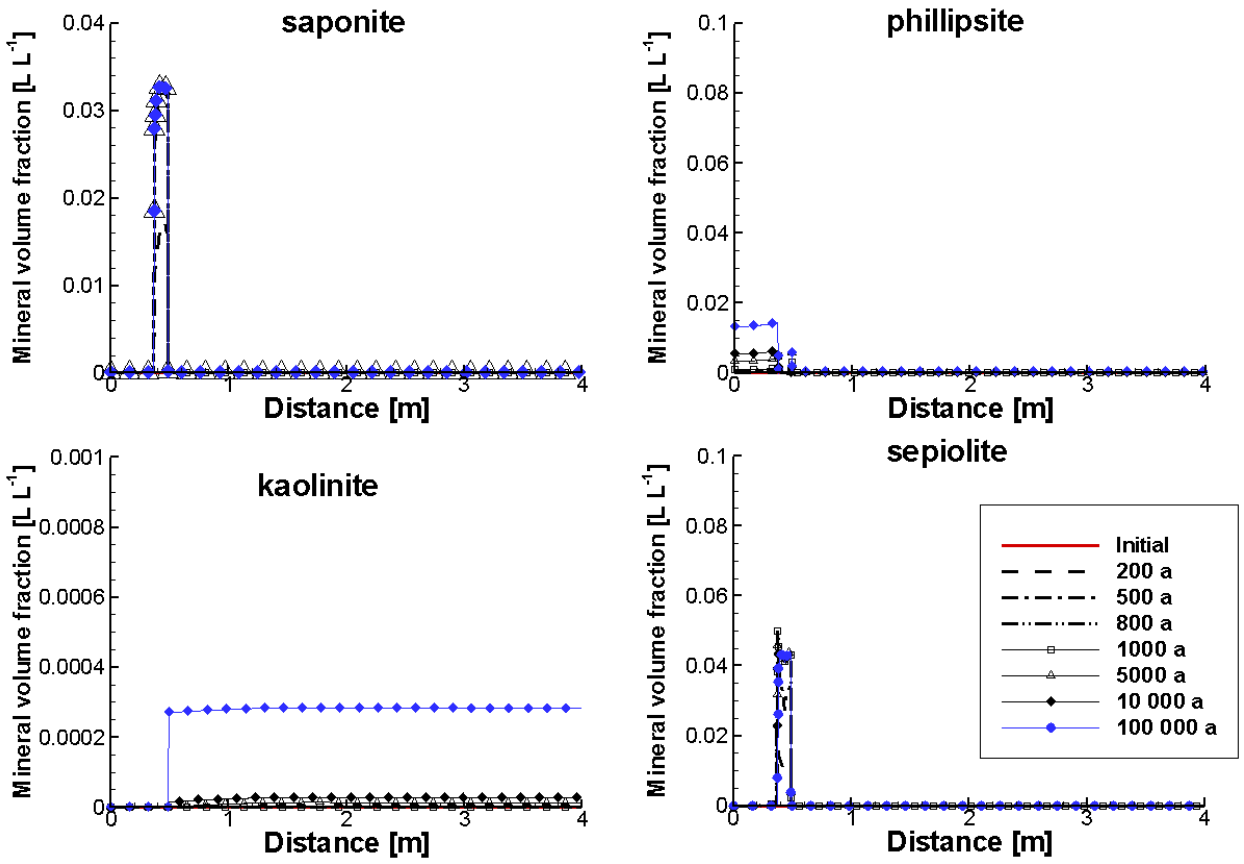

Figure A- 40: Profiles of the Volume Fractions of Secondary Minerals at Selected Times (Case 3UP)

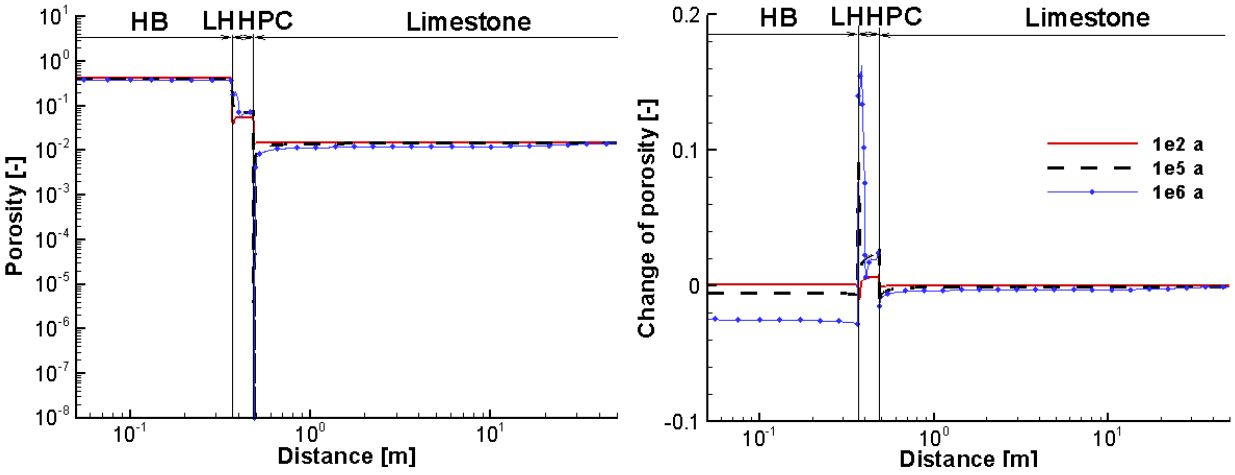

Figure A- 41: Profiles of Porosity (Left) and the Change of the Porosity (Right) at Selected Times (Case 3UP)

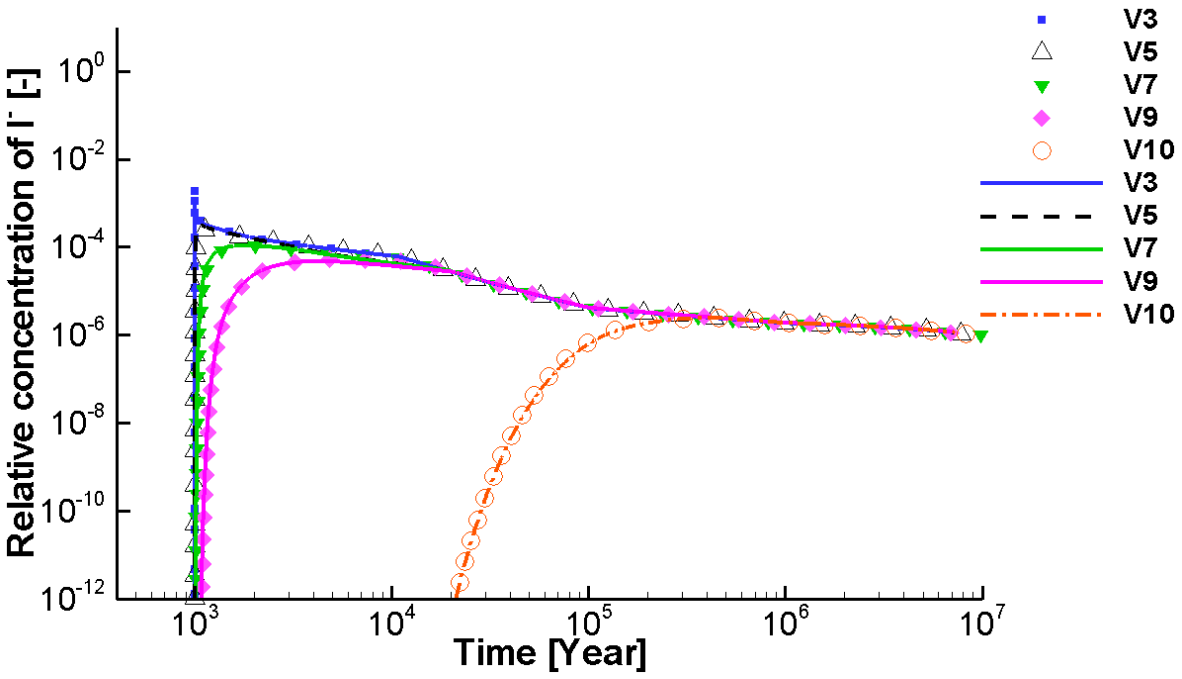

Figure A- 42: Comparison of Breakthrough Curves at Selected Observation Points for a Large Defect Occurring at 1,000 Years (Lines – Case 3rCP, Symbols – Case 3rUP). V3 (LHHPC), V5 to V10 (Limestone)

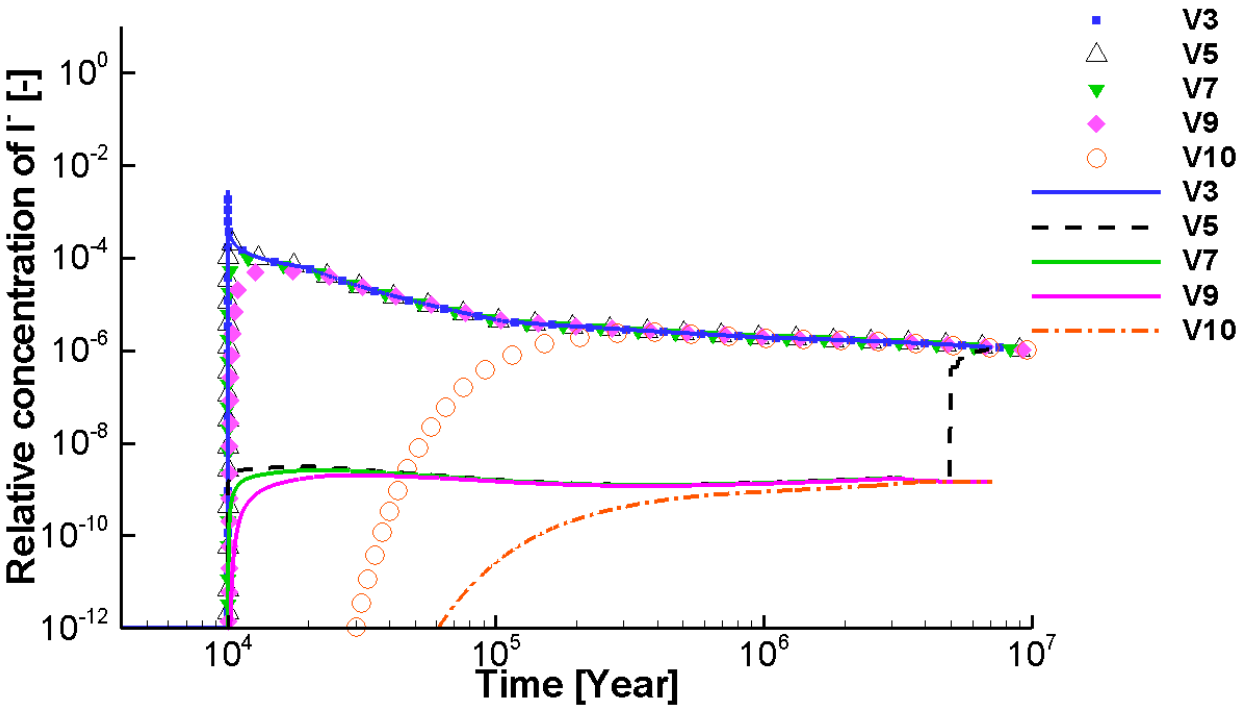

Figure A- 43: Comparison of Breakthrough Curves at Selected Observation Points for a Large Defect Occurring at 10,000 Years (Lines – Case 3rCP, Symbols – Case 3rUP). V3 (LHHPC), V5 to V10 (Limestone)

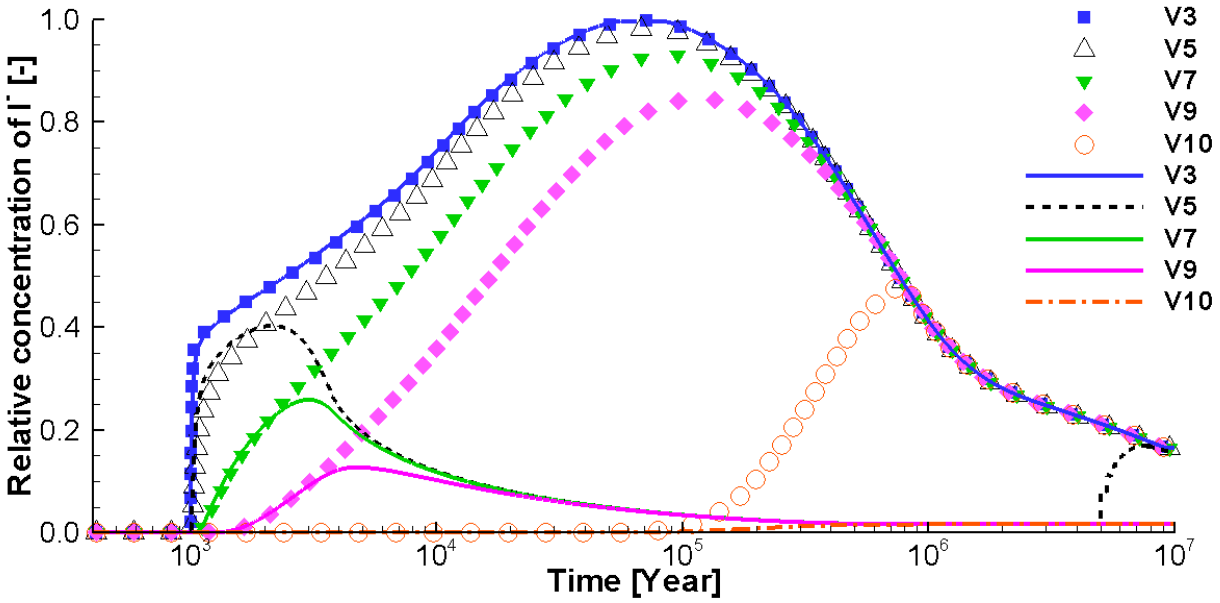

Figure A- 44: Comparison of Breakthrough Curves at Selected Observation Points for a Small Defect Occurring at 1,000 Years (Lines – Case 3rCP, Symbols – Case 3rUP). V3 (LHHPC), V5 to V10 (Limestone)

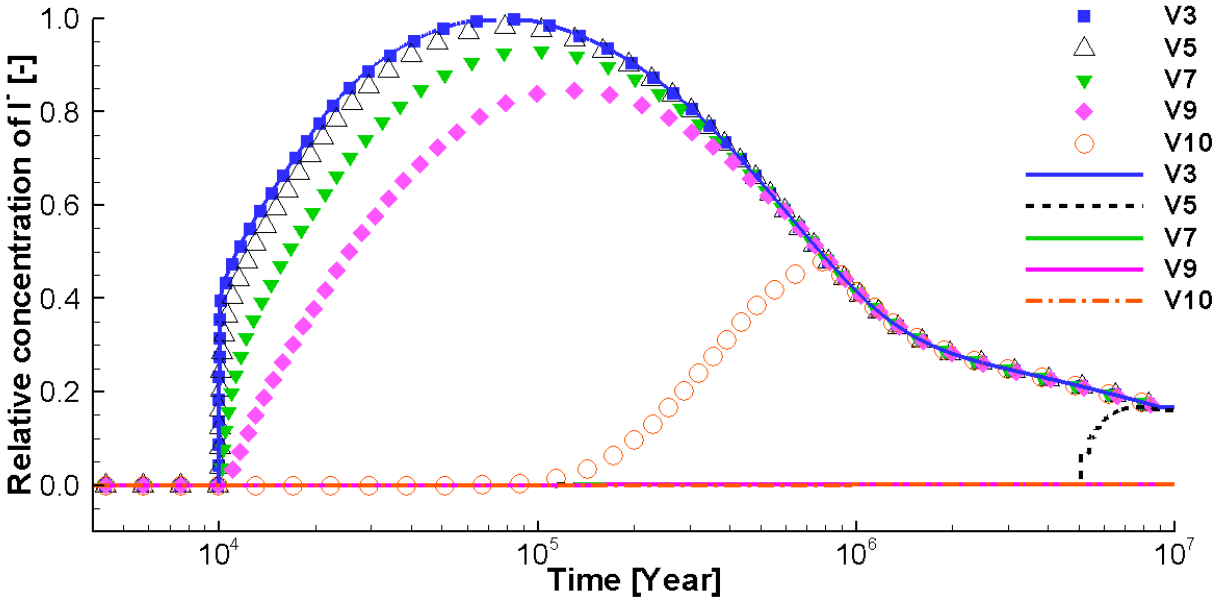

Figure A- 45: Comparison of Breakthrough Curves at Selected Observation Points for a Small Defect Occurring at 10,000 Years (Lines – Case 3rCP, Symbols – Case 3rUP). V3 (LHHPC), V5 to V10 (Limestone)

A.5.2. Case 3EDZCP and Case 3EDZUP

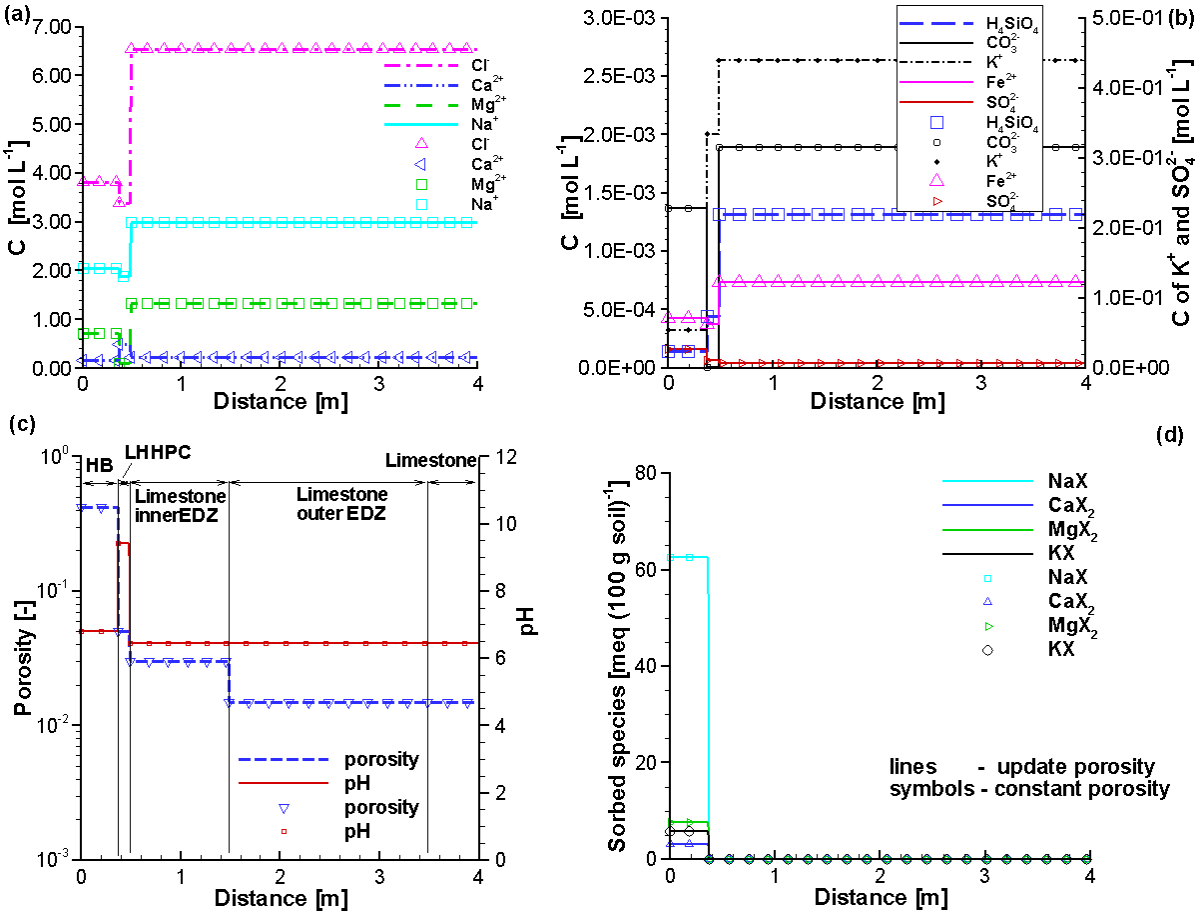

Figure A- 46: Profiles of Initial Component Concentrations (Symbols – Case 3EDZCP, Lines – Case 3EDZUP)

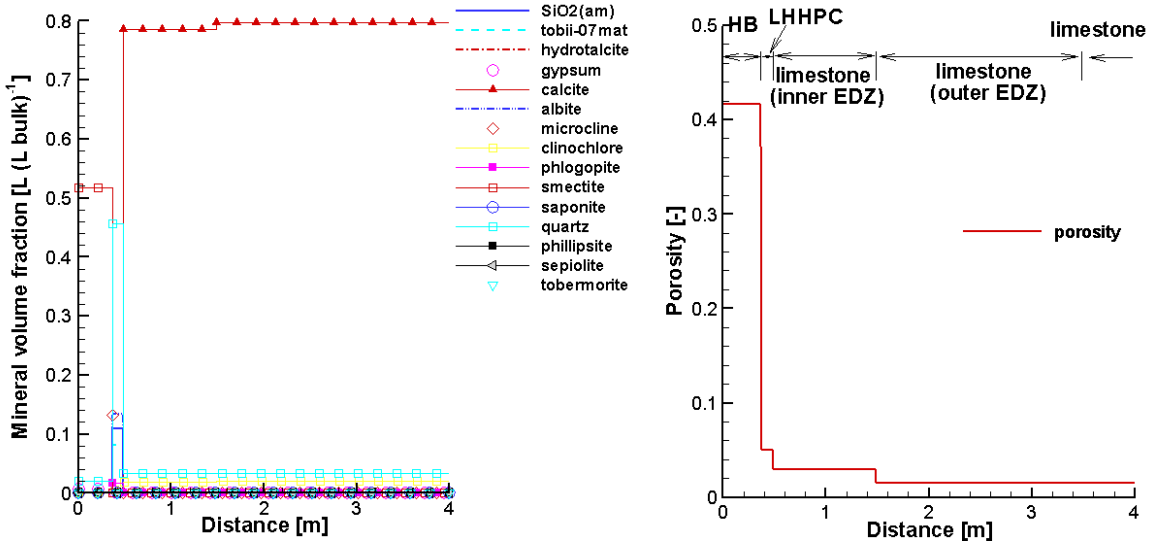

Figure A- 47: Profiles of Initial Volume Fractions of Minerals (Left) and Initial Porosity (Right) (Case 3EDZUP and Case 3EDZCP)

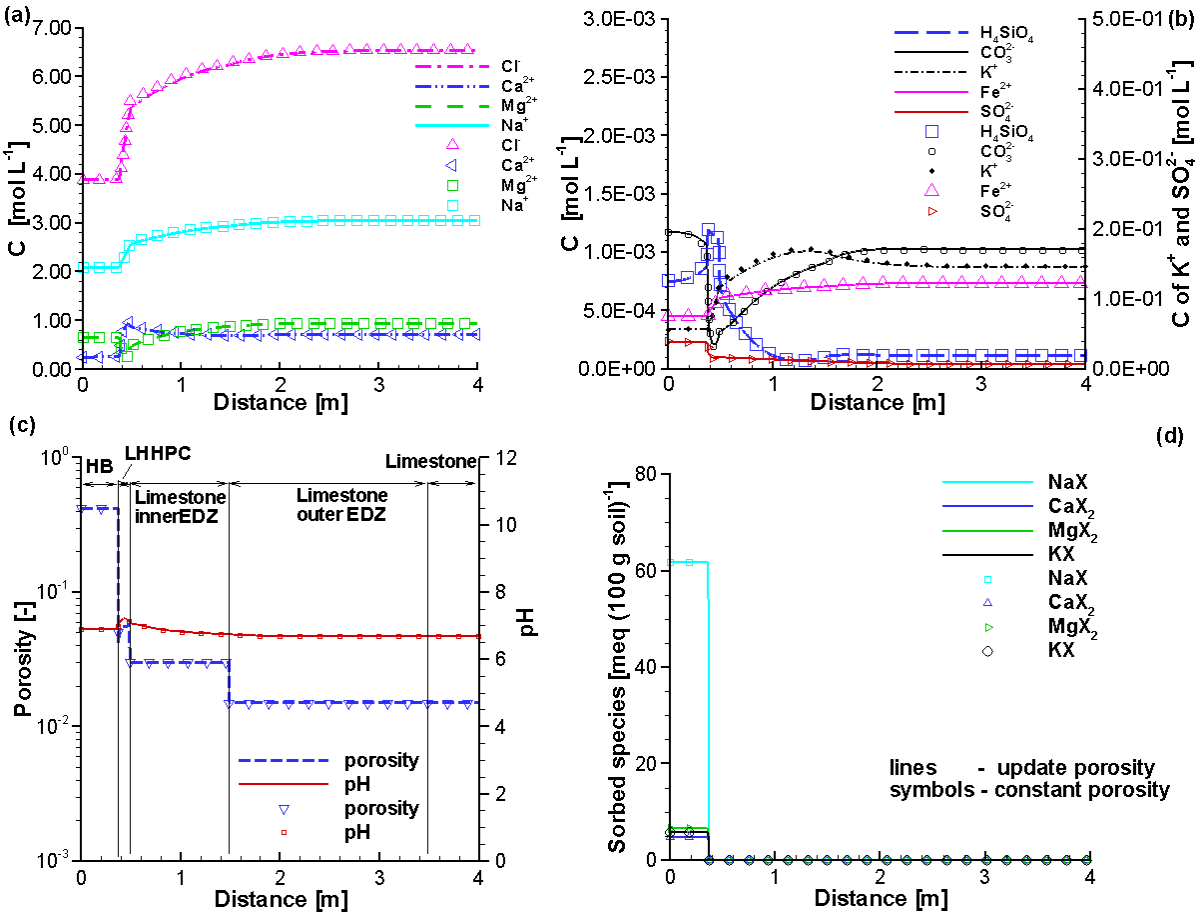

Figure A- 48: Profiles of Component Concentrations at 100 Years (Symbols – Case 3EDZCP, Lines – Case 3EDZUP)

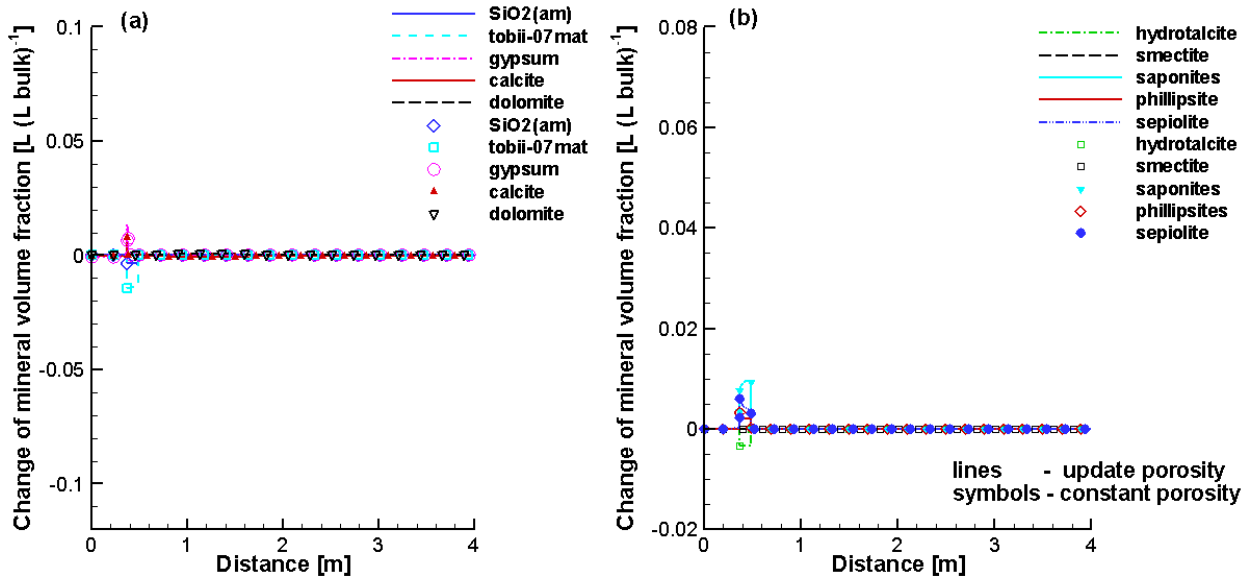

Figure A- 49: Comparison of Profiles of Mineral Volume Fraction Changes at 100 Years (Symbols – Case 3EDZCP, Lines – Case 3EDZUP)

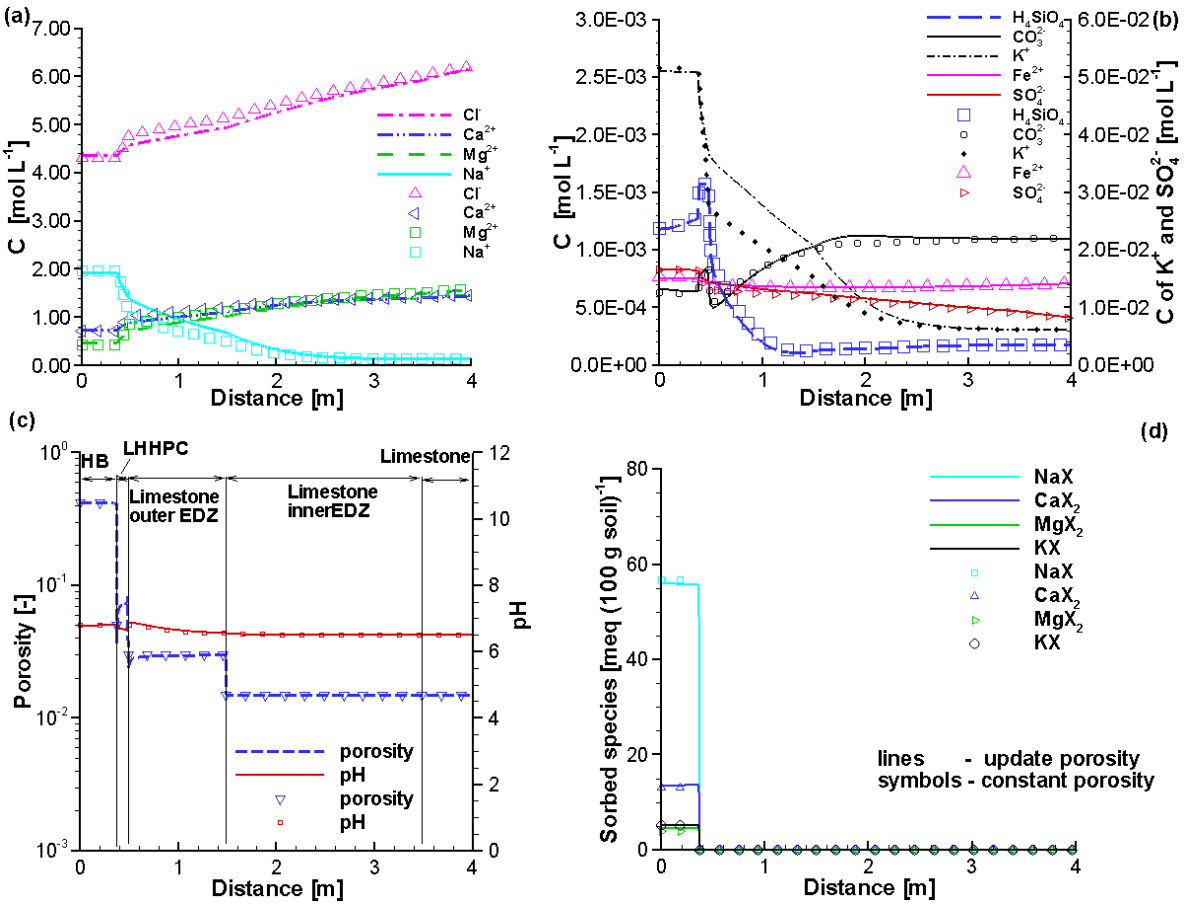

Figure A- 50: Profiles of Component Concentrations at 1,000 Years (Symbols – Case 3EDZCP, Lines – Case 3EDZUP)

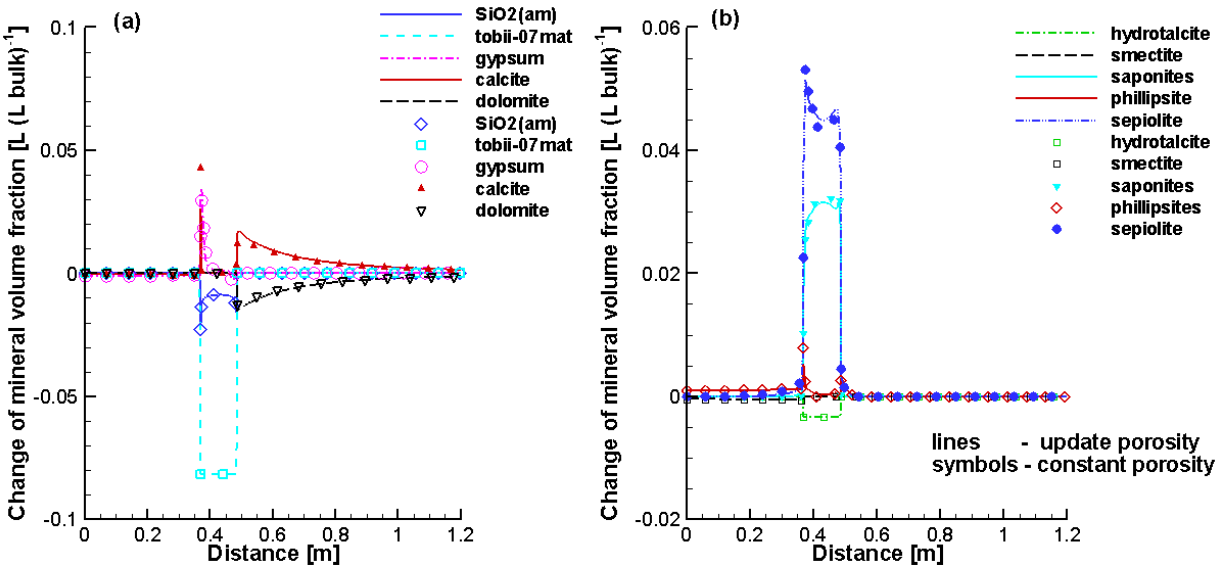

Figure A- 51: Comparison of Profiles of Mineral Volume Fraction Changes at 1,000 Years (Symbols – Case 3EDZCP, Lines – Case 3EDZUP)

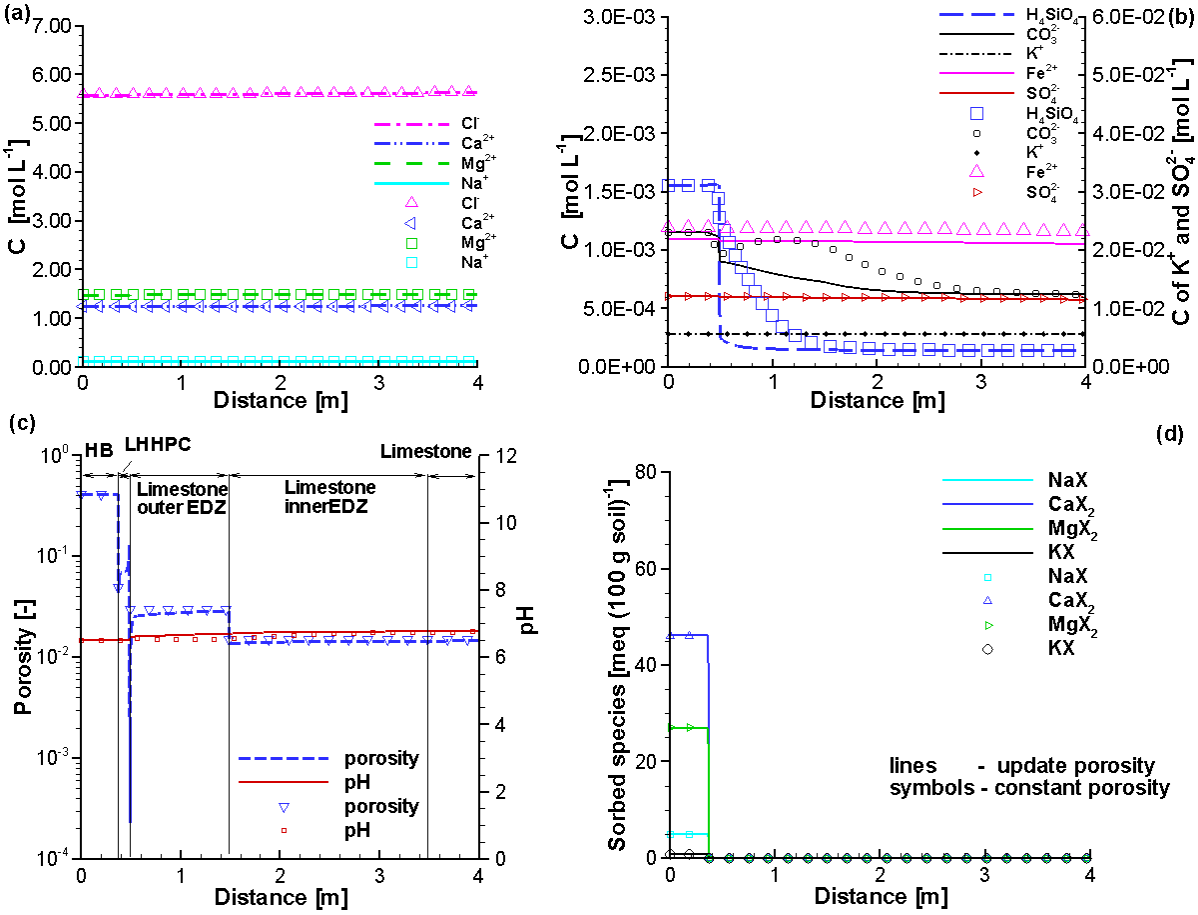

Figure A- 52: Profiles of Component Concentrations at 100,000 Years (Symbols – Case 3EDZCP, Lines – Case 3EDZUP)

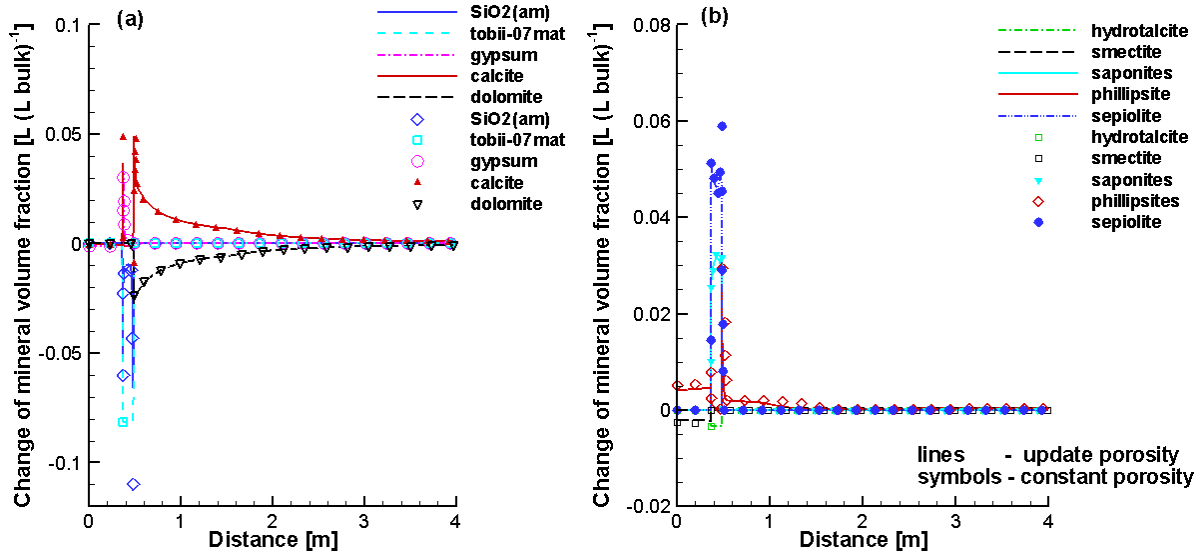

Figure A- 53: Comparison of Profiles of Mineral Volume Fraction Changes at 100,000 Years (Symbols – Case 3EDZCP, Lines – Case 3EDZUP)

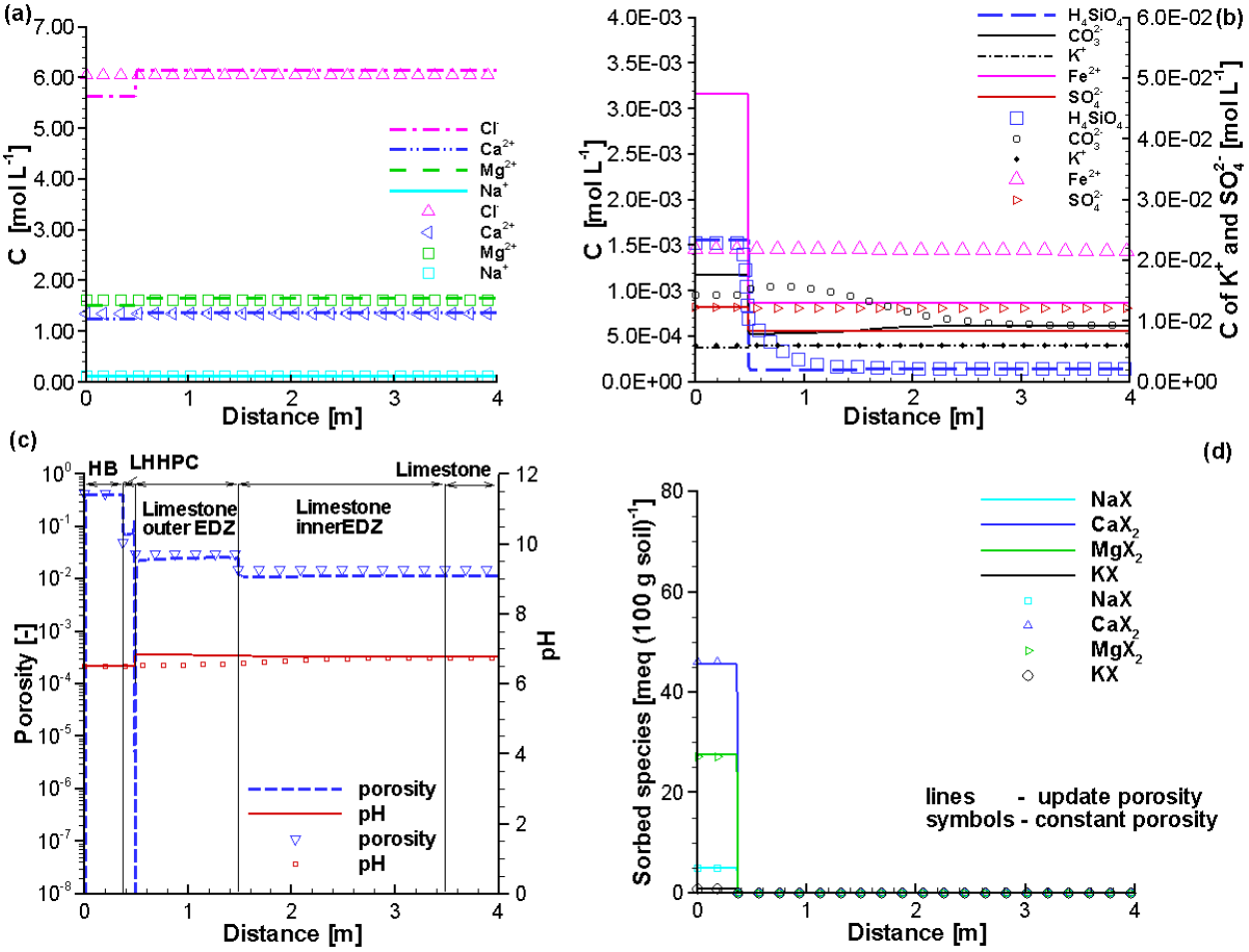

Figure A- 54: Profiles of Component Concentrations at 1,000,000 Years (Symbols – Case 3EDZCP, Lines – Case 3EDZUP)

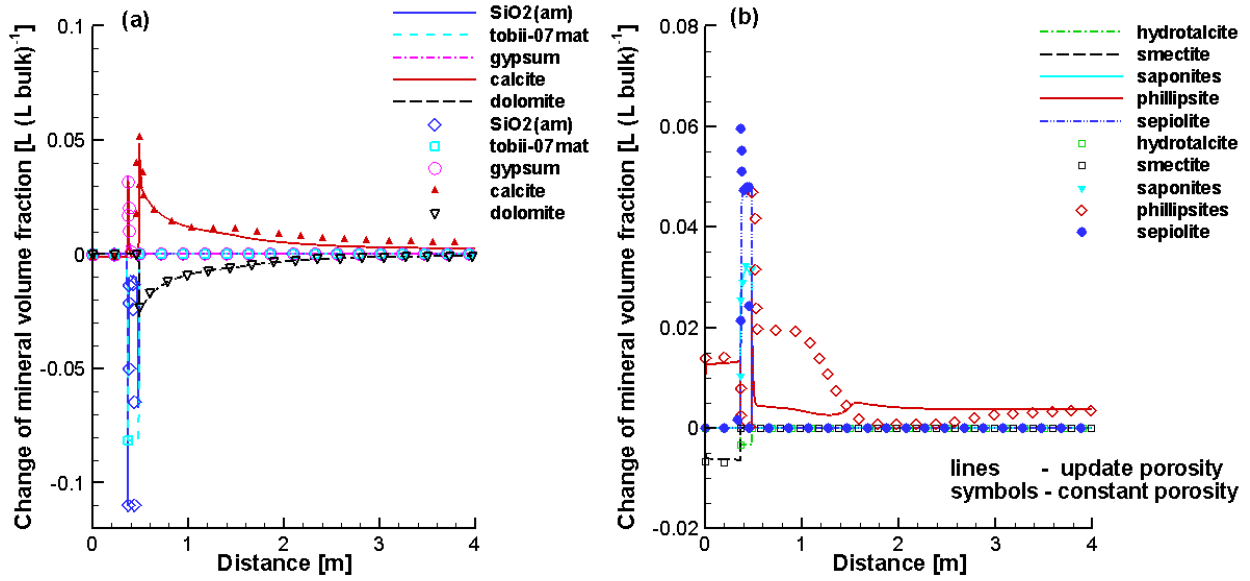

Figure A- 55: Comparison of Profiles of Mineral Volume Fraction Changes at 1,000,000 Years (Symbols – Case 3EDZCP, Lines – Case 3EDZUP)

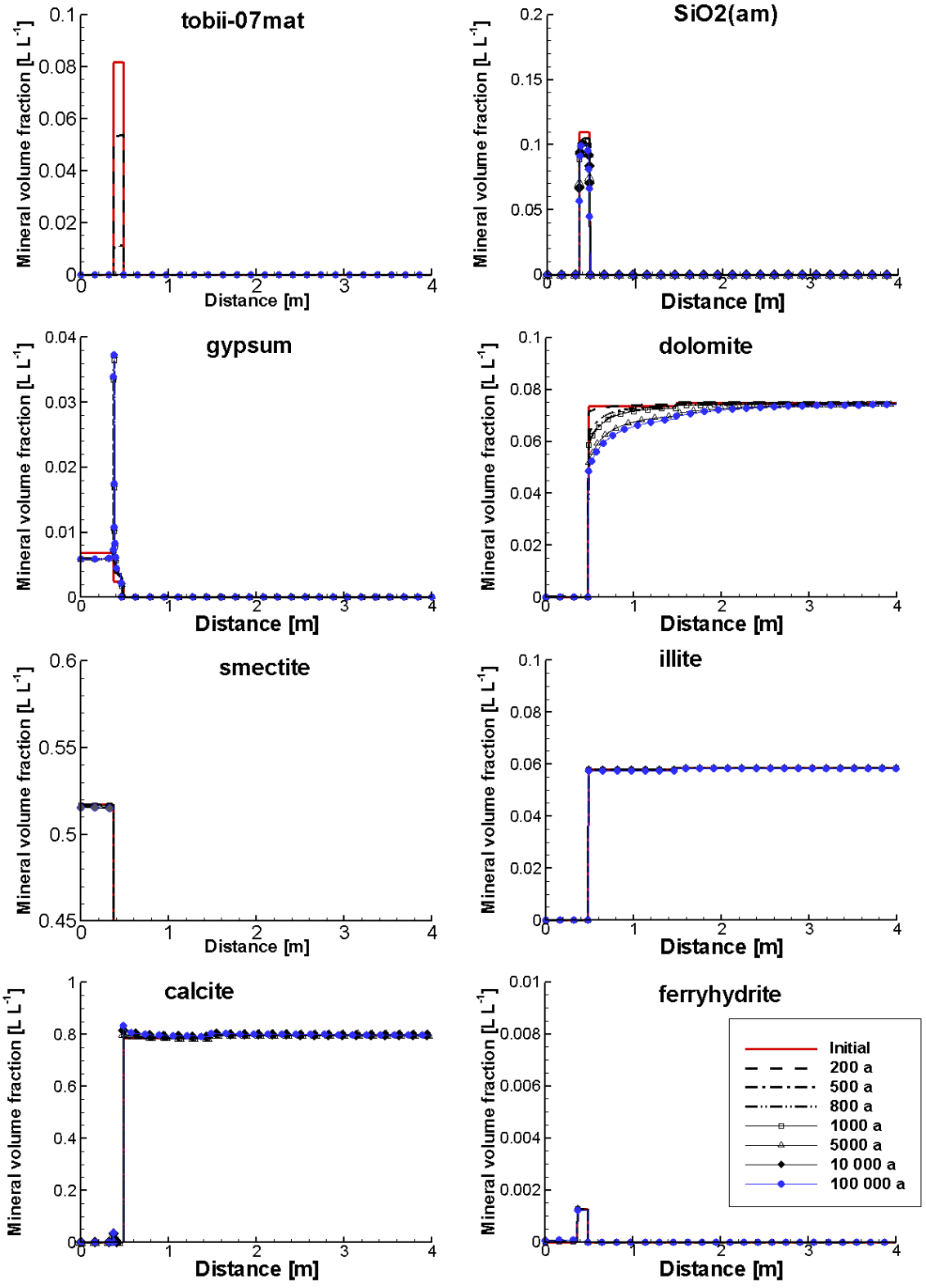

Figure A- 56: Profiles of the Volume Fractions of Primary Minerals at Selected Times (Case 3EDZUP)

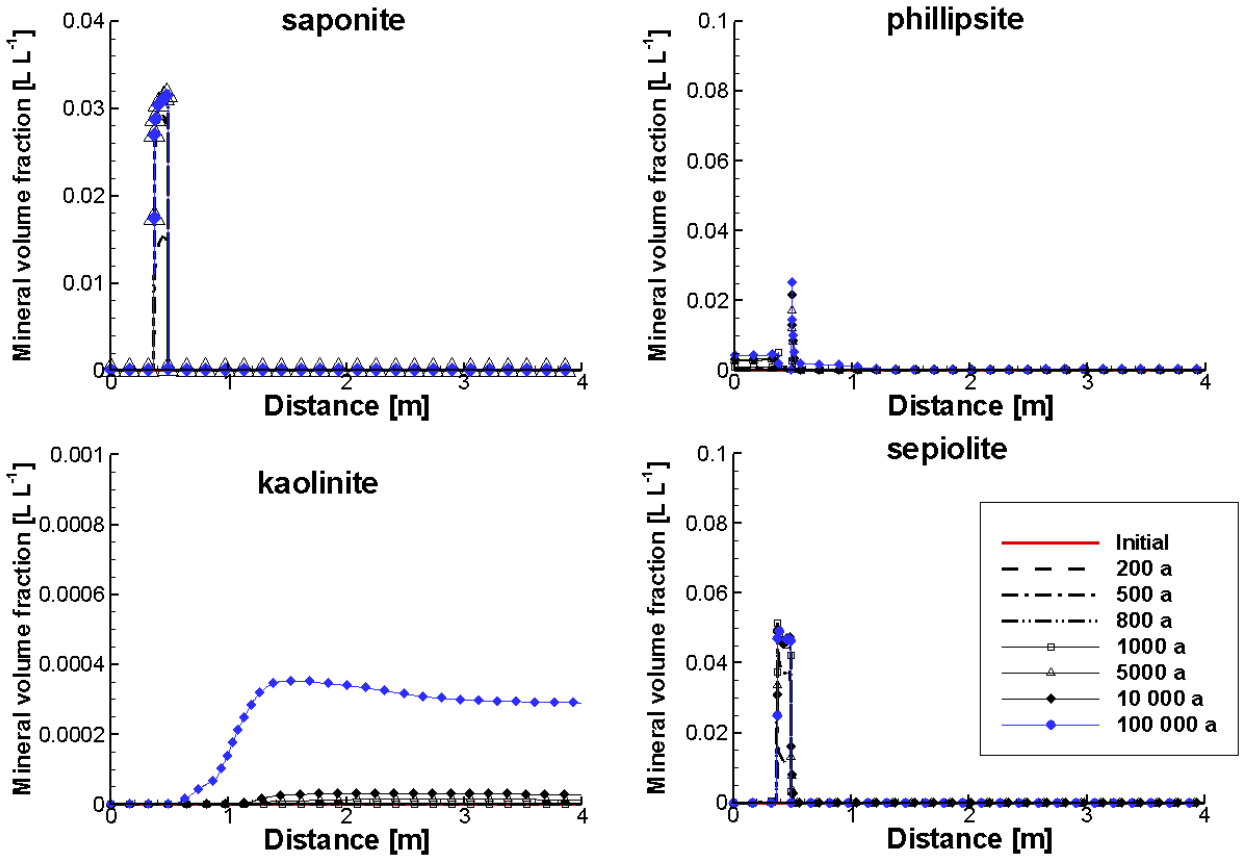

Figure A- 57: Profiles of the Volume Fractions of Secondary Minerals at Selected Times (Case 3EDZUP)

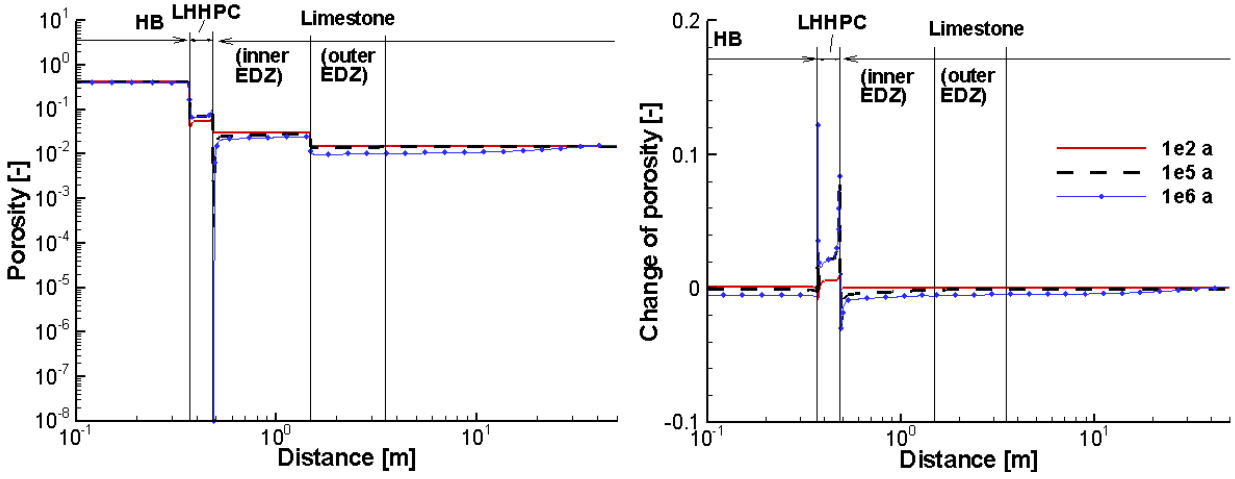

Figure A- 58: Profiles of the Porosity (Left) and Porosity Change (Right) at 100, 100,000 and 1,000,000 Years for Case 3EDZUP

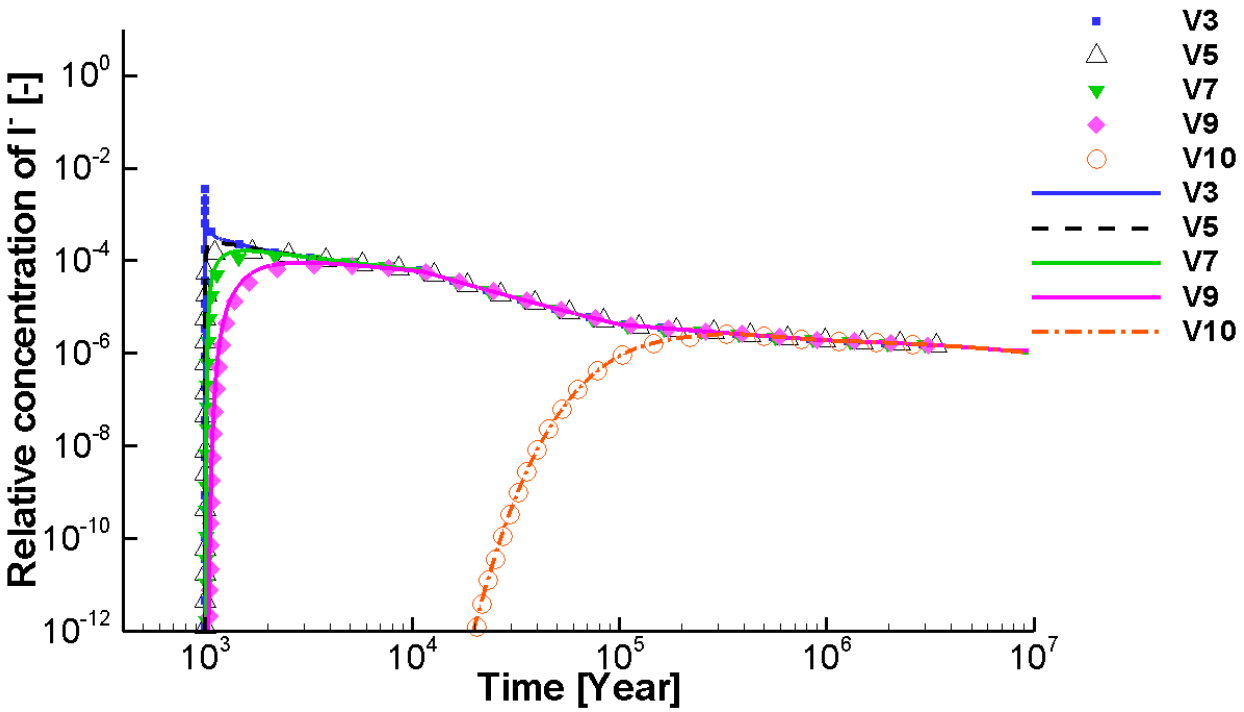

Figure A- 59: Comparison of Breakthrough Curves at Selected Observation Points for a Large Defect Occurring at 1,000 Years for Case 3rEDZCP (Symbols) and Case 3rEDZUP (Lines). V3 (HB), V5 (Inner EDZ), V7 (Outer EDZ), and V9 & V10 (Intact Limestone)

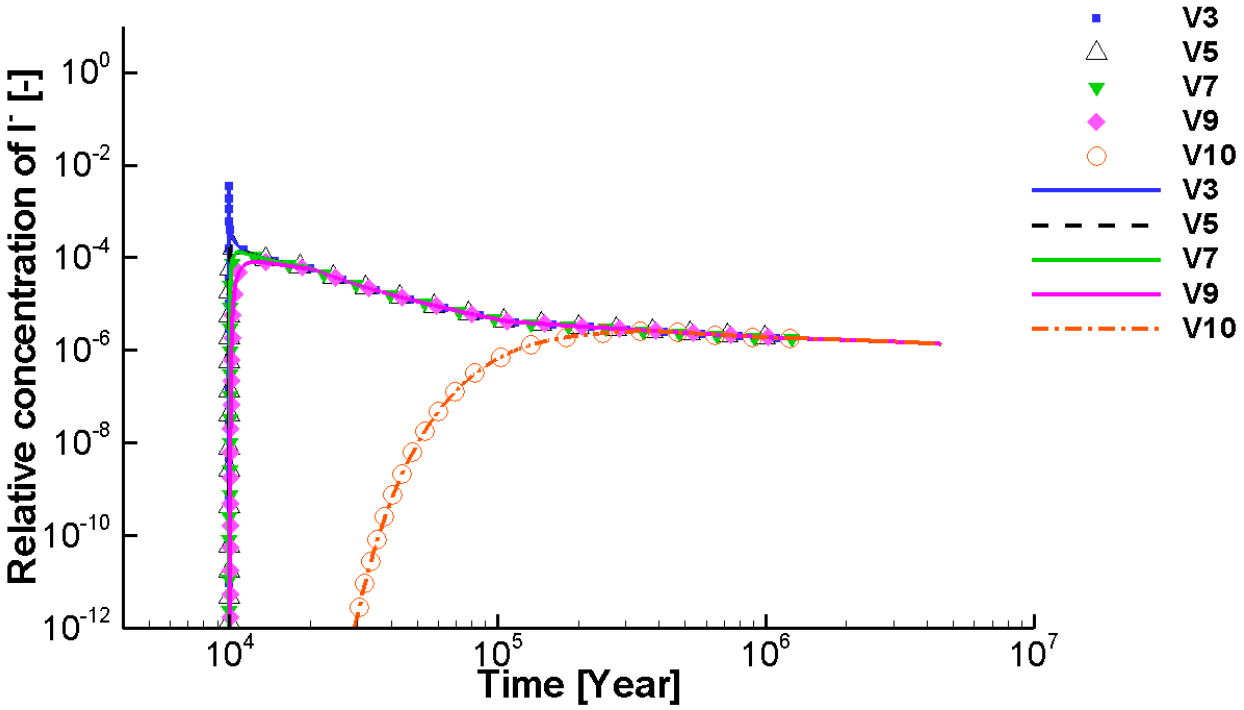

Figure A- 60: Comparison of Breakthrough Curves at Selected Observation Points for a Large Defect Occurring at 10,000 Years for Case 3rEDZCP (Symbols) and Case 3rEDZUP (Lines). V3 (HB), V5 (Inner EDZ), V7 (Outer EDZ), and V9 & V10 (Intact Limestone)

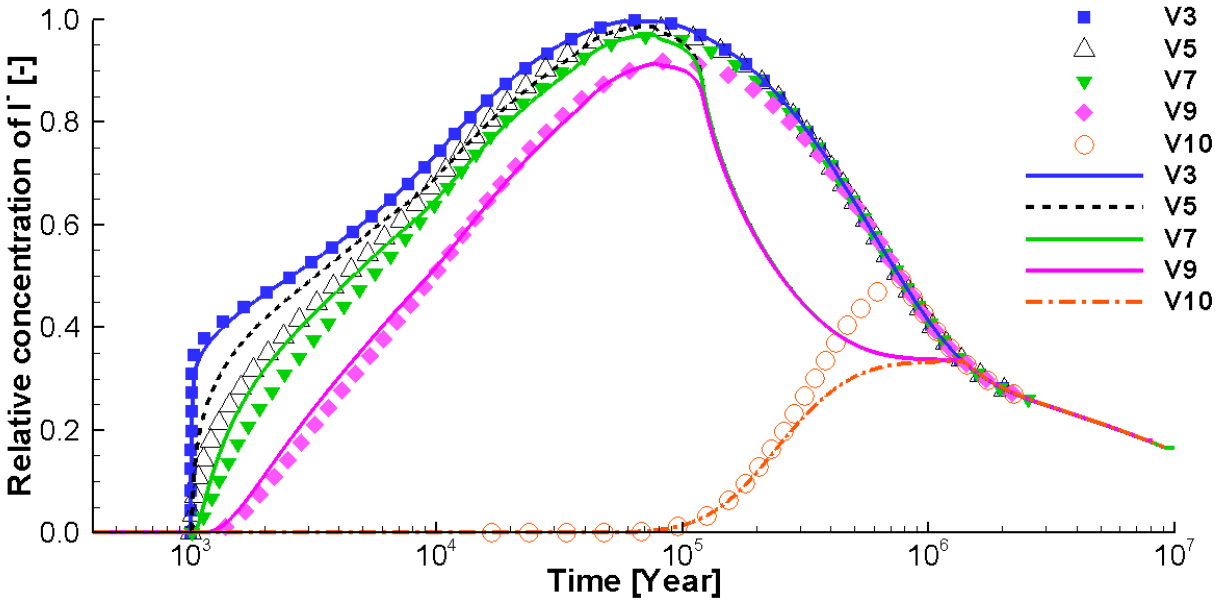

Figure A- 61: Comparison of Breakthrough Curves at Selected Observation Points for a Small Defect Occurring at 1,000 Years for Case 3rEDZCP (Symbols) and Case 3rEDZUP (Lines). V3 (HB), V5 (Inner EDZ), V7 (Outer EDZ), and V9 & V10 (Intact Limestone)

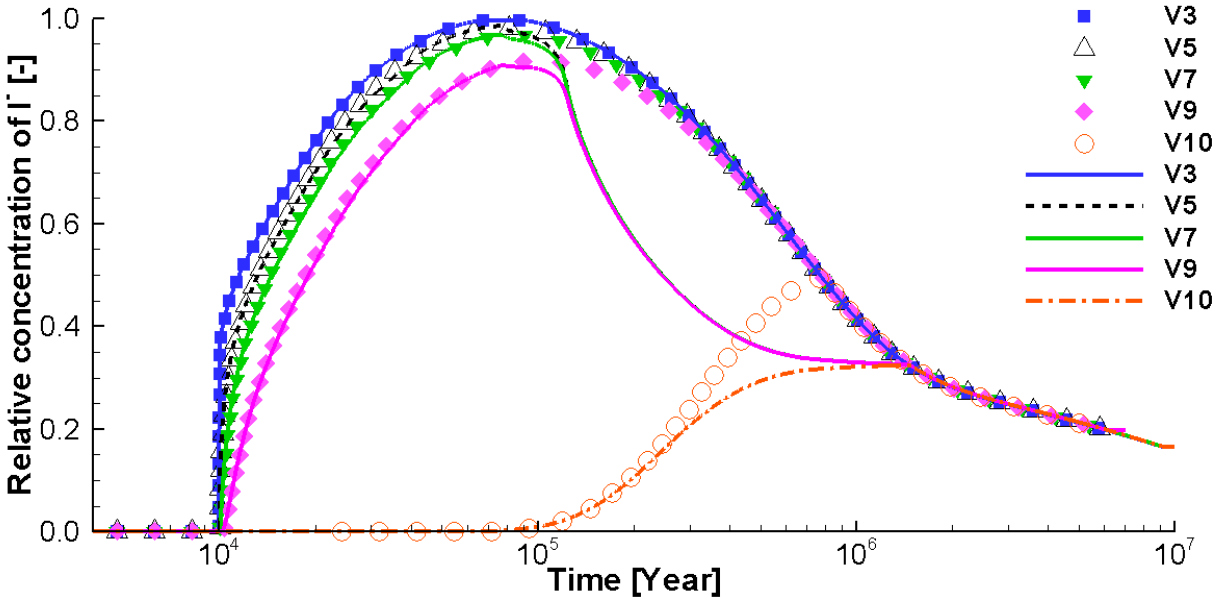

Figure A- 62: Comparison of Breakthrough Curves at Selected Observation Points for a Small Defect Occurring at 10,000 Years for Case 3rEDZCP (Symbols) and Case 3rEDZUP (Lines). V3 (HB), V5 (Inner EDZ), V7 (Outer EDZ), and V9 & V10 (Intact Limestone)

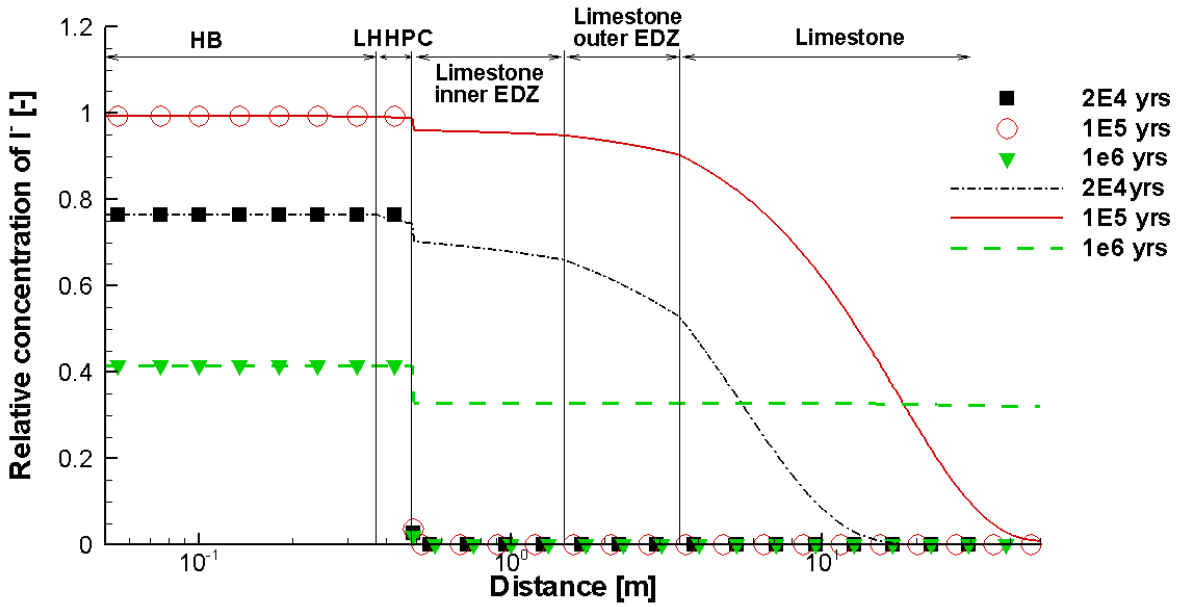

Figure A- 63: Comparison of Relative Concentration Profiles of I^- at Selected Times for a Small Defect Occurring at 10,000 Years for Case 3rUP (Symbols) and Case 3rEDZUP (Lines)

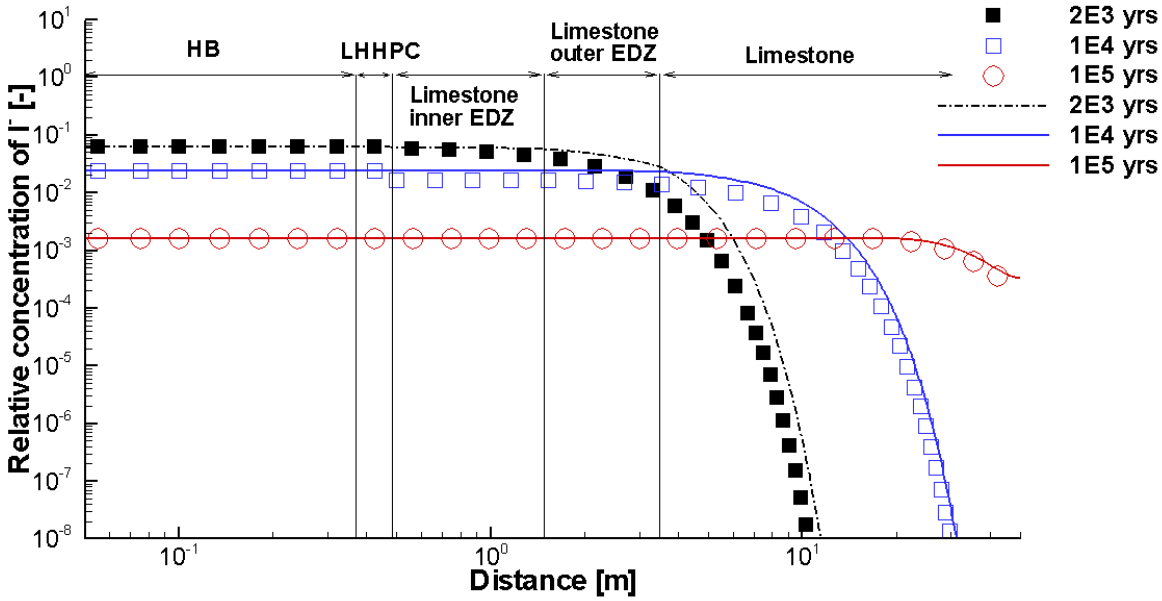

Figure A- 64: Comparison of Relative Concentration Profiles of I^- at Selected Times for a Large Defect Occurring at 1,000 Years for Case 3rUP (Symbols) and Case 3rEDZUP (Lines)

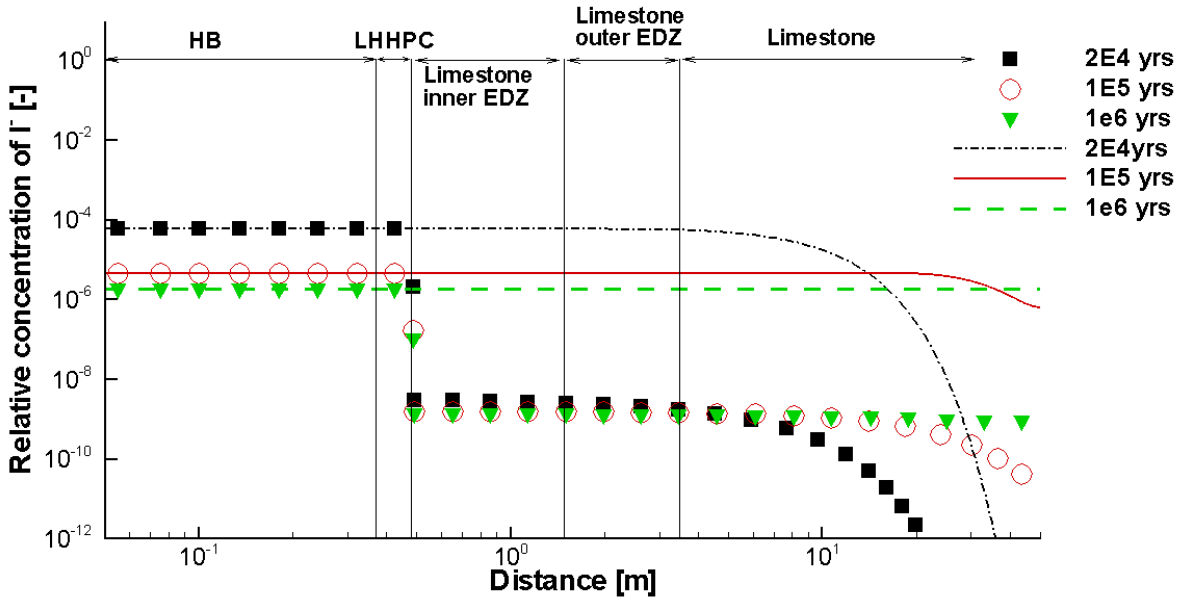

Figure A- 65: Comparison of Relative Concentration Profiles of I^- at Selected Times for a Large Defect Occurring at 10,000 Years for Case 3rUP (Symbols) and Case 3rEDZUP (Lines)

A.6 *CASE 4– HB/LHHPC/LIMESTONE*

A.6.1. Case 4CP and Case 4UP

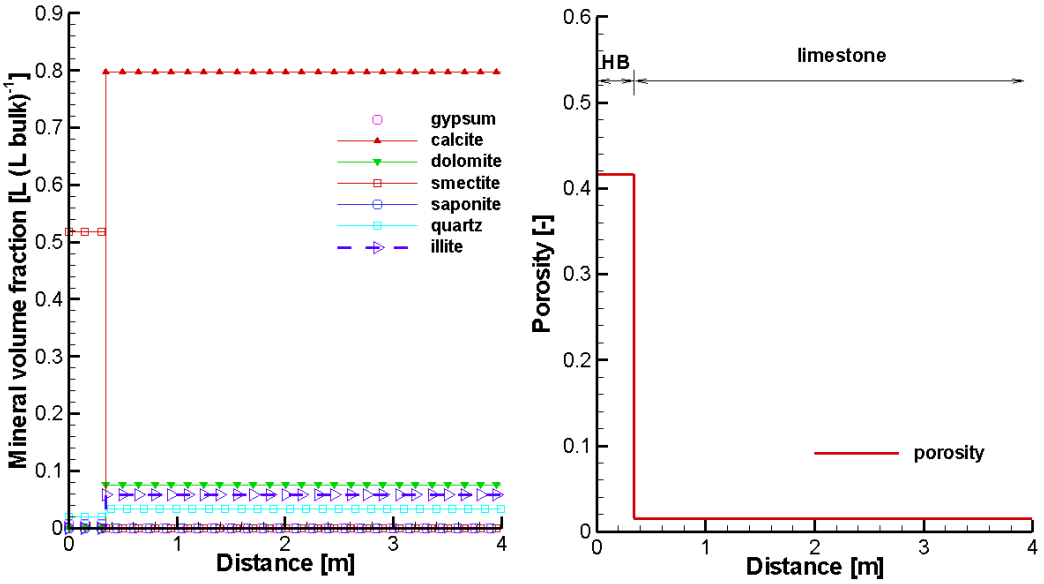

Figure A- 66: Profiles of Initial Volume Fractions of Minerals (Left) and Initial Porosity (Right) (Case 4UP and Case 4CP)

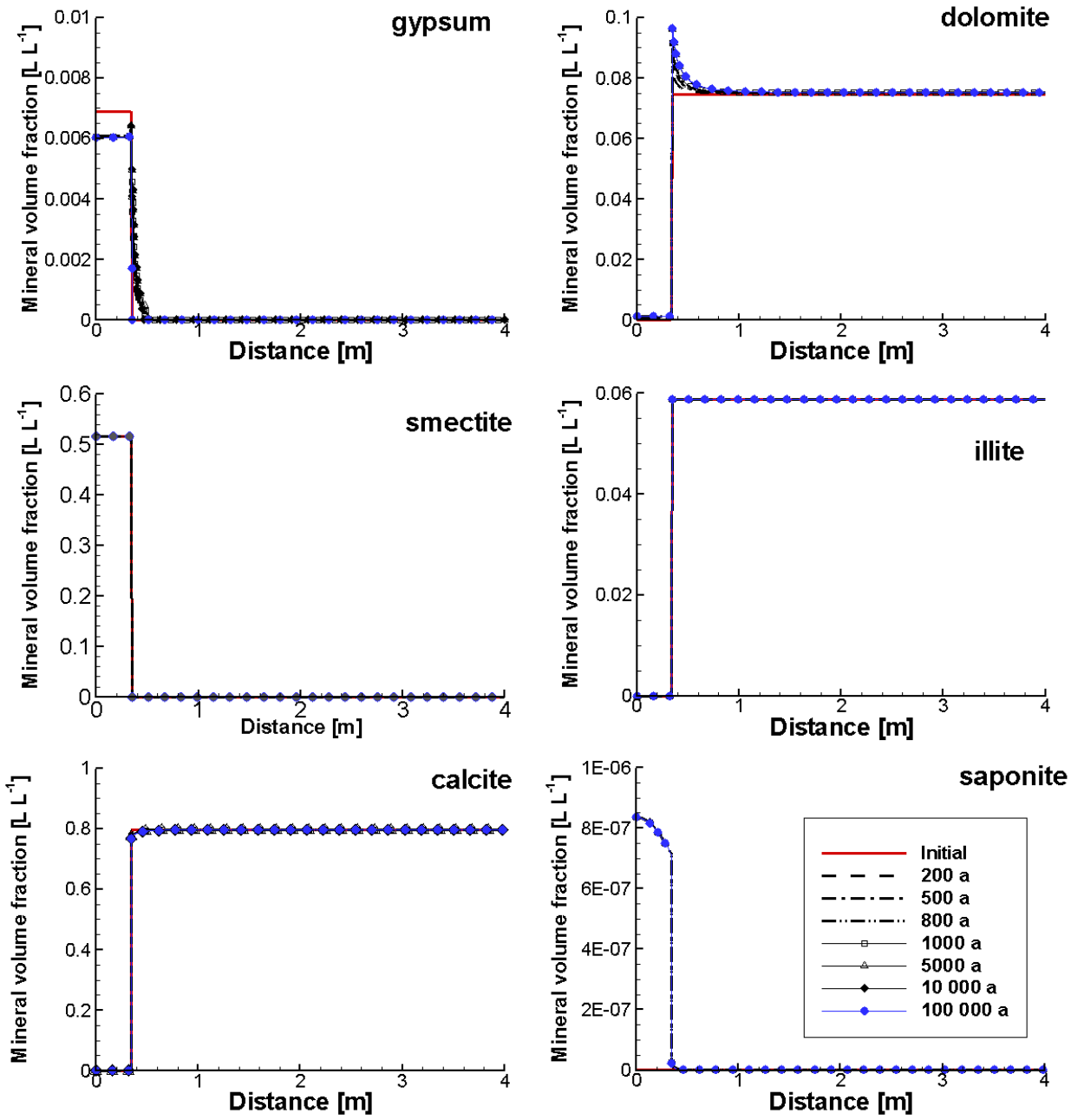

Figure A- 67: Profiles of Mineral Volume Fractions at Selected Times (Case 4UP)

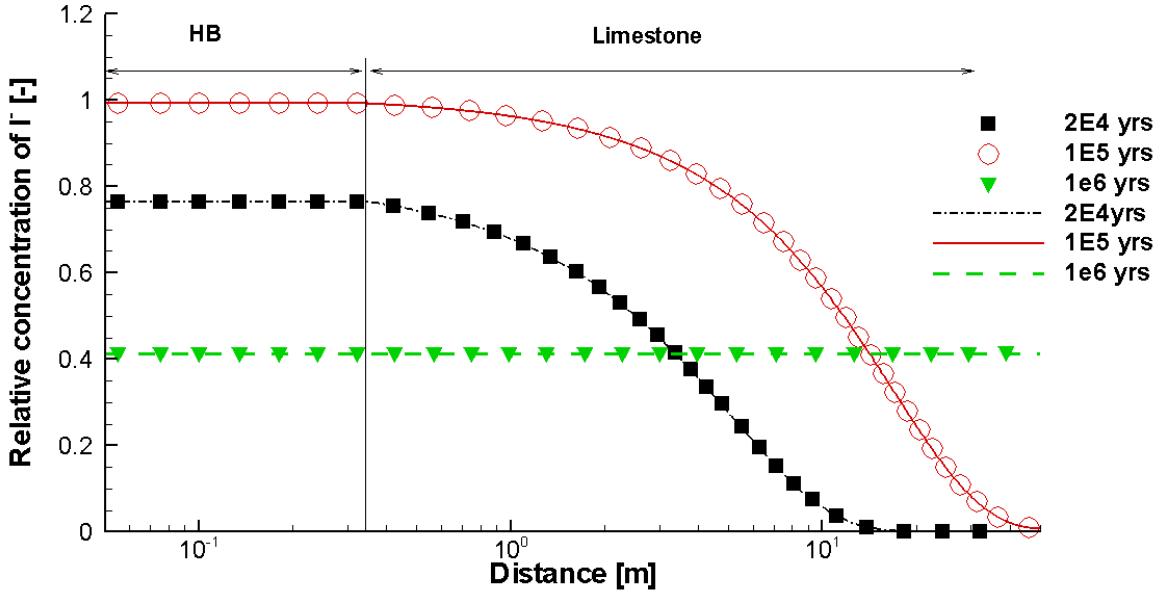

Figure A- 68: Relative Concentration Profiles of I^- at Selected Times for Case 4rCP (Lines) and Case 4rUP (Symbols) for the Canister Failure Scenario – Small Defect at 10,000 Years

A.6.2. Case 4EDZCP and Case 4EDZUP

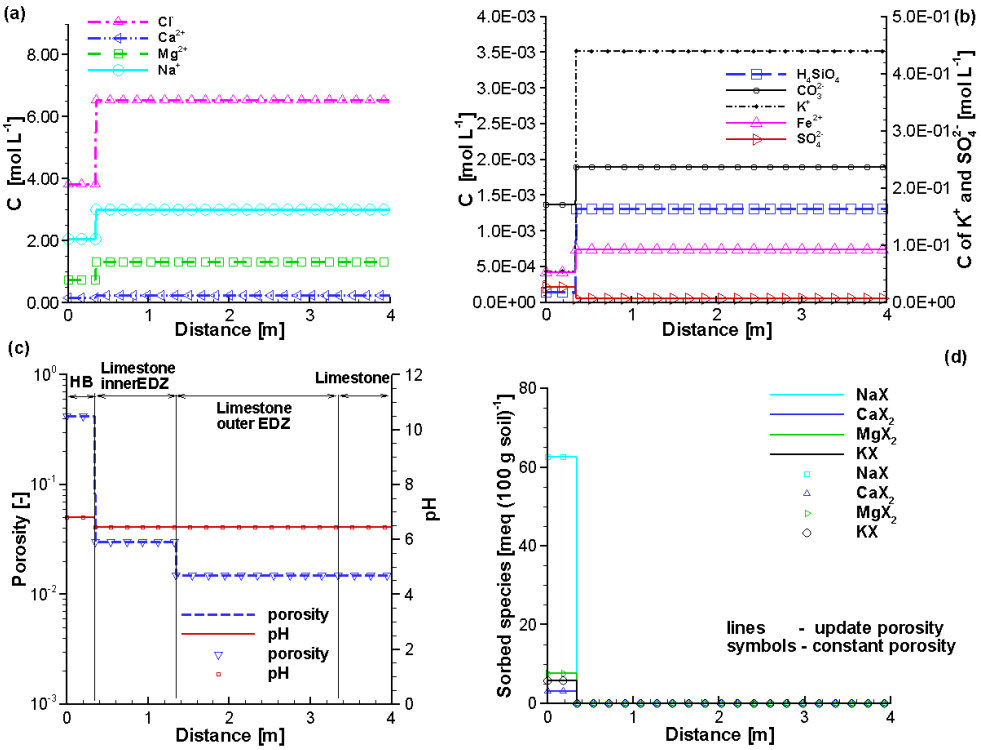

Figure A- 69: Profiles of Initial Component Concentrations (Symbols - Case 4EDZCP, Lines - Case 4EDZUP)

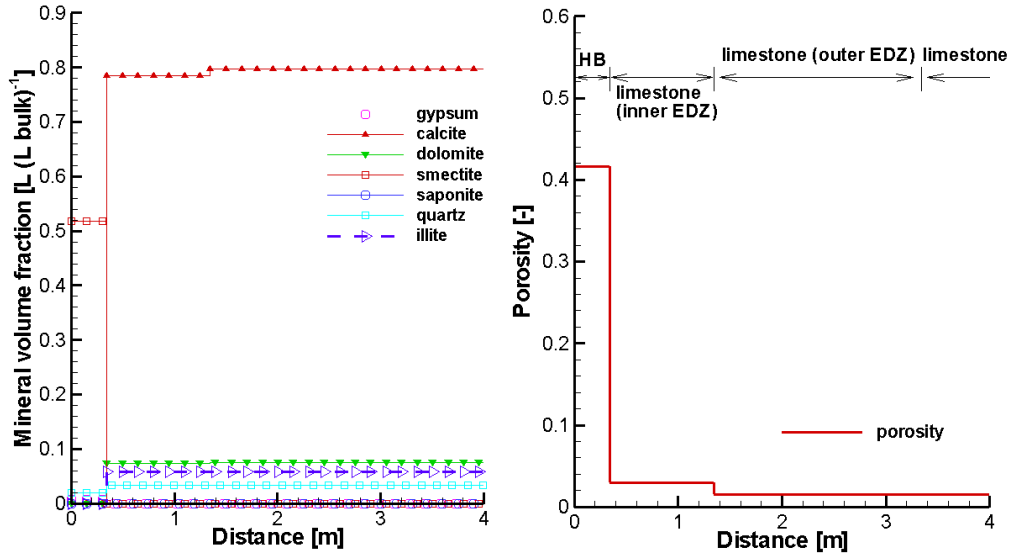

Figure A- 70: Profiles of Initial Volume Fractions of Minerals (Left) and Initial Porosity (Right) (the Same for Case 4EDZUP and Case 4EDZCP)

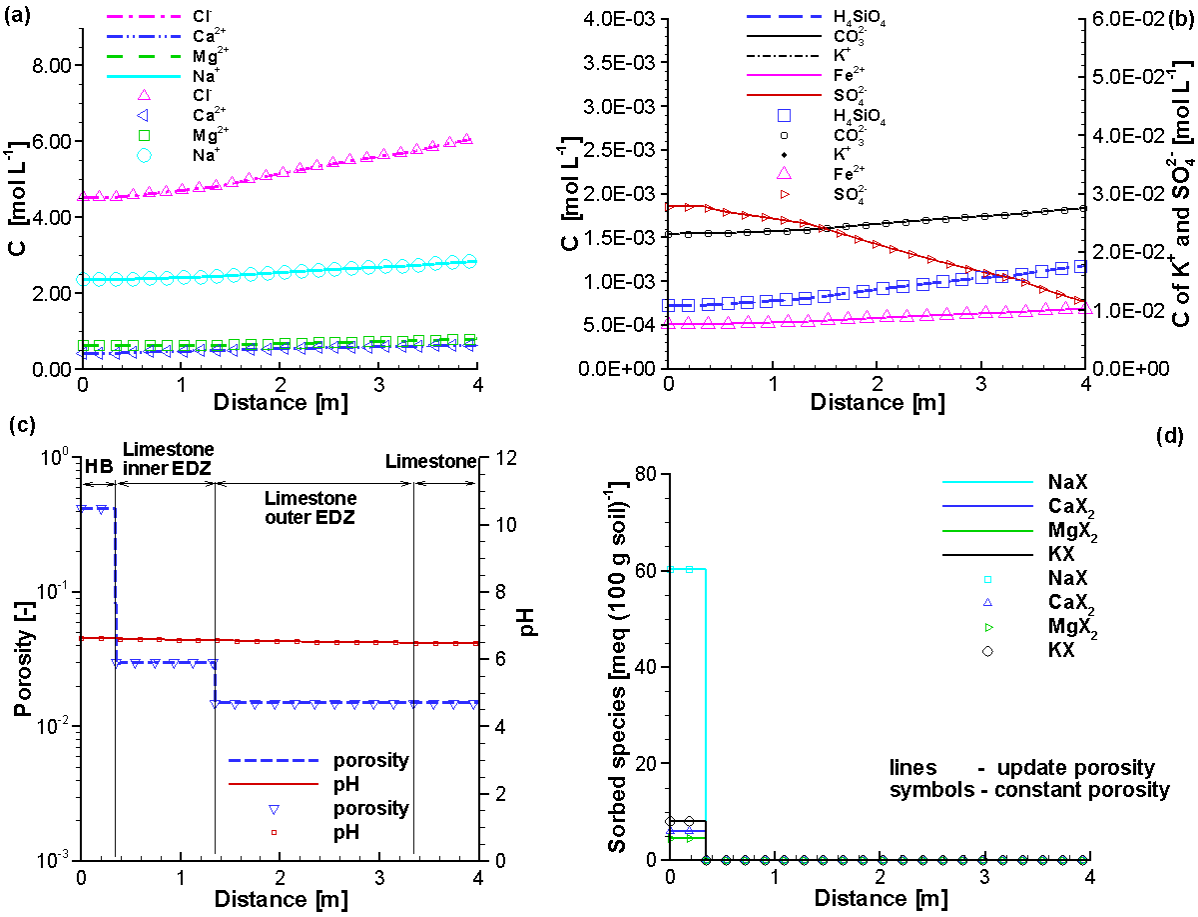

Figure A- 71: Profiles of Component Concentrations at 1,000 Years (Symbols - Case 4EDZCP, Lines - Case 4EDZUP)

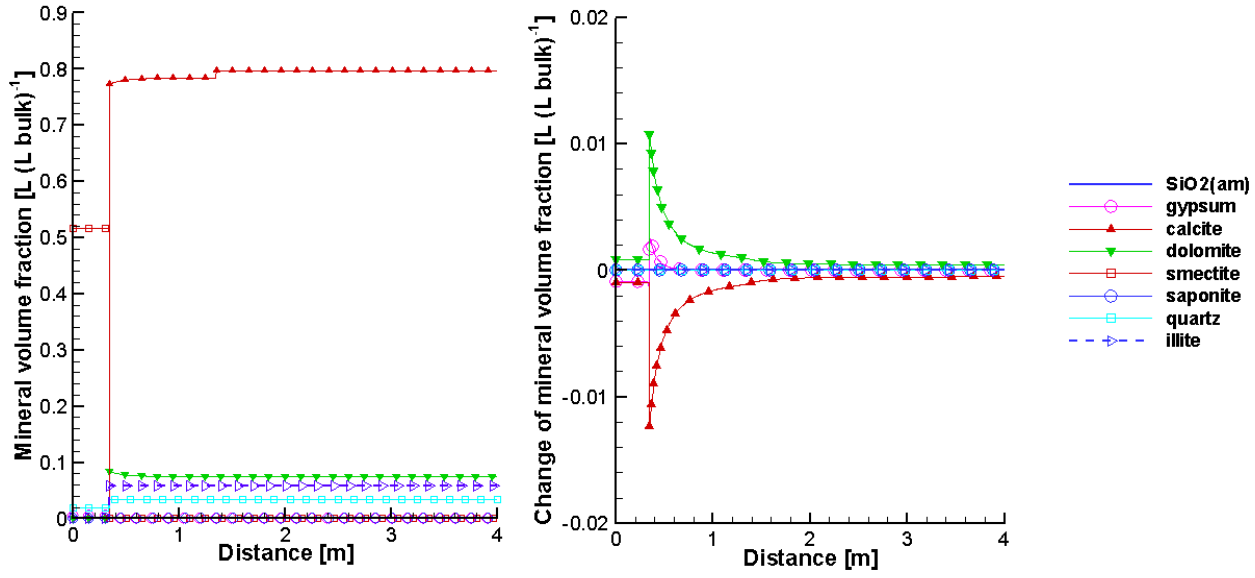

Figure A- 72: Profiles of Volume Fractions of Minerals (Left) and Their Changes (Right) at 1,000 Years (Case 4EDZUP)

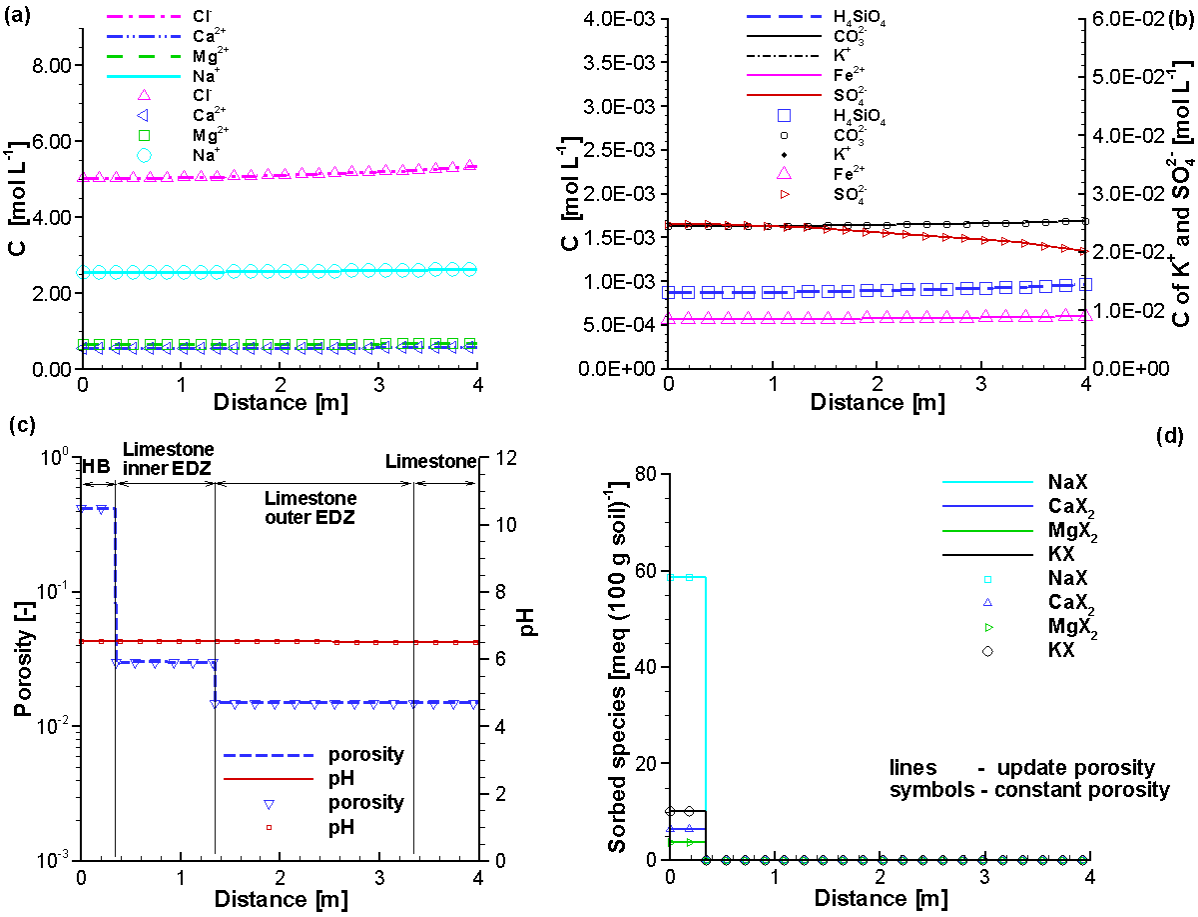

Figure A- 73: Profiles of Component Concentrations at 10,000 Years (Symbols - Case 4EDZCP, Lines - Case 4EDZUP)

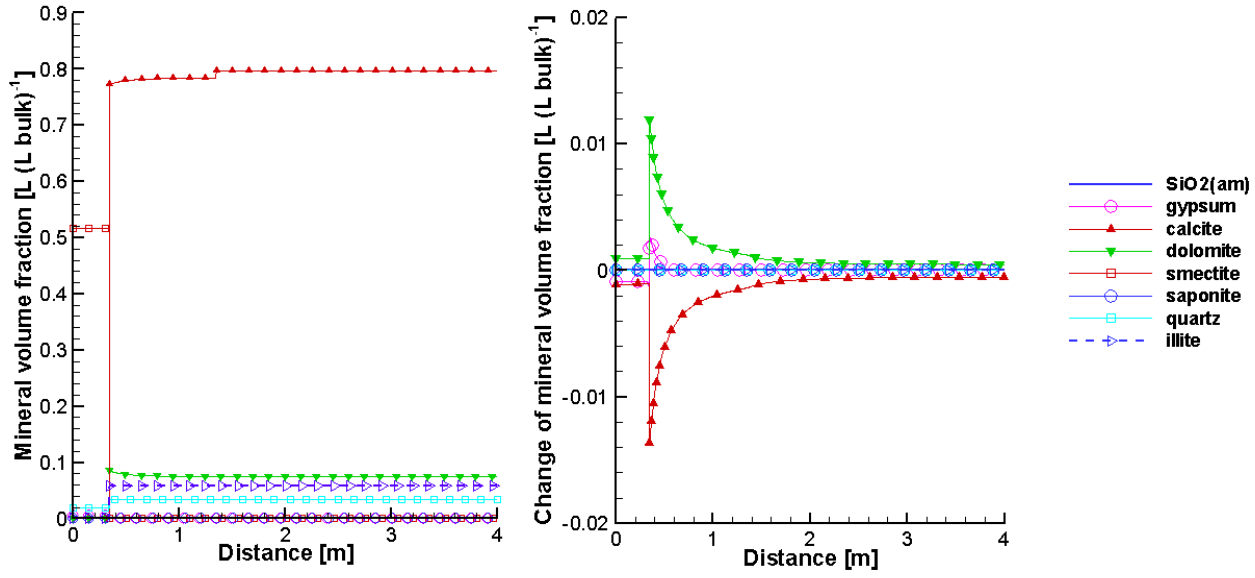

Figure A- 74: Profiles of Volume Fractions of Minerals (Left) and Their Changes (Right) at 10,000 Years (Case 4EDZUP)

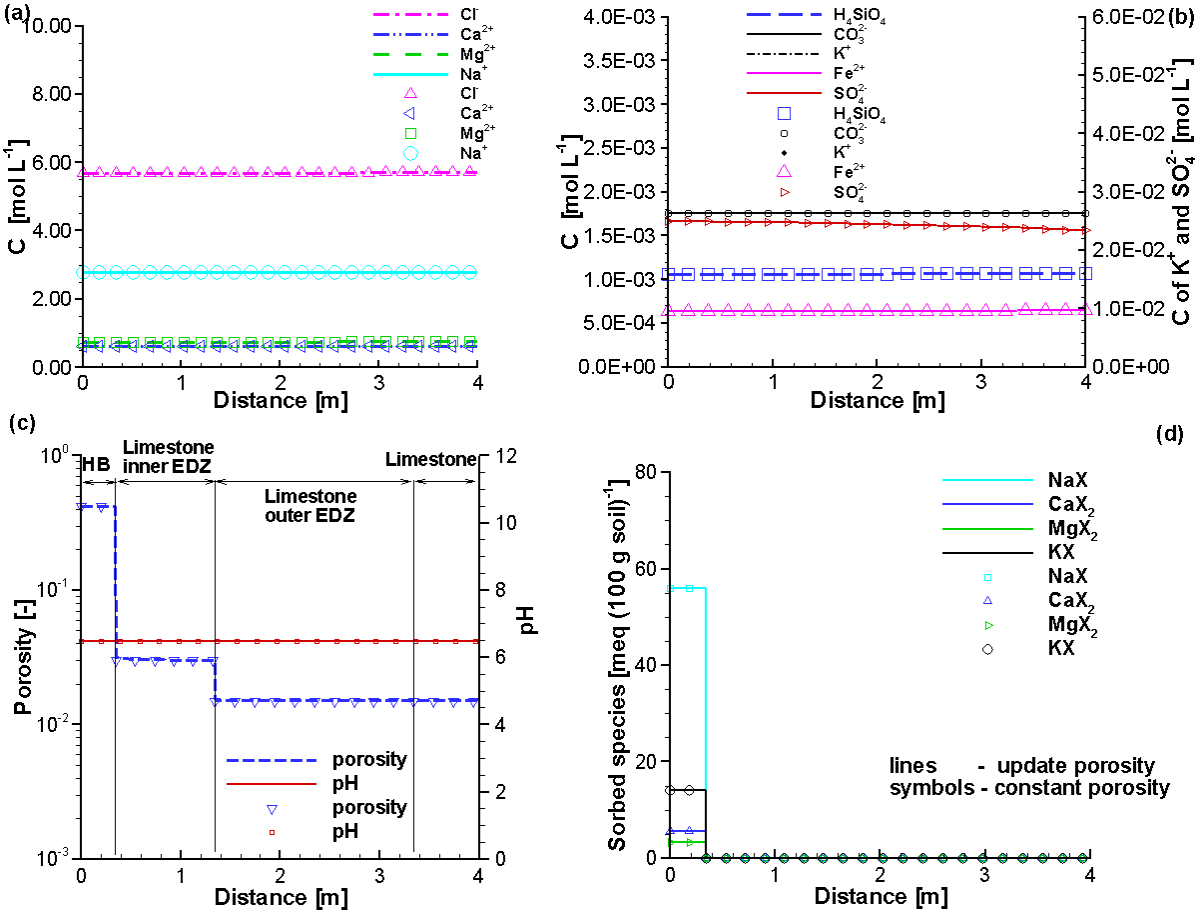

Figure A- 75: Profiles of Component Concentrations at 100,000 Years (Symbols - Case 4EDZCP, Lines - Case 4EDZUP)

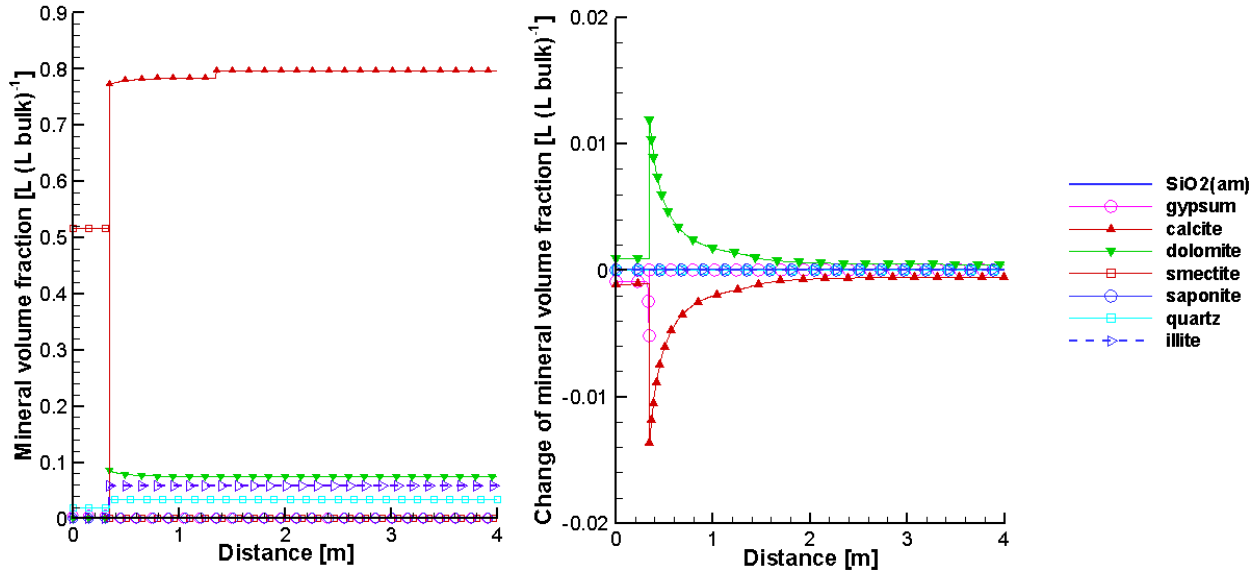

Figure A- 76: Profiles of Volume Fractions of Minerals (Left) and Their Changes (Right) at 100,000 Years (Case 4EDZUP)

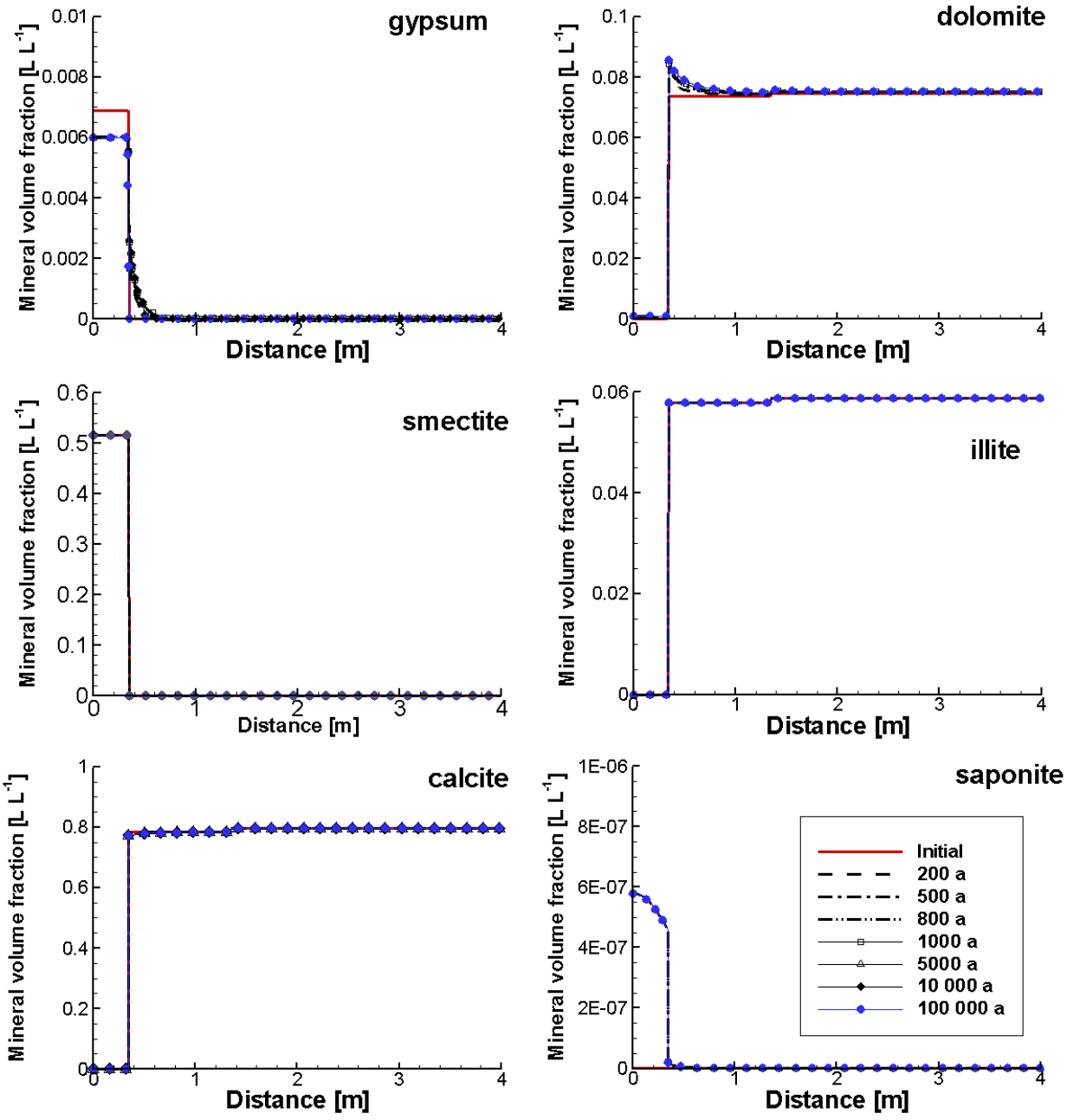

Figure A- 77: Profiles of Mineral Volume Fractions at Selected Times (Case 4EDZUP)

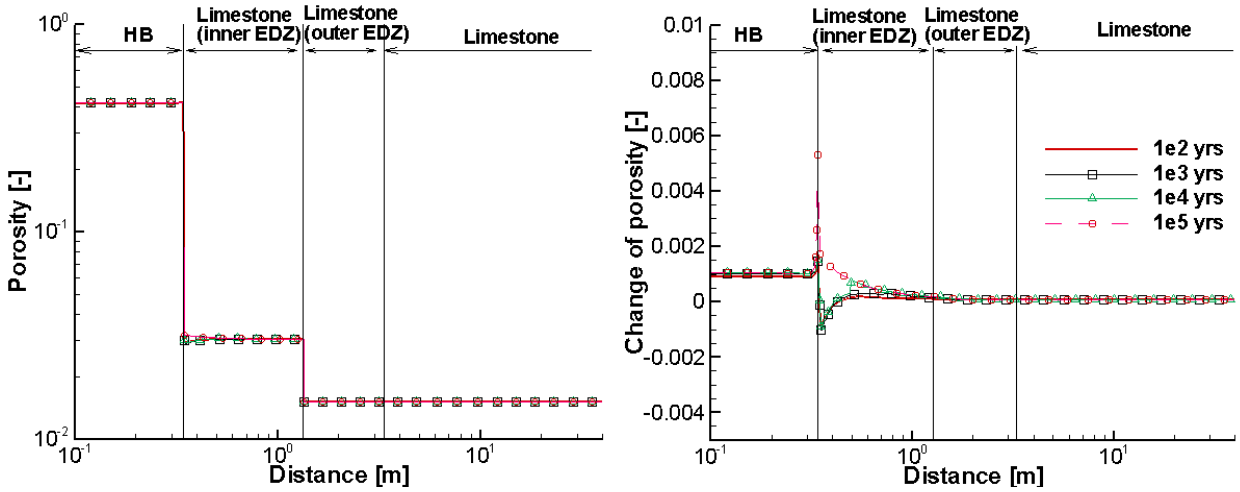

Figure A- 78: Profiles of Porosity (Left) and Porosity Changes at Selected Times (Case 4EDZUP)

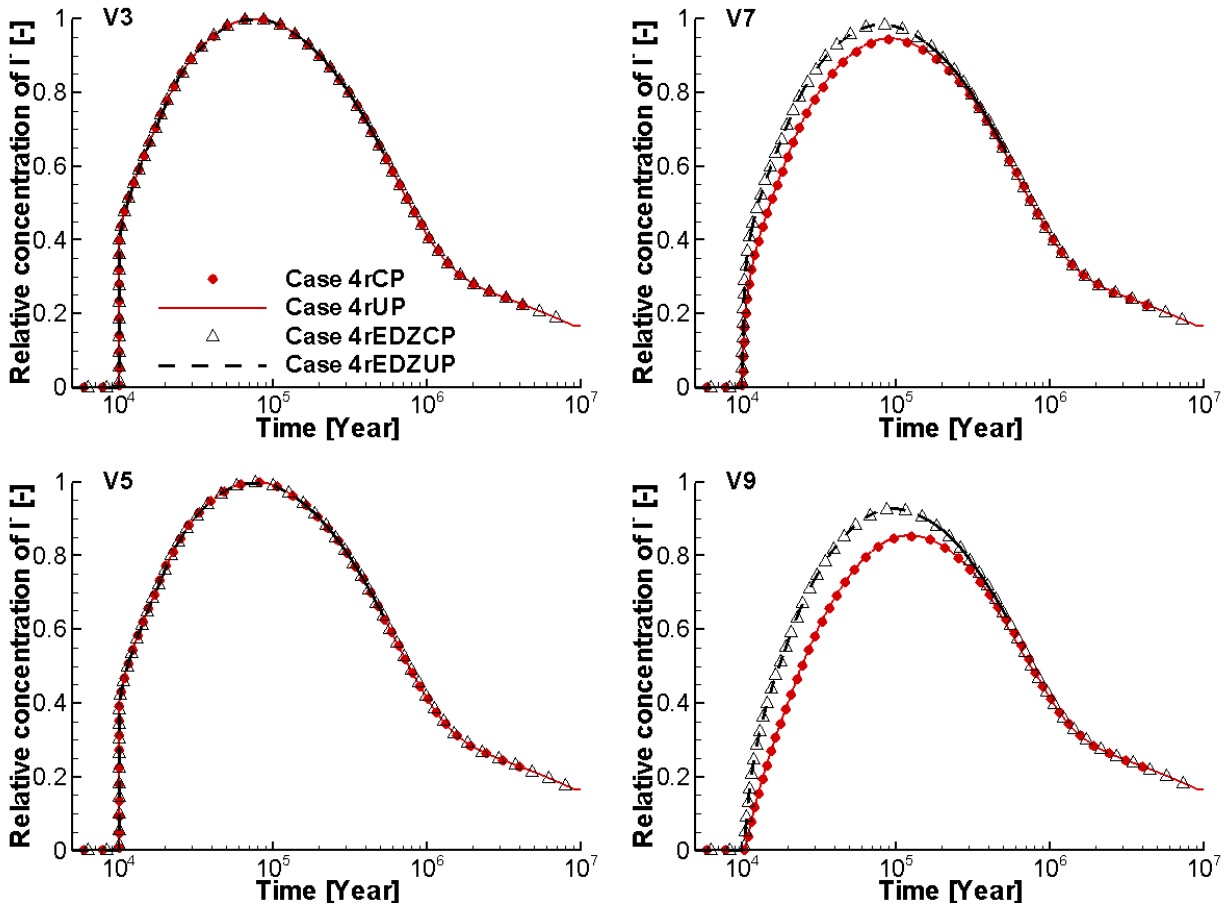

Figure A- 79: Breakthrough Curves at Selected Observation Points for a Small Defect Occurring at 10,000 Years for Cases 4rCP, 4rUP, 4rEDZCP and 4rEDZUP. V3 (HB), V5 (Inner EDZ), V7 (Outer EDZ) and V9 (Intact Limestone)

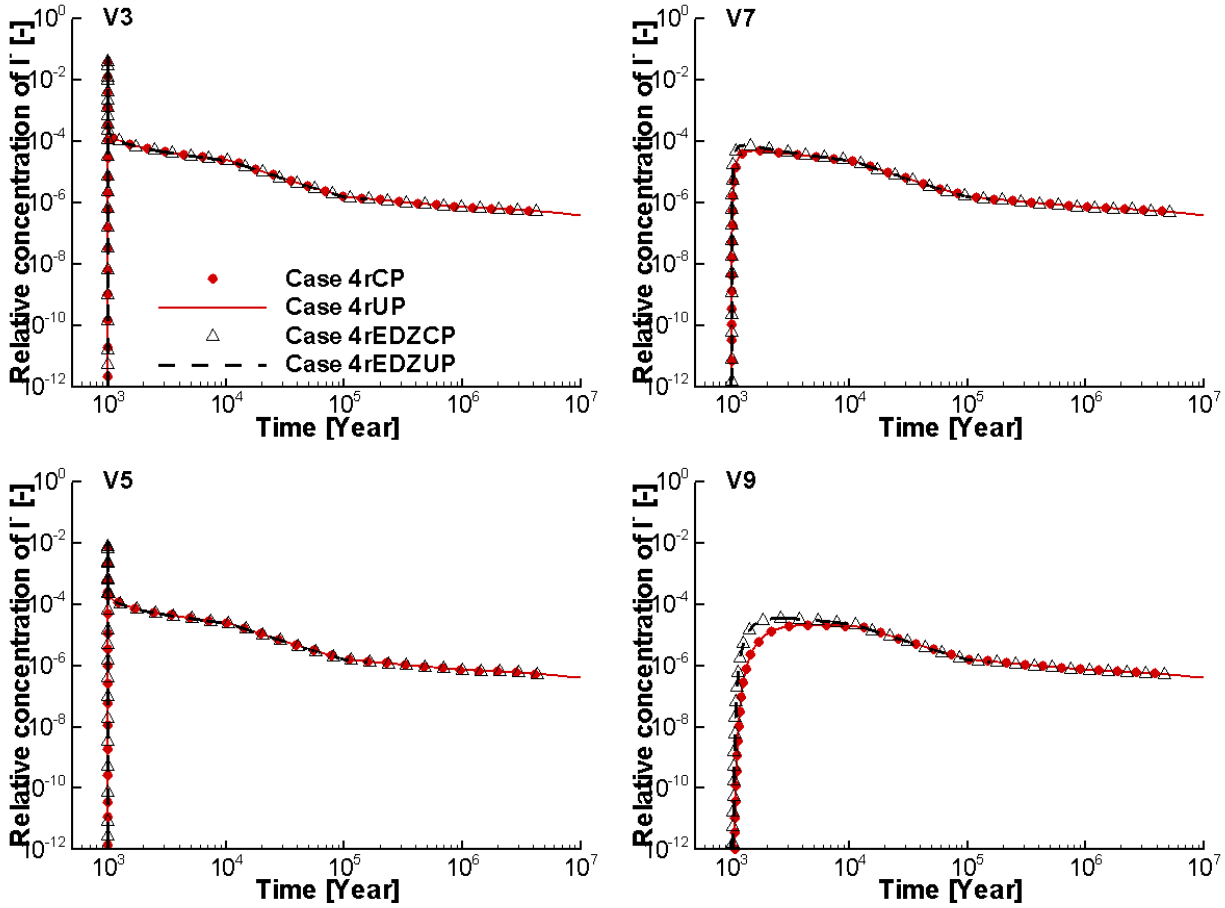

Figure A- 80: Breakthrough Curves at Selected Observation Points for a Large Defect Occurring at 1,000 Years for Cases 4rCP, 4rUP, 4rEDZCP and 4rEDZUP. V3 (HB), V5 (Inner EDZ), V7 (Outer EDZ) and V9 (Intact Limestone)

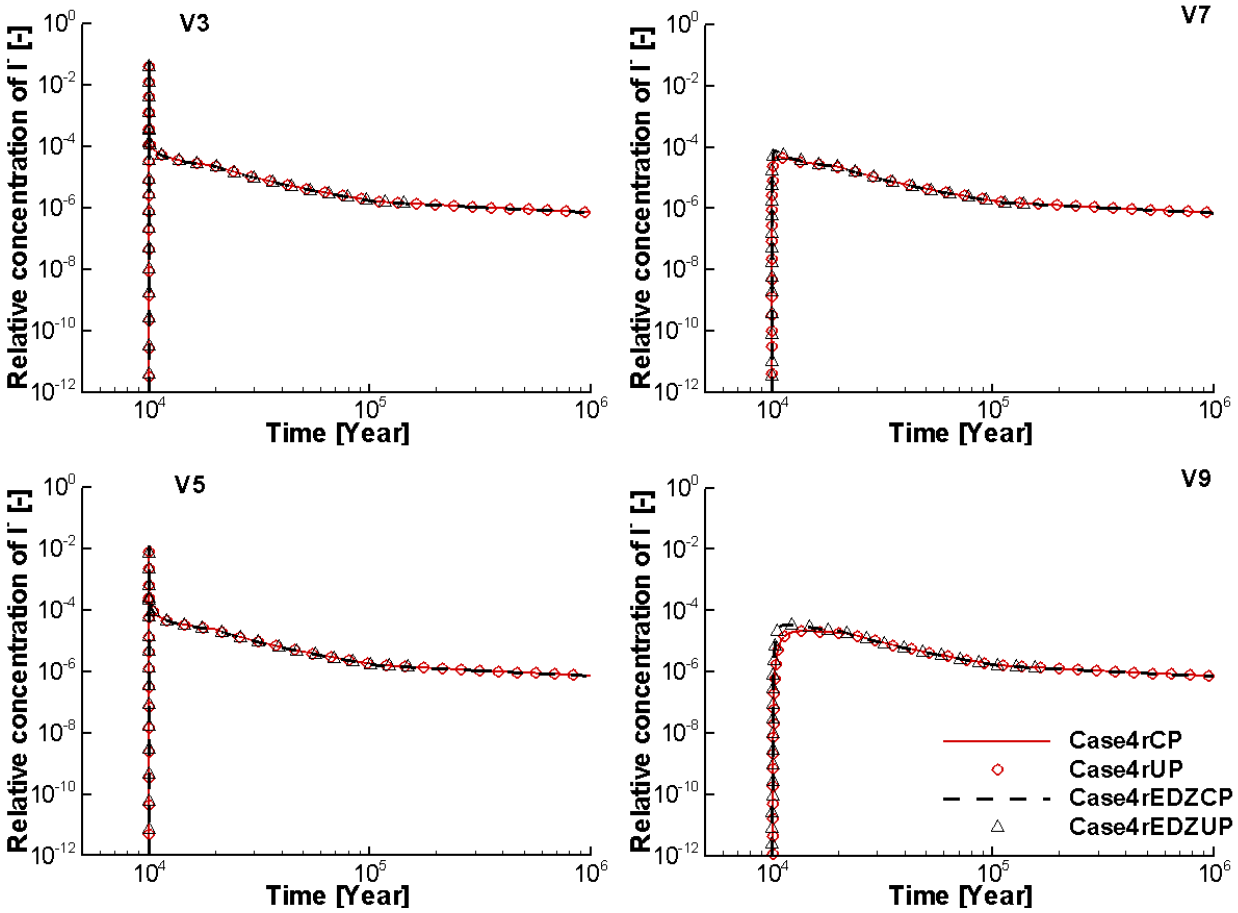

Figure A- 81: Breakthrough Curves at Selected Observation Points for a Large Defect Occurring at 10,000 Years for Cases 4rCP, 4rUP, 4rEDZCP and 4rEDZUP. V3 (HB), V5 (Inner EDZ), V7 (Outer EDZ) and V9 (Intact Limestone)

REFERENCES A

AMEC. 2015. APPENDIX A-P - CRH CEMENT TYPE GU, Project Number TB152037.

Bea, S.A., K.U. Mayer and K.T.B. MacQuarrie. 2011. Modelling Reactive Transport in Sedimentary Rock Environments - Phase II MIN3P code enhancements and illustrative simulations for a glaciation scenario. Nuclear Waste Management Organization Technical Report NWMO TR-2011-13.

Blanc, P., V. Philippe, H. Gailhanou, S. Gaboreau, N. Marty, F. Claret, B. Made and E. Giffaut. 2015. ThermoChimie Database Developments in the Framework of Cement/Clay Interactions. Applied Geochemistry. 10.1016/j.apgeochem.2014.12.006.

Hobbs, M.Y., S.K. Frape, O. Shouakar-Stash and L.R. Kennell. 2011. Regional Hydrogeochemistry -Southern Ontario. Nuclear Waste Management Organization Report NWMO DGR-TR-2011-12 R000. Toronto, Canada.

Kulik, D.A. 2011. Improving the Structural Consistency of C-S-H Solid Solution Thermodynamic Models. Cement and Concrete Research 41(5):477-495.

Kulik, D.A., T. Wagner, S.V. Dmytrieva, G. Kosakowski, F.F. Hingerl, K.V. Chudnenko and U. Berner. 2013. GEM-Selektor geochemical modeling package: revised algorithm and GEMS3K numerical kernel for coupled simulation codes. Computational Geosciences 17, 1-24.

Lothenbach, B., T. Matschei, G. Möschner and F.P. Glasser. 2008. Thermodynamic modelling of the effect of temperature on the hydration and porosity of Portland cement. Cement and Concrete Research, 38 (2008), pp. 1-18

Lothenbach, B., K. Scrivener and R.D. Hooton. 2011. Supplementary cementitious materials. Cement and Concrete Research, 41 (12), pp. 1244-1256.

Parkhurst, D.L. and C.A.J. Appelo. 2013. Description of input and examples for PHREEQC version 3 − A computer program for speciation, batch-reaction, one-dimensional transport, and inverse geochemical calculations: U.S. Geological Survey Techniques and Methods, book 6, chap. A43, 497 p. http://pubs.usgs.gov/tm/06/a43/.